ACOUSTIC PHASE MEASUREMENTS FROM VOLUME SCATTER IN THE OCEAN

ACCEPTED
FACULTY OF GRADUATE STUDIES

DEAN

DATE

by

Robert Delmar Huston

B.Sc., University of Victoria, 1983

A THESIS SUBMITTED IN PARTIAL FULFILLMENT OF THE
REQUIREMENTS FOR THE DEGREE OF
DOCTOR OF PHILOSOPHY

in the Department of Physics

We accept this thesis as conforming to the required standard

Dr. D. M. Farmer

Dr. A. D. Booth

Dr. R. E. Horita

Dr. J. T. Weaver

Dr. G. O. Mackie

Dr. M. B. Hocking

Dr. T. Sanford

UNIVERSITY OF VICTORIA &
INSTITUTE OF OCEAN SCIENCES

MAY 1987

PARTIAL COPYRIGHT LICENSE

Title of Thesis:

ACOUSTIC PHASE MEASUREMENTS FROM VOLUME SCATTER
IN THE OCEAN

Author

R. Del Huston
May 11, 1987

Supervisors: Dr. D.M. Farmer and Dr. R.E. Horita

ABSTRACT

A primary goal of this thesis has been to demonstrate that stable, useful measurements of the orientation of the acoustic signal vector as a function of range and time can be obtained from ocean backscatter, and that this orientation, or acoustic phase, can be related to the local sound speed distribution. Such a measurement is quite distinct from the related problem of detecting the rate of phase change, which forms the basis of Doppler technology. Doppler measurements can be made using echoes from a single point, or a sparsely distributed set of targets. Consistent and useful measurement of absolute phase is inherently more difficult, since it depends upon the positions of individual scatterers, which are normally random and sparse relative to the acoustic wavelength.

This difficulty has been overcome by coherent superposition of echoes from successive transmissions, such that the effective density of acoustic targets progressively increases as the summation proceeds. The theoretical basis of this type of coherent processing has been developed and examined in the limiting case, in which it approximates a scatterer continuum for which an analytic expression has been found. An important simplification in this development is the use of the single scatter approximation which remains valid, even in the limit, since individual transmissions result in echoes from a sparsely distributed set of scatterers. The theory provides fundamental insights to the behaviour of both the amplitude and phase of volume scatter.

It has been shown that coherent superposition of echoes from successive transmissions may be represented by complex Ricean statistics. As the ratio of coherent to incoherent signal increases with successive superposition of the echoes, the phase statistics evolve from a uniform to a nearly Gaussian distribution. The rate at which the ratio of coherent to incoherent signal changes as a function of the number of superpositions, is related to the density of acoustic targets in the scattering volume. Once the phase signal is bounded to within ±45°, the basic requirement for a coherent 'volume mirror' has been met and reliable interferometric estimates are possible.

The experimental work serves to confirm the theoretical concepts and demonstrates that within the quite limited range of environmental conditions that were studied, the acoustic results are consistent with independent measurements of the evolving sound speed profile. Further experiments and instrument development are required before the full potential of the concept can be demonstrated. The main contribution of this thesis has been to lay a firm theoretical and experimental foundation for the use of volume backscatter in acoustic interferometer devices. Based on these results, the potential for new types of oceanographic measurements using these techniques appears both realistic and encouraging.

Examined by:

Dr. D. M. Farmer

Dr. A. D. Booth

Dr. R. E. Horita

Dr. J. T. Weaver

Dr. G. O. Mackie

Dr. M. B. Hocking

Dr. T. Sanford

TABLE OF CONTENTS

EXPERIMENTAL RESULTS:

LIST OF FIGURES

LIST OF TABLES

ACKNOWLEDGMENTS

This research project represents contributions from many individuals. Drs. David Farmer and Donald Booth provided the foundation to this stage of my education. Their combined experience provided me with direct access to the tools of the trade but more important was the inspiration they provided which helped me to persevere through the difficult stages of this project. Technical support from Grace Kamitakahara-King (computer programing) and Ron Teichrob (electronics and system design) made it possible to interface theory with the real world - in addition to answering a multitude of questions.

The implementation of this work was made possible through the facilities and staff of the Institute of Ocean Sciences, Sidney, B.C., Canada. A number of individuals were of particular assistance, namely; Dr. A. Bennett, George Chase, and Netta Delacretaz. Engineering support was given through Jim Galloway, Bob Smith, Jim Steeples, and Don Redman.

The crew and captain of the VECTOR and crew of the PENDER gave practical assistance throughout the experimental stages of the project. The cooperation of Ships Division at IOS in coordinating our special requests is greatly appreciated.

I must also thank my fellow graduate students: Len Zedel, Svein Vagle, Ben Huber, Richard Dewey ~~and~~ Greg Crawford for the many discussions on science and life in general.

Special notice must be given to Dr. Yannis (John) Papadakis whose philosophical discussions broadened my view of science.

Financial support was from the Department of Fisheries and Oceans, the National Oceanographic and Atmospheric Administration (U.S.), the Natural Sciences and Engineering Research Council, and the University of Victoria.

This work owes much to the initial support of our sponsors, Bill Woodward and John Gilheaney and to Ted Brown who first thought of the echometer principle and stimulated interest in this project.

Finally, the emotional support and encouragement from my loving wife Diane must be fully recognized. She helped provide the stability I needed.

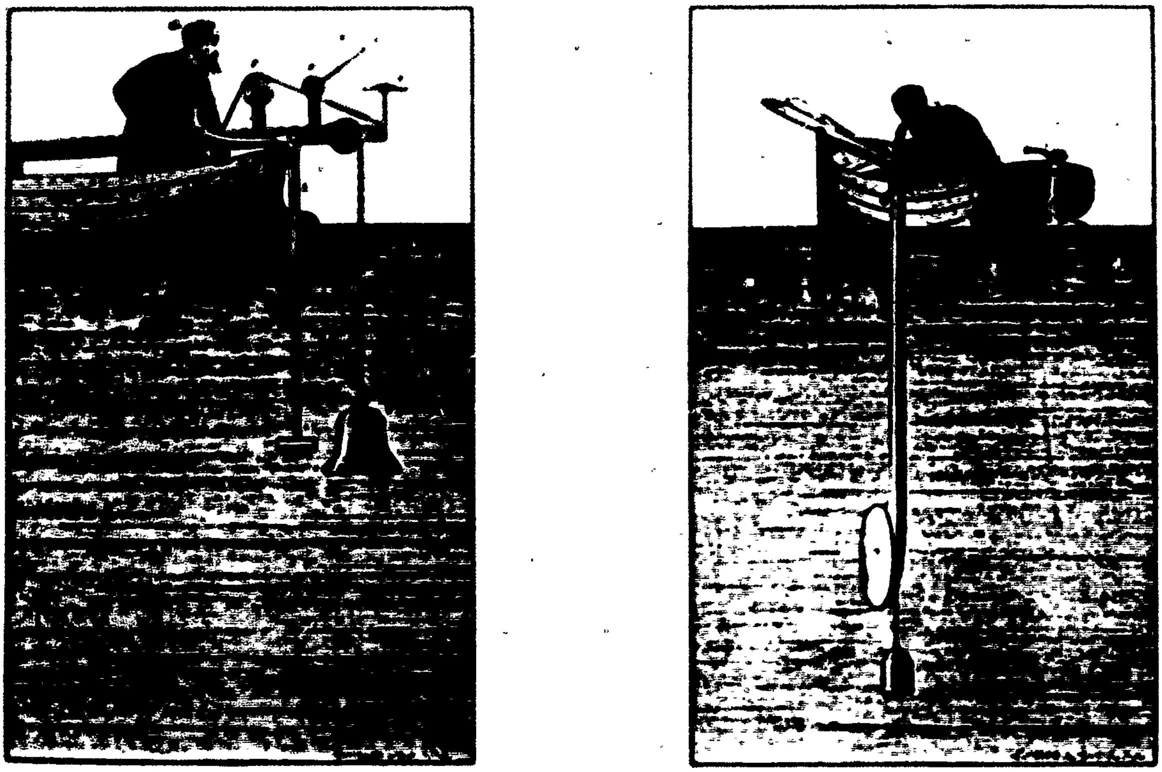

Earliest measurement of the speed of sound in water. "I had my station at Thonon, my ear attached to the extremity of an acoustic tube. The boat was oriented so that my face was turned in the direction of Rolle. I was thus able to see the light accompanying the striking of the bell and to hold the watch which served to measure the time taken by the sound to reach me." (J.D. Colladon, *Souvenirs et memoires, Aubert-Schuchardt, Geneva, 1893*).

INTRODUCTION

This thesis is concerned with the scattering of sound by particles in the ocean. The subject has a long history, not only from the viewpoint of zooplankton (i.e. Holliday and Peiper, 1980) and more recently bubble studies (i.e. Thorpe, 1982), but also from the perspective of remote velocity sensing through Doppler and related techniques (Pinkel, 1980; Dickey, 1981). Previous effort has focussed on two aspects of backscattered sound: (i) the amplitude of the signal and its associated statistics (Stanton and Clay, 1986), and (ii) the rate of phase change or Doppler spectrum. The research described in this thesis involves the related, but quite different, property of the absolute orientation of the received signal vector in phase space at a particular range and time.

The absolute phase of backscattered sound becomes important when we attempt to use the distributed acoustic scatterers in the ocean (chiefly zooplankton at the frequencies of interest in this study) as a 'volume mirror', capable of providing consistent and coherent backscatter at one end of an acoustic interferometer. For typical scatterer distributions the sparse and random nature of the targets causes the received phase signal also to be random. If it can be made to work, however, the potential of such a device is far-reaching. A primary application, and the one that provided the motivation for the present study, is the remote detection of vertical temperature profiles. Remote temperature profiling, or strictly speaking, sound speed profiling instruments, mounted on ships of opportunity traversing the world's oceans, would constitute a valuable measurement scheme for climatic and other oceanographic studies, supplementing satellite and moored instrument data, and adding to our limited knowledge of processes in the upper ocean boundary layer. Acoustic measurements are particularily attractive for this purpose, since in principle they can be left unattended for long periods, do not involve the use of towed or expendable devices, and need have no moving parts.

The basic concept for such an instrument was first described by Brown, Little and Wright (1978) and preliminary atmospheric (Brown and Keeler, 1981) and oceanographic (Brown et al., 1984) tests were carried out. These tests confirmed the operational characteristics of the special projector, which generates a series of narrow fringes by wave interference, and provided suggestive but inconclusive measurements of the sound speed and/or temperature profile.

In June 1985 a new set of measurements were carried out from the I.O.S. research vessel VECTOR, using essentially the same technique as Brown et al. (1984). A careful analysis of the results showed that the phase signal was completely random. The problem arises from the fact that the acoustic targets are *far apart from each other relative to the acoustic wavelength.* This result identified the essential challenge of this thesis: How to use the echo from sparse, randomly spaced targets in the ocean, as a reflective component of an acoustic interferometer, and how to interpret the results in terms of the acoustic environment.

The work evolved through an alternating sequence of experiments, modelling studies and theoretical analysis, as an understanding of the basic principles, coupled with useful field measurements, gradually advanced. The thesis has been organized systematically rather than chronologically. The first 7 chapters present the principles involved in the extraction of stable phase signals from volume backscatter. Chapter 1 gives the motivation and defines the system geometry used subsequently. This is followed by an analysis of acoustic arrival times for a linear profile (Chapter 2) and a discussion and error analysis of various acoustic backscatter sound speed profiling approaches. Environmental factors other than sound speed are addressed in Chapter 3. A numerical model of the discrete system is discussed in Chapter 4. The general theory of an ideal scattering continuum (Chapter 5) provides a basis for the coherent processing technique. Chapter 6 covers the statistical principles for scattering from discrete targets, including the statistical mechanism by which a random phase signal can evolve to a stable mean phase through coherent processing. Chapter 7 addresses the physical basis underlying the second moment of the received phase, which has interesting measurement applications unrelated to the sound speed properties.

The final chapters of the thesis incorporate the results of the experimental work. Chapter 8 describes the apparatus and discusses the evolution of the experimental methods. The results of transducer calibrations are given in Chapter 9. The data collected from a cruise on the research barge PENDER (November, 1985) are given a detailed analysis in Chapters 10, 11 and 12. A final chapter summarises the results of this work and makes recommendations for further areas of research.

The experimental work serves to confirm the theoretical concepts and demonstrates that within the quite limited range of environmental conditions that were studied, the acoustic results are consistent with independent measurements of the evolving sound speed profile. Further experiments and instrument development are required before the full potential of the concept can be demonstrated. The main contribution of this thesis has been to lay a firm theoretical and experimental foundation for the use of volume backscatter in acoustic interferometer devices. Based on these results, the potential for new types of oceanographic measurements using these techniques appears both realistic and encouraging.

1 MOTIVATION AND SYSTEM CONFIGURATION

A variety of methods have been developed to measure the speed of sound in sea water (c): This measurement was among the earliest of investigations in the propagation of sound in water. In 1827, Colladon and Sturm, set up an experiment in Lake Geneva (Wood, 1941). With an apparatus which simultaneously struck a bell underwater and produced a flash of light, an observer in a boat measured the delay in arrival time of the sound source. The results gave an estimate of 1440m/s at 8.1°C which only differs by 0.8m/s from the modern value in distilled water. This first example relied simply on measuring the arrival time in a fixed path length system to estimate the speed of sound propagation. The next development in measuring c utilized Newton's equation which states,

$$c = \sqrt{K/\rho} \tag{1.1.1}$$

where K is the adiabatic volume elasticity and ρ is the fluid density. From this equation and static measurements of density at various pressures, the first tables of c as a function of temperature T, and salinity S were obtained. With the improvements in electronics in the post World War II years a variety of techniques developed which utilized measurement of the pulse arrival time over a known path length within a small volume of sea water (Urick, 1982). By combining laboratory and oceanographic measurements empirical relationships have been derived which relate c with T, S and depth z. A variety of the relationships are available in the literature with accuracies ranging from 1m/s to 0.05m/s. The formulation used in this thesis was developed by Mackenzie (1977) and gives,

$$\begin{aligned} c = {} & 1448.96 + 4.1591T - 5.340 \times 10^{-2}T^2 + 2.374 \times 10^{-4}T^3 \\ & + 1.340(S-35) + 1.630 \times 10^{-2}z + 1.657 \times 10^{-7}z^2 \\ & - 1.025 \times 10^{-2}T(S-35) - 7.139 \times 10^{-13}Tz^3 \end{aligned} \tag{1.1.2}$$

This equation is accurate to within ±0.07m/s over the ranges, $0 \leq T \leq 30°$C, $30 \leq S \leq 40$ppt and $0 \leq z \leq 8000$m.

From an oceanographic point of view, much of the interest in knowing sound speed properties, stems from this relationship to the variables S, T and pressure. These variables in turn determine the density field associated with the dynamics, and the temperature field associated with the heat content and heat flux of the ocean. For sound propagation studies, the sound speed distribution itself is crucial.

Measurements of the sound speed depth profile, $c(z)$, at a given location require lowering a probe which can be used to measure $c(z)$ at discrete depths. In the oceans the main changes in $c(z)$ usually occur in the top 300m. This region contains the seasonal thermocline which corresponds to seasonal heating and cooling effects. The initial motivation behind this thesis was to develop a technique for remotely measuring $c(z)$ in the upper ocean.

A remote measurement of $c(z)$ requires a projector which transmits an acoustic pulse, a reliable scattering mechanism to reflect the pulse and a receiver which detects the pulse. As in the original sound speed measurements, the path length must be known. For a monostatic echosounder (transmitting and receiving vertically from the same transducer) the pulse arrival time T is given by,

$$T = 2\int_0^z c^{-1}(\zeta)d\zeta. \tag{1.1.3}$$

Both z and T must be independently measured to be useful in estimating $c(z)$. Since it is impractical to suspend fixed targets at discrete depths in the ocean an alternative transducer configuration is a preferable solution. By separating the projector and hydrophone, and using transducers with narrow angular beams, the spatial location of the scattering volume is determined by the projector angle θ (see Figure 1.1) and baseline separation b. This mode of operation is called a bistatic configuration. The details of estimating $c(z)$ with this system are presented in chapter 2.

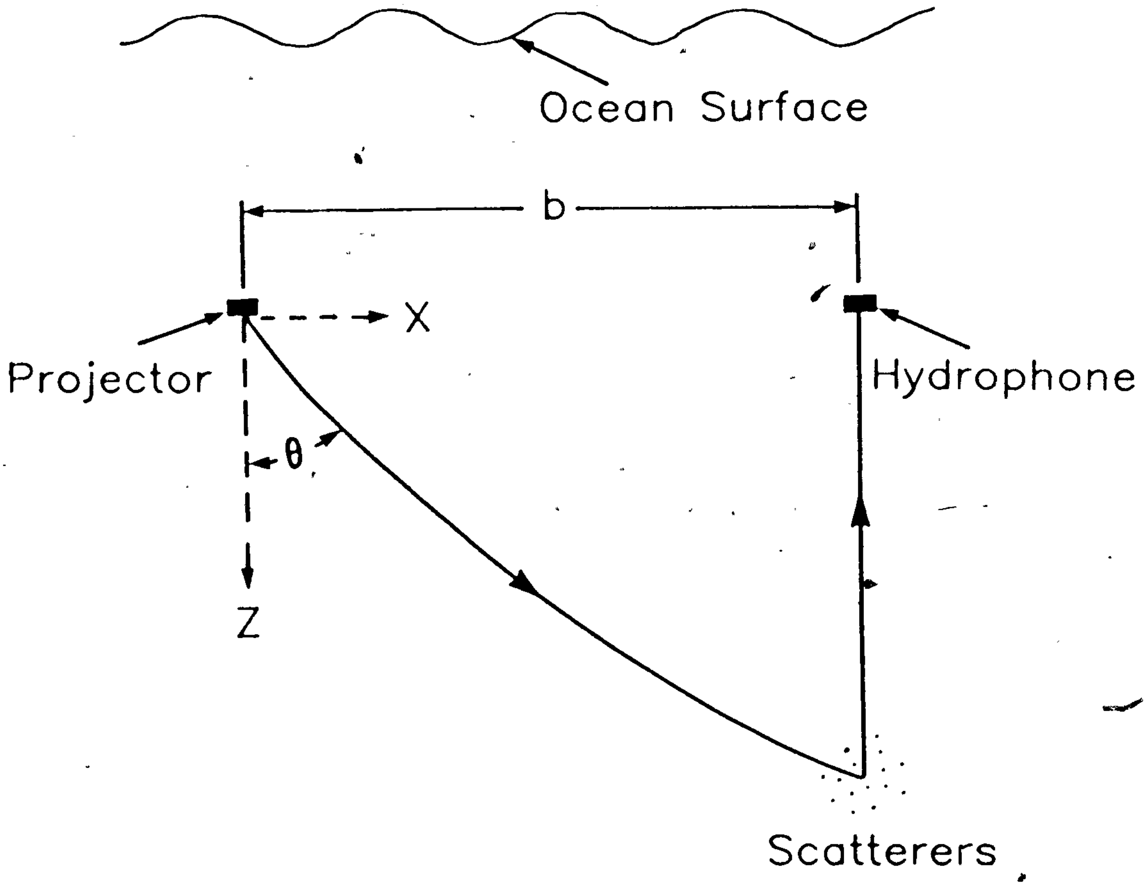

Figure 1.1 A schematic of an acoustic bistatic configuration showing the basic geometry for a single ray tracing between the projector and hydrophone.

The effects of refraction are best measured in the frequency (f) range for which ray theory applies. The principles of ray tracing are valid when

$f >> 100$ Hz and $dc/dz < f$. This latter constraint simply states that the sound speed changes very little over a distance of one acoustic wavelength. The benefits of ray theory are that the propagation properties are independent of frequency and follow Snell's Law. For a linear sound speed profile, $c = c_o + gz$, it can be shown (Urick, 1982) that the radius of curvature (R) of a ray with initial angle θ (relative to the vertical) is given by,

$$\frac{1}{R} = -\frac{g \sin\theta}{c_o}. \tag{1.1.4}$$

This shows that a positive sound speed gradient causes upwards refraction while a negative gradient causes downwards refraction.

The transducers in the bistatic configuration (Figure 1.1) both need narrow beam angles. The design of transducers is a complicated task however and fundamental constraints serve to bound the design criteria. Beam angles are dependant on physical size and operating frequency. For example, a circular piston with radius a (in m) and frequency f (in Hz) has a beam width (BW) (in degrees) which is approximated by:

$$BW \simeq \frac{4.572 \times 10^4}{fa}, \tag{1.1.5}$$

where BW is relative to the -3dB (half power) levels. With this relationship we see that a one degree BW can be obtained when $fa = 4.573 \times 10^4 s^{-1} m$. Large piezoelectric transducers ($a > 3cm$) become increasingly difficult and expensive to produce so that very high frequencies ($f >$ 1MHz) become necessary to achieve narrow beam angles. Operation in the MHz region is often undesirable since the absorption properties of sea water and scattering off particulates greatly reduces the effective range of transmissions. For example, at 1MHz absorption reduces the signal intensity by approximately 0.5dB/m, while a 100kHz signal would only be reduced by approximately 0.05dB/m. An alternative method for achieving narrow beams, is to use an array composed of smaller transducers.

The properties of a linear array of point sources can be derived from first principles (Kinsler, et al., 1982). The angular beam pattern relationship between N elements in a linear array with equal spacing d and wavenumber k, is given by,

$$H^2(\theta) = \frac{1}{N^2}\frac{\sin^2(\frac{N}{2}kd\sin\theta)}{\sin^2(\frac{1}{2}kd\sin\theta)} \tag{1.1.6}$$

where $H^2(\theta)$ is the normalized intensity relative to $\theta = 0$. This representation is valid for ranges r which are bounded by $r >> (N-1)d$ (the far field). The resulting beam pattern is characterised by dominant peaks (fringes), and subsidiary maxima (side lobes) which are separated by sharp null locations. The fringe locations occur whenever $\frac{1}{2}kd\sin\theta = m\pi$, since $H(\theta) = 1/N$ (both numerator and denominator vanish). The angular fringe relationship in the far field is then given by,

$$\sin\theta = \frac{mc}{fd} \qquad m = 0,1,2,...,M \tag{1.1.7}$$

where $M = int(fd/c)$ is the number of fringes within $0 \leq \theta \leq 90^o$.

The beamwidth of a fringe is found by setting

$$x \pm \Delta x = \frac{1}{2}kd\sin(\theta \pm d\theta) \tag{1.1.8}$$

and finding Δx when $H^2(\theta) = 1/2$ (the half power points of the fringe). Since $\sin(Nx) = 0$ at a fringe location equation 1.1.6 reduces to give,

$$\sin(N\Delta x) - \frac{N}{\sqrt{2}}\sin\Delta x = 0. \tag{1.1.9}$$

Roots of this equation for a given N can be found by a numerical method (i.e. bisection or Newton-Raphson). Solutions for $2 \leq N \leq 10$ are given in Table

1.1 and show that the relative change in Δx diminishes as N is increased. The projector used in the experimental work of this thesis used $N = 6$ and $M = 14$ so that 14 narrow fringes with narrow beams could be generated. This projector will further be referred to as the "echometer projector".

Table 1.1 Numerically derived solutions to equation 1.1.9 for the first 10 values of N.

N	Δx
1	π
2	0.7854
3	0.4878
4	0.3577
5	0.2832
6	0.2348
7	0.2006
8	0.1751
9	0.1554
10	0.1398

The beam width of a fringe ($BW = 2d\theta$) is related to Δx by,

$$BW = \frac{2\lambda\Delta x}{\pi d\cos\theta} \qquad \text{[in rad]} \tag{1.1.10}$$

so for the projector with $d/\lambda \simeq 14$ and $\Delta x = 0.2348$ the beam width of a fringe is approximately $0.6/\cos\theta$ [deg].

This treatment of beam properties has been confined to the vertical plane (xz plane) which contains the linear array. Appendix 1 looks at the three dimensional properties of a fringe and confirms that equation 1.1.7 is valid for small angular deviations ϕ in the xy plane. A fringe occurs whenever the distance between a position in space and an array element differs by $m\lambda$ from an adjacent array elements distance to the same spatial position. Thus, for array elements composed of point sources lying on the x axis, the fringes will have cylindrical symmetry about the x axis (i.e. $H^2(\theta,\phi) = H^2(\theta)$).

When an array is composed of transducers with individual beam patterns given by $G^2(\theta,\phi)$, the product theorem (Kinsler, 1982), states that the beam pattern of an array of identical sources is the product of $H^2(\theta,\phi)$ and $G^2(\theta,\phi)$. So if the individual array elements have a 10 degree beam width which is symmetric about the z axis then the composite beam pattern will be reduced to 10 degrees in the yz plane, while only the relative intensities of the fringes in the xz plane will be affected.

The hydrophone used in the experimental work is a 2 dimensional array with its elements arranged in concentric rings. The resulting beam pattern has a nominal 1^o beam width which is symmetric about its z axis. Numerical simulations and direct calibrations of both the echometer projector and the hydrophone have been performed (see chapter 9).

The volume of insonification V_i, is defined by the 3 dimensional intersection of a fringe with the hydrophone beam. By using the half power (-3dB) points to define the boundaries, the volume resembles a conic section which is sliced by the projector beams (see Figure 1.2). The volume defined by these beams can be approximated by the following method. The center of the fringe with initial angle θ defines a conic volume of,

$$V = \frac{\pi}{3} b \cot\theta (b \cot\theta \tan(\beta/2))^2 \qquad (1.1.11)$$

where β is the hydrophone beam width. Differentiating this expression with respect to θ gives,

$$V_i \simeq \pi b^3 \frac{\cos^2\theta}{\sin^4\theta} \tan^2(\beta/2)\alpha \qquad (1.1.12)$$

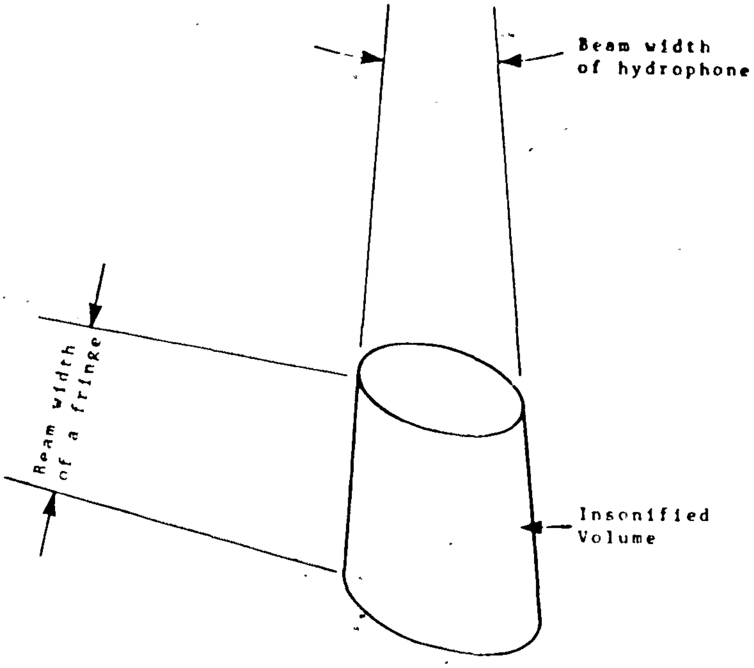

Figure 1.2 A typical volume of insonification V_i which is defined by the -3dB boundaries on both the fringe beam width and the conical hydrophone main lobe.

where α is the beam width of the fringe (equation 1.1.10).

For a simple sound speed profile with $c(z) = c_o$, both the maximum depth of a fringe (z) and the echo arrival time (T) can be derived from the basic system geometry in Figure 1.1. These are,

$$z = b \cot \theta \tag{1.1.13}$$

and,

$$\begin{aligned} T &= \frac{b}{c_o}(\csc \theta + \cot \theta) \\ &= \frac{b}{c_o} \cot(\theta/2). \end{aligned} \tag{1.1.14}$$

Table 1.2 uses the echometer projector with $f = 215\text{kHz}$, $c_o = 1475\text{m/s}$ and a 1 deg hydrophone separated 11.58m from the projector to summarize the basic properties of the bistatic configuration used in the experimental work.

Table 1.2 Relationships between fringe number m, initial angle θ, maximum ray depth z, arrival time T, and insonified volume V_i. Using the echometer projector and bistatic configuration with $b = 11.58\text{m}$, $c_o = 1475\text{m/s}$, $f = 215\text{kHz}$ and $d = 10\text{cm}$.

m	θ [deg]	T [ms]	z [m]	V_i [m^3]
1	3.94	228.5	168.3	1.29×10^{2}
2	7.90	113.6	83.4	8.00×10^{0}
3	11.94	75.1	54.8	1.54×10^{0}
4	16.07	55.6	40.2	4.71×10^{-1}
5	20.34	43.8	31.2	1.85×10^{-1}
6	24.78	35.7	25.1	8.47×10^{-2}
7	29.42	29.9	20.5	4.31×10^{-2}
8	34.32	25.4	17.0	2.35×10^{-2}
9	39.53	21.8	14.0	1.35×10^{-2}
10	45.11	18.9	11.5	8.07×10^{-3}
11	51.16	16.4	9.32	4.91×10^{-3}
12	57.85	14.2	7.28	2.98×10^{-3}
13	65.58	12.2	5.26	1.73×10^{-3}
14	75.73	10.1	2.94	8.05×10^{-4}

2 REMOTE MEASUREMENTS OF SOUND SPEED

This chapter introduces various methods for estimating sound speed at discrete depths $c(z)$ with a remote sensing acoustic device. Each method utilizes a bistatic configuration with narrow beam transducers and a reliable scattering mechanism. With the horizontal propagation fixed by the baseline length and the initial transmit angle known, then the arrival time (T) of the acoustic signal at the receiver will contain information on the refraction caused by the sound speed profile. The first section in this chapter develops the basic equations, obtains exact solutions for a simple linear sound speed profile and reduces the expressions through a first order approximation. The methods proposed by Brown and Ostashev are then presented separately. A comparison of these methods with the exact results from section 2.1 follows their theoretical developments. These detailed error analyses are a new development. An alternative general solution to the problem is also presented which uses the difference in arrival time. The accuracy requirements for arrival time measurements from the leading edge of an amplitude echo are then discussed and the final section presents other methods for measuring arrival time.

2.1 Linear sound speed profiles

The arrival time t for an acoustic pulse in a refractive medium is determined from the line integral,

$$t = \int_0^s \frac{ds}{c(z)} \qquad (2.1.1)$$

where s is the length of the path and c(z) is the depth dependent sound speed. For an initial angle θ_o from the vertical, Snell's Law gives,

$$p = \frac{\sin\theta_o}{c_o} = \frac{\sin\theta(z)}{c(z)}. \qquad (2.1.2)$$

For an incremental depth change dz with angle $\theta(z)$ the ds term in equation 2.1.1 becomes,

$$ds = dz/\cos\theta(z)$$

and by including the expression for $\sin\theta(z)$ in equation 2.1.2 the arrival time can be expressed as,

$$t = \int_0^z \frac{dz}{c(z)\sqrt{1 - p^2c^2(z)}}. \qquad (2.1.3)$$

By a similar development the horizontal range χ of the acoustic pulse can be expressed in terms of the sound speed profile and the constant p value from Snell's Law. The resulting equation is,

$$\begin{aligned} \chi(z) &= \int_0^z \tan\theta(z)dz \\ &= \int_0^z \frac{pc(z)}{\sqrt{1 - p^2c^2(z)}}dz \end{aligned} \qquad (2.1.4)$$

For a simple linear sound speed profile defined by

$$c(z) = c_o + gz$$

equations 2.1.3 and 2.1.4 have exact solutions (see 2.246 and 2.242 in Gradshteyn and Ryznik,1980). These are,

$$t = \frac{1}{g}\ln\left[\frac{1 + \cos\theta_o}{1 + \sqrt{1 - p^2(c_o + gz)^2}} \, \frac{c_o + gz}{c_o}\right] \qquad (2.1.5)$$

and,

$$\chi(z) = \frac{1}{gp}\left[\cos\theta_o - \sqrt{1 - p^2(c_o + gz)^2}\right]. \qquad (2.1.6)$$

By applying a first order analysis to these last two equations a more direct interpretation of the influence of θ_o and g on the results can be found. Both of these equations have the term gz and in typical oceanographic conditions,

$$\nu = \frac{gz}{c_o} << 1$$

is true. By utilizing this constraint and bounding θ_o to values less than 80° the arrival time simplifies to,

$$
\begin{aligned}
t &= \frac{-1}{g}\ln\left[\frac{1+\sqrt{1-\sin^2\theta_o(1+\nu)^2}}{1+\cos\theta_o}\frac{1}{1+\nu}\right] \\
&\simeq \frac{-1}{g}\ln\left[\frac{1+\cos\theta_o(1-\nu\tan^2\theta_o-\nu^2(\tan^2\theta_o\sec^2\theta_o)/2)}{1+\cos\theta_o}(1-\nu+\nu^2)\right] \qquad (2.1.7)\\
&= \frac{-1}{g}\ln\left[(1-\frac{\nu}{\cos\theta_o}-\nu^2(\frac{(1-\cos\theta_o)}{2\cos^3\theta_o}-\frac{1}{\cos\theta_o})\right]
\end{aligned}
$$

By using the Taylor expansion of,

$$\ln(1-Ax-Bx^2) = -Ax-(A^2+2B)\frac{x^2}{2}+(A^3+3BA)\frac{x^3}{3}-\ldots$$

which is valid for $|x| \leq 1$, then equation 2.1.7 further simplifies, to second order, to,

$$t \simeq \frac{1}{g}\left[\frac{1}{\cos\theta_o}\nu+\frac{1}{2}(\frac{1}{\cos^3\theta_o}-\frac{2}{\cos\theta_o})\nu^2\right]. \qquad (2.1.8)$$

When expressed in terms of $z, c_o,$ and g this expression becomes,

$$t \simeq \frac{z}{c_o\cos\theta_o}+\frac{1}{2c_o^2}(\frac{1}{\cos^3\theta_o}-\frac{2}{\cos\theta_o})gz^2. \qquad (2.1.9)$$

Notice that the first term gives the travel time in a constant sound speed profile (no refraction).

For a bistatic acoustic echosounder (see Figure 1.1), the total travel time T for a pulse which is transmitted at initial angle θ, reflected at depth z, and received in the vertical orientation above z, will be given by,

$$T = \frac{1}{g}\ln\left[\frac{1+\cos\theta_o}{1+\sqrt{1-p^2(c_o+gz)^2}}\frac{(c_o+gz)^2}{c_o^2}\right]. \qquad (2.1.10)$$

The first order approximation in equation 2.1.9 simplifies this expression and gives,

$$T = \frac{z}{c_o}(1+\frac{1}{\cos\theta})+\frac{gz^2}{2c_o^2}(1+\frac{1}{\cos^2\theta}). \qquad (2.1.11)$$

For a bistatic echosounder the horizontal range is fixed to $\chi(z) = b$. By inverting equation 2.1.6 the expression for the depth is,

$$z = \frac{c_o}{g}\left[\frac{1}{\sin\theta}\sqrt{1 - (\cos\theta - \frac{gb\sin\theta}{c_o})^2} - 1\right]. \tag{2.1.12}$$

This expression can also be reduced through the assumptions of $gb/c_o << 1$ and the added restriction of $\theta > 10^o$.

$$\begin{aligned} z &\simeq \frac{c_o}{g}\left[\frac{1}{\sin\theta}\sqrt{1 - \cos^2\theta + \frac{2gb}{c_o}\sin\theta\cos\theta - \frac{g^2b^2}{c_o^2}\sin^2\theta} - 1\right] \\ &= \frac{c_o}{g}\left[\frac{1}{\sin\theta}\sqrt{\sin^2\theta + \frac{2gb}{c_o}\sin\theta\cos\theta - \frac{g^2b^2}{c_o^2}\sin^2\theta} - 1\right] \\ &= \frac{c_o}{g}\left[\sqrt{1 + \frac{2gb}{c_o}\frac{1}{\tan\theta} - \frac{g^2b^2}{c_o^2}} - 1\right] \\ &\simeq \frac{c_o}{g}\left(\frac{gb}{c_o}\frac{1}{\tan\theta} - (\frac{gb}{c_o})^2\left[\frac{1}{2} - \frac{1}{\tan^2\theta}\right]\right) \\ &= \frac{b}{\tan\theta} + \frac{gb^2}{c_o}\left[\frac{1}{\tan^2\theta} - \frac{1}{2}\right]. \end{aligned} \tag{2.1.13}$$

As expected the depth decreases with a positive gradient due to upward refraction and vise versa for a negative gradient. (Notice that once again the first term gives the solution for a constant sound speed profile.)

The accuracy of these first order approximations can be quantified by comparing their numerical values with the exact representations in equations 2.1.6 and 2.1.10. Values of g ranging from 0.001 to 1.0 s^{-1} were used to evaluate these equations with $b = 11.58$m, $c_o = 1475$m/s and the initial angles determined by the echometer projector relationship. The percent difference in the maximum ray depth measurement is presented in Figure 2.1 as a function of $\log(g)$. The choice of using the echometer projector fringe angles in this example was a matter of convenience. The smallest fringe number represents a ray with the steepest initial angle and hence has the deepest fringe number (see Table 1.1 for the relationship between fringe number, initial angle and maximum depth). As expected the middle fringe numbers (i.e. 6 to 12) have the best agreement. Notice how all the fringes have positive differences and have depth estimates bounded by 0% and 0.5% for $g \leq 0.1\text{s}^{-1}$ when equation 2.1.13 is used to approximate the maximum ray depth.

Calculations of arrival time rely on the maximum ray depth value. Substituting equation 2.1.13 into 2.1.11 gives a first order approximation of the arrival time. Similarly, combining equations 2.1.12 into 2.1.10 gives the exact arrival time in a linear sound speed profile. The percent difference between these two arrival time values is presented in Figure 2.2 as a function of $\log(g)$ for the even fringe numbers. As in Figure 2.1 the deviation from a direct correlation (0%) decreases as the fringe number increases. This figure also shows that for $g \leq 0.1\text{s}^{-1}$ the first order approximation is accurate to better than 0.5% for all initial angles $\geq 16^{o}$ (fringe numbers ≥ 4).

2.2 Method proposed by Brown

An extension of the echometer principle as proposed by Brown involves the transmission of two frequencies simultaneously. From the unique properties of the echometer projector the fringe angle is a function of frequency (equation 1.1.7) so by selecting frequency pairs which have a small difference value, the resulting two ray paths will be close together. For the first z meters which the two rays have in common, the effects of refraction will be very similar for both rays. Therefore, the change in the arrival time difference between these rays will be primarily caused by changes in sound speed within the small vee, which is defined by the depth region that only the deeper ray traverses.

Brown's work assumed that the sound speed profile could be modelled as a constant (c_o) through the region that both ray paths have in common (i.e.

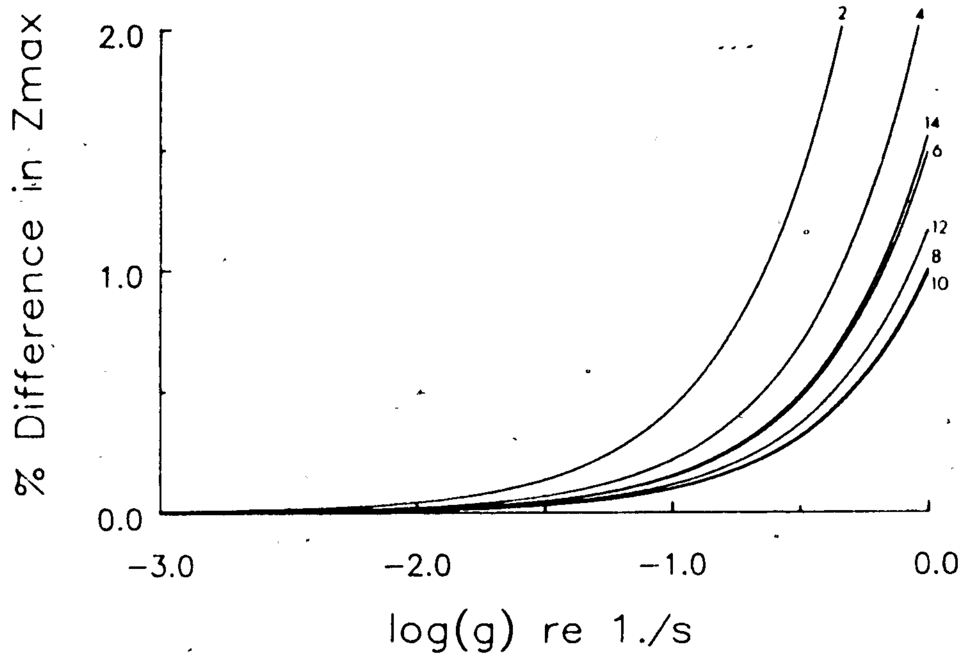

Figure 2.1 Percent difference in the first order solution of the maximum ray depth ($z_{\max}$) relative to the exact solution for a linear sound speed profile with gradient g, plotted as a function of $\log(g)$ for the even fringe numbers.

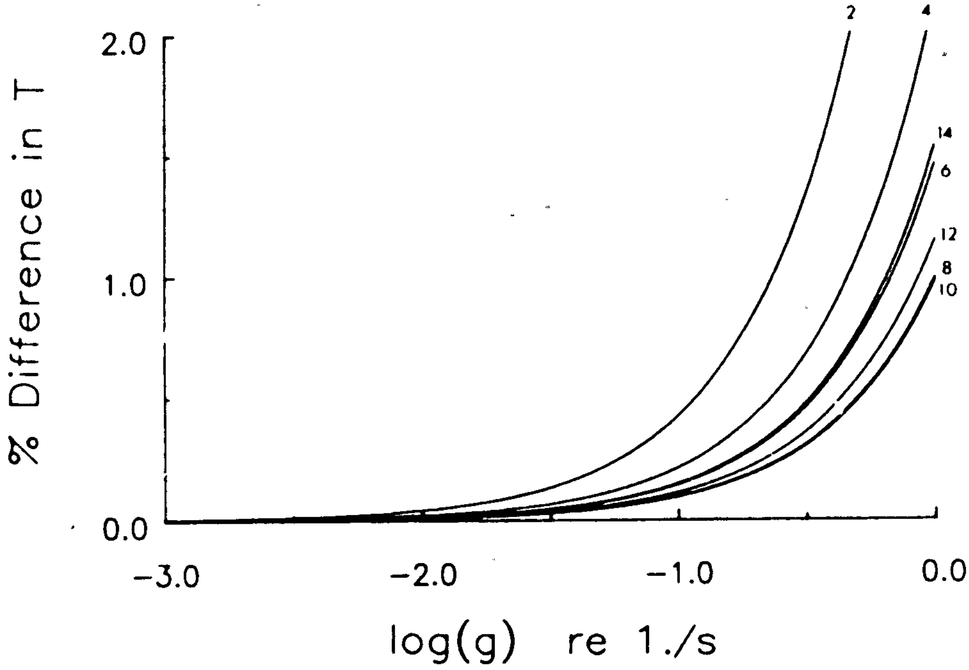

Figure 2.2 Percent difference in the first order solution of the arrival time (T) relative to the exact solution for a linear sound speed profile with gradient g, plotted as a function of $\log(g)$ for the even fringe numbers.

the first z meters in depth) and a second constant $(c_o + \Delta c)$ in the small depth region that only the deeper penetrating ray passes through. This is equivalent to a two layered model with,

$$c(z) = \bar{c} \qquad 0 \leq z \leq z_1$$

and,

$$c(z) = \bar{c} + \Delta c \qquad z_1 \leq z \leq z_1 + \Delta z.$$

The difference in arrival time between these two rays is a small number so the phase difference $\Delta\phi$ was selected as the measurable quantity. Appendix 2 gives the derivation of relationship between $\Delta\phi$ and Δc for the 2 layered model with a fixed baseline (b), and initial angle (θ_1). The resulting expression is,

$$\Delta c = \bar{c}\cos^2\theta_1 (1 - \frac{\Delta\phi}{\Delta\phi_o}) \qquad (2.2.1)$$

where,

$$\theta_1 = \sin^{-1}(\frac{m\bar{c}}{f_1 d})$$
$$\Delta\phi_o = \frac{\Delta f b}{\bar{c}\sin\theta_1}(1 + \cos\theta_1)(1 + \sec\theta_1)$$
$$\Delta f << f_1.$$

2.3 Accuracy of Brown's Method

The derivation of equation 2.2.1 utilized a number of first order approximations. The accuracy of this formula can be found by comparison with an exact numerical evaluation. For this two layered $c(z)$ model the arrival time of the first ray is precisely determined by,

$$t_1 = \frac{b}{\bar{c}}\cot(\frac{\theta_1}{2}) \qquad (2.3.1)$$

while the second ray arrival time will be,

$$t_2 = \frac{\chi}{\bar{c}}\cot(\frac{\theta_2}{2}) + \frac{b - \chi}{\bar{c} + \Delta c}\cot(\frac{\theta_2'}{2}) \qquad (2.3.2)$$

where,

$$\chi = b\cot\theta_1\tan\theta_2$$

$$\theta_1 = \sin^{-1}(\frac{m\bar{c}}{f_1 d})$$

$$\theta_2 = \sin^{-1}(\frac{m\bar{c}}{f_2 d})$$

$$\theta_2' = \sin^{-1}(\sin\theta_2\frac{\bar{c}+\Delta c}{\bar{c}})$$

$$f_2 = f_1 + \Delta f$$

The reference $\Delta\phi$ value will then be given by,

$$\Delta\phi_r = f_2 t_2 - f_1 t_1. \tag{2.3.3}$$

with the arrival times computed from equations 2.3.1 and 2.3.2. With this numerical model the exact value of $\Delta\phi$ can be found for a given Δc value. For the echometer projector in chapter 1: $f_1 = 215\text{kHz}$, $d = 0.1\text{m}$, and $\bar{c} \simeq 1475\text{m/s}$ so that the fringe number m, is bounded by $1 \leq m \leq 14$. Using these parameters plus $\Delta f = 1\text{kHz}$ and $b = 11.58\text{m}$, equation 2.3.3 was evaluated for Δc_r ranging from 0.01m/s to 10m/s. The resulting $\Delta\phi_r$ values, along with the other parameters, were then used to evaluate equation 2.2.1. The ratio of $\Delta c/\Delta c_r$ versus $\log(\Delta c_r)$ is plotted in Figure 2.3 for the even fringe numbers. Large deviations from unity occur for Δc_r values < 1 m/s. The primary cause of this poor fit at small Δc_r values is the $\Delta\phi_o$ term in equation 2.2.1.

An improvement in the $\Delta c/\Delta c_r$ ratio occurs when $\Delta\phi_o$ is represented by,

$$\Delta\phi_o' = \frac{b}{\bar{c}}[f_2\cot(\theta_2/2) - f_1\cot(\theta_1/2)] \tag{2.3.4}$$

which is the phase difference when $\Delta c = 0$. With this modification to equation 2.2.1 the ratio $\Delta c'/\Delta c_r$ was computed for various $\log(\Delta c_r)$ values and even fringe numbers. The resulting curves are shown in Figure 2.4. Notice the linear nature of the these curves; this confirms that the $1 - \Delta\phi/\Delta\phi_o'$ term in equation

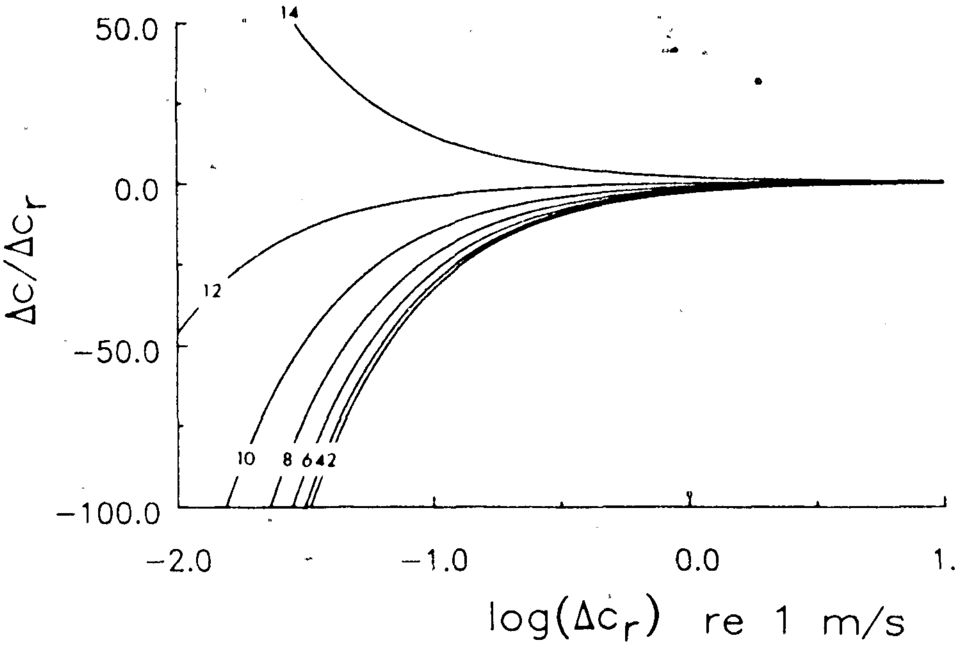

Figure 2.3 The accuracy relationships between Δc computed by equation 2.2.1 and the true value Δc_r are plotted for the even fringe numbers.

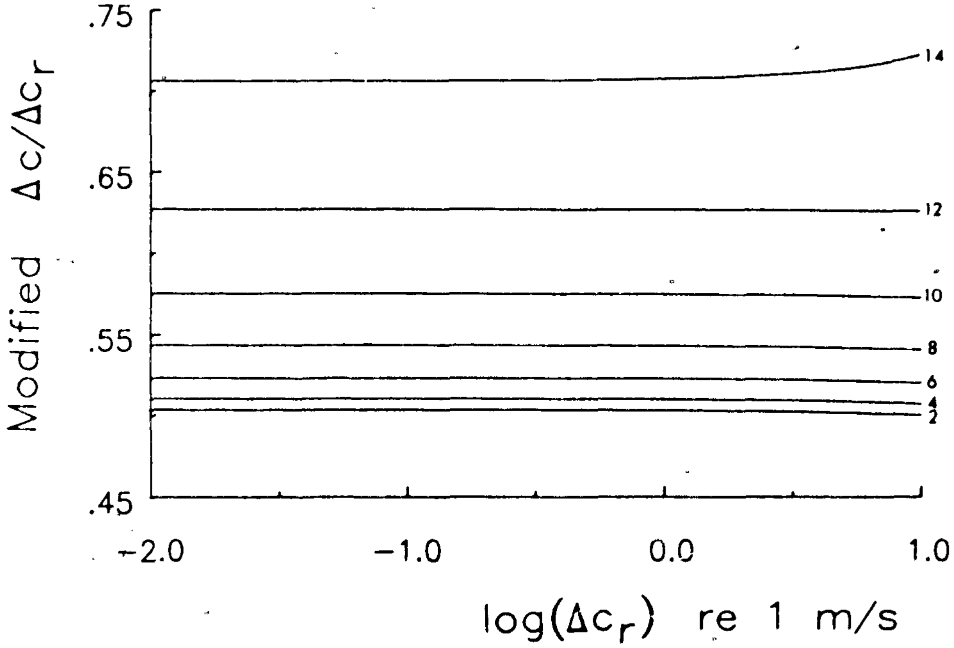

Figure 2.4 The accuracy relationships are plotted between a modified version of equation 2.2.1 and the true Δc values for the even fringe numbers.

2.2.1 gives an accurate representation of the sensitivity of Δc on $\Delta\phi$. The increase in the vertical offsets in figure 2.2 for each increase in fringe number demonstrates that the $\cos^2\theta_1$ term in equation 2.2.1 must also be modified for an accurate correlation with the exact representation.

This exercise has shown how the formulation proposed by Brown must be significantly modified before consistent results are found within a simple 2 layer model. An empirical relationship for the specific operating parameters can then be found, to relate Δc with $\Delta\phi$, which utilizes the framework of equation 2.2.1.

2.4 Travel time and depth for a general $c(z)$.

The problem of reconstructing the vertical profiles of sound speed from acoustic echoes in either the atmosphere or ocean has been examined by Ostashev(1984) for a general bistatic configuration. He utilized a first order analysis to simplify the integral equations for arrival time and maximum depth of a pulsed signal. This section will present the method proposed by Ostashev as it applies to the bistatic configuration of Figure 1.1.

Sound speed profiles in the ocean (and atmosphere) have non-linear time evolving forms which can be approximated by analytic functions only in special cases. For these general conditions the integrals in equations 2.1.3 and 2.1.4 can be evaluated or inverted only by numerical methods which require large numbers of data points for accurate solutions. An alternative approach is to simplify the integral equation by applying a first order analysis. By defining,

$$\eta(z) \equiv 1 - \frac{c^2(z)}{c_o^2} \tag{2.4.1}$$

where c_o is the sound speed at the surface, then expressions involving $c(z)$ can be expressed as,

$$c(z) = c_o\sqrt{1-\eta(z)}. \tag{2.4.2}$$

The definition of $\eta(z)$ was chosen because of its numerically small values. Throughout the world's oceans and lower atmosphere the condition,

$$\eta(z) << 1$$

holds. The square root term in the denominator is common to both equations 2.1.3 and 2.1.4. Using equations 2.1.2 and 2.4.2 it follows that:

$$\begin{aligned}\sqrt{1-p^2c^2(z)} &= \sqrt{1-\sin^2\theta(1-\eta(z))}\\ &= \sqrt{\cos^2\theta+\eta(z)\sin^2\theta}\\ &= \cos\theta\sqrt{1+\eta(z)\tan^2\theta}.\end{aligned} \tag{2.4.3}$$

With the added constraint that,

$$\eta(z)\tan^2\theta << 1$$

the square root term can be expanded in a Taylor series to give,

$$\sqrt{1-p^2c^2(z)} \simeq \cos\theta(1+\frac{1}{2}\eta(z)\tan^2\theta). \tag{2.4.4}$$

Combining equations 2.4.4, 2.4.2 and 2.1.3 produces,

$$\begin{aligned}t(z) &= \frac{1}{c_o\cos\theta}\int_0^z \frac{dz}{\sqrt{1-\eta(z)}(1+\frac{1}{2}\eta(z)\tan^2\theta)}\\ &\simeq \frac{1}{c_o\cos\theta}\int_0^z (1+\frac{1}{2}\eta(z))(1-\frac{1}{2}\eta(z)\tan^2\theta)dz\\ &\simeq \frac{1}{c_o\cos\theta}\int_0^z 1+\frac{\eta(z)}{2}(1-\tan^2\theta)dz\\ &= \frac{1}{c_o\cos\theta}(z+\frac{I(z)}{2}(1-\tan^2\theta))\end{aligned} \tag{2.4.5}$$

where $I(z)$ is called the integral characteristic of the profile and is equivalent to,

$$I(z) \equiv \int_0^z (1 - \frac{c^2(z)}{c_o^2})dz. \tag{2.4.6}$$

Similarly substituting equations 2.4.4 and 2.4.2 into 2.1.4 produces,

$$\begin{aligned} \chi(z) &= \frac{\sin\theta}{\cos\theta}\int_0^z \frac{\sqrt{1-\eta(z)}}{1+\frac{1}{2}\eta(z)\tan^2\theta}dz \\ &\simeq \tan\theta\int_0^z (1-\frac{1}{2}\eta(z))(1-\frac{1}{2}\eta(z)\tan^2\theta)dz \\ &\simeq \tan\theta\int_0^z (1-\frac{1}{2}\eta(z)(1+\tan^2\theta))dz \\ &= \tan\theta(z - \frac{1}{2}I(z)\sec^2\theta). \end{aligned} \tag{2.4.7}$$

Rewriting this last equation in terms of z gives,

$$z = \frac{\chi(z)}{\tan\theta} + \frac{I(z)}{2\cos^2\theta}. \tag{2.4.8}$$

The total travel time T of the pulsed signal in Figure 2.1 will include the vertical ray path ($\theta = 0$) and from equation 2.4.5 the combined travel times are given by,

$$T = \frac{z}{c_o}(1+\sec\theta) + \frac{I(z)}{2c_o}(\frac{1-\tan^2\theta}{\cos\theta}+1). \tag{2.4.9}$$

From these last two equations it is now possible to specify $I(z)$ and z in terms of the measurable quantities T and θ for $\chi(z) = b$. By defining t_o as the arrival time for $c(z) = c_o$ and substituting equation 2.4.8 into 2.4.9 the total arrival time becomes,

$$T = \frac{I(z)}{2c_o\cos^2\theta}(1+\cos\theta)^2 + t_o \tag{2.4.10}$$

where,

$$t_o = \frac{b}{c_o\tan\theta}(1+\sec\theta).$$

Rewriting equation 2.4.10 in terms of the integral characteristic gives,

$$I(z) = \frac{2c_o}{(1 + \sec\theta)^2}(T - t_o). \tag{2.4.11}$$

The final expression for depth is then found by substituting 2.4.11 into 2.4.8 which gives,

$$z = \frac{b}{\tan\theta} + \frac{c_o(T - t_o)}{(1 + \cos\theta)^2}. \tag{2.4.12}$$

These last 2 equations both rely on measuring the deviation in arrival time from t_o, which is a measure of the degree of refraction being introduced to the transmitted pulse. Estimates of $c(z)$ can be found by measuring $I(z)$ at various depths and using the following relationship. From the definition of $I(z)$ (equation 2.4.6) the differential relationship,

$$\frac{dI}{dz} = \eta(z) \tag{2.4.13}$$

is found directly. Substituting equation 2.4.13 into 2.4.2 and computing a first order approximation yields,

$$c(z) \simeq c_o(1 - \frac{1}{2}\frac{dI}{dz}). \tag{2.4.14}$$

This equation shows how it is possible to estimate the sound speed at depth z from only 2 arrival time measurements.

2.5 Accuracy of Ostashev's method

This section will compare the results of the previous section with the exact solutions for a linear sound speed profile developed in section 2.1. Once again the dimensions; b = 11.58m, c_o = 1475.m/s, were used with initial angles determined by the echometer projector fringes. Equation 2.4.12 gives the maximum depth of the ray ($z_{\mathbf{max}}$) where $T - t_o$ is computed by equation 2.4.10.

The exact value of $z_{\max}$ will be given by equation 2.1.12. Figure 2.5 plots the percent difference in these two values of $z_{\max}$ as a function of $\log(g)$ for the even fringe numbers. This figure shows that equation 2.4.12 gives estimates of depth which are lower than the true value but only by <0.005% for $g \leq 0.1\mathrm{s}^{-1}$.

The accuracy of equation 2.4.11 can be established by computing $I(z)$ for the linear $c(z)$. The resulting expression is,

$$I(z) = -\frac{gz^2}{c_o}(1 + \frac{gz}{3c_o}). \qquad (2.5.1)$$

Figure 2.6 plots the percent difference in these two values of $I(z)$ as a function of $\log(g)$ for the even fringe numbers. Both positive and negative differences are observed. For $g < 0.1$ equation 2.4.11 is accurate to better than ±0.5%.

Estimates of $c(z)$ can be found from the difference in $I(z)$ and the difference in $z_{\max}$ for two rays with similar initial angles. These differences provide an estimate of dI/dz which is required to estimate $c(z)$ in equation 2.4.14. With the echometer projector operating with one frequency at 215kHz, a second frequency with a 1kHz frequency difference will provide the second ray path. By repeating the previous calculations of $I(z)$ and $z_{\max}$ for this second ray, estimates of $\Delta c = c(z) - c_o$ were found. The exact Δc values were simply the product of g and the mean $z_{\max}$ value for the two rays. Figure 2.7 plots the difference between these Δc values ($\Delta c - g\bar{z}_{\max}$) as a function of $\log(g)$ for the even fringe numbers. These results are very similar to the previous figure and verify that Ostashev's method is very accurate in typical oceanographic environments (i.e. Δc accurate to better than ±0.01m/s for g <0.1 s^{-1} and $m > 2$).

The sensitivity of Ostashev's method to the accuracy of the arrival time measurements (T) will now be analysed. For the purpose of quantifying two

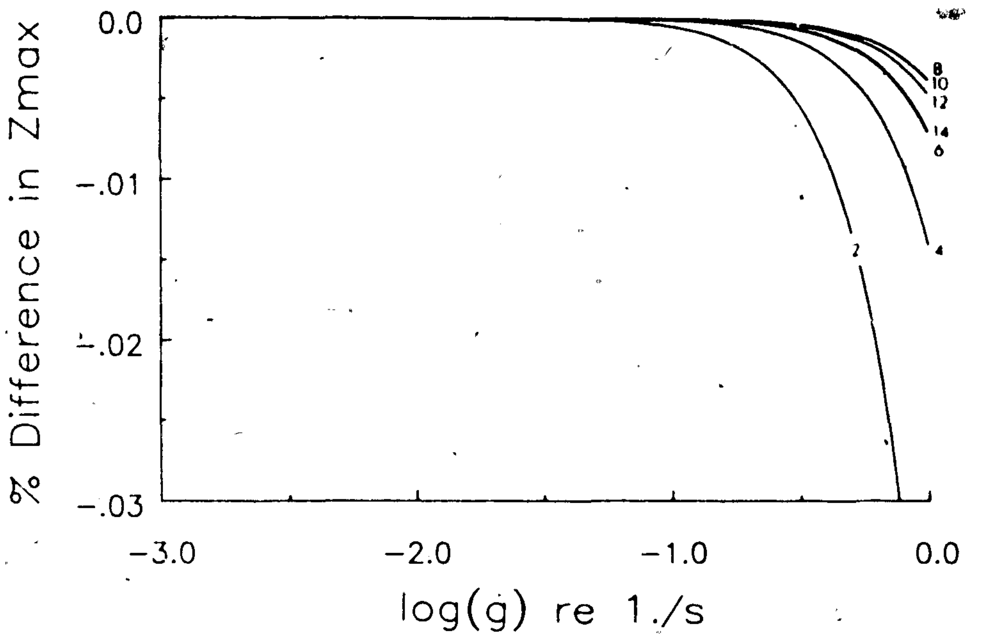

Figure 2.5 Accuracy relationship for the maximum ray depth as computed by Ostashev's method relative to the exact solution for a linear sound speed profile. The plot gives the percent difference in z_{max} as a function of log(g) for the even fringe numbers where g is the gradient in the linear sound speed profile.

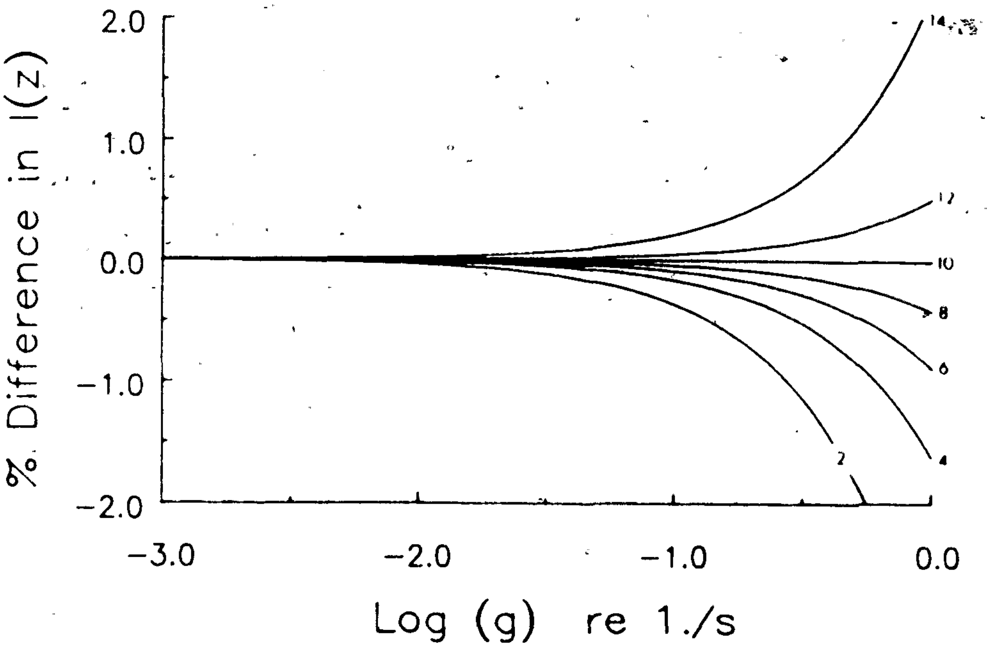

Figure 2.6 Accuracy relationship for $I(z)$ as computed by Ostashev's method relative to the exact solution for a linear sound speed profile. The plot gives the percent difference in $I(z)$ as a function of log(g) for the even fringe numbers where g is the gradient in the linear sound speed profile.

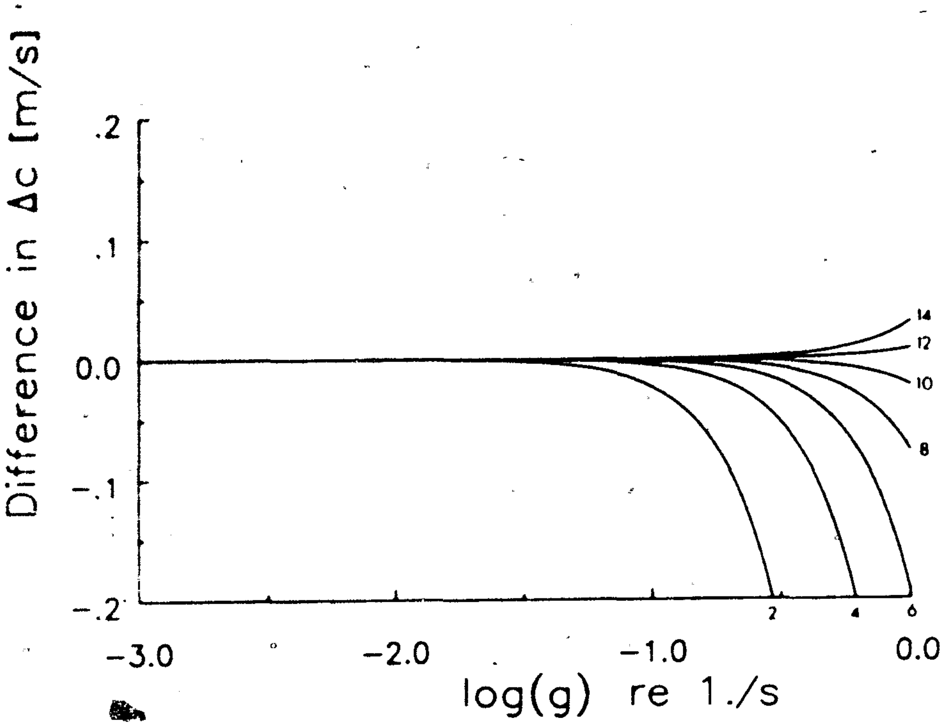

Figure 2.7 Accuracy relationship for Δc as computed by Ostashev's method relative to the exact solution for a linear sound speed profile. The plot gives the difference in Δc as a function of $\log(g)$ for the even fringe numbers where g is the gradient in the linear sound speed profile.

closely spaced rays the echometer projector will be utilized in this analysis. Measurements of Δl and Δz require two arrival times T_1 and T_2 which have initial angles θ and $\theta - \Delta\theta$ respectively. The error introduced by fluctuations in arrival time ϵ_T will cause Δl to change by.

$$\begin{aligned}
\epsilon_{\Delta l} &= 2c_o\left((1 + \sec(\theta - \Delta\theta))^{-2} - (1 + \sec\theta)^{-2}\right)\epsilon_T \\
&\simeq 2c_o\left((1 + \sec\theta(1 - \Delta\theta\tan\theta))^{-2} - (1 + \sec\theta)^{-2}\right)\epsilon_T \\
&\simeq 2c_o\cos^2\theta\left((1 + \cos\theta - \Delta\theta\tan\theta)^{-2} - (1 + \cos\theta)^{-2}\right)\epsilon_T \\
&\simeq \frac{4\Delta\theta c_o\cos\theta\sin\theta}{(1 + \cos\theta)^3}\epsilon_T.
\end{aligned} \tag{2.5.2}$$

Similarly, ϵ_T will cause Δz to change by,

$$\begin{aligned} \epsilon_{\Delta z} &= c_o\big((1+\cos(\theta-\Delta\theta))^{-2} - (1+\cos\theta)^{-2}\big)\epsilon_T \\ &\simeq c_o\big((1+\cos\theta+\Delta\theta\sin\theta))^{-2} - (1+\cos\theta)^{-2}\big)\epsilon_T \\ &\simeq \frac{-2\Delta\theta c_o \sin\theta}{(1+\cos\theta)^3}\epsilon_T. \end{aligned} \tag{2.5.3}$$

The effect of these two error terms on estimates of $\Delta c = -c_o\Delta I/(2\Delta z)$ are found by differentiating equation 2.4.14 with respect to its two variables. This gives,

$$\begin{aligned} \epsilon_{\Delta c} &= \frac{\partial(\Delta c)}{\partial(\Delta z)}\epsilon_{\Delta z} + \frac{\partial(\Delta c)}{\partial(\Delta I)}\epsilon_{\Delta I} \\ &= \frac{c_o\Delta I}{2\Delta z^2}\epsilon_{\Delta z} - \frac{c_o}{2\Delta z}\epsilon_{\Delta I}. \end{aligned} \tag{2.5.4}$$

The last three equations utilize Δz and $\Delta\theta$. First order expressions for these terms can be found by differentiating their full expressions in a simple constant sound speed profile. Differentiating the arcsine of equation 1.1.7 (the fringe angle relationship) with respect to frequency and multiplying by the difference in frequency (Δf) gives,

$$\Delta\theta \simeq -\tan\theta\frac{\Delta f}{f}. \tag{2.5.5}$$

From the system geometry, the depth and intial ray angle are related by,

$$z = b\cot\theta.$$

Differentiating this expression with respect to θ and multiplying the result by equation 2.5.5 gives,

$$\Delta z \simeq \frac{b}{\sin\theta\cos\theta}\frac{\Delta f}{f}. \tag{2.5.6}$$

Combining equations 2.5.2 to 2.5.6 gives,

$$\epsilon_{\Delta c} = \frac{2c_o\sin^3\theta}{b(1+\cos\theta)^3}\left(c_o\cos\theta - \frac{\Delta c b}{\sin\theta\cos\theta}\frac{\Delta f}{f}\right)\epsilon_T. \tag{2.5.7}$$

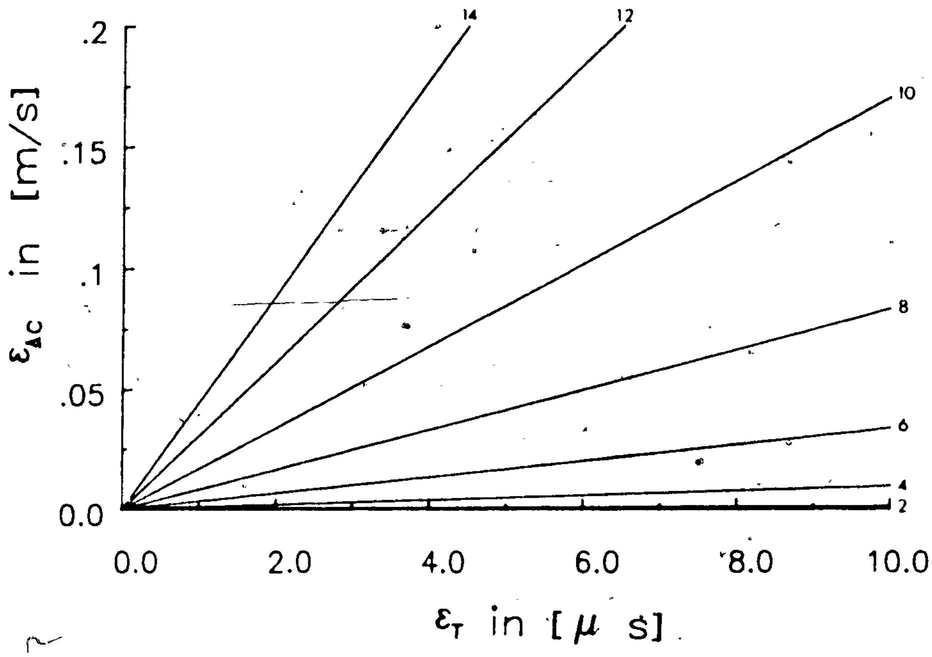

Figure 2.8 Accuracy in the estimate of $c(z)$, $\epsilon_{\Delta c}$, as computed by equation 2.4.14 , as a function of the accuracy in the arrival time, ϵ_T, for the even fringe numbers.

Since $\Delta c << c$ and $\Delta f << f$ the second term in equation 2.5.7 (the error contribution from Δz) will be negligible for $\theta < 80°$. Thus, equation 2.5.7 simplifies to,

$$\epsilon_{\Delta c} = \frac{2c_o^2 \cos\theta \sin^3\theta}{b(1+\cos\theta)^3}\epsilon_T. \tag{2.5.8}$$

For $c_o = 1475$ m/s, b=11.58 and $0 \le \epsilon_T \le 10\mu$s the corresponding values of $\epsilon_{\Delta c}$ have been computed for the even fringe numbers in Figure 2.8. This set of linear slopes demonstrates the high accuracy in arrival time measurement which is necessary for resolving the sound speed profile. For example, to resolve $c(z)$ to within ±0.05m/s then the arrival times for each ray must be measured to an accuracy of at least $\pm 1\mu$s.

It is often very difficult or impossible to measure the absolute arrival time to the accuracies neccessary to resolve the $c(z)$ profile because of the nature of the scattering process. An alternative solution can be found by measuring the relative arrival time difference (ΔT) between two rays which are initially separated by a small angle $\Delta\theta$. Rewriting ΔI in terms of T and ΔT gives,

$$\Delta I = k_1 T + k_2 \Delta T + k_3 \tag{2.5.9}$$

where,

$$k_1 = \frac{4\Delta\theta c_o \cos\theta \sin\theta}{(1 + \cos\theta)^3}$$

$$k_2 = \frac{2c_o}{(1 + \sec(\theta - \Delta\theta))^2}$$

$$k_3 = 2b\left(\frac{\cot\theta}{1 + \sec\theta} - \frac{\cot(\theta - \Delta\theta)}{1 + \sec(\theta - \Delta\theta)}\right)$$

$$T = T_1$$

$$\Delta T = T_2 - T_1.$$

Simple estimates of T and ΔT can be used to compare the relative importance of the two terms in equation 2.5.9. With $c_o T \simeq b\cot(\theta/2)$ and $c_o \Delta T \simeq -0.5b\Delta\theta\csc^2(\theta/2)$. The ratio of these terms becomes,

$$\frac{k_1 T}{k_2 \Delta T} \simeq \frac{2\tan^2\theta}{1 + \sec\theta}. \tag{2.5.10}$$

This result shows that for θ bounded by $10^\circ < \theta < 80^\circ$ the two terms are comparable so that both terms must be utilized, to obtain accurate measurements of ΔI.

The accuracy of ΔI in equation 2.5.9 will be given by,

$$\epsilon_{\Delta I} = k_1 \epsilon_T + k_2 \epsilon_{\Delta T}. \tag{2.5.11}$$

The relative importance of each arrival time accuracy (ϵ_T and $\epsilon_{\Delta T}$) can be found by assuming that the two terms in equation 2.5.11 are equal. This relationship gives,

$$\epsilon_T \simeq -\frac{1 + \cos\theta}{2\Delta\theta\tan\theta}\epsilon_{\Delta T}. \tag{2.5.12}$$

This result shows that the absolute arrival time T does not require the same high degree of accuracy as the relative arrival time ΔT. With the appropriate selection of θ and $\Delta\theta$ it is possible to measure only ΔT and use an estimator such as equation 2.1.11 to find T to the required accuracy.

2.6 Estimating $c(z)$ from the relative arrival time.

An alternative method for deriving the $c(z)$ profile from the difference in arrival time between two rays ΔT can be found by expanding the differential form of equation 2.1.3 for a bistatic configuration. This gives,

$$\frac{\partial T}{\partial z} = \frac{1}{c(z)}\left[\frac{1}{\sqrt{1-p^2c^2(z)}}+1\right]. \qquad (2.6.1)$$

With $F = \partial T/\partial z$ this equation can be rewritten as a cubic equation in $c(z)$. This results in,

$$c^3(z) - \frac{2}{F}c^2(z) + \left(\frac{1}{F^2} - \frac{1}{p^2}\right)c(z) + \frac{2}{Fp^2} = 0. \qquad (2.6.2)$$

The solutions to this equation are exact and only rely on measurements of F. In practice, only the change in c(z) is required, so with

$$c(z) = c_o + \eta(z) \qquad (2.6.3)$$

substituted into equation 2.6.2 a cubic equation in $\eta(z)$ is obtained. The resulting form is,

$$\eta^3(z)+\left(3c_o-\frac{2}{F}\right)\eta^2(z)+\left(3c_o^2-\frac{4c_o}{F}+\frac{1}{F^2}-\frac{1}{p^2}\right)\eta(z)+\left(c_o^3-\frac{2c_o^2}{F}+\frac{c_o}{F^2}-\frac{c_o}{p^2}+\frac{2}{Fp^2}\right) = 0. \qquad (2.6.4)$$

A linearization of equation 2.6.4 can be performed by utilizing the $\eta(z)/c_o << 1$ relationship. Recalling $p = \sin\theta/c(z)$, this gives,

$$F \simeq \frac{1}{c_o\cos\theta}\left(1+\cos\theta+\frac{\eta(z)}{c_o}(\tan^2\theta-\cos\theta-1)\right). \qquad (2.6.5)$$

Rewriting this expression in terms of $\eta(z)$ gives,

$$\eta(z) \simeq c_o \frac{c_o F \cos\theta - 1 - \cos\theta}{\tan^2\theta - \cos\theta - 1}. \tag{2.6.6}$$

This equation has a pole near $\theta = 51.8^o$ so estimates of $\eta(z)$ from measurements of F will be unstable about this angular region.

The total arrival time T is a function of c_o, θ, z and the change in c(z) with depth $g(z)$. The first order terms in the partial time derivative with respect to depth will then be given by,

$$\frac{\partial T}{\partial z} = \frac{dT}{dz} - \frac{\partial T}{\partial \theta}\frac{d\theta}{dz} - \frac{\partial T}{\partial g}\frac{dg}{dz}. \tag{2.6.7}$$

For a linear sound speed profile, $g(z) = g$,and the last term in equation 2.6.7 reduces to zero. In general, the small region of interest bounded by z and $z + \Delta z$ can be treated as a linear segment of $c(z)$ so that dg/dz will be negligible.

In practice, a measurement of ΔT is obtained by transmitting pulses along two different ray paths, with initial angles separated by $\Delta\theta$. These two difference values give an estimate of $dT/d\theta$, which can be transformed into a measurement of dT/dz by,

$$\frac{dT}{dz} = \frac{dT}{d\theta}\frac{d\theta}{dz} \tag{2.6.8}$$

when $\Delta\theta$ is small so that,

$$\frac{dT}{d\theta} = \frac{\Delta T}{\Delta\theta}.$$

The estimation of F from measurable quantities then requires knowledge of $d\theta/dz$,and $\partial T/\partial\theta$ for a first order approximation of F.

The accuracy of this method of estimating F was tested by differentiating the arrival time and maximum ray depth for a linear profile (equations 2.1.10 and 2.1.12). The resulting equations are,

$$\frac{\partial T}{\partial \theta} = -\frac{\sin\theta}{g(1+\cos\theta)}\left[1 - \frac{\cos\theta}{\sqrt{1-p^2c^2(z)}}\frac{1+\cos\theta}{1+\sqrt{1-p^2c^2(z)}}\left(\frac{c(z)}{c_o}\right)^2\right] \tag{2.6.9}$$

and,

$$\frac{dz}{d\theta} = -b\csc^2\theta / \sqrt{\csc^2\theta - (\frac{bg}{c_o} - \cot\theta)^2}. \qquad (2.6.10)$$

By simulating the transmission of two rays from the echometer projector with frequencies differing by 1kHz exact values of dT and $d\theta$ were computed for various m and g values. A comparison of F, as computed by equations 2.6.1 and 2.6.7, was then possible. Figure 2.9 displays the percent difference in F versus $\log(g)$ for even fringe numbers. These results show that for $m < 12$ and $g < 0.1$ equation 2.6.7 gives estimates of F with better than 0.02% accuracy. However, for $m > 12$ and/or $g > 0.1$ the second order effects in estimates of F (i.e.$\partial^2 T/\partial\theta^2$ and $\partial^2 T/\partial\theta\partial z$) become increasingly more significant.

The sensitivity of F to changes in $c(z)$ can be estimated by differentiating equation 2.6.1 with respect to $c(z)$. This gives,

$$dF = \left[-\frac{F}{c(z)} + p^2(c(z)F - 1)^3 \right] d(c(z)). \qquad (2.6.11)$$

The relative accuracy of F can be found by the approximation,

$$F \simeq \frac{1}{c(z)}(\sec\theta + 1).$$

Then,

$$\frac{dF}{F} \simeq \left[\frac{\tan^2\theta}{1 + \cos\theta} - 1 \right] \frac{\epsilon_c}{c(z)} \qquad (2.6.12)$$

where ϵ_c is the accuracy of $c(z)$. The trigonometric term in equation 2.6.12 provides three regions of interest. For $0^o \leq \theta < 43^o$ ($m < 10$) the relative accuracy of F is bounded by,

$$-\frac{\epsilon_c}{c_o} \leq \frac{dF}{F} \leq -0.5\frac{\epsilon_c}{c_o}$$

so F must be measured to a similar accuracy as the sound speed. For example, with c_o = 1500m/s and ϵ_c = 0.5m/s then F must be measured to within

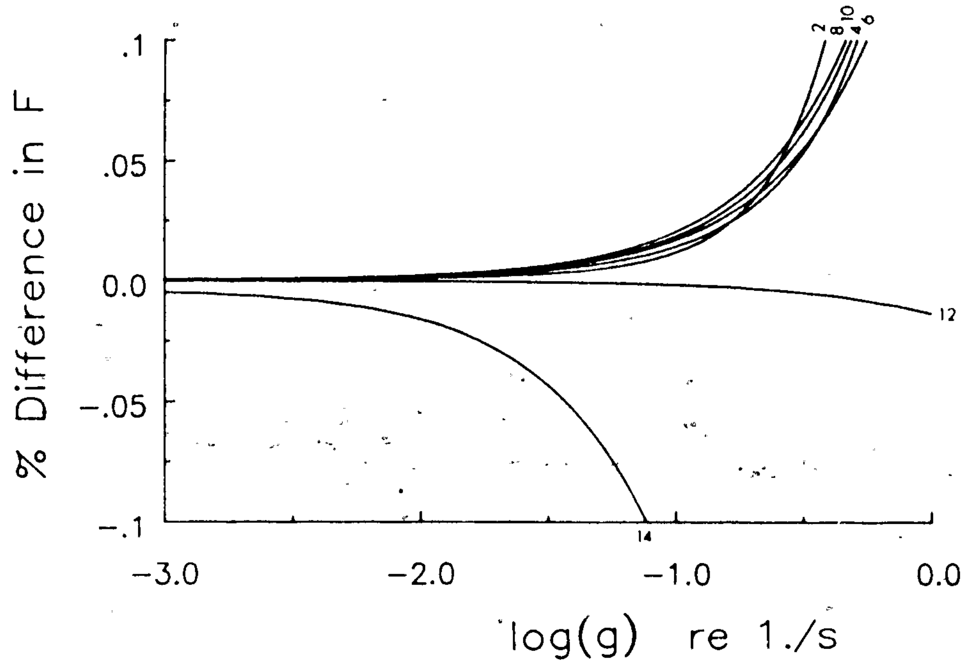

Figure 2.9 The percent difference in estimates of F from its first derivatives (equation 2.6.7) as a function of log(g) for the even fringe numbers.

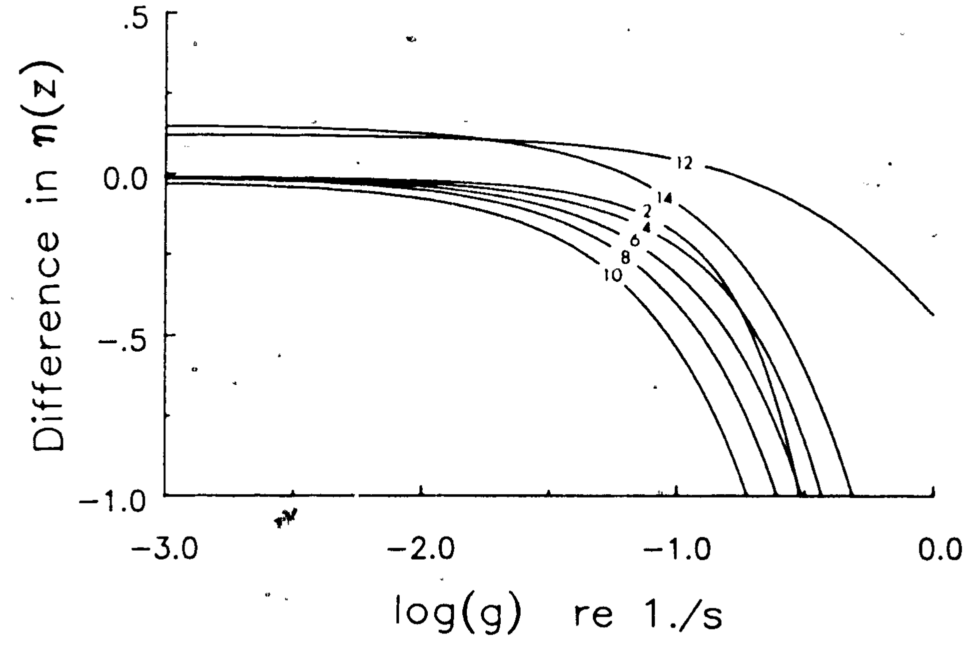

Figure 2.10 The difference in estimates of $\eta(z)$ from their true value as function of log(g) for even fringe numbers. Estimates of $\eta(z)$ were found by using a linear sound speed profile with slope g to evaluate the required derivatives for a first order estimate of F and then solving equation 2.6.4 (using the smallest root).

1 part in 3000 (0.033%). In the angular region bounded by $43^o < \theta < 60^o$ $(9 < m < 13)$ the relative accuracy of F is bounded by,

$$-0.5\frac{\epsilon_c}{c_o} \leq \frac{dF}{F} \leq \frac{\epsilon_c}{c_o},$$

which shows that F becomes less sensitive to changes in $c(z)$. This effect occurs because of the differential rates of change in T and z as the initial angle θ is changed. For $60^o < \theta < 90^o$ $(m > 12)$ F becomes increasingly sensitive to changes in $c(z)$. This region will then provide the most accurate estimates of $c(z)$ from measurements of F, but Figure 2.9 shows that this angular region is also subject to second order effects when estimating F. In order to quantify the errors introduced to estimates of $\eta(z)$ by the errors in the estimates of F the same estimates of F used in Figure 2.9 were applied to equation 2.6.1. Figure 2.10 plots the resulting difference between the estimated and exact values of $\eta(z)$ as a function of $\log(g)$ for the even fringe numbers. This plot demonstates that in a linear sound speed profile where $dz/d\theta$ and $\partial T/\partial\theta$ are known, then estimates of $\eta(z)$ can be biased by up to 0.5m/s for $m \leq 10$ and $g < 0.1$.

When compared to the Figure 2.7 (Ostashev's method) the results in Figure 2.10 are inferior and require knowledge of the mean $c(z)$ profile so that estimates of $dz/d\theta$ and $\partial T/\partial\theta$ can be found. However, Ostashev's method does require a measurement of the absolute arrival time (see section 2.6) so it may not always be the most practical solution.

2.7 Accuracy requirements for the arrival time

In practice the received signal has a complex signature which is distorted by transducer properties and physical processes. Arrival time measurements of a transmitted pulse can be determined by; 1) detecting the leading edge of the received echo, 2) applying an autocorrelation to the received echo to determine the center of the echo pulse, or 3) applying an interferometric technique which utilizes the phase signal of the received pulse. The accuracies of these various techniques are dependent on the beam widths of the transducers, system geometry, scatterer distribution, distortions of the wavefronts from turbulence or internal waves, and bulk fluid motions or currents. The effect of the first two of these variables will be derived from first principles.

The finite beam width of the transducers has the effect of spreading out the edges of the transmit pulse. In the previous development the received signal has had a vertical alignment as depicted in Figure 1.1. When the receiver detects signals from an angle β relative to the vertical axis then the arrival time of a pulse will differ from the formulation used in equation 2.1.10. The point of reflection (x, z) in a constant sound speed profile (c_o) is dependent on two equations,

$$x = z \tan \theta \tag{2.7.1}$$

and,

$$x - b = z \tan \beta. \tag{2.7.2}$$

These combine to give,

$$x = \frac{b \tan \theta}{\tan \theta - \tan \beta}. \tag{2.7.3}$$

The pulse arrival time is then given by,

$$\begin{aligned} t'_o &= \frac{x}{c_o \sin \theta} + \frac{x}{c_o \tan \theta \cos \beta} \\ &= \frac{b}{c_o(\tan \theta - \tan \beta)}[\sec \beta + \sec \theta] \\ &\simeq \frac{b}{c_o(\tan \theta - \beta)}[1 + \sec \theta]. \end{aligned} \tag{2.7.4}$$

The sensitivity of t'_o on the angle θ and β can now be found by differentiating equation 2.7.4 with respect to these variables. This gives,

$$\frac{\partial t'_o}{\partial \theta} = \frac{-b\sec^2\theta}{c_o(\tan\theta - \beta)^2}[1 + \sec\theta] + \frac{b}{c_o(\tan\theta - \beta)}\frac{\sin\theta}{\cos^2\theta} \tag{2.7.5}$$

and,

$$\frac{\partial t'_o}{\partial \beta} = \frac{b}{c_o(\tan\theta - \beta)^2}[1 + \sec\theta]. \tag{2.7.6}$$

By taking the ratio of these two partial derivatives a simplified expression for dt'_o can be found.

$$\begin{aligned} \frac{\partial t'_o}{\partial \theta} / \frac{\partial t'_o}{\partial \beta} &= -\sec^2\theta + \frac{\tan\theta - \beta}{1 + \cos\theta}\tan\theta \\ &\leq -\sec^2\theta(1 - \frac{\sin^2\theta}{1 + \cos\theta}) \\ &= -\sec\theta. \end{aligned} \tag{2.7.7}$$

By equating the beam widths in both transducers to find the largest change in dt'_o $(d\theta = -\beta)$ and using narrow beams $(|\beta| << 1)$ then the accuracy in arrival time measurements are bounded by,

$$\begin{aligned} dt'_o &\leq \frac{b\beta}{c_o(\tan\theta - \beta)^2}(1 + \sec\theta)^2 \\ &\simeq \frac{\beta c_o}{b}(t'_o)^2. \end{aligned} \tag{2.7.8}$$

This relationship then sets a lower bound on the accuracy of arrival time measurements from the edge of the received pulse.

For a linear sound speed profile $(c(z) = c_o + gz)$ the integral characteristic is given by,

$$\begin{aligned} I(z) &= \frac{-gz^2}{c_o}(1 + \frac{gz}{3c_o}) \\ &\simeq \frac{-gz^2}{c_o}. \end{aligned} \tag{2.7.9}$$

Combining this last expression with equation 2.4.11 and expressing the result in terms of the arrival time difference gives,

$$
\begin{aligned}
T - t_o &\simeq -\frac{gz^2}{2c_o^2}\frac{(1+\cos\theta)^2}{\cos^2\theta} \\
&\simeq -\frac{gb^2}{2c_o^2\tan^2\theta}(1+\sec\theta)^2 \qquad (2.7.10)\\
&\simeq -\frac{g}{2}t_o^2.
\end{aligned}
$$

The lower limit of detectability in a linear sound speed gradient can now be found by taking the ratio of equations 2.7.10 and 2.7.8. This gives,

$$\frac{T - t_o}{dt'_o} \geq \frac{-gb}{2c_o\beta}. \qquad (2.7.11)$$

For measurements of arrival time which contain meaningful information on the amount of refraction then,

$$T - t_o > dt_o$$

must be true. This constraint simply states that the signal $(T - t_o)$ must be larger than its accuracy limit or the signal to noise ratio must be greater than 1. Equation 2.7.11 simplifies to $(T - t_o)/dt'_o \simeq -g/2$, for a 12m baseline, a 0.5 degree half angle beam width on the transducers and a reference sound speed of 1475m/s. For this example, only extemely large gradients in the sound speed profile can provide meaningful arrival time estimates. In practice, values of $g > 1$ are only found over small depth ranges during seasonal or climatic changes in some oceanographic locations. Clearly, the measurement of arrival time from the edge of a received pulse requires a much larger baseline and/or a much smaller transducer beam width.

2.8 Other methods for measuring arrival time

The previous section showed that the edges of the received echo envelope will be spread out in time by the finite transducer beam widths which constrains this method of measuring arrival times to applications with baselines much larger than typical ship dimensions. When the shape of the received amplitude signal is consistent between transmissions then estimates of arrival time can be improved by utilising cross-correlations. With the amplitude of the received echo and a reference echo represented by $A(t)$ and $A_o(t)$ respectively then the cross-correlation function $R(\tau)$ is given by,

$$R(\tau) = \langle A_o(t)A(t+\tau)\rangle. \tag{2.8.1}$$

The location of the peak of $R(\tau)$ then gives an estimate of the arrival time which utilises the full received signal. For a scattering mechanism which retains the original pulse shape, such as a single scatterer, arrival time measurements with higher accuracy than the pulse edge detection can be obtained (Huber,1986).

It is only when the volume scattering mechanism approximates an isotropic and homogeneous scattering continuum that the scattered pulse will have a consistent shape. In practice, the scattering mechanism is discrete with mean spacings much larger than the carrier wavelength and is stochastic in both scattering strength and distribution of scattering centers. When the echoes from adjacent scatterers superimpose, constructive and destructive interference occurs and distorts the received echo from its original shape. These distortions represent the noise component of $A(t)$. A statistical analysis of $A(t)$ shows that it has a Rayleigh distribution (see chapter 5) at a given t value. Estimates of the accuracy of the cross-correlation for this type of noise is a difficult problem. In addition, a high digitization rate would be required to resolve the peak location to within the desired arrival time accuracy.

The received echo is actually composed of two time variable signals which both contain information about the medium of propagation. These are amplitude $A(t)$ and phase $\phi(t)$. When the phase signal is stable in the center of the received pulse an interferometric measurement is possible. This gives a very high resolution time measurement. For example, a 215kHz carrier has a period of 4.65μs, so if the phase signal is measured to within a tenth of a cycle then arrival time estimates with an accuracy of ±0.5μs will be obtained. Phase measurements can only give accurate measurements of the relative change in arrival time. If the absolute arrival time is also required with a high precision then the phase signal can be utilized much like a vernier scale to increase the resolution. For this method to work the first order measuring system (i.e. arrival time from location of the mean peak in the received echo) must be able to resolve the arrival time to within one cycle of the carrier to resolve phase ambiguities.

The experimental work in this thesis has concentrated on utilizing the phase signal from volume scatter.

3 ENVIRONMENTAL FACTORS

The experimental work in this thesis required the use of a large laboratory – namely the ocean. The objectives of making meaningful measurements can only be met by understanding how the oceanic environment interacts with the experimental apparatus and signals. This chapter outlines the environmental factors, other than sound speed, which influence acoustic echo measurements in the 200kHz range.

3.1 Acoustic scattering

The scattering of a monochromatic acoustic signal in an oceanic environment has been studied since the 1930's. Theoretical studies of scattering theory have shown that there are four dominant scattering mechanisms. Orr (1980) has identified three of the sources of scattering and they are; 1/temperature fluctuations caused by turbulent mixing; 2/spacial temperature gradients; and, 3/ animate and inanimate particulate distributions. For operating frequencies above 100kHz Orr shows that particulate scattering dominates by at least 3 orders of magnitude. Experimental evidence (Jobst, 1972) has also verified that discrete scatterers are the primary source of volume reverberation in the ocean. A fourth mechanism is the resonant scattering observed from micro-bubbles generated from breaking waves. These scatterers are typically restricted to the upper 5m of the ocean during normal oceanic conditions and have been observed in plumes as deep as 20m during storms (Crawford and Farmer, 1987).

Frequencies below 30kHz were initially used to study the marine environment acoustically. In this frequency range fishes and other creatures with gas-filled swim bladders or floats, dominate the scattering of the incident signal (Anderson,1977). Frequencies above 30kHz are typically used to relate the observed scattered signal with the distribution and abundance of zooplankton. A variety of independent experiments (Pieper,1984) have identified crustaceous species such as copepods and euphausiids as the predominant zooplankton which scatter high frequency (f >100kHz) acoustic energy. The light sensitive euphausiids undergo a daily migration, to the surface at sunset, then back to a specific depth at dawn. This known behaviour and their common abundance has been utilized for many high frequency scattering studies.

For estimating the abundance of zooplankton populations from the backscattered signal the reflective properties of a typical individual specimen are usually required. The reflectivity is measured in terms of the ratio of incident intensity at the scatterer location I_{in} divided by the scatterer intensity at a range of one meter I_{scat}. This ratio is commonly represented in a dB scale and referred to as target strength TS where,

$$TS = 10\log\frac{I_{in}}{I_{scat}}. \tag{3.1.1}$$

Scattering from zooplankton is largely dependent upon the physical size a, density ρ, and sound speed c of the specimen. Various theoretical approximations of the target strength of biological scatterers have been based on their physical parameters. The exact and approximate fluid sphere models of Anderson and Johnson (Johnson, 1977) respectively, are typically described by their ka dependence, the product of wavenumber (k) and an effective sphere radius (a). As ka decreases ($ka < 1$) both models converge to the Rayleigh model with the scattering function proportional to $(ka)^4$. More complex models which are intuitively attractive have also been proposed. A crustacean with an exoskeleton has been modeled by Machlup (1952) by encasing a fluid sphere model with an elastic shell. While Yeh (1967) has derived an applicable solution for scattering from a fluid prolate spheroid. An more recent development of scattering from a fluid finite cyclinder has been developed by Stanton (1986).

Verification of these models relies on ; 1/ accurate measurements of the physical parameters (a, ρ, c) which can often only be approximated and 2/ spacially isolating and identifying the target. Greenlaw (1977) has performed laboratory backscatter measurements on preserved copepods, euphausiids and shrimp of varying sizes. He selected 8 frequencies ranging from 220-1100kHz. Measurements of ρ and c were performed and a linear relationship was established to relate the specimen length with an effective spherical radius. For $ka \geq 1$ good agreement was found with the fluid sphere model for all three species when the aspect angle was constant. Directional properties in the backscattered signal were observed between the anterior and dorsal or side aspect for both the shrimp and euphausiid. A maximum difference at 220kHz of $\sim$ 20dB was observed, and the variation decreased with increasing ka number. Greenlaw used an empirically derived formula to relate the effective radius a to the euphausiid length L (in mm) which is,

$$a = 0.095 + 0.134L \qquad [\mathrm{mm}]. \tag{3.1.2}$$

In situ measurements of volume backscatter when compared with biological sampling (nets and pumps) have also served to verify scattering models. For example, Holliday(1980) found good agreement in the fluid sphere model of Anderson for $ka < 3$. A review paper by Pieper(1983) compares the results of various estimates for the TS of euphausiid populations at 102 kHz . Pieper demonstrates that if the minimum and maximum values for g and h (density and sound speed ratios respectively) are used in Anderson's model then a 6dB range in the TS value is produced which bounds the results of Greenlaw. A comparison of independent in situ measurements in Saanich Inlet by Beamish(1969) and Pieper(1979) have a 20dB discrepancy.

Although there have been large discrepancies in these estimates of target strength some general properties can be summarized. 1/ The fluid sphere model is frequently used by biologists to describe the general acoustic signatures observed from zooplankton. 2/ The estimates of g and h are biased towards the higher values found in the literature to force good agreement between the model and data. This is consistent with a method for compensating for the exoskeleton or carapace of these creatures. 3/ During daylight hours the euphausiids are in a horizontal position at deeper depths however, while feeding at night their orientation is a stochastic variable which causes a higher incidence of anterior orientations. Thus, target strength measurements made in the evening hours will be biased towards lower estimates. 4/ Fish or high number densities of particulate matter can dominate the acoustic signal from the zooplankton populations.

Recent studies of euphausiid scattering properties have demonstrated that for a fixed size distribution the target strength resonates about $ka = 0.5$ (Kristensen and Dalen, 1986). By using equation 3.1.2 an optimum frequency for investigating the euphausiids can be found. For example, an 18 mm euphausiid will resonate at a frequency $f = c_o/4\pi a = 48$ kHz.

The local waters of Saanich Inlet and Georgia Strait in which the experiments described subsequently were carried out, have been surveyed by marine biologists for the purpose of understanding the ecology and harvesting of euphausiids. The euphausiids are known to follow a seasonal cycle in their relative abundance, which peaks during October and December (Heath, 1976). Net hauls in the upper 25 m revealed population densities up to $500/\mathrm{m}^3$, with body lengths L distributed between 8 and 20 mm. Heath also observed both local and seasonal variability in their horizontal distributions. A separate study on the relative abundance of planktonic organisms was performed

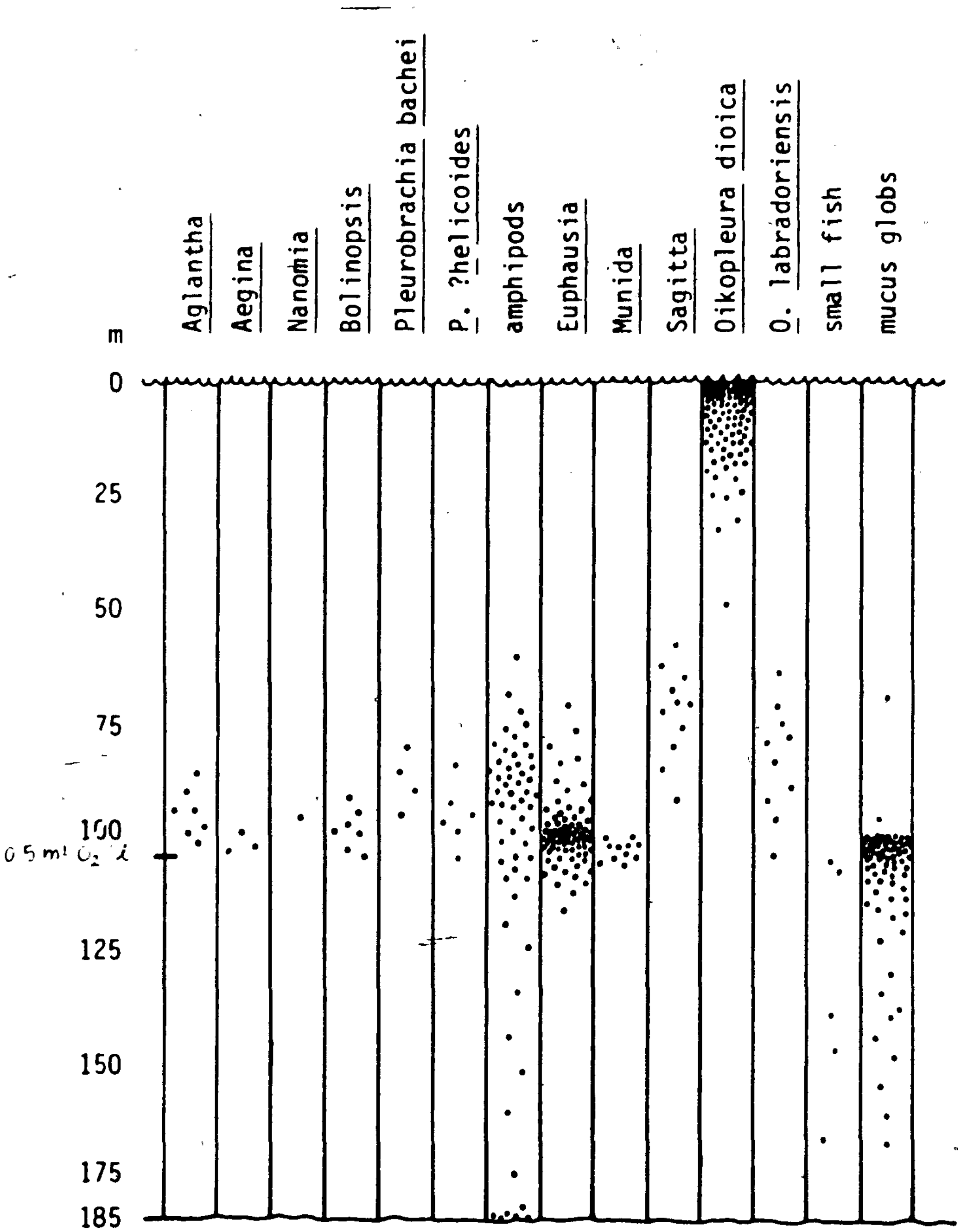

Figure 3.1a Relative abundance of planktonic organisms at Station C, Saanich Inlet, March 11-12, 1981 (Day: 1300-1700) (Mills,1982).

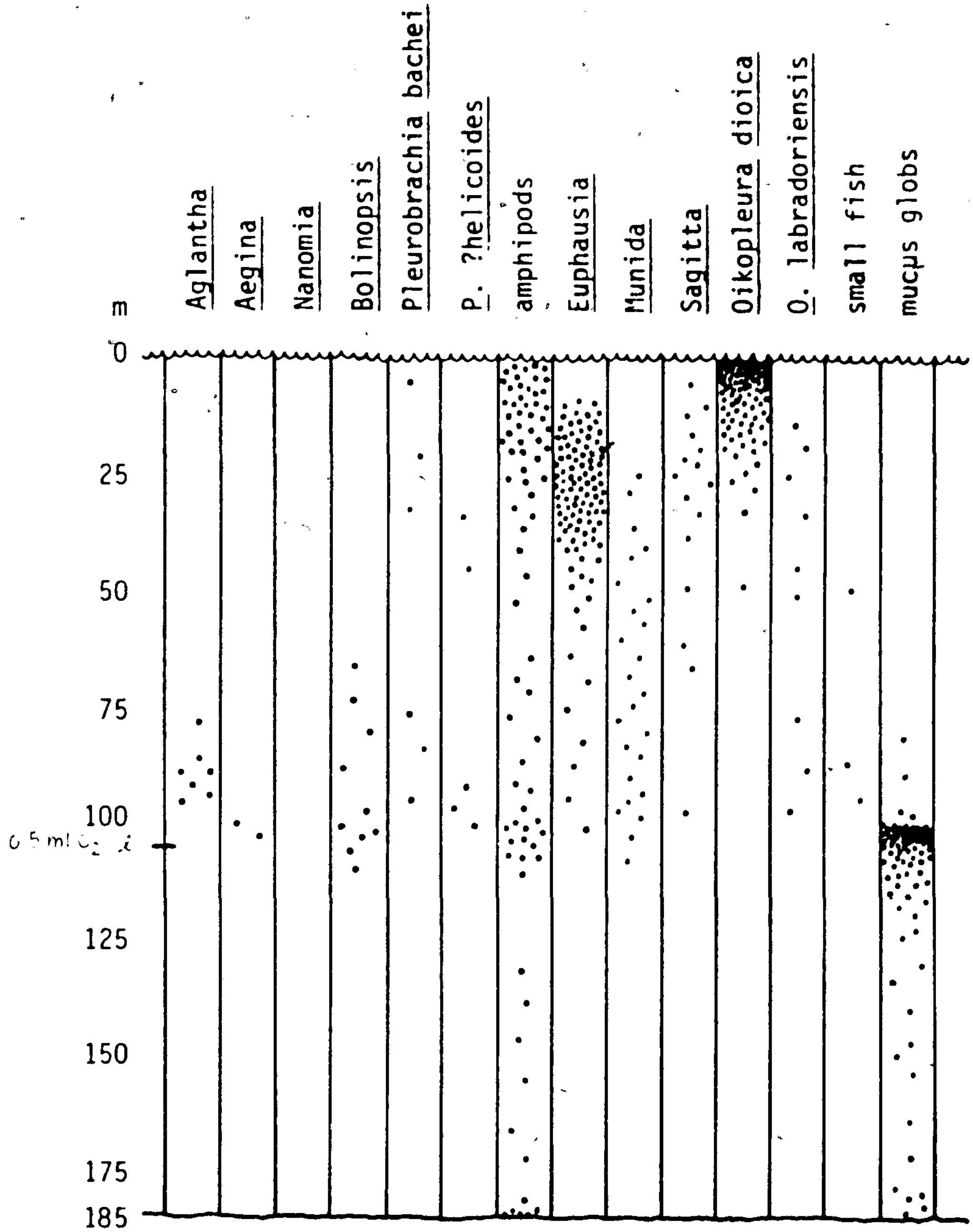

Figure 3.1b Relative abundance of planktonic organisms at Station C, Saanich Inlet, March 11-12, 1981 (Night: 2100-233 0) (Mills,1982).

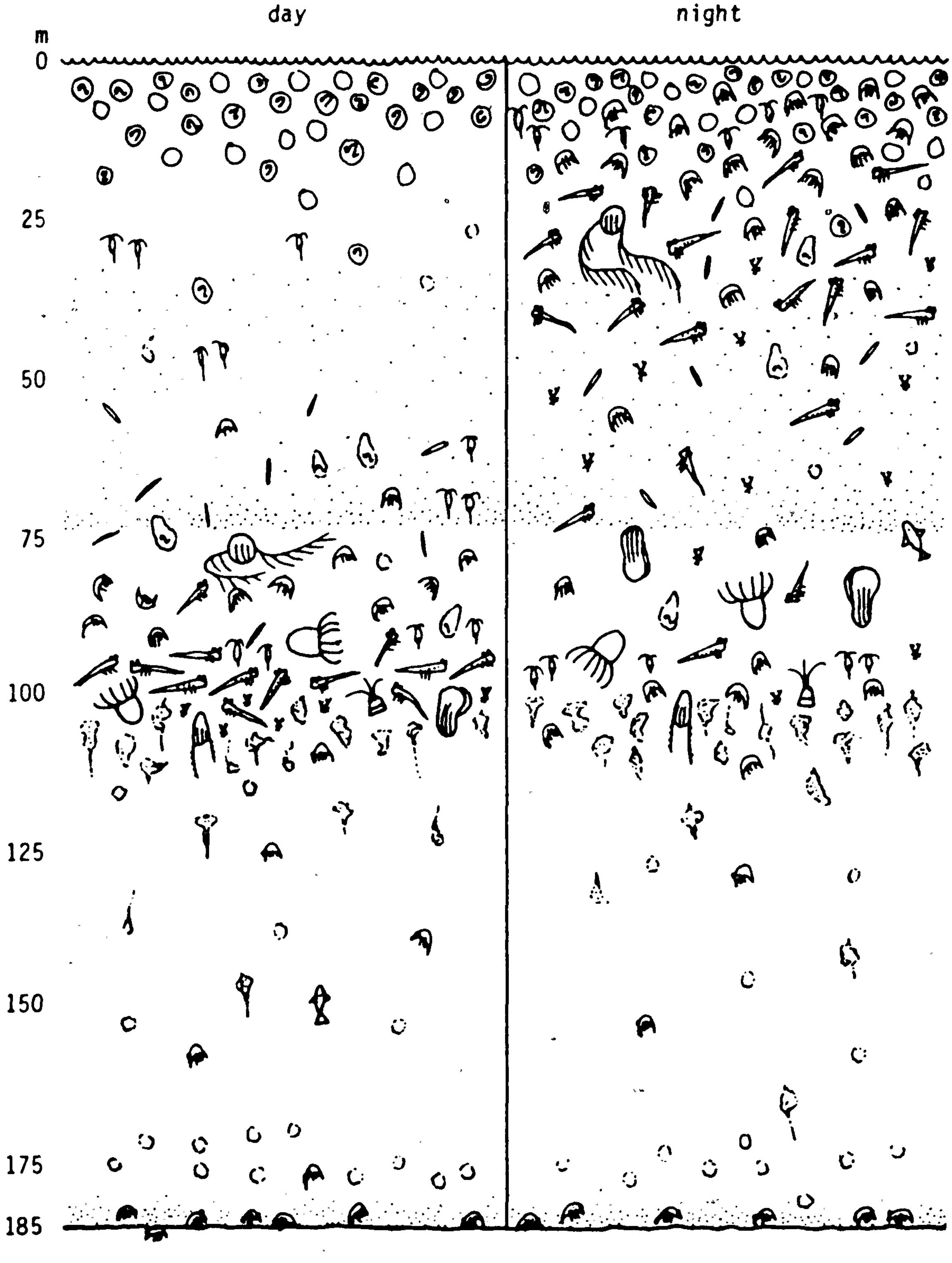

Figure 3.1c Pictorial representation of the water column at Station C, Saanich Inlet, March 11-12, 1981 during the day (1300-1700) and at night (2100-2330) (Mills,1982).

in Saanich Inlet by direct observations from within the manned submersible PISCES (Mills, 1982). This study confirms that euphausiids were the dominant zooplankton in the local waters with population densities up to $500/m^3$ in the 10 to 40 m depth region (during the night). A typical plot of the relative species distribution is given in Figure 3.1a,b, and c. These plots (reproduced by permission) demonstrate the relative changes in the amphipods and euphausiid populations between day and night observations.

The study performed by Greenlaw on preserved specimens provides an estimation of the mean target strenth of the crustaceous zooplankton for a frequency of 220 kHz. The mean species length and TS are given in Table 3.1. and demonstrate the significant differences between the species. A study on high frequency sound scattering by swimbladdered fish (Foote, 1985) shows that for a 120 kHz signal,

$$TS \simeq 20 \log l - 64 \quad [\mathrm{dB}] \qquad (3.1.3)$$

where l is the length of the fish in cm. For even a small 10 cm fish there is a large (38 dB) difference in target strength from that of a euphausiid.

Table 3.1 Mean target strength (TS) for dominant zooplankton scatterers at 220kHz.

Species	Mean length [mm]	Mean TS [dB]
Copepods	3.0	-104
Amphipods	8.5	- 90
Euphausiids	18.5	- 82

This general survey of TS and relative species abundance demonstrates that the backscattered acoustic signal from a given volume can have a large dynamic range in the echo intensity. The principle feature of the echo amplitude will then depend upon the species, size distributions, orientations and population densities.

In this thesis an acoustic model of each scatterer as an array of small fluid spheres with uniform properties becomes important in the theoretical developments. This model incorporates the directional properties of the dominant scatterer and provides an isotropic scatterer of finite size, which acts as a fundamental quantity of the total composite acoustic signature. With a unit fluid sphere whose radius is smaller than the acoustic wavelength, it is possible to model any individual biological target with similar values of g and h. Clay and Medwin (1977) show that a complex acoustical topography can be modeled by a collection of Huygen sources. For this case the received intensity from an ensemble of backscattered signals, for a large number of aspect angles, will approximate a Rayleigh distribution. This is equivalent to an assumption of an incoherent scattering process. The model has been experimentally verified for both prawn (Sofoulis,1978) and fish (Kung,1977) targets, when operating in the geometric scattering region $ka > 1$.

3.2 Absorption and spherical spreading

The previous section quantified the reflective properties of acoustic radiation which scatters off biological targets. There are two other factors which reduce the signal strength within the propagation medium. These are, molecular absorption and spherical spreading.

Absorption losses in sea water have been attributed to 3 separate molecules. The bulk and shear viscosity of fresh water (H_2O) provides the most significant term. These viscous properties convert some of the acoustic pressure into heat when cycled through compressions and rarifactions. The other 2 causes of absorption are chemical relaxations of magnesium sulfate ($MgSO_4$) and boric acid ($B(OH)_3$). Surprisingly, sodium chloride causes no absorption losses to the acoustic energy. All of these molecular relaxations are influenced by temperature and empirical relationships have been developed to compute the absorption coefficient α in [dB/m re 1μPa] as a function of in situ temperature and acoustic frequency for a salinity of 35ppt (parts per thousand) (see Kinsler, 1982). For a temperature of 5°C the total absorption of sea water is approximately 0.066 dB/m for a 215kHz sinusoid.

Spherical spreading losses are purely a property of radiation from a source. Since the surface area of a sphere is proportional to r^2 the acoustic energy per unit area is proportional to $1/r^2$. In terms of a decibel scale this gives a transmission loss (TL) of,

$$\mathrm{TL} = 20 \log \mathrm{r} \qquad [\mathrm{dB\ re\ 1\mu Pa}] \tag{3.2.1}$$

where the path length is measured in meters. When combined with absorption the TL becomes,

$$\mathrm{TL} = 20 \log \mathrm{r} + \alpha(\mathrm{r} - 1) \qquad [\mathrm{dB\ re\ 1\mu Pa}]. \tag{3.2.2}$$

This formulation results from the pressure amplitude $P(r)$ of a damped spherical wave relative to 1m from the source which is described by,

$$P(r) \propto \frac{1}{r} e^{-\alpha(r-1)}. \tag{3.2.3}$$

3.3 The sonar equation

When the target strength and transmission loss terms are included with the strength of the source and sensitivity of the receiver, the sound pressure level at the receiver (SPL) can be found. The resulting formulation is known as the sonar equation. This equation incorporates the transducer properties which affect the transmission and reception of acoustic radiation and subtracts the losses encountered in the medium.

The acoustic power transmitted by the projector is dependent upon both the ability of the transducer to convert electrical energy into acoustical energy and the directionality of the acoustic energy. The first term is quantified in terms of the transmit response which is measured in units of dB re 1 μPa/V at a reference distance of 1m. For the echometer projector each element has a transmit voltage response (TVR) of 161.5 at 215kHz. The interpretation of this number is as follows. When an open-circuit rms voltage of 1 volt is applied across the projector terminals then a rms pressure of $10^{161.5/20}\mu$Pa (=118.9 Pa) is created at a range of 1 m from the projector. This measurement is determined relative to the main lobe of the projector and gives the pressure in the axial direction (P_{ax}).

Similarily, the ability of the hydrophone to convert acoustic energy into electrical energy is measured relative to the acoustic axis of the transducer. This is quantified in terms of the receive voltage response (RVR) and is measured in units of dB re 1 V/μPa. The hydrophone and pre-amp used in the experimental work of this thesis has a receive response of -193 at 215kHz. This corresponds to producing an open-circuit rms voltage of $10^{-193/20}$ V (=224pV) when a 215kHz signal with a rms pressure of 1μPa sonifies the hydrophone and originates from a sound source in the direction of the acoustic axis. This very small voltage corresponds to the small unit of pressure which is used as a reference. For example, a normal human ear has a lower threshold of detection at 20 μPa for a 1000Hz tone.

The total radiated power is obtained by integrating the intensity over each unit solid angle with radius r in the farfield. When the ratio of this integral and the result for an omnidirectional projector are compared the directivity index (DI) is found. The total intensity at a fixed range, is proportional to $P_{ax}^2 B(\theta, \phi)$, where $B(\theta, \phi)$ is the intensity beam pattern.

The directional properties are quantified by DI. For a projector this term measures the effect of funnelling the acoustic power into a beam instead of letting it spread out omnidirectionally. In the case of a hydrophone, the Directivity Index relates the acoustic power received from a specific direction to the acoustic power of an isotropic ambient noise field. A directional source will always have a greater intensity at a distance r on the acoustic axis than a simple omnidirectional source with the same total acoustic power.

With a beam pattern intensity $B(\theta, \phi)$ the DI (in dB) is given by,

$$\mathrm{DI} = 10 \log \left[\frac{4\pi \mathrm{B}(0, \pi)}{\int_0^{2\pi} \int_0^{\pi} \mathrm{B}(\theta, \phi) \sin \theta \mathrm{d}\theta \mathrm{d}\phi} \right]. \qquad (3.3.1)$$

This definition uses the usual polar coordinates with θ measured relative to the z axis and ϕ measured in the xy plane relative to the x axis. The evaluation of DI can often be simplified because of the symmetry in the beam pattern. For an omnidirectional transducer $B(\theta, \phi) = 1$. Typical transducer beam patterns are separable so $B(\theta, \phi) = g(\theta) h(\phi)$ and $B(\theta, \phi)$ is often symetrical about the z axis ($h(\phi) = 1$) and negligible in the lower hemisphere of the xy plane. The representation of equation 3.3.1 then simplifies to give,

$$\mathrm{DI} = 10 \log(4\pi) + 10 \log(\mathrm{B}(0, \phi)) - 10 \log\left(\int_0^{2\pi} \mathrm{h}(\phi) \mathrm{d}\phi\right) - 10 \log\left(\int_0^{\pi/2} \mathrm{g}(\theta) \sin \theta \mathrm{d}\theta\right). \qquad (3.3.2)$$

The DI for the echometer projector (DI_1) was computed by using numerical integration to evaluate the integrals in equation 3.3.2. The intensity distribution was digitized into 0.1 degree increments and Simpsons rule was used to estimate the area of $g(\theta)\sin\theta$ between 0 and $\pi/2$. The resulting directivity index for each fringe in the echometer projector is given in Table 3.2. A similar analysis was performed on the narrow beam hydrophone and the resulting value was $DI_2 = 46.4$ dB .

Table 3.2 Directivity index of the echometer projector in each fringe direction in units of dB.

m	$g(\theta)$	DI_1
0	-35.0	-.20
1	-34.0	0.8
2	-29.7	5.1
3	-32.6	2.2
4	-24.9	9.9
5	-16.5	18.3
6	- 5.6	29.2
7	0.0	34.8
8	- 0.8	34.0
9	-10.3	24.5
10	-24.3	10.5
11	-33.7	1.1
12	-31.4	3.4
13	-34.4	0.4
14	-24.6	10.2

Combining the transducer properties with the losses in the medium gives the sonar equation in terms of the open-circuit voltage across the hydrophone terminals (SVL),

$$\mathrm{SVL} = (\mathrm{TVR} + \mathrm{DI}_1) + (\mathrm{RVR} + \mathrm{DI}_2) - (\mathrm{TL}_1 + \mathrm{TL}_2 - \mathrm{TS}) \tag{3.3.3}$$

where the subscripts on the transmission loss terms (1 and 2) refer to the path lengths to and from the scatterers respectively (see Figure 1.1). With the bistatic configuration the path lengths r_1 and r_2 are given by,

$$r_1 = b \csc \theta \tag{3.3.4}$$

and,

$$r_2 = b \cot \theta. \tag{3.3.5}$$

By using the echometer projector to determine θ the transmission losses can easily be computed from equation 3.2.2. Table 3.3 contains these values of TL_1 and TL_2 for each fringe of the echometer projector and $b = 11.58$m. The fourth column in this table combines the previous 2 columns with the mean TS value for a euphausiid (-82dB) and gives an estimate of the total losses in the system (TTL). The fifth column estimates the number of scatterers within the insonified volume V_i (see Table 1.2) assuming a scatterer number density of $100/\mathrm{m}^3$ and respresents this in dB with NTS=10log($100V_i$). The final column gives an estimate of the mean total loss in the medium when scattering from a euphausiid population with 100 scatterers per cubic meter. This column also demonstates the large dynamic range (27dB) in the received signal as m (and θ) increases.

By combining the last columns of Tables 3.2 and 3.3 estimates of the signal ~~strength~~ at the receiver for a uniform distribution of euphausiids can be found. For example, the 7th fringe (m=7) has a directivity index of 34.8 dB and has a 132.1 dB loss. The SVL for a 1 volt input then becomes,

$$\begin{aligned} \mathrm{SVL} &= (161.5 + 34.8) + (-193.0 + 46.4) - 132.1 \\ &= -82.4 \quad \mathrm{dB\ re\ 1\ V} \\ &= 75.9\mu\mathrm{V}. \end{aligned}$$

Table 3.3 Transmission losses in the bistatic system (dB re 1μPa) with the echometer projector determining the fringe number m and a baseline separation of 11.58m.

m	TL_1	TL_2	TTL	NTS	TTL-NTS
1	55.6	55.6	193.2	41.1	152.1
2	44.0	43.9	169.9	29.0	140.9
3	38.6	38.3	158.9	21.9	137.0
4	35.1	34.7	151.8	16.7	135.1
5	32.6	31.9	146.5	12.7	133.8
6	30.6	29.6	142.2	9.3	132.9
7	28.9	27.5	138.4	6.3	132.1
8	27.5	25.6	131.5	3.7	127.8
9	26.3	23.8	132.1	1.3	130.8
10	25.3	21.9	129.2	-0.9	131.1
11	24.4	19.9	126.3	-3.1	129.4
12	23.6	17.7	123.3	-5.3	128.6
13	22.9	14.7	119.6	-7.6	127.2
14	22.3	9.5	113.7	-10.9	124.6

During typical operations a 215kHz signal with an rms voltage of 1 kV was transmitted. For this case the received rms voltage would then be 75.9 mV for the 7th fringe. This example is based on a euphausiid population density of 100/m^3. If the number per cubic meter were to double then the SVL intensity would also double (or increase by 3dB). In this way the relative amplitude of the received echo can be used to discriminate the relative abundance of the scatterers.

This analysis of the signal strength has neglected the ambient noise which is also present in the ocean. This includes waves breaking, snapping shrimp, whales, rain and shipping noise. For frequencies above 100kHz however the dominant source of ambient noise is from thermal interactions in the medium. This effect is empirically described by (Urick,1983),

$$\mathrm{NL} = -15 + 20\log \mathrm{f} - \mathrm{DI}_2 + \mathrm{RVR} \tag{3.3.6}$$

where NL is the noise level in dB re 1 volt and f is in kHz. For the 215kHz hydrophone the rms thermal noise is approximately 41 pV. When compared with the signal strength in the previous example the signal-to-noise-ratio would be 2.6×10^9 or 94 dB.

3.4 Currents and turbulence

There are two basic types of water motions which can affect acoustic propagation. These are bulk fluid flows (currents) and random fluid motions (turbulence). Subtle spacial changes in the received echo can be utilized to measure the current field by a cross correlation technique (Dickey, 1981); however for most applications the changes in the amplitude signal are negligible. A different technique which measures the current field is the Doppler method. This system measures the rate of change in the echo phase signal (Pinkel, 1980). For the bistatic configuration in Figure 1.1 a horizontal current v in the x direction will only cause a Doppler shift in the $\theta/2$ direction. This reduces the effective velocity to $v\sin(\theta/2)$. If a passive scatterer in this current field moves at 1 cm/s in the $\theta/2$ direction then for a 1 ms pulse the scatterer will move 0.01 mm. For an operating wavelength of 7 mm this positional change, while being insonified, can result in a phase shift bounded by ±0.6 deg (the sign is dependent on the direction of motion). This example uses a small velocity component. For a ship under way the relative horizontal velocity relative to the ships heading is typically 14 knots (6.5 m/s). Under these conditions with $\theta = 30$ deg the Doppler shift corresponds to a change in phase of ±86.5 deg.

These large changes in phase must be corrected when absolute phase measurements are required. This can be accomplished by placing a second projector on the opposite side of the hydrophone. By transmitting alternately from each projector and adding the resulting phase from both echoes the Doppler shifts will cancel out. During the experimental work of this thesis the bistatic configuration was orthogonal to the ship's heading so that the effects of Doppler shifts were minimal (as in the first example).

Currents have a direct effect on the echo arrival time for the echometer projector and bistatic configuration. Following an analysis proposed by Brown, the influence of currents in the xz plane (the vertical plane which contains the projector and hydrophone) on the arrival time, is given in Appendix 3. With v representing the velocity in the x direction the deviation in arrival time *dT* is approximately.

$$\mathrm{dT} = -\frac{\mathrm{vb}}{\mathrm{c}_o^2}\left(\frac{2+\cos\theta}{1+\sin\theta} + \frac{1-\cos^3\theta}{\cos\theta-\cos^3\theta}\right). \tag{3.4.1}$$

This term becomes $< 2\mu s$ when θ lies within the interval $0 \leq \theta < 60\text{deg}$ with b=10m, c_o = 1475m/s and v < 10cm/s. For currents in the y direction the volume of insonification will be rotated (about the x axis) from its original location. Since this current is orthogonal to the physics which is occuring in the xz plane there will be no change in the arrival time of the transmit pulse. These currents cause the beam patterns of both the projector and hydrophone to be deflected. The amount of deflection will not be identical since the travel time to the scatterers differs from the scatterer to hydrophone time. This small difference in deflection will change the beam pattern weighting and hence the amplitude of the received echo. However, the echometer projector has a much broader beam than the hydrophone (10 deg and 1 deg respectively) so even this effect will be negligible for a strong cross flow.

In some oceanographic environments the horizontal currents have a vertical stratification or shear. These changing velocity components with depth will also refract acoustic signals so that when $c(z)$ is measured by the methods of Chapter 2 the velocity components in the direction of the bistatic baseline will included in the estimate of $c(z)$. This measurement is a more complete representation of the sound speed profile. For estimates of the temperature profile from $c(z)$ these effects of shear must be measured independently (i.e. via Doppler current profiler) and subtracted from the complete estimate of the sound speed profile.

The effects of turbulence on the phase signal within an acoustic pulse have been investigated by measuring the spacial and temporal variability of forward scattered radiation (Farmer and Clifford, 1986). Direct measurements of the phase variations in a 660 m path which undergoes energetic mixing during a tidal cycle gives an upper bound of ±10 deg for a 70 kHz carrier frequency. Transferring this data to a 215 kHz signal over a 150 m range gives a maximal change in phase of 0.7 deg when operating in the center of a tidal channel. The effects of turbulence caused by internal waves or other mixing processes in the oceans have lower rates of change than a tidal channel. Therefore, the phase shifts from turbulence will be negligible.

4 A NUMERICAL SIMULATION OF THE ACOUSTIC SYSTEM

In the initial stages of this research a numerical model was developed to explore the influence of various instrument and scatterer properties on the amplitude of the received signal. The inputs to the computer program included projector and hydrophone beam characteristics, scatterer type, and number density, refraction, absorption, spherical spreading, and target strength. The theoretical beam shapes defined a volume of insonification (see Figure 1.2) where random distributions of scatterers were simulated so that the composite signal at the receiver could be computed. The program was limited to simulating the received signal from one of the echometer projector fringes to minimize the demands on the computing facilities. The results from this program were used in the design stage of the instrument development. For typical in situ scatterer densities it was found that only the middle fringes $5 \leq m \leq 11$ would give useful signals. This was due to the large dynamic range in the insonified volume (see Table 1.2). Tests with various pulse lengths τ_p demonstrated that the signal strength increased with τ_p but for $\tau_p > 3$ms the shallow fringes $m \leq 9$ would be contaminated by overlapping between adjacent fringes.

The phase signal is of primary importance. The properties of the phase in the received echo were then implemented in the numerical model to provide insight into the signal received from discrete scatterers. The details of this version of the model are documented in Appendix 4.

A typical plot of amplitude and phase time series derived from the model with $f = 216$kHz and $\rho_n = 600\text{m}^{-3}$ for fringe number 7 is given in Figure 4.1. The composite amplitude time series displays the basic shape of the convolved transmit pulse. It coarsely approximates a Gaussian shape with a 3ms width at the half amplitude points ($\tau_p = 3$ms). The divergence of the signal from a

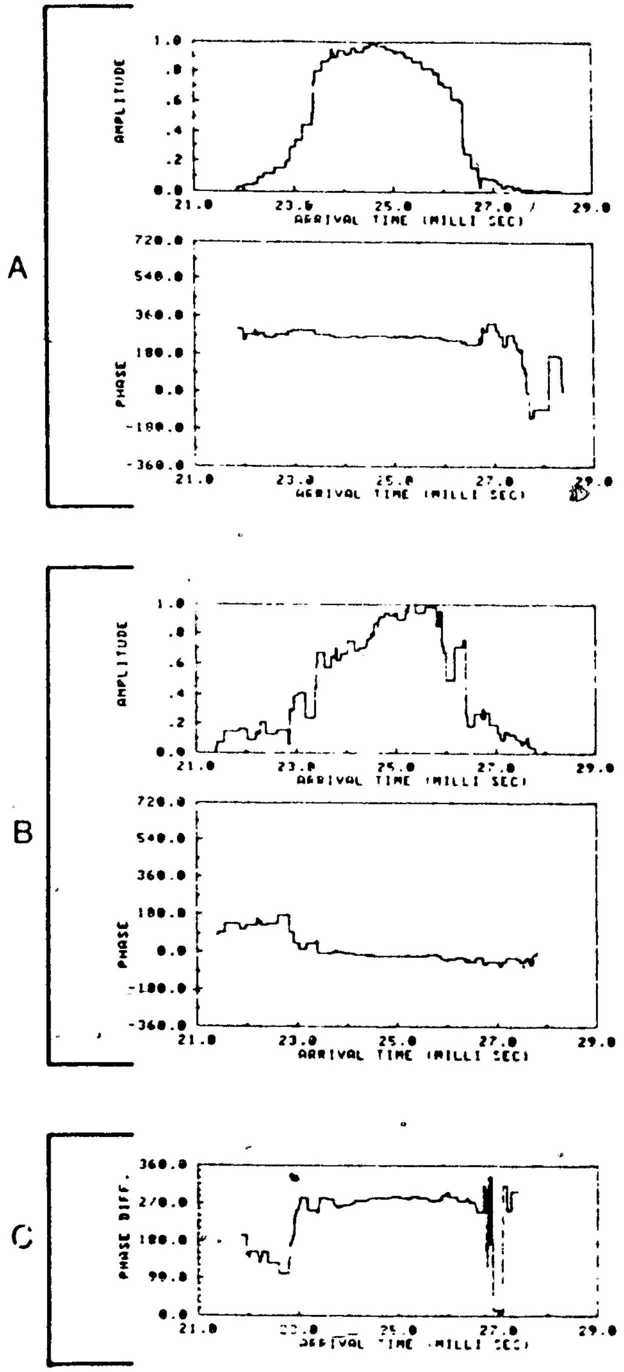

Figure 4.1 . Simulated amplitude and phase time series for fringe 7 of the echometer projector. All plots have assume a linear sounds speed profile with $g = 0.1\mathrm{s}^{-1}$. A 216kHz transmit frequency is used in (a) and a 214kHz transmit frequency is used in (b). Section (c) plots the difference in phase between (a) and (b).

pure form is caused by perturbations from discrete scatterers with arrival times and phases which deviate significantly from the mean expected value. Since the scatterers are relatively close the effects of attenuation and spherical spreading are negligible between neighbouring targets. In Figure 4.1a, the fine structure in the phase and amplitude plot arises from the discrete range set of the randomly positioned targets. For the chosen scatterer concentrations, this fine structure has a typical time scale of 10^{-5} to 10^{-4}s corresponding to acoustic path differences of the order of 2 to 20cm. Since this range separation is more than the carrier wavelength ($\lambda = 0.7$cm) the phases are effectively independent. Thus, the amplitude time series can be considered as composite pulses summed together with random individual phases where the individual amplitudes are primarily dependent on the projector and hydrophone beam patterns. The composite phase time series in Figure 4.1a gives the sequential values of the composite phase as each new pulse arrives at the receiver. In the region corresponding to maximum amplitude the composite phase has a minimal variance. In the neighbourhood of the fringe center the resulting amplitude of the scattered signals is the product of many overlapping components; for arrival times away from the fringe center the amplitude of the signals is reduced, and the variance in the phase signal increases. This result demonstrates that the amplitude region, defined by normalized amplitudes > 0.5, has a corresponding phase signal with a relatively small variance. For a pencil ray following the path of the fringe center, the expected phase at the receiver is 301.5° for the linear sound speed profile used in this model. Figure 4.1a shows the phase in the fringe center to be 264° ± 10° for this pseudo random scatterer distribution. This discrepancy will be explained later.

A second set of plots generated by the numerical model are based on a new carrier frequency of 214kHz, see Figure 4.1b. The model initially generates a set of target positions which contains the insonified volume for both frequency cases. This allows the simulation of the received signal when 2 frequencies are transmitted simultaneously. For the amplitude and phase time series the same basic form is observed but the fine scale variations are completely different. Additionally, the smoother region in the phase return has a different value. This phase difference is expected since the two frequencies travel slightly different paths. The insonified volumes for these two frequencies have a relative shift of only 10cm in depth so that the same set of targets are scattering the signals. The interference between scatterered pulses however will be different for each frequency.

A similar set of results is given in Figure 4.2, which shows the signals produced when a new distribution of targets is generated by selecting a different initial seed to the random number generator. Comparing Figures 4.1a and b with 4.2a and b, the difference is similar to changing the fine scale variations and adding a phase offset. Thus, the phase return is dependent on the particular scatterer distribution for typical scatterer densities. This explains the discrepancy in the phase measurements from their theoretical value.

In the theory proposed by Brown and Keeler (1981) the parameter of interest is the phase difference between two simultaneously transmitted frequencies. A plot of phase difference between the 2 frequencies, as a function of arrival time (i.e. range), for fringe 7 is given in Figure 4.1c. This plot is similar to the phase time series for a single frequency and demonstrates an increase in variability away from the center of the fringe. Figure 4.2c shows the phase difference for a new pseudo random scatterer distribution. This time series is similar to Figure 4.1c but shows a quite different phase offset at the fringe center although all other parameters remain fixed. A number of plots were generated based on different scatterer distributions and showed the phase difference to be random for typical operating and environmental parameters. This

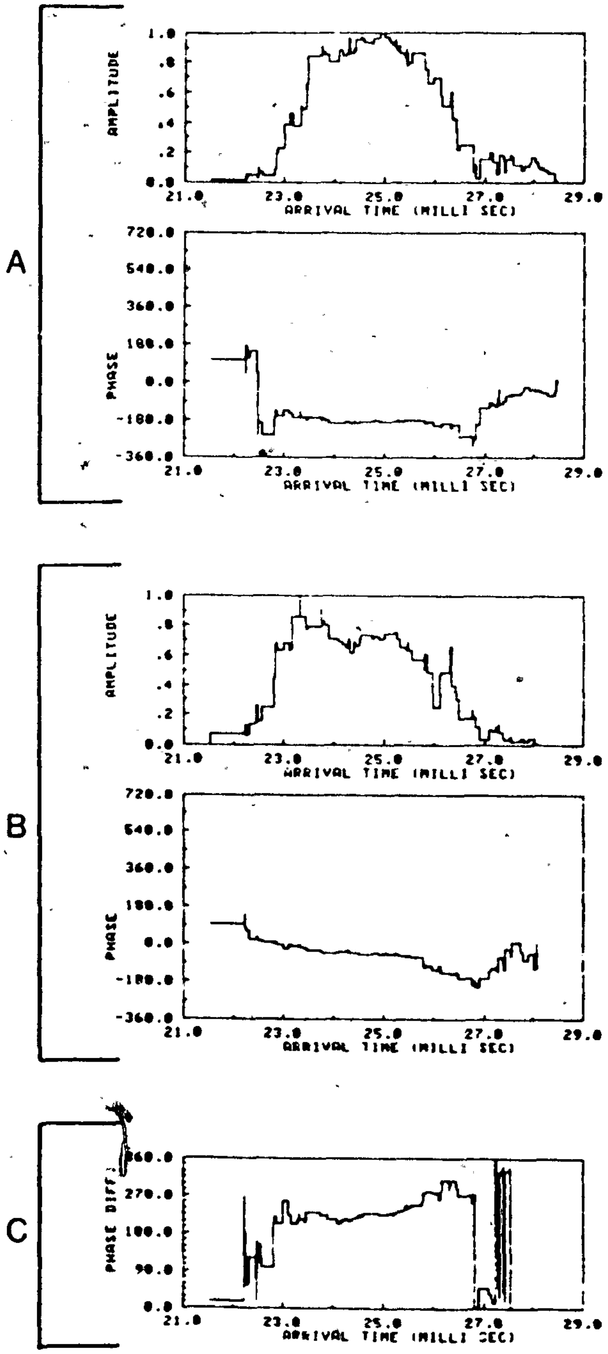

Figure 4.2 Same as in Figure 4.1 but using a different seed number for the pseudo random number generator.

result casts serious doubt on the viability of operating in the mode used by Brown et al. (1984). The model indicates that stable phase estimates require a much higher scatterer density than found in typical oceanographic conditions.

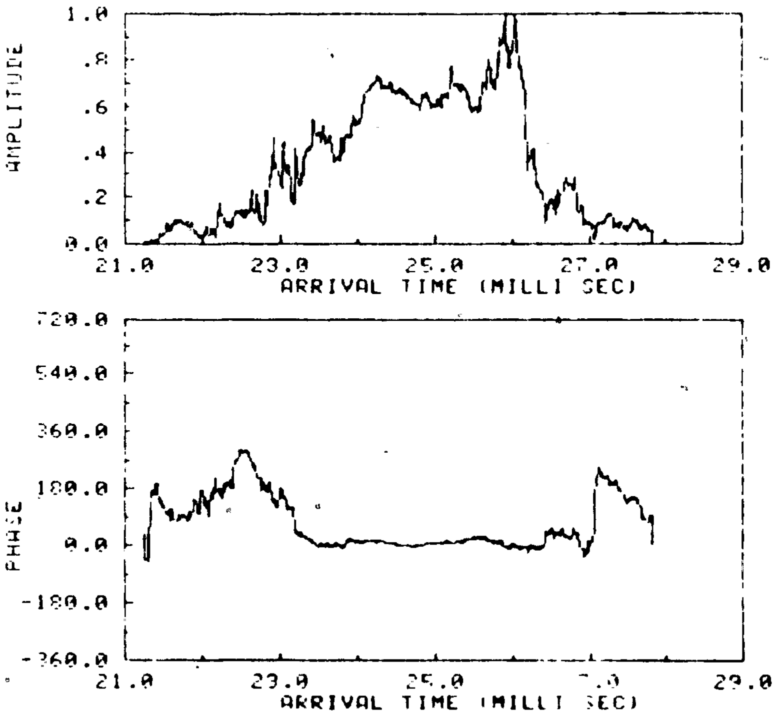

Figure 4.3a Simulated amplitude and phase time series after coherently processing 50 independent signals.

A quite different approach was then investigated in which data from successive transmissions are summed coherently, to achieve the same effect as would be obtained with higher scatterer densities. The model was modified to permit the summation of the in-phase and quadrature components between successive transmissions. This was accomplished by recording the amplitude and phase time series in small digital increments (100 points per millisecond) for each transmission. The composite amplitude and phase was later reconstructed from the coherent sum at each digital location. Plots of the resulting signal for a single frequency are given in Figure 4.3a and b. These correspond to coherent averages of 50 and 100 or $\rho_n = 30,000$ and $60,000\mathrm{m}^{-3}$ respectively. The mean target separations for these high number densities are approximately 9cm and 7cm respectively. The mean target separation (d) and density of scatterers (ρ_N) are related through the assumption of closest packing of spheres (face-centered or hexagonal packing) which utilize 74% of the total volume (Van Vlack, 1970). This gives,

$$\begin{aligned} \rho_N &= 0.74/\left(\frac{4}{3}\pi(\frac{d}{2})^3\right) \\ &= \frac{1.41}{d^3}. \end{aligned} \tag{4.1.1}$$

For both amplitude and phase the variability in Figure 4.3 has a finer scale than the previous figures, as expected by the higher scatterer concentrations. The scatterer density is doubled between Figures 4.3a and 4.3b and the phase shifted approximately 90°. In addition, the fine scale structure of the phase time series changed dramatically. This model shows that for point scatterers the phase signal requires even higher scatterer densities before stable estimates are obtained.

Much smaller mean target spacings (i.e. higher scatterer densities) were investigated on the Univac 1106 computer. For this purpose the insonified volume was reduced to a simple cube of dimensions $(28.6\lambda)^3$ for computational efficiency. The coherent processing scheme was then used to simulate mean target spacings from 3.5λ down to 0.1λ. The composite phase angle was calculated for many such cases, each one with unique random scatterer distributions.

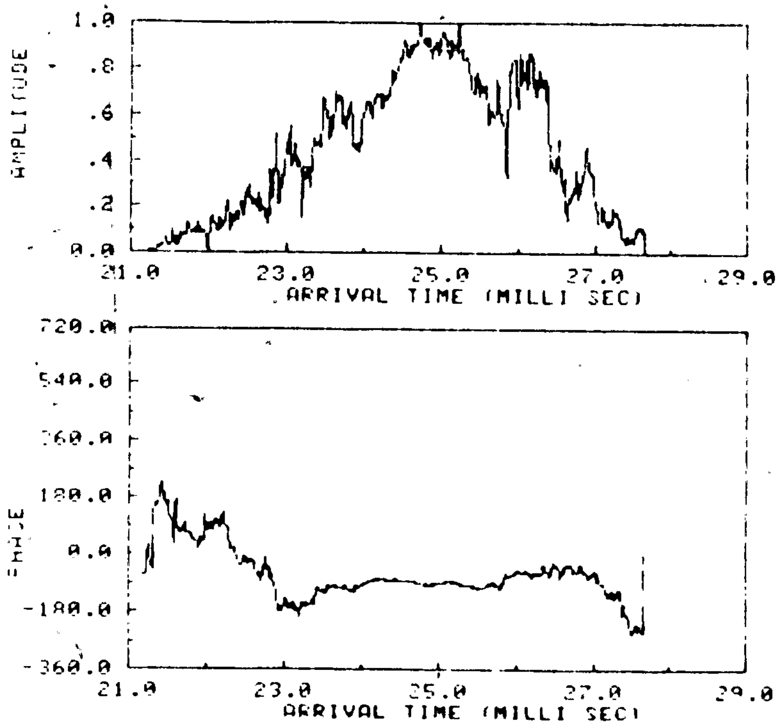

Figure 4.3b Simulated amplitude and phase time series after coherently processing 100 independent signals.

The results are plotted in Figure 4.4. For mean separations less than 0.6λ the calculated phases converge to a stable value. For a mean separation of 0.1λ, the standard deviation of phase estimates based on 10 independent sets of scatterer distributions is 0.07°. Figure 4.4 graphically illustrates the necessity for coherent processing of returns from many transmissions to achieve stable phase estimates. For point scatterers these results could be used to determine the relationship between the second moment of phase and the mean target spacing (see chapter 7).

The numerical models used in this chapter have all assumed the targets

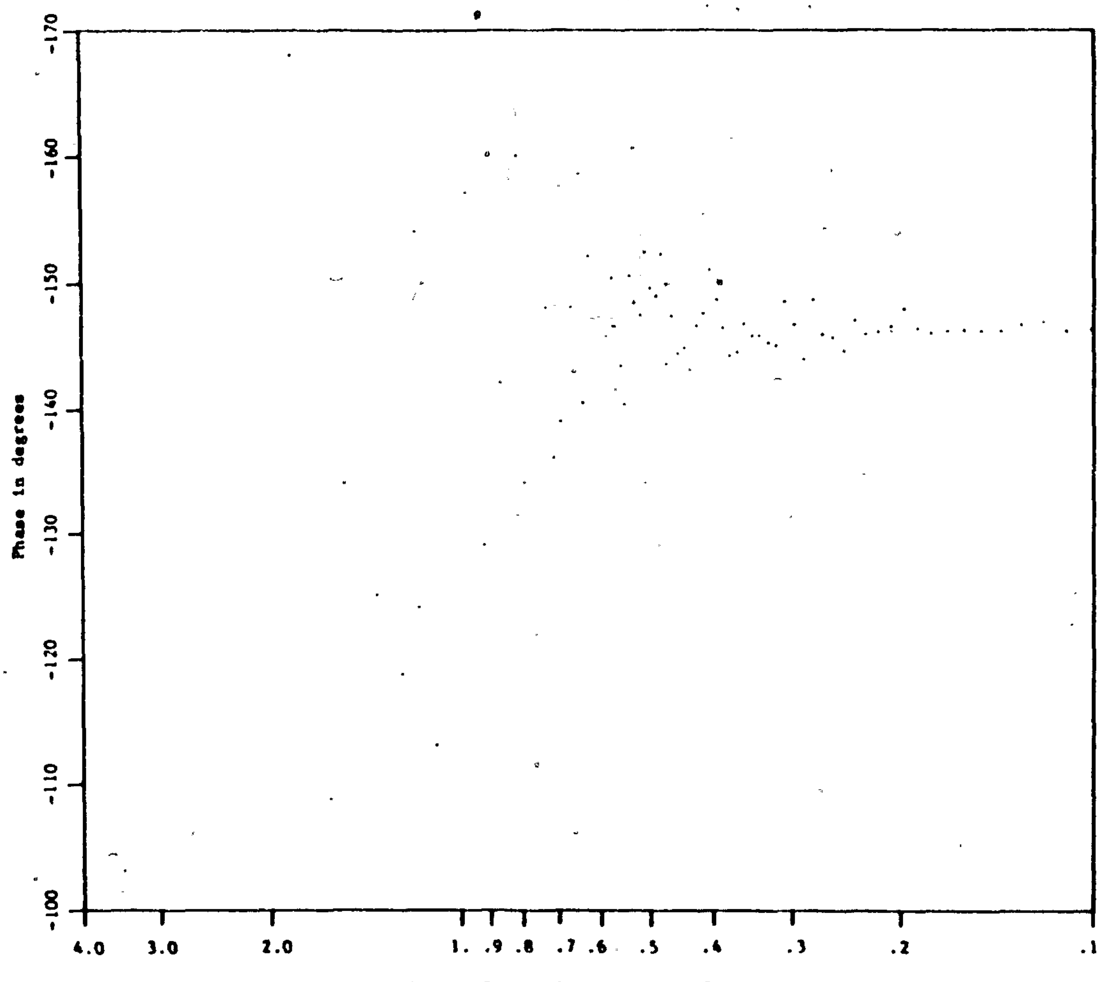

Figure 4.4 Composite phase for independent sets of scatterer distributions within a 28.6λ cube versus mean target separation on a semi-logarithmic scale.

behave as point scatterers. As mentioned in section 3.1 the crustaceous zooplankton have a finite acoustic scattering cross-section. This suggests that the convergence of the received phase signal towards a stable value, will be faster for real scatterers. The final verification of this method will depend on the results from field measurements which are composed of dynamically varying distributions of biological scatterers.

In summary, this numerical model of the bistatic configuration described in chapter 1, has given insight to the behaviour of the amplitude and phase signal in an echo from volume scatterers. Using in situ scatterer densities, the phase signal was found to be random between independent scatterer distributions. In order to overcome this problem a superposition technique was used to simulate the received waveform for much higher scatterer densities. The resulting phase signal from a set of point scatterers was demonstrated to converge to a stable value.

5 CONTINUUM SCATTERING

The various methods for estimating $c(z)$ in chapter 2 assume that the scattering mechanism within the insonified volume approximates that from a continuous scattering medium. This means that any unit volume has identical reflective properties (both isotropic and homogeneous). The experimental work used a carrier frequency of 215kHz. In the ocean, discrete targets are the dominant scatterer mechanism in this frequency range (Orr,1980, and Jobst,1972)). Clearly the distinction between continuous and discrete scatterers must be resolved so that valid comparisons between theoretical and experimental results can be made. This chapter begins with a development of the impulse weighting function for a scatterer continuum within a bistatic system. The system filters are then presented in the context of their frequency space representation. The final section combines the concepts developed in the previous sections and evaluates the the received signal from a symmetric and skewed scattering continuum.

5.1 General theory

The numerical model (chapter 4) shows how effective scatterer densities much larger than nominal values are required for discrete targets to produce a stable composite phase signal between successive transmissions. For successively larger densities within the same volume, the separation between adjacent targets reduces and the discrete system can eventually approximate a continuum of scatterers. For discrete systems the received signal from N targets can be represented by,

$$s(t) = \sum_{i=1}^{N} a_i \sin(wt - \phi_i) \tag{5.1.1}$$

where a_i, the received amplitude from each i^{th} scatterer, is a function of scatterer position, source level, beam characterization, transmission loss, target strength and pulse length. The phase ϕ_i, is a function of the path length from the transmitter to i_{th} scatterer to receiver distance, and the wavenumber k. The assumption of an acoustically hard scatterer implies that no change in phase occurs at the scatterer. Multiple scattering and absorption of acoustic energy by the scatterers themselves is presumed insignificant. Phase shifts from scatterers with a complex acoustic impedance will only cause an offset in the absolute phase signal.

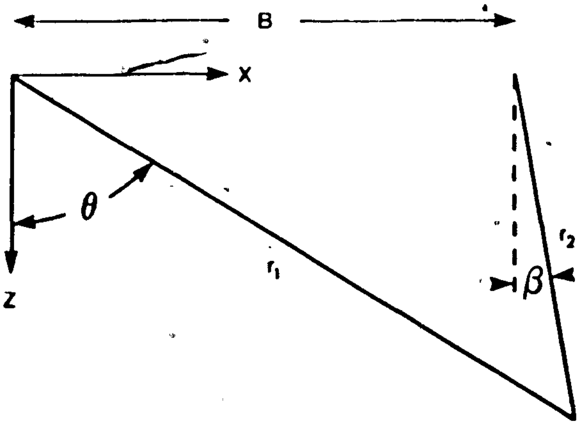

Figure 5.1 Geometry of a single scatterer for a bistatic echosounder with a fixed baseline B.

An evaluation of $s(t)$ requires a knowledge of the weighting functions which influence each value of a_i. The appropriate weighting function can be derived from the geometry of the bistatic acoustic system. Refering to Figure 5.1 we see a single scatterer position in the x-z plane can be represented by its spacial coordinates or equivalently by the two angles θ and β. For all positions with $r_1 + r_2$ =constant, the phase at the receiver will also be constant and these positions will represent points on an ellipse. By keeping this constraint of constant path length and allowing the point to rotate through an angle η about the x-axis, the surface of a prolate spheroid will be defined. The narrow beam properties of the transmitter and receiver used in this study can be described by these three angles (θ, β, η) and are given in Table 5.1. A Gaussian with peak value of 1, provides a good representation of a narrow beam. With this formulation the gain weighting function due to both the projector and hydrophone can be represented by,

$$G(\theta, \beta, \eta) = \exp\left[-(a_1(\theta - \theta_o)^2 - b_1\beta^2 - (b_1 + a_2)\eta^2\right] \tag{5.1.2}$$

where, the coefficients a_1, a_2, b_1 are determined from the beamwidths in Table 5.1.

Table 5.1 Narrow beam properties of the echometer projector and narrow beam hydrophone.

Projector (typical fringe θ_o):	$0.5^o \leq \theta - \theta_o \leq 0.5^o$	re -10dB
	$-8^o \leq \eta \leq 8^o$	re -10dB
Hydrophone (main lobe):	$-0.8^o \leq \beta \leq 0.8^o$	re -20dB
	$-0.8^o \leq \eta \leq 0.8^o$	re -20db

With the exception of target strength σ the remaining amplitude weighting factors, spherical spreading and absorption, are dependent on r_1 and r_2. Thus, the total gain weighting function H is given by,

$$H = \frac{G(\theta,\beta,\eta)}{r_1^2 r_2^2} 10^{-0.1\alpha(r_1+r_2)} \cdot \sigma \tag{5.1.3}$$

where,

$$\begin{aligned} r_1 &= B\frac{\cos\beta}{\sin(\theta-\beta)} \\ r_2 &= B\frac{\cos\theta}{\sin(\theta-\beta)} \\ \alpha &= \text{absorption coefficient [dB/m]}. \end{aligned}$$

In the following analysis the target strength σ will be assumed to be isotropic and normalized. The initial purpose of this idealized condition is to find the effects of the parameters which are system dependent, and then later to show how the processing technique approximates these conditions. Absorption effects can also be treated as a constant for each fringe. The fluctuations in range have only a small contribution to the change in intensity.

An evaluation of $s(t)$ can be simplified by evaluating H over total constant path lengths ($R = r_1 + r_2$). A constant phase surface which contains the center of an insonified volume ($\beta = \eta = 0$) has a path length range R_o given by,

$$R_o = \frac{B}{\sin\theta_o}(1 + \cos\theta_o) \tag{5.1.4}$$

where, θ_o = center of a fringe (see Table 1.2). Using the definitions of r_1 and r_2 in 5.1.3 we can construct a more general expression for R when $\beta \neq 0$. This is,

$$R = \frac{B}{\sin(\theta-\beta)}(\cos\beta + \cos\theta). \tag{5.1.5}$$

A plot of H has been computed to investigate the behaviour of H over a constant phase surface. This calculation required the inversion of 5.1.5 to find $\theta(\beta)$. Figure 5.2 displays the resulting value of H in terms of the two angles β

and η with $R_o = 43\text{m}$ and $\theta = 30°$. This plot demonstrates that the constant phase surface has a two dimensional Gaussian-like representation with a broader weighting along the η -axis. Notice that if some reference height, say $e^{-1}H$, is selected the resulting contour will approximate an ellipse which is a property of the beam intersections. This boundary may also be used to represent the noise field where all the values below a reference height contribute to background noise.

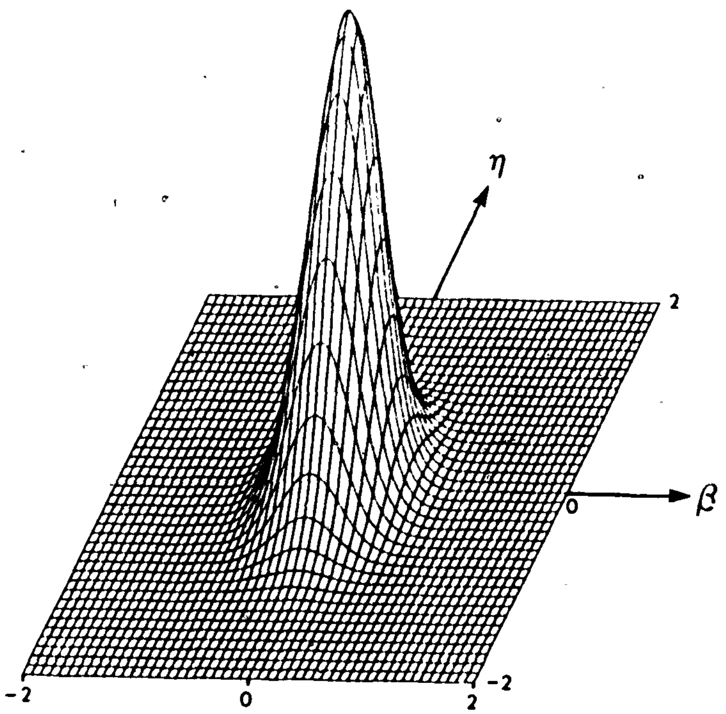

Figure 5.2 Amplitude weighting function H as a function of two angles β and η (in degrees) when $R_o = 43\text{m}$ and $\theta = 30°$.

An evaluation of the dependence of H on path length R was carried out by using a Monte Carlo technique. For a homogeneous distribution of scatterers on any phase surface with path length R an evaluation of the total impulse weighting function, $W(R)$, involves summing the individual values of R at each location on the surface. This technique is equivalent to a Monte Carlo evaluation of the surface integral whose surface is represented in Figure 5.2. This numerical evaluation was repeated over a series of ranges throughout the insonified volume and the normalized results are plotted in Figure 5.3 with no smoothing. The continuous nature of this plot verifies that; 1/the numerical method had negligible error terms for the purpose of demonstrating the dependence of the total gain function on range, and 2/ the evaluation of $s(t)$ reduces to a one dimensional analysis.

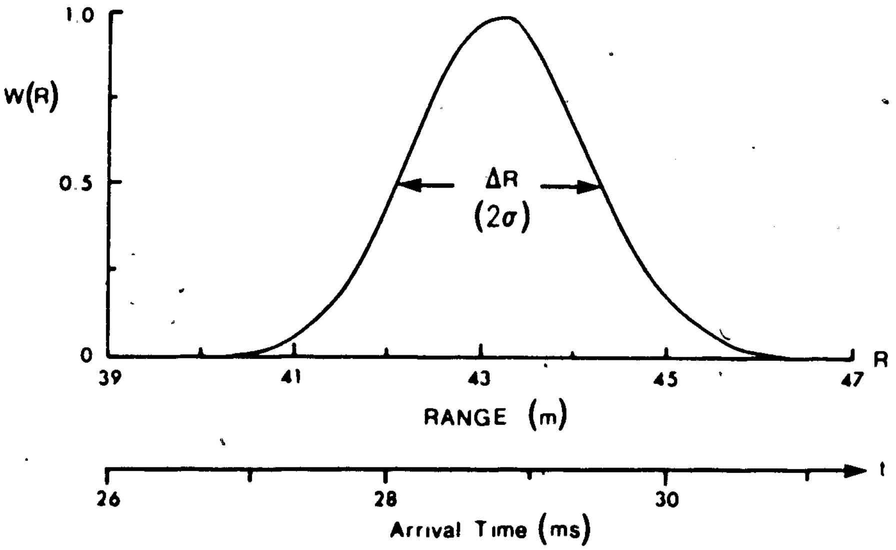

Figure 5.3 The resulting amplitude weighting function for a homogeneous distribution of scatterers within the insonified volume defined by fringe number 7.

The function $W(R)$ in Figure 5.3 represents a continuous probability density function of amplitude as a function of range (path length). $W(R)$ can be represented analytically by a skewed Gaussian. The center of the fringe R_o can be taken as the reference coordinate to simplify the analysis. With $u = R - R_o$ the normalized and transformed function $W(u)$, is given by,

$$W(u) = \sqrt{\frac{a}{\pi}}(1 + bu)\exp[-au^2] \tag{5.1.6}$$

where,

$$a = \frac{1}{2}\langle u^2 \rangle$$

$$b = \frac{4}{3}a^2\langle u^3 \rangle$$

$\langle u^2 \rangle$ =second moment of u

$\langle u^3 \rangle$ =third moment of u.

The statistical properties of u serve to define $W(u)$ and give some physical insight into its properties. The first moment of u is a biased estimate of the fringe center R_o since it lies below the maximum weighting value due to the asymmetry in $W(u)$. The second moment of u shows the effective width of a fringe. For example, with $\theta_o = 30$ deg, $R_o = 43.2$m then the width of $W(u)$ at its e^{-1} points, ΔR, is approximately 3.4m. Similarly at a deeper fringe with $\theta_o = 16$ deg and $R_o = 82.4$m we find $\Delta R = 9.0$m. The effective fringe width is proportional to the depth of a fringe center. Finally the asymmetry, the third moment of u, depends upon; 1/ changes in spherical spreading losses throughout the insonified volume, which increase with fringe depth, and 2/ the angle of inclination of the constant phase surface in the x-z plane, which decreases with fringe depth. It was also observed that if $W(u)$ was computed by only using values of $H(R)$ above a 10% threshold that the asymmetry decreased 72% and the effective width decreased 31%. Clearly the sensitivity of the resulting signal amplitude and phase on these parameters must be established.

By assuming the insonified volume contains a continuum of scatterers for which simple scattering theory applies (i.e. no multiple scatterering or diffusion) the evaluation of $s(t)$ reduces to solving an integral. Before transferring from the discrete to continuous case the concept of a scattering volume is necessary to keep the solution bounded. The mathematical model requires a distribution of isotropic targets with a mean spacial separation $<< \lambda$, but as the mean spacing tends towards zero the target strength from a unit volume approaches infinity. If the target strength is represented as a path length dependent quantity, $\sigma(R)$, so that for a constant phase surface bounded by R and R+dR, the target strength per unit volume is constant, then the evaluation of $s(t)$ will be bounded.

5.2 Using Fourier Space

The problem of interpreting the received time series can be condensed into a general formulation of pulse propagation and scattering in a time varying medium. Before introducing the general case an example based on ideal scatterers will be presented. This modest beginning provides the basis for describing the concepts of time convolution and transfer function.

For the case of simple transmitted pulses these physically realizable signals have the following property,

$$f(t) = 0 \qquad t < 0.$$

With $t = 0$ defining the relative time of transmission, this property simply states that there is no input signal prior to the initial time of transmission.

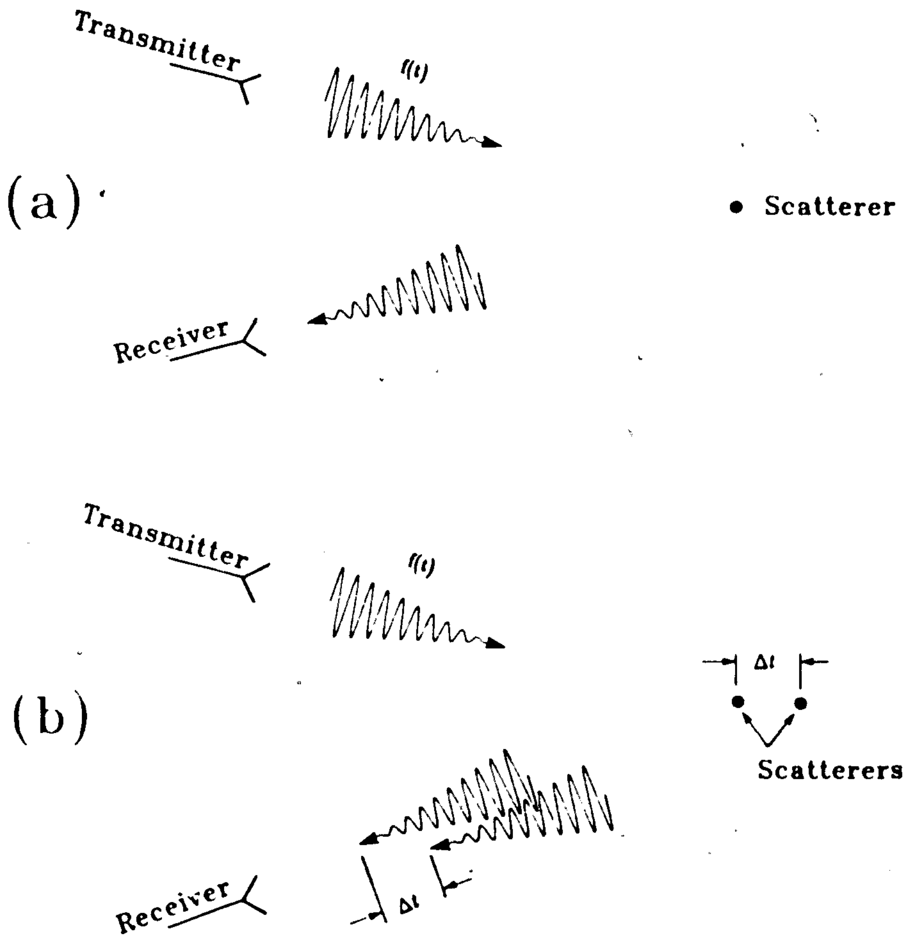

Figure 5.4 Schematic representation of a pulse $f(t)$ which is scatterered off a single scatterer (a) and then two scatterers separated Δt in time (b).

When a deterministic or physically realizable pulse $f(t)$ is transmitted into a lossless medium with a single ideal scatterer with unit amplitude at $t = t_o$ then the received signal $s(t)$ will be equivalent to the transmit pulse with a time delay, $s(t) = f(t - t_o)$ (see Figure 5.4a). The position of the scatterer in time (or space) can be represented by <u>an</u> impulse function $\delta(t)$ which has the unique properties of,

$$\int_{-\infty}^{\infty} \delta(t)dt = 1$$

and,

$$\delta(t) = 0 \qquad t \neq 0.$$

If two ideal scatterers with amplitudes α and β occur with time separations (Δt) less than the pulse length then the received signal is composed of two scattered pulses which reverse, shift and add (see Figure 5.4b). This process is referred to as a convolution in time. The received signal for this two scatterer example can be mathematically represented by,

$$s(t) = \alpha f(t - t_o) + \beta f(t - (t_o + \Delta t)). \qquad (5.2.1)$$

The amplitude and positions of the two scatterers, which help produce the output signal in equation 5.2.1, can also be represented mathematically. With the first scatterer time position at t_o the system weighting function $h(t)$ is given by,

$$h(t) = \alpha\delta(t - t_o) + \beta\delta(t - (t_o + \Delta t)) \qquad (5.2.2)$$

Notice that $h(t)$ is also deterministic and that $h(t) = 0$ when $t < 0$. The received signal at any time t depends upon both $f(t)$ and its previous time history which is described by $h(t - \tau)$ where τ is the relative time and bounded by $0 \leq \tau \leq t$. This relationship is completely described by,

$$s(t) = \int_0^t f(\tau)h(t - \tau)d\tau \qquad (5.2.3)$$

which is the integral representation of a time convolution and has an equivalent notation $f(t) * h(t)$. Equation 5.2.3 shows that $s(t)$ is a weighted linear sum which is evaluated over the entire time history of the input function $f(t)$. If $h(t)$ is unknown then one method of measuring it is to transmit an impulse function. For this special case the received signal will give $s(t) \approx h(t)$. In general the system weighting function is not time invariant. With the time between transmisions represented by T (the real time), then the weighting function will be described by $h(\mathrm{T}, t)$.

In the previous example the superposition principle was implied. That is, the addition of two scattered waves is a linear process since both addition and multiplication by a constant are conserved by the system. For example, for input signals $f_1(t)$ and $f_2(t)$, which have output signals $s_1(t)$ and $s_2(t)$ respectively, then an input of $\alpha f_1(t) + \beta f_2(t)$ will have an output of $\alpha s_1(t) + \beta s_2(t)$ when α and β are constants.

The analysis in the previous section was restricted to the time domain. A more complete description of the system is possible by working in the frequency domain. A Fourier transform of $f(t)$ gives a complex number $F(\omega)$ defined by,

$$F(\omega) = \int_{-\infty}^{\infty} f(t) e^{-j\omega t} dt \tag{5.2.4}$$

where $\omega = 2\pi f$ is the angular frequency. The properties of this operator and its inverse which is given by,

$$f(t) = \frac{1}{2\pi} \int_{-\infty}^{\infty} F(\omega) e^{j\omega t} d\omega \tag{5.2.5}$$

are summarised in Table 5.2 (see Lathi,1968 for derivations).

The time convolution in equation 5.2.3 corresponds to a product $F(\omega)H(\omega)$ in Fourier space (see Table 5.2). The frequency response or effective filter of the system is contained within $H(\omega)$. This term includes the effects of transducer beam patterns, scatterer positions and frequency response,

Table 5.2 Properties of Fourier transform pairs.

Operation	$f(t)$	$F(\omega)$
Linearity	$a_1 f_1(t) + a_2 f_2(t)$	$a_1 F_1(\omega) + a_2 F_2(\omega)$
Scaling	$f(at)$	$\frac{1}{\lvert a\rvert} F(\frac{\omega}{a})$
Time Shifting	$f(t - t_o)$	$F(\omega) e^{-j\omega t_o}$
Frequency Shifting	$f(t) e^{j\omega_o t}$	$F(\omega - \omega_o)$
Time Convolution	$f_1(t) * f_2(t)$	$F_1(\omega) F_2(\omega)$
Frequency Convolution	$f_1(t) f_2(t)$	$\frac{1}{2\pi}[F_1(\omega) * F_2(\omega)]$

plus all the other environmental conditions mentioned in chapter 3. These filters can be subdivided into 3 basic groups. The frequency response of the individual scatterers $H_1(\omega)$ is the first group. For a euphausiid this can be approximated by a high pass filter (solid line in Figure 5.5a) or for a more accurate representation the recent results of Kristensen and Dalen (1986) can be used (dashed line in Figure 5.5a). The frequency response of the transducers and electronics can be lumped together into a second group. This will typically define a bandpass filter (see Figure 5.5b).

Only the magnitude of the Fourier space representation has been given in both Figures 5.5a and 5.5b where,

$$|H(\omega)| = \sqrt{H_R^2(\omega) + H_I^2(\omega)} \tag{5.2.6}$$

and the subscripts R and I represent the real and imaginary components. The

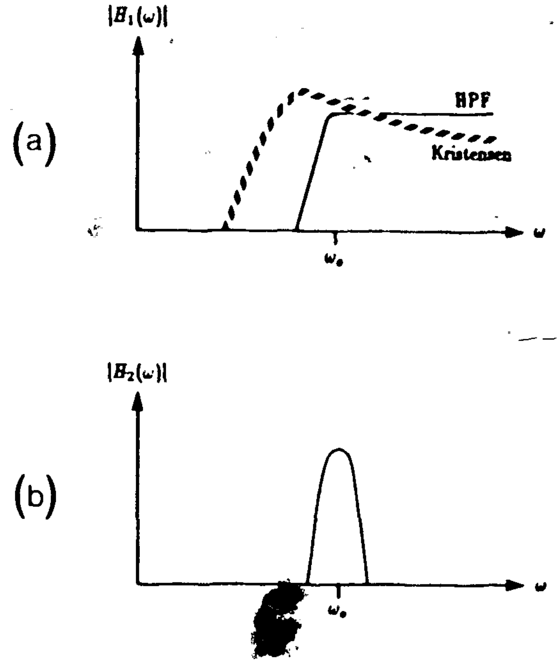

Figure 5.5 Frequency response of the zooplankton scatterers (a) and the effective bandpass filter of the acoustic transducers and electronics (b).

phase factor of the complex frequency response $\phi(\omega)$ is defined by,

$$\phi(\omega) = \tan^{-1}\left[\frac{H_I(\omega)}{H_R(\omega)}\right]. \tag{5.2.7}$$

The phase factor for both the euphausiid and transducer/electronics frequency response will typically be a time invariant function of ω.

The third filter in the group represents the Fourier transform of the scatterer distribution and amplitude. A typical weighting function in the time domain is given in Figure 5.6 for one realization of the spatial scatterer distributions. This weighting function can be represented by,

$$h(\mathrm{T},t) = \sum_{i=-n}^{n} W(t - t_o)\delta(t - (t_o + \Delta t_i(\mathrm{T})) + a_o \tag{5.2.8}$$

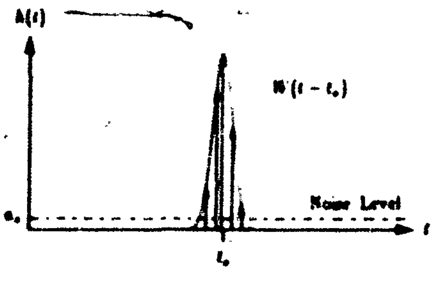

Figure 5.6 A typical weighting function $h(t)$ in the time domain for one realization of the spatial scatterer distribution.

where $W()$ combines the transmission losses and beam pattern weighting (equation 5.1.6) and a_o represents background noise. The Fourier transform of equation 5.2.8 is given by,

$$H(T,\omega) = e^{-j\omega t_o}\sum_{i=-n}^{n} W(\Delta t_i(T))e^{-j\omega\Delta t_i(T)} + 2\pi a_o\delta(\omega) \tag{5.2.9}$$

and is referred to as the transfer function. Notice that the sidelobe contamination (a_o) will only cause a change to the d.c. offset at $\omega = 0$.

An interpretation of equation 5.2.9, the frequency response of the scatterer distribution, will now be given. For the simple 2 scatterer case with equal amplitudes ($a_1 = a_{-1}$ and $a_o = 0$) which are separated by Δt and centered about t_o, equation 5.2.9 simplifies to,

$$H(\omega) = 2a_1\cos(\frac{\omega}{2}\Delta t)\cos(\omega t_o) - j2a_1\cos(\frac{\omega}{2}\Delta t)\sin(\omega t_o). \tag{5.2.10}$$

Both the real and imaginary parts of $H(\omega)$ represent a carrier with a period $2\pi/t_o$ which is being modulated by an envelope with a period of $4\pi/\Delta t$. Figure 5.7 shows the graphical representation of this Fourier transform pair with the transfer function showing both its real and imaginary components. In complex

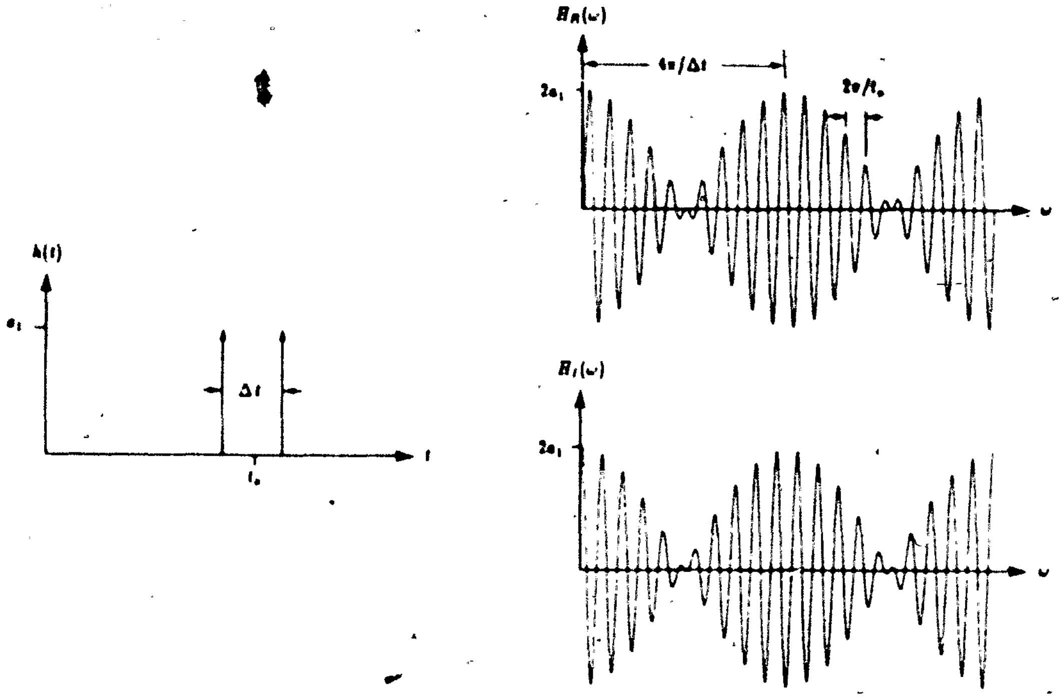

Figure 5.7 Fourier transform of two ideal discrete scatterers in time. The frequency space representation shows the real and imaginary components for positive ω ($H_3(\omega) = H_3(-\omega)$).

polar notation this transfer function has a more compact representation which gives the envelope and phase information,

$$H(\omega) = 2a_1 \cos(\frac{\omega}{2}\Delta t)e^{-j\omega t_0}. \qquad (5.2.11)$$

When $\omega\Delta t/2$ is an integral multiple of π then constructive inteference will occur. Similarly when $\omega\Delta t/2$ is an odd integral multiple of $\pi/2$ then destructive inteference will occur. Notice however that the received amplitude then has a cosine probability distribution and that the case of complete destructive interference has the lowest probability of occurrence. The phase factor in equation

5.2.11 contains the information of the center of the impulse weighting function. The time shifting property in Table 5.2 shows that a phase factor which is linear and passes through $\omega = 0$ shifts the origin in the time domain. When the received signal is sinusoidal $\omega = \omega_o$, this time shift is equivalent to a phase shift of $\omega_o t_o$. In Figure 5.4b the received signal can be divided into three regions. The first and last will have phases which depend upon the scatterer locations in time and the phase of the middle region depends upon the mean scatterer time location.

For a general scatterer distribution the actual number of scatterers within an arbitrary time window Δt will follow a Poisson distribution. The statistical properties of this distribution are not important at this time and the reader is referred to chapter 6 for a detailed presentation of the scatterer statistics. The point of interest is that when each realization or transmit pulse provides a statistically independent waveform then the waveform from much higher density scatterer distributions can be simulated by superposition. The advantage of this result is that the simulated dense population will not have the complications of multiple scattering or diffusion. The only requirements for this method are that the system be linear and that the scatterer distribution for the individual transmission is sparse enough so that simple scattering theory applies. By increasing the number of superimposed waveforms the resulting waveform will begin to approximate the results from a scatterer continuum. The equivalent mathematical relationships will now be presented.

Assuming the scatterers have a uniform spacing Δt and that $t_i = \Delta t_i(T) = i\Delta t_i$, where T is the real time, then the summation in equation 5.2.9 can be replaced by,

$$\sum_{i=-n}^{n} \exp[-t_i^2/2\sigma^2 - j\omega t_i]\Delta t$$

when $W(t_i)$ is an exponential with a standard deviation σ. By letting the number of scatterers become very large (i.e. $n \rightarrow \infty$) and the separation between scatterers become very small relative to the carrier wavelength (i.e. $\Delta t \rightarrow dt$) then the summation can be replaced by an integral. This gives,

$$\begin{aligned} H_3(\omega) &= e^{-j\omega t_o} \int_{-\infty}^{\infty} e^{-t^2/2\sigma^2} \cos(\omega t) dt \\ &= \sigma\sqrt{2\pi} e^{-\sigma^2\omega^2/2} e^{j\omega t_o}. \end{aligned} \tag{5.2.12}$$

The corresponding time and frequency space representations of this Gaussian weighting function are given in Figure 5.8. This example also demonstrates how a Gaussian in time yields a Gaussian in frequency. When $W()$ is not symmetric about its first moment in time $H_3(\omega)$ will have a more complex representation.

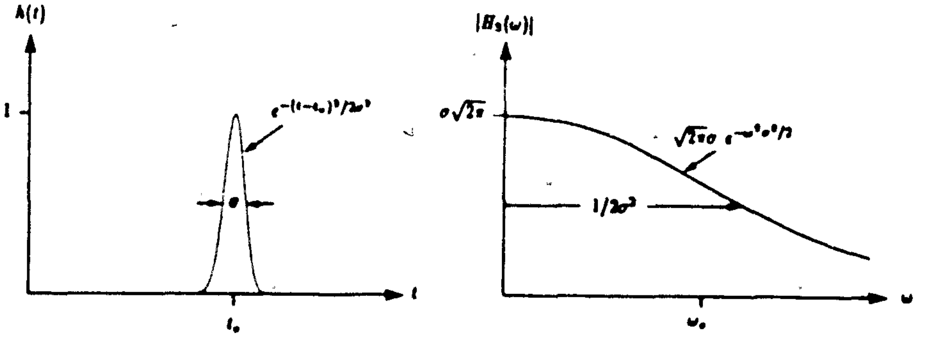

Figure 5.8 Fourier transform pair of a Gaussian where only the magnitude of the frequency space is presented (it has a phase factor of $-j\omega t_o$) and $|H_3(\omega)|$ is symmetric about $\omega = 0$.

Since the system is linear the three filter groups will combine by multiplication and define the total system frequency response $H(\omega)$. This gives,

$$\begin{aligned} H(\omega,\mathrm{T}) &= H_1(\omega)H_2(\omega)H_3(\omega,\mathrm{T}) \\ &= |H_1(\omega)||H_2(\omega)||H_3(\omega)|e^{-j(\phi_1(\omega)+\phi_2(\omega)+\phi_3(\omega,\mathrm{T}))} \end{aligned} \qquad (5.2.13)$$

Only the scatterer distribution response function is time dependent. Refraction, due to changes in the sound speed profile, will then be detected by time dependent changes in t_o, the first moment of $h_3(t)$.

A pulsed transmit signal $f(t)$ with a sinusoidal carrier ω_o will have a Fourier transform given by,

$$F(\omega) = iA\tau\left[\frac{\sin((\omega-\omega_o)\tau/2)}{(\omega-\omega_o)\tau/2} - \frac{\sin((\omega+\omega_o)\tau/2)}{(\omega+\omega_o)\tau/2}\right] \qquad (5.2.14)$$

where τ is the pulse width in time and A is the maximum amplitude of the pulse.

A variety of analytic models can be used to construct $H(\omega)$. For example, low pass and high pass filters can be expressed as complex polynomials and a Gaussian representation for the scatterer distribution would give a first order model of $H(\omega)$. Once $H(\omega)$ is known or approximated then $s(t)$ can be found by 2 basic methods. Calculation of the inverse Fourier transform of $F(\omega)H(\omega)$ is one approach. If this is not practical then $h(t)$ can be found by taking the inverse Fourier transform of $H(\omega)$ and used in the time convolution with $f(t)$ (equation 5.2.3) to compute $s(t)$. The resulting integrals which must be computed to reconstruct $s(t)$ become very complicated and do not have analytic solutions. Once a working algorithm is found however the effects of spacial gradients in the scatterer distribution and perturbations in the scatterer response $H_1(\omega)$ can be quantified.

5.3. Estimating $s(t)$

The previous section developed the concepts for determining $s(t)$, the received echo from a scatterer continuum. In this section the characteristic features of the amplitude and phase of the received echo will be presented by evaluating the time convolution $f * h$. The general solution for a skewed Gaussian is presented and followed by a first order expression of $h_3(t)$ (a skewed quadratic). The system filters are then applied ($h_1(t)$ and $h_2(t)$) and the amplitude and phase of the resulting waveform is discussed.

The evaluation of a convolution is not an intuitive process. One of the time series ($f(t)$ or $h(t)$) must be time reversed and shifted before integrating to find $s(t)$ for a specific t value. In addition, the effective limits of integration can also be dependent on the t values and characteristics of the times series.

Using equation 5.1.6 (a skewed Gaussian) to represent $h_3(t)$ and a sinusoid for $f(t)$ the time convolution $f * h_3$ is given by,

$$s(t) = \int_0^t \sin(\omega_o \tau)(1 + b(t - t_2 - \tau))e^{-a(t-t_2-\tau)^2} d\tau \qquad (5.3.1)$$

where t_2 is the time location of the peak value of $h_3(t)$ (when $b = 0$). The solution of this integral involves a basic change of variables, integation by parts and the evaluation of,

$$\int \sin(\omega(t' - t))e^{-at^2} dt.$$

This indefinite integral was evaluated by utilizing the MACSYMA program from M.I.T. which gives,

$$\frac{\sqrt{\pi}}{4\sqrt{a}} e^{-\omega^2/4a} \{(\mathrm{erf}(z) + \mathrm{erf}(z^*)) \sin \omega t' + i(\mathrm{erf}(z^*) - \mathrm{erf}(z)) \cos \omega t'\} \qquad (5.3.2)$$

where,

$$z = \frac{2at + i\omega}{2\sqrt{a}}$$

and,

$$\mathrm{erf}(z) = \frac{\sqrt{\pi}}{2} \int_0^z e^{-\zeta^2} d\zeta$$

is the error function. The complete solution to equation 5.3.1 is then given by,

$$s(t) = \Bigg\{ -\frac{b}{2a}\sin((\omega_o(t-t_2)) - \omega_o\tau)e^{-a\tau^2} \\ + \frac{\sqrt{\pi}}{2\sqrt{a}}e^{-\omega_o^2/4a}\Bigg[\sin(\omega_o(t-t_2))\left(\mathrm{Re}[\mathrm{erf}(\frac{2a\tau+i\omega_o}{2\sqrt{a}})] + \frac{b\omega_o}{2a}\mathrm{Im}[\mathrm{erf}(\frac{2a\tau+i\omega_o}{2\sqrt{a}})]\right) \\ + \cos(\omega_o(t-t_2))\left(\mathrm{Im}[\mathrm{erf}(\frac{2a\tau+i\omega_o}{2\sqrt{a}})] - \frac{b\omega_o}{2a}\mathrm{Re}[\mathrm{erf}(\frac{2a\tau+i\omega_o}{2\sqrt{a}})]\right)\Bigg]\Bigg\}\Bigg|_{t-t_2-t_o}^{t-t_2}. \tag{5.3.3}$$

A further evaluation of this expression becomes an exercise in numerical analysis and will not be continued here.

The essential features of $s(t)$ can be found by using a skewed quadratic to represent $h_3(t)$. This simplification allows a more direct analytic evaluation of $s(t)$. With the width of the Gaussian impulse function given by 2σ and b controlling the skewness then $h_3(t)$ can be reduced to,

$$h_3(t) = \begin{cases} (1+b(t-t_2))(1-\frac{1}{2\sigma^2}(t-t_2)^2) & |t-t_2| \le \sqrt{2}\sigma; \\ 0 & \text{elsewhere.} \end{cases} \tag{5.3.4}$$

The edges of $h_3(t)$ will be defined by,

$$t_1 \equiv t_2 - \sqrt{2}\sigma$$

and,

$$t_3 \equiv t_2 + \sqrt{2}\sigma.$$

The transmit pulse $f(t)$ also has a limited region of non-zero values. It can be described by,

$$f(t) = \begin{cases} \sin(\omega_o t) & 0 \le t \le t_o; \\ 0 & \text{elsewhere,} \end{cases} \tag{5.3.5}$$

where ω_o is the carrier angular frequency.

The integral or time convolution then reduces to,

$$s(t) = \int_0^{t_o} \sin\omega_o\tau(1+b(t-t_2-\tau))(1-\frac{(t-t_2-\tau)^2}{2\sigma^2})d\tau. \tag{5.3.6}$$

Notice that the upper integration bound is now t_o because of the bounds on $f(t)$. The zero values of $h_3(t)$ will also affect the limits of integration in equation 5.3.6 and are best found through a graphical example.

Table 5.3 Integration limits for the time convolution in equation 5.3.6 when $t_o \geq t_3 - t_1$ is true.

Time Region	1st limit (τ_a)	2nd limit (τ_b)
$t_1 \leq t \leq t_3$	0	$t - t_1$
$t_3 < t < t_1 + t_o$	$t - t_3$	$t - t_1$
$t_1 + t_o \leq t \leq t_3 + t_o$	$t - t_3$	t_o

Table 5.4 Integration limits for the time convolution in equation 5.3.6 when $t_o < t_3 - t_1$ is true.

Time Region	1st limit (τ_a)	2nd limit (τ_b)
$t_1 \leq t \leq t_1 + t_o$	0	$t - t_1$
$t_1 + t_o < t < t_3$	0	t_o
$t_3 \leq t \leq t_3 + t_o$	$t - t_3$	t_o

There are 2 general cases for determining the integration limits in equation 5.3.6 which depend upon the relative time width of $f(t)$ and $h_3(t)$. The first case applies when $t_o < t_3 - t_1$ (transmit time < width of $h_3(t)$). Figure 5.9a shows the 3 regions with similar properties which occur. These diagrams show the positions of $h_3(t - \tau)$ at different times t in τ space. The solid lines are used when $f(\tau)$ and $h(t - \tau)$ are multiplied (prior to integration). Integration then gives the area under the resulting curves within the specified bounds in τ space. Figure 5.9b shows the second case with $t_o \geq t_3 - t_1$. The basic difference between these two cases occurs in the middle region. In the first case $h_3(t)$ is narrower than $f(t)$ so $h_3(t)$ sets the limits of integration in the middle region. The converse is true in the second case since $f(t)$ is wider than $h_3(t)$. The exact limits of integration for these 2 cases and 3 time regions are given in Tables 5.1 and 5.2 respectively. Notice that for $t \leq t_1$ and $t \geq t_3 + t_o$ there will be no received signal.

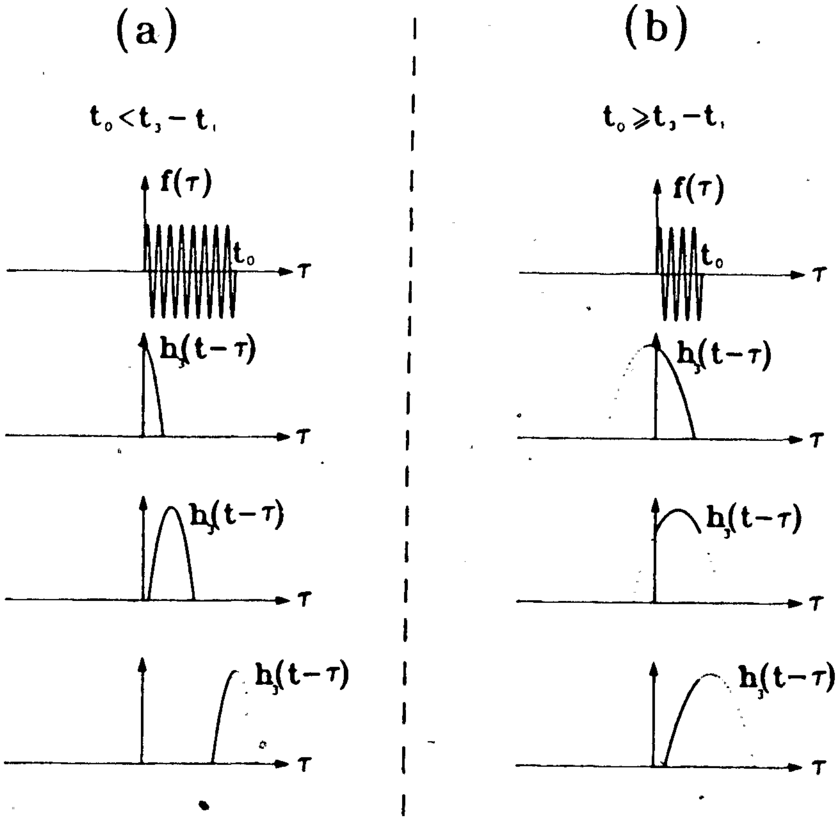

Figure 5.9 The relationships between $f(\tau)$ and $h_3(t-\tau)$ at different times t in τ space, for the 2 cases $t_0 < t_3 - t_1$ in (a) and $t_0 \geq t_3 - t_1$ in (b).

The time convolution can now be expressed as,

$$s(t) = \int_{\tau_a}^{\tau_b} f(\tau)h_3(t-\tau)d\tau. \tag{5.3.7}$$

Under the transformation $u = t - \tau$,

$$s(t) = \int_{t-\tau_b}^{t-\tau_a} f(t-u)h_3(u)du. \tag{5.3.8}$$

This integral has an exact solution given by,

$$s(t) = g_1(u)\sin(\omega_o(t - t_2 - u)) + g_2(u)\cos(\omega_o(t - t_2 - u))\Big|_{t-\tau_b}^{t-\tau_a} \tag{5.3.9}$$

where,

$$g_1(u) = \frac{1}{\omega_o}(1 + bu - \frac{1}{2\sigma^2}u^2 - \frac{b}{2\sigma^2}u^3) + \frac{1}{\sigma^2\omega_o^3}(3bu + 1)$$

and,

$$g_2(u) = \frac{1}{\omega_o^2}(\frac{-3b}{2\sigma^2}u^2 - \frac{1}{\sigma^2}u + b) + \frac{3b}{\sigma^2\omega_o^4}.$$

Now $g_1(u)$ and $g_2(u)$ can be expressed in polar notation (both are independent scalars):

$$\phi(u) = \tan^{-1}(g_1(u)/g_2(u))$$

and,

$$A(u) = \sqrt{g_1^2(u) + g_2^2(u)}$$

since,

$$g_1(u) = A(u)\sin(\phi(u))$$

and,

$$g_2(u) = A(u)\cos(\phi(u)).$$

The advantage of this transformation is that equation 5.3.9 can now be further reduced through a standard trigonometric identity to give,

$$s(t) = A(u)\cos(\omega_o(t - t_2 - u) - \phi(u))\Big|_{t-\tau_b}^{t-\tau_a}. \tag{5.3.10}$$

This expression for $s(t)$ shows the received echo to be the difference between two modulated signals with time evolving envelopes which depend upon $A()$ and $\phi()$ (the envelope is a complex time series).

The structure of the received signal can be represented graphically through a high resolution numerical evaluation of equation 5.3.10. Figure 5.10 gives an example with f_o = 2kHz, t_o = 4ms, σ = 1ms and b = 0s^{-1} (b controls the symmetry of $h_3(t)$). The location of $h(t)$ is completely relative as long as $t > t_o$. The peculiar structure of $s(t)$ is representative of the 3 regions outlined in Figure 5.9. The first and third regions have time evolving limits of integration as the pulse enters and leaves $h_3(t)$ respectively, while the middle region corresponds to a change in symmetry as the limits of integration pass through one cycle of ω_o.

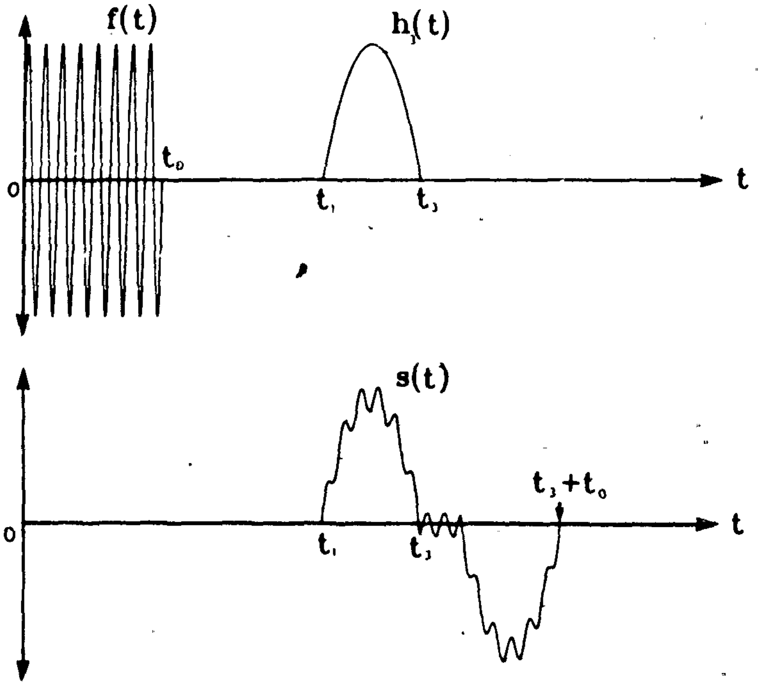

Figure 5.10 The time convolution $s(t)$ of $f(t)$ and $h_3(t)$ when $f(t)$ is a sinusoidal pulse and $h_3(t)$ is approximated by a quadratic.

The received signal $s(t)$ in Figure 5.10 would never be observed in nature.

The assumption that the scattering mechanism reflects all frequencies with a uniform amplitude weighting (and no phase shift) is implicit in this result. The scattering mechanism often behaves like a high pass filter (see Figure 5.5a) so the low frequency effects in Figure 5.10 are not observed. This high pass filter can be numerically implemented to improve the model of $s(t)$. A 36 point Chebyshev finite impulse response filter (a linear phase digital filter) was generated and numerically convolved with $s(t)$ to remove the low frequency components and the result is denoted by $\acute{s}(t)$.

An additional filter ($H_2(\omega)$) from the finite bandwidth of the system also effects $\acute{s}(t)$. This filter however can be combined with the demodulation procedure.

In this thesis, the complex envelope of $\acute{s}(t)$ contains the information of interest and the carrier (ω_o) can be removed. This is referred to as demodulation or mixing to zero frequency. The real component of the complex envelope is found by multiplying $\acute{s}(t)$ by $\cos(\omega_o t)$ and then applying a low pass filter. A low pass filter with cut off frequency $\omega_c << 2\omega_o$ removes the high frequency components and leaves the in-phase component (I) of the complex envelope. The lower bound of ω_c (the passband) will then determine the bandwidth of the received signal. A similar result is obtained when $\sin(\omega_o t)$ is multiplied with $\acute{s}(t)$ and then low pass filtered. This process gives the quadrature component (Q) of the complex envelope. The resulting amplitude $\mathbf{A}(t)$ and phase $\phi(t)$ of the envelope which describes $\acute{s}(t)$ are then found by,

$$\mathbf{A}(t) = \sqrt{I^2 + Q^2} \tag{5.3.11}$$

and,

$$\phi(t) = \tan^{-1}(Q/I). \tag{5.3.12}$$

Figure 5.11a shows the resulting amplitude and phase time series of the envelope of $\acute{s}(t)$ for a 200kHz carrier, 4ms pulse length and σ = 1ms. Before applying the high pass filter to this signal the time series was of the same form as in the previous figure (but with a much shorter wavelength). Notice that once again 3 distinct regions occur in the time series of Figure 5.11a. The overshoot at the discontinuties is an artifact of the discrete changes in $h_3(t)$ at $t = t_1$ and $t = t_3$. For a continuous impulse weighting function such as 5.1.6 a smooth transition between the 3 regions will occur.

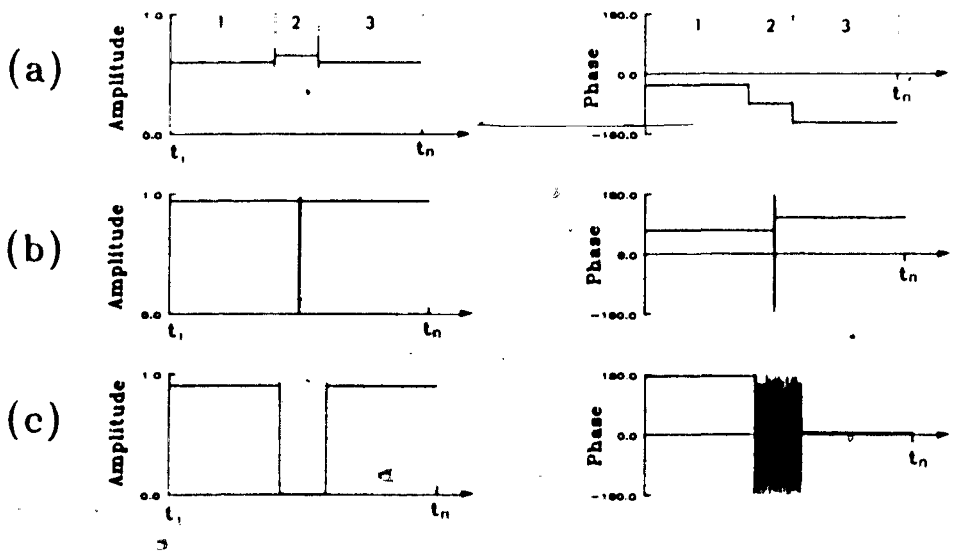

Figure 5.11 Normalized amplitude **A**(t) and phase $\phi(t)$ plots of the received echo $\acute{s}(t)$, for a 200kHz carrier for 3 different r_t values. The signals in (a) have $r_t = 1/\sqrt{2}$, (b) have $r_t = 1.01$ and (c) have $r_t = \sqrt{2}$. Note $t_n = t_3 + t_o$.

The characteristic features of $\acute{s}(t)$ are dependent on the ratio r_t which is given by,

$$r_t \equiv \frac{t_o}{\sqrt{8}\sigma} = \frac{t_o}{t_3 - t_1}. \tag{5.3.12}$$

The previous 2 examples of $s(t)$ have had a pulse length greater than the width of $h_3(t)$ ($r_t = 1/\sqrt{2}$). As $r_t \rightarrow 1$ the middle region collapses to a negligible width with zero amplitude and a random or meaningless phase (see Figure 5.11b). For values of $r_t > 1$ the middle region with zero amplitude increases in width and the corresponding phase is random (see Figure 5.11c). All of the examples in Figure 5.11 demonstrate a symmetric amplitude and asymmetric phase. The symmetry in $h_3(t)$ is reflected in the amplitude of $\dot{s}(t)$ but not in its phase signal. The phase values in Figure 5.11a are dependent on $\omega_o t_1$, $\omega_o t_2$, and $\omega_o t_3$ (the relative time locations determine the phase). Since $t_2 = (t_1 + t_2)/2$ the phase in the middle location can be estimated from the phase values in the 1st and 3rd regions. This allows estimates of the center (1st moment) of $h_3(t)$ even when $r_t \geq 1$.

When a skewness ($|b| > 0$) is introduced into $h_3(t)$ the symmetry in **A** and ϕ is lost. As mentioned in section 5.1 the impulse weighting function is slightly skewed. The presence of gradients in the vertical distribution of scatterers can also increase the skewness. The skewness factor in equation 5.3.4 has an upper bound of $|b| = 1/\sqrt{2}\sigma$. For values greater than this, negative values of $h_3(t)$ occur which have no physical meaning. If the volume target strength was observed to increase by a factor of two over a time scale of 4ms (a range of (1500m/s)(2ms)=3m for backscatter sound in the ocean) then b would have a value of 500s^{-1}. The diagrams at the far right of Figure 5.12 demonstrates the change in $h_3(t)$ for 3 different positive values of b. As b increases the trailing edge becomes steeper while the leading edge becomes flatter. For negative b values the converse is true. The corresponding changes in the envelope of $\dot{s}(t)$ are also contained in Figure 5.12. Refering to the 3 amplitude time series in

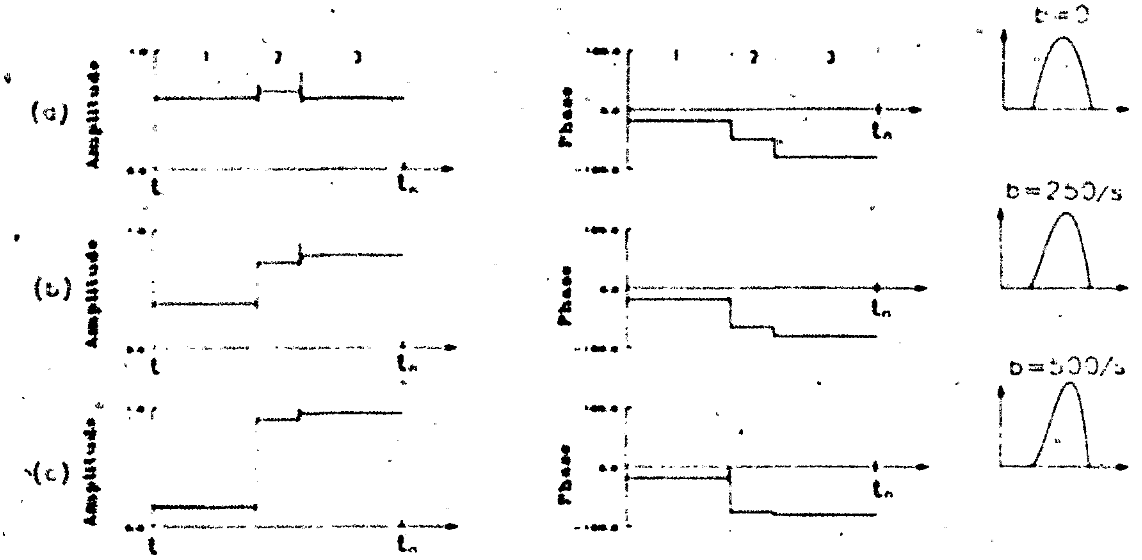

Figure 5.12 Examples of the skewness factor b on $\dot{s}(t)$ and $h_3(t)$. The normalized amplitude $\mathbf{A}(t)$ and phase $\phi(t)$ plots of the received echo $\dot{s}(t)$, for a 200kHz carrier with $t_o = 4$ms and $\sigma = 1$ms ($r_t = 1/\sqrt{2}$) are displayed and the impulse weighting function $h_3(t)$ is given at the far right. The 3 sets of plots have corresponding b values of: $b = 0\mathrm{s}^{-1}$ in (a), $b = 250\mathrm{s}^{-1}$ in (b), and $b = 500\mathrm{s}^{-1}$ in (c).

this figure it is observed that the amplitude in the first region decreased as b increases while the other two regions increase. This result is caused by the decrease in relative target strength on the left side of $h_3(t)$ (an increase on the right side) and an increase in the height of the peak. For the phase time series in Figure 5.12 only the middle region has a detectable change as b is increased. This result shows that the 1st and 3rd region are useful indicators of the location of $h(t)$ even in an environment which is subjected to gradients in the volume target strength distribution.

A more detailed look at the effect of skewness on the amplitude and phase

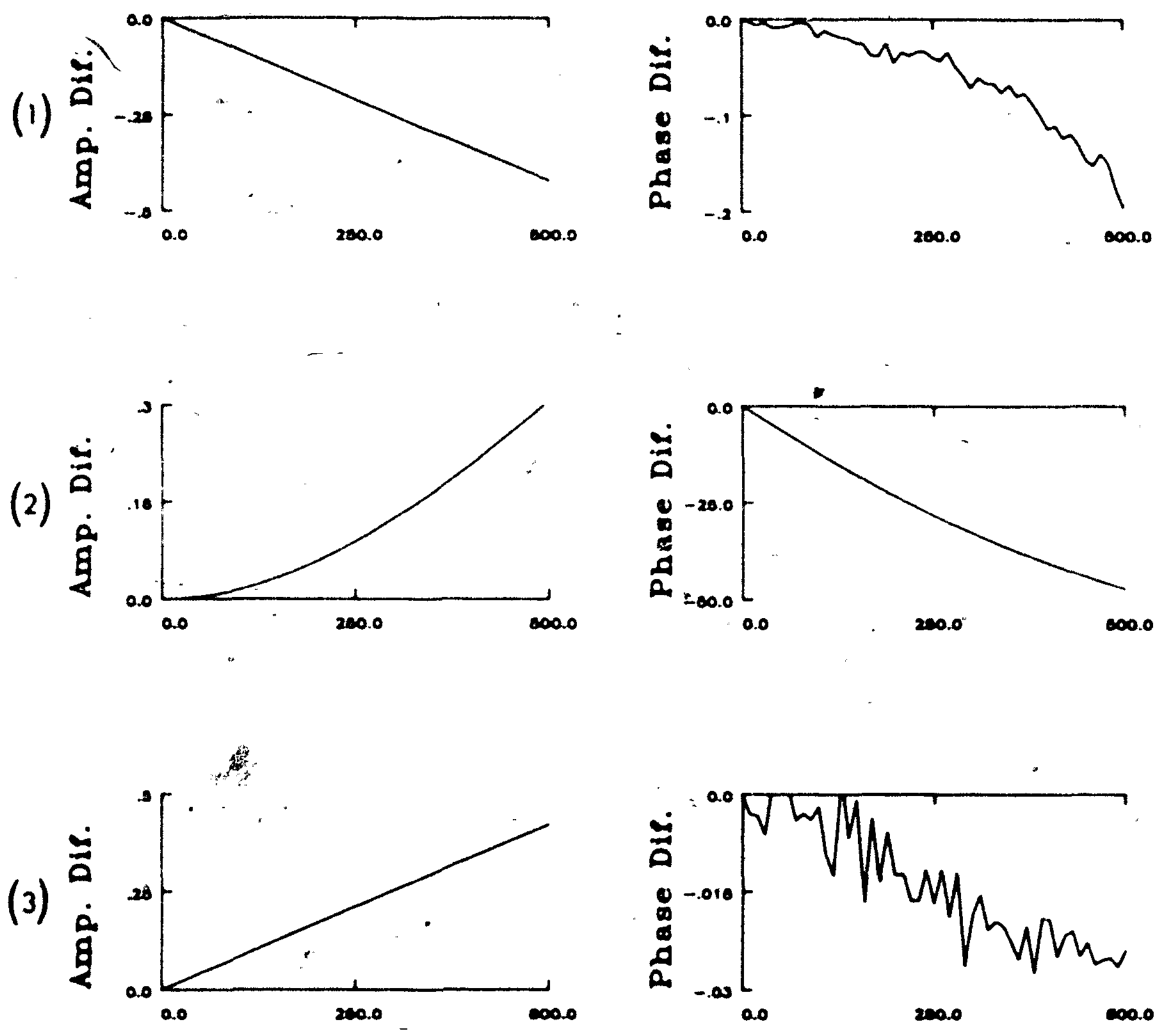

Figure 5.13 Changes in the amplitude and phase of $\dot{s}(t)$ for positive b values up to $500s^{-1}$. The 3 plots correspond to the 3 regions of $\dot{s}(t)$. Notice the change of scale.

of $\acute{s}(t)$ is given in Figure 5.13. This set of 3 plots compares the amplitude and phase in the middle of each of the 3 regions for a given b value relative to their amplitude and phase when $b = 0$. Figure 5.13(1) shows the relative change in the first region. As indicated in the previous figure, the amplitude decreases with increasing b and the phase only changes by 0.2 deg over the entire range. Figure 5.13(2) shows how the relative amplitude increases with b in the middle region. This figure also documents the large change in phase which corresponds to the shift in the peak location. The effects of skewness on the 3rd region are given in Figure 5.13(3). Once again the amplitude increases and at the same rate (but opposite sign) as in the first region. The phase change in this plot is very minimal (-0.03 deg maximum) and has a large noise component which is an artifact of the numerical resolution. The plots in Figure 5.13 also confirm that if variations in the skewness are occurring during a phase measurement then only the 1st and 3rd regions will give accurate results.

In summary, this chapter has shown how a scattering continuum in which single scatterering theory applies can provide a stable phase signature in the received echo when a sinusoidal pulse is transmitted. This result is of fundamental importance to utilizing an interferometric technique for estimating the arrival time of an acoustic pulse. The problem of transforming the received echo from a discrete set of scatterers into an echo which approximates the return from a scatterer continuum is treated through a statistical analysis in the next chapter.

6 STATISTICS OF STOCHASTIC SCATTERING

6.1 Introduction

Through the superposition of successive scattered acoustic returns, the coherent processing scheme numerically simulates the received signal from a scatterer distribution with a much higher scatterer number density than is true for each individual transmission. In the ocean, the biological targets often have a mean separation of many wavelengths. Under these conditions the phase of the received signal from a fixed range cell will be uncorrelated with previous transmissions because the scatterer distribution is constantly evolving in time. This fact can readily be verified in real data sets. However, as the in-phase and quadrature components of the signal at a fixed range are summed coherently over a larger number of independent transmissions the resulting phase signal converges towards a stable value. As these conditions are being approximated the returns from the range cell can be modelled by the sum of both a coherent and incoherent distribution of targets.

This chapter will develop the statistical properties of the coherently processed signal. Probability density functions (pdf) and moments of both the amplitude and phase signals are derived and expressed in terms of acoustic parameters. A final section shows the statistical behaviour of coherent processing and relates this to acoustic parameters.

6.2 Amplitude statistics

Lord Rayleigh (Rayleigh,1877) was the first to show that if n sources with uniform amplitude have random phases then in the limit $n \rightarrow \infty$ the amplitude pdf $P(A)$ is given by,

$$P(A) = \frac{A}{\sigma^2} \exp\left[-\frac{A^2}{2\sigma^2}\right]. \tag{6.2.1}$$

$P(A)$ is known as the Rayleigh distribution. It has the unique characteristic of being completely defined by the single parameter σ^2 which is equivalent to the variance of the received amplitude.

The Rayleigh distribution also applies to a uniform spacial distribution of discrete scatterers with a mean spacing greater than the insonifying wavelength. When these targets are randomly distributed in space the phase from each target will have a uniform pdf. This will be referred to as the incoherent field.

When scattering off a large target or a tightly packed group of small targets the phase of the received signal will remain constant. This will be referred to as the coherent field.

When a coherent signal is present in an incoherent field the statistical properties will be altered. Following a derivation similar to Ishimaru(1978) and Rice(1954), these properties will now be derived.

The general received signal from a group of targets about $\vec{r} = (x, y, z)$ which are insonified by a narrow band signal with a center frequency ω can be represented by,

$$u[\vec{r}(t)] = A_{in}[\vec{r}(t)]e^{i\omega t} + A_{co}[\vec{r}(t)]e^{i\omega t}. \qquad (6.2.2)$$

The $A[\vec{r}(t)]$ terms are complex phasor amplitudes with modulus $|A[\vec{r}(t)]|$ and argument $\phi(t)$. The subscripts *in* and *co* refer to the incoherent and coherent signals respectively. In general,

$$A[\vec{r}(t)] = \sum_{j=1}^{N} |A_j[\vec{r}(t)]| \exp[i\phi_j(t)] \qquad (6.2.3)$$

where N represents the total number of targets from the insonified volume at r. This summation can best be understood as a random walk in the complex

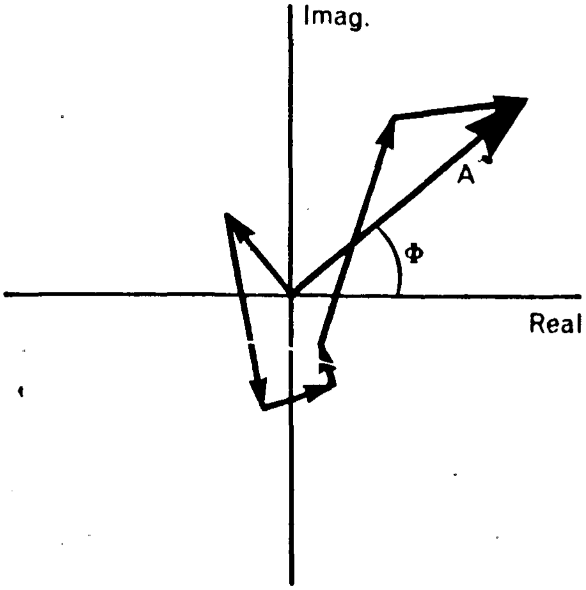

Figure 6.1 A random walk in the complex plane.

plane. Figure 6.1 shows how $A[\vec{r}(t)]$ is simply the vector addition of individual components.

For the incoherent signal each term is statistically independent. The resulting amplitude (envelope of the received signal) will follow Rayleigh statistics for large N and the phase will be uniformly distributed. A pure coherent signal however will have a constant phase value $\phi_j = \phi_o$ so that the resulting amplitude becomes the sum of the individual values. When the coherent properties are stable (reflective properties remain constant) both the resulting amplitude and phase of the received signal will have Dirac delta functions for their pdf's (assuming the system noise is negligible).

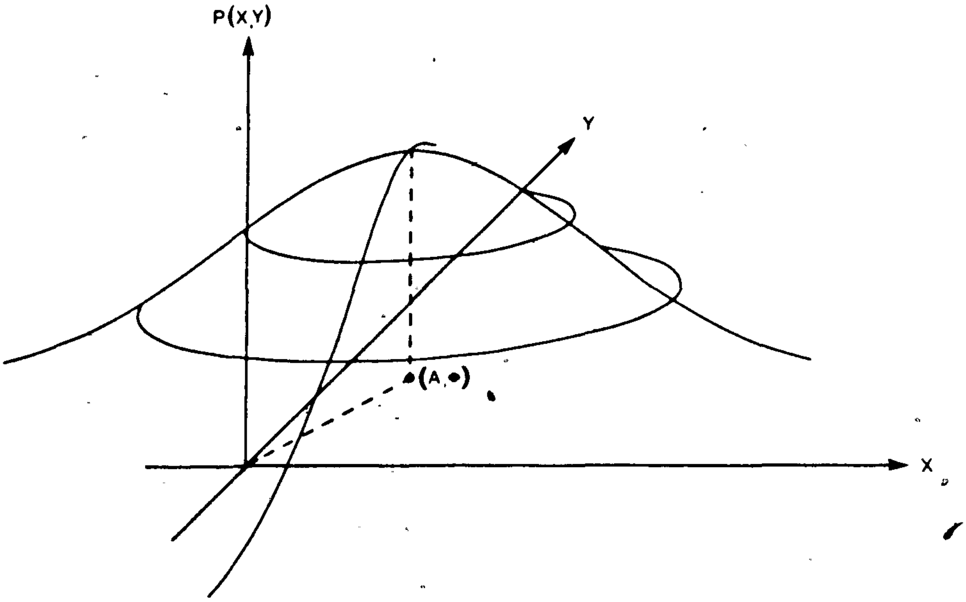

Figure 6.2 The joint probability density function $P(X, Y)$.

The in-phase and quadrature components of the received signal, X and Y respectively, can be represented by,

$$
\begin{aligned}
X &= a_o \cos\phi_o + \sum_{j=1}^{N} a_j \cos\phi_j = x_{co} + x_{in} \\
Y &= a_o \sin\phi_o + \sum_{j=1}^{N} a_j \sin\phi_j = y_{co} + y_{in}
\end{aligned}
\tag{6.2.4}
$$

where the amplitude and phase of the coherent signal are represented by a_o and ϕ_o. When the terms in the summation are independent random variables, Gaussian statistics can be used to describe x_{in} and y_{in}. As $N \rightarrow \infty$ the central limit theorem (c.f. Davenport and Root,1958) states that the probability distribution of a sum of N independent random variables approaches a normal distribution. Since quadrature components are uncorrelated, the joint pdf of

x_{in} and y_{in} will be given by,

$$P(x_{in},y_{in}) = P(X,Y) = \frac{1}{2\pi\psi}\exp\left[\frac{-1}{2\psi}((X-x_{co})^2+(Y-y_{co})^2)\right] \qquad (6.2.5)$$

where, $\psi = \langle (X-x_{co})^2\rangle = \langle (Y-y_{co})^2\rangle$. It is more desirable to transform these statistics into amplitude A and phase Φ space. Using the transformation,

$$\begin{aligned} X &= A\cos\Phi \\ Y &= A\sin\Phi \end{aligned} \qquad (6.2.6)$$

Then,

$$P(A,\Phi)\,dAd\Phi = \frac{A}{2\pi\psi}\exp\left[-\frac{1}{2\psi}(A^2+a_o^2-2Aa_o\cos(\Phi-\phi_o))\right] dAd\Phi. \qquad (6.2.7)$$

A diagram of $P(X,Y)$ and $P(A,\Phi)$ is shown in Figure 6.2 This pictorial representation helps in the interpretation of the various probability functions. By defining an arbitrary area $dXdY$ about the point (X,Y) the probability of an event occurring in this area will be $P(X,Y)dXdY$. Using this identity the amplitude pdf can be derived by finding the probability within a concentric ring with radius A and thickness dA. Using equation 6.2.7 this gives,

$$\begin{aligned} P(A)\,dA &= \int_0^{2\pi} P(A,\Phi)\,d\Phi dA \\ &= \frac{A}{\psi}\exp\left[-\frac{A^2+a_o^2}{2\psi}\right] I_o\left(\frac{Aa_o}{\psi}\right)dA \end{aligned} \qquad (6.2.8)$$

where $I_o(\ )$ is the modified Bessel function (Abramowitz and Stegun,1960). Notice that $P(A)$ is independent of the coherent phase as expected. This distribution is commonly known as the Ricean distribution and has been used in various applications (Goodman,1976) including statistical communication theory, speckle in optics, synthetic aperture radar, and shot noise theory. An example of how this distribution can also be applied to modelling the amplitude statistics of the acoustic backscatter from individual fish has been recently developed by Clay and Heist(1984).

When the received signal is composed of a superposition of signals from a set of scatterers the total scattering cross-section σ_T is the sum of coherent and incoherent scattering cross-sections (Fried,1976). The scattering cross-section σ is defined by,

$$\sigma \equiv 4\pi \frac{I_s}{I_r} = \kappa^2 I_s \tag{6.2.9}$$

where,

I_s =intensity of the scattered signal,

I_r =reference intensity.

For the coherent signal

$$\sigma_{co} = \kappa^2 a_o^2 \tag{6.2.9}$$

while the incoherent signal is described by

$$\sigma_{in} = \kappa^2 2\psi. \tag{6.2.10}$$

The factor of 2 in the incoherent signal arises from the definition of intensity being used (i.e. $I \propto (\text{amplitude})^2$ and amplitude $= \sqrt{2}$ root-mean-square amplitude). The Ricean pdf then becomes,

$$P(A) = \frac{2\kappa^2 A}{\sigma_{in}} \exp[-\frac{\kappa^2 A^2 + \sigma_{co}}{\sigma_{in}}]\, I_o(\frac{2\kappa A\sqrt{\sigma_{co}}}{\sigma_{in}}). \tag{6.2.11}$$

A further simplification can be made by defining,

$$\gamma \equiv \frac{\sigma_{co}}{\sigma_{in}} = \frac{\text{coherent echo energy}}{\text{incoherent echo energy}} \tag{6.2.12}$$

and redefining σ_{co} and σ_{in} in terms of γ and σ_T gives,

$$\begin{aligned} \sigma_{in} &= \sigma_T/(1+\gamma) \\ \sigma_{co} &= \gamma\sigma_T/(1+\gamma). \end{aligned} \tag{6.2.13}$$

Then the Ricean pdf expressed in terms of these acoustic parameters is,

$$P(A) = \frac{2\kappa^2 A(1+\gamma)}{\sigma_T} \exp[-\frac{\kappa^2 A^2(1+\gamma)}{\sigma_T} - \gamma]\, I_o(\frac{2\kappa A\sqrt{\gamma(1+\gamma)}}{\sqrt{\sigma_T}}). \tag{6.2.14}$$

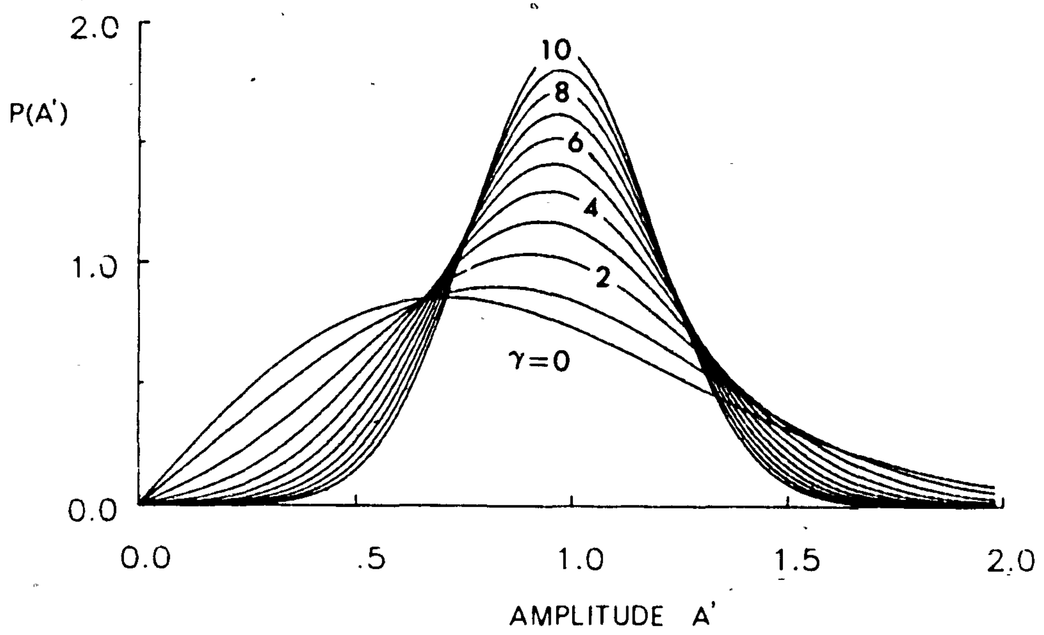

Figure 6.3 The amplitude probability density function $P(A')$ as function of the normalized amplitude for various coherent/incoherent energy ratios (γ).

A similar representation has been used by Clay and Heist(1984) to identify fish from σ_T and γ while using a single beam sonar. Their derivation of $P(A)$ however neglected the proportionality constant κ.

A dimensionless plot of equation 6.2.14 can be obtained by using the transformation $A' = \kappa A/\sqrt{\sigma_T}$. A plot of $P(A')$ versus A' for various values of γ is given in Figure 6.3. A continuous transition from a Rayleigh distribution when $\gamma = 0$ to a Gaussian centered about $A' = 1$ for large γ is observed. In the limit as $\gamma \to \infty$ the pdf will approximate a Delta function (Middleton,1960). These results are consistent with an interpretation of a pure incoherent signal when $\gamma = 0$ and a pure coherent signal when $\gamma^{-1} = 0$.

6.3 Moments of the amplitude

With the amplitude pdf independent of phase the ν^{th} amplitude moment can be obtained by evaluating,

$$\langle A^{\nu}\rangle = \int_0^{\infty} A^{\nu} P(A)\, dA. \tag{6.3.1}$$

By substituting 6.2.14 into 6.3.1 the moments of the received amplitude can be represented in terms of its acoustic parameters. Using the transformation,

$$I_o(z) = J_o(z e^{\imath\pi/2}), \tag{6.3.2}$$

where $J_o(\,)$ is the Bessel function, then 6.3.1 can be put into the form of Hankel's exponential integral (Gradshteyn and Ryzhik,1980,6.6.31),

$$\int_0^{\infty} x^{\mu} \exp[-\alpha x^2] J_o(\beta x)\, dx = \frac{\Gamma((\mu+1)/2)}{2\alpha^{((\mu+1)/2)}}\, {}_1F_1(\frac{\mu+1)}{2}; 1; -\frac{\beta^2}{4\alpha}). \tag{6.3.3}$$

The resulting evaluation of 6.3.1 becomes,

$$\langle A^{\nu}\rangle = [\frac{\sigma_T}{\kappa^2(1+\gamma)}]^{\nu/2} \Gamma(\frac{\nu}{2}+1) e^{-\gamma}\, {}_1F_1(\frac{\nu}{2}+1; 1; \gamma) \tag{6.3.4}$$

where $\Gamma(\,)$ is the gamma function and ${}_1F_1(\,)$ is the confluent hypergeometric function. Using Kummer's transformation (Middleton,1960,A.1.17a),

$${}_1F_1(\alpha; \beta; x) = e^{x}\, {}_1F_1(\beta - \alpha; \beta; -x) \tag{6.3.5}$$

we can simplify 6.3.4 to give,

$$\langle A^{\nu}\rangle = [\frac{\sigma_T}{\kappa^2(1+\gamma)}]^{\nu/2} \Gamma(\frac{\nu}{2}+1)\, {}_1F_1(-\frac{\nu}{2}; 1; -\gamma). \tag{6.3.6}$$

The confluent hypergeometric function represents various combinations of polynomial, exponential, Bessel and other special fuctions. The interpretation of a specific result depends upon its three parameters and many of the standard forms have been tabulated (Abramowitz and Stegun,1960,13.6). A total of six independent recurrence relationships exist for evaluating standard forms not found in the tables.

Two characteristic forms of 6.3.6 exist which depend on ν being even or odd. The first moment is easily found from (Middleton,1960, A.1.31.a)

$$ {}_1F_1(-\frac{1}{2};1;-\gamma) = e^{-\frac{\gamma}{2}}\left[(1+\gamma)I_0(\frac{\gamma}{2}) + \gamma I_1(\frac{\gamma}{2})\right], \tag{6.3.7} $$

which gives,

$$ \langle A^1 \rangle = \sqrt{\frac{\sigma_T}{\kappa^2(1+\gamma)}}\,\frac{\sqrt{\pi}}{2}\,e^{-\frac{\gamma}{2}}\left[(1+\gamma)I_0(\frac{\gamma}{2}) + \gamma I_1(\frac{\gamma}{2})\right]. \tag{6.3.8} $$

By utilizing the recurrence relationships the higher order odd moments can also be found and will be expressed in terms of polynomial, exponential and Bessel functions.

The even moments can be related to a specialized polynomial. The confluent hypergeometric function is a solution to Kummer's differential equation (d.e.) (Abramowitz and Stegun,1960,13.1.1)

$$ x\,\frac{d^2F}{dx^2} + (\beta - x)\,\frac{dF}{dx} - \alpha F = 0 \tag{6.3.9} $$

which has solutions ${}_1F_1(\alpha;\beta;x)$. For even moments of 6.3.6 the d.e. which corresponds to ${}_1F_1(-\frac{\nu}{2};1;\gamma)$ becomes,

$$ \gamma\,\frac{d^2F}{d\gamma^2} + (1-\gamma)\,\frac{dF}{d\gamma} + \nu F = 0. \tag{6.3.10} $$

This d.e. has a solution defined by Laguerre polynomials $L_{\frac{\nu}{2}}(\gamma)$ (Gradshteyn and Ryzhik,1980,8.97), whose properties have been documented. By transforming $\gamma \rightarrow -\gamma$ the proper form of 6.3.6 can be found. Thus for ν even,

$$ \langle A^\nu \rangle = \left[\frac{\sigma_T}{\kappa^2(1+\gamma)}\right]^{\nu/2}\left(\frac{\nu}{2}!\right) L_{\frac{\nu}{2}}(-\gamma). \tag{6.3.11} $$

Using the result $L_1(x) = 1 - x$, the second moment of the received amplitude ($\nu = 2$) simplifies to,

$$\langle A^2 \rangle = \frac{\sigma_T}{\kappa^2}. \tag{6.3.12}$$

This relationship shows that the total received energy is directly related to the second moment of the amplitude. The higher order even moments become more complicated polynomial expressions.

6.4 Phase Statistics

The statistical properties of the amplitude signal have been used extensively in the analysis of speckle, shot noise, radar and acoustic backscattering. The phase signal however is seldom included. For the case of an incoherent signal the corresponding phase pdf is uniform (Ishimaru,1978). However a pure coherent signal will have a delta function phase pdf centered about the reference phase ϕ_o. The general phase pdf $P(\Phi)$ ~~which~~ incorporates this transition will now be developed from the joint pdf $P(A, \Phi)$.

$P(\Phi)$ is determined by finding the probability of an event occurring within an angular sector defined by Φ and $\Phi + d\Phi$. This corresponds to integrating the joint pdf in 6.2.7 over all possible values of A

$$P(\Phi)d\Phi = \int_0^\infty P(A, \Phi)\, dA d\Phi. \tag{6.4.1}$$

A straightforward evaluation of this integral is given in Appendix 5 with the phase offset $\phi_o = 0$. When $\phi_o \neq 0$ a simple transformation must be applied to Φ in the following results. The resulting expression for 6.4.1 is,

$$P(\Phi) = \frac{1}{2\pi} e^{-\gamma} + \frac{\sqrt{\gamma}}{2\sqrt{\pi}} \cos\Phi \exp[-\gamma \sin^2\Phi] \left(1 + \frac{\cos\Phi}{|\cos\Phi|} \mathrm{erf}(\sqrt{\gamma}\cos\Phi)\right). \tag{6.4.2}$$

Notice that the phase pdf is independent of σ_T. A plot of $P(\Phi)$ for $-\pi \leq \Phi \leq \pi$ and various values of γ is given in Figure 6.4. A continuous transition from

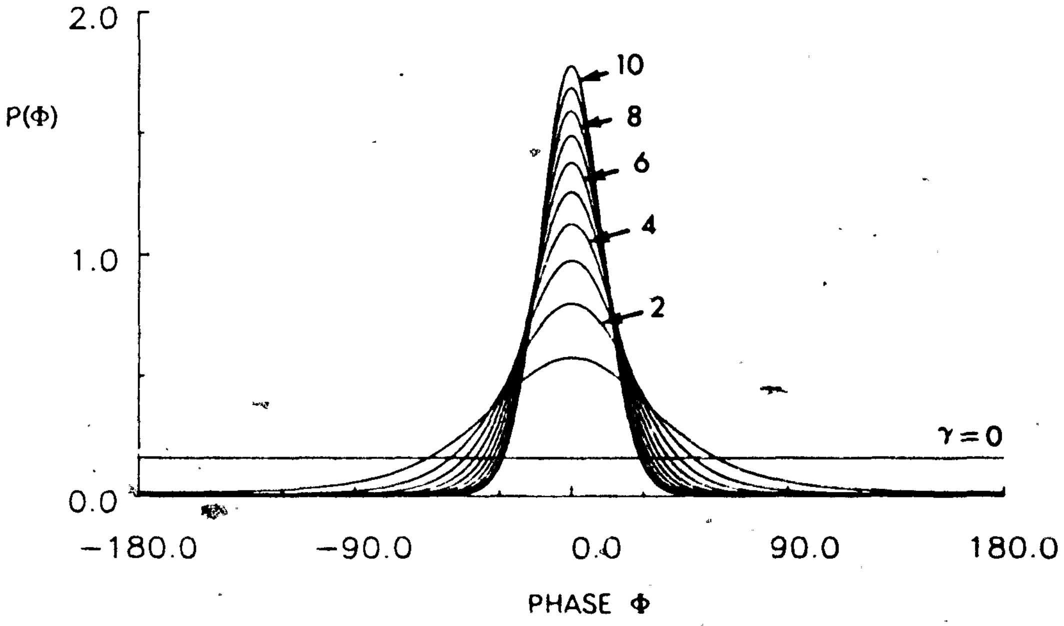

Figure 6.4 The phase probability density function $P(\Phi)$ for phase values centered about zero and various coherent/incoherent energy ratios (γ).

a uniform distribution when $\gamma = 0$ to a Gaussian centered about $\Phi = 0$ for larger γ is observed. These results are also consistent with the interpretation of a pure incoherent signal when $\gamma = 0$ and a pure coherent signal when $\gamma^{-1} = 0$.

6.5 Moments of the phase

Similar to the amplitude statistics the ν^{th} phase moment is generated by evaluating,

$$\langle \Phi^{\nu} \rangle = \int_{-\pi}^{\pi} \Phi^{\nu} P(\Phi)\, d\Phi. \tag{6.5.1}$$

For simplicity we will assume $\langle \Phi^1 \rangle = 0$ in this analysis. In general this will not be true and the phase offset ϕ_o must be included. The evaluation of 6.5.1

is complicated by the error function (erf) in 6.4.2. An alternative method is possible by expressing $P(\Phi)$ as a series. The joint pdf in 6.2.7 can be simplified by expressing $\exp[(Aa_o \cos\Phi)/\psi]$ as a series. Then after the appropriate integrations and transformations (Middleton,1960) the resulting form is,

$$P(\Phi) = \frac{1}{2\pi} \sum_{m=0}^{\infty} \epsilon_m \frac{\Gamma(m/2+1)}{\Gamma(m+1)} {}_1F_1(m/2; m+1; -\gamma) \cos m\Phi, \tag{6.5.2}$$

where ϵ_m = Newmans factor with $\epsilon_0 = 1$ and $\epsilon_n = 2$ $(n \neq 0)$. By combining the terms in the summation which are independent of Φ into one term $G(m, -\gamma)$ where

$$G(m, -\gamma) = \frac{\Gamma(m/2+1)}{\Gamma(m+1)} {}_1F_1(m/2; m+1; -\gamma), \tag{6.5.3}$$

6.5.2 then simplifies to,

$$P(\Phi) = \frac{1}{2\pi} \sum_{m=0}^{\infty} \epsilon_m G(m, -\gamma) \cos m\Phi. \tag{6.5.4}$$

The second moment of the phase signal is then found by substituting 6.5.4 into 6.5.1 and integrating by parts. Noting the special case for $m = 0$ the result is,

$$\langle \Phi^2 \rangle = \frac{\pi^2}{3} + 2 \sum_{m=1}^{\infty} \frac{(-1)^m}{m^2} G(m, -\gamma). \tag{6.5.5}$$

The evaluation of this expression however is non-trivial because it does not have a representation in terms of standard functions. Two infinite sums must be evaluated for each value of γ in 6.5.5.

Since any practical evaluation will utilize digital computers a simpler algorithm is found by substituting 6.4.2 into 6.5.1 and numerically integrating. By using Simpson's rule to evaluate 6.5.1 a plot of $\langle \Phi^2 \rangle$ as a function of γ has been produced and is displayed in Figure 6.5. Notice the rapid change in the second moment for $\gamma \leq 2$. This is an important concept for acoustic measurements which will be further developed in Chapter 7.

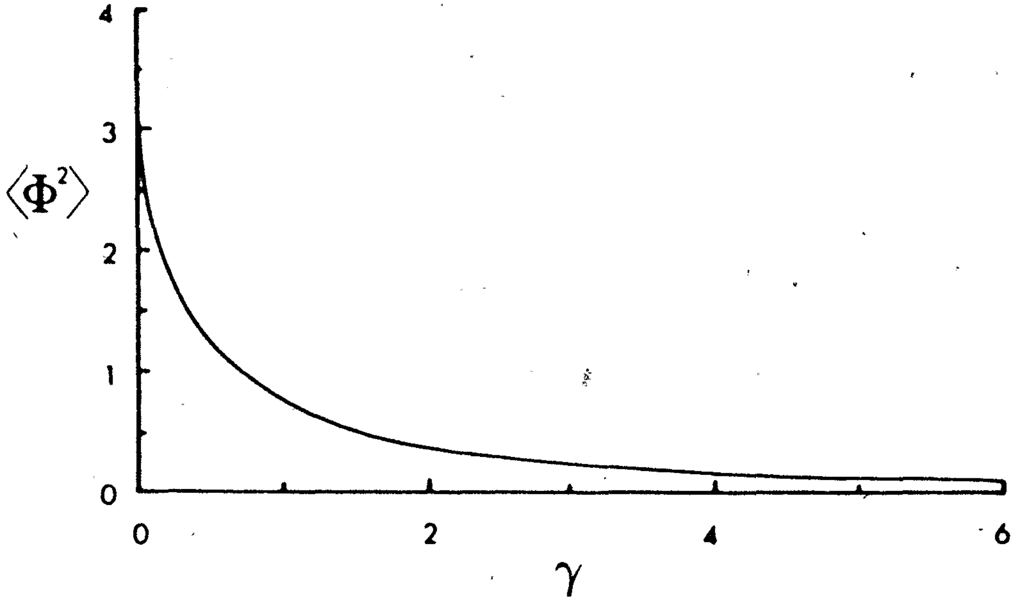

Figure 6.5 The second moment (about zero), in units of rad², of the phase probability density function as a function of γ.

An empirical relationship to the resulting plot in Figure 6.5 has been found by expressing $\langle\Phi^2\rangle$ as an exponential.

$$\langle\Phi^2\rangle = \frac{\pi^2}{3} e^{f(\gamma)} \tag{6.5.6}$$

where $f(\gamma)$ is a 3rd order polynomial.

$$f(\gamma) = 0.329 + 1.34\gamma - 0.239\gamma^2 + 0.0186\gamma^3$$

and has a variance of ± 0.0143 for $\gamma \leq 5$.

6.6 Coherent processing statistics

This section develops the statistical processes behind coherent processing. Using a binary representation the distribution of events and spacing between events is derived. The relationship between the first and second moments of the scatterer distribution after coherent processing are then related to their acoustic parameters.

When the scattering mechanism can be modelled as a simple isotropic scatterer or an array of such scatterers (see section 3.2) a binary string can be used to represent the spacial distribution of targets in one dimension. In Chapter 5 the analytic analysis was reduced to evaluating the system as a function of path length or constant phase surfaces. Thus we need only be concerned with the distribution of scatterers within our insonified volume as a function of path length R. For example, if each 1 corresponds to a unit target (an event) within a bin of width δR and each 0 corresponds to no event or the space between events then one possible distribution of unit targets between R and $R + dR$ can be discribed by,

$$01011000101010\cdots011001101010$$

where $dR = n\delta R$ for a total of n digits.

A Poisson process has the following properties (Miller and Freund,1985): (1) each trial is independent of previous values, (2) l trials are made that result in either a success or failure, (3) the total number of successes y in l trials is a random variable. Clearly the binary string model corresponds to a Poisson process.

For a total number of digits n, the number of events m, and a density of events $p = m/n$, the probability of k events occurring $P(k;n,p)$ is explicitly given by the binomial distribution,

$$P(k;n,p) = p^k(1-p)^{n-k}\binom{n}{k}. \qquad (6.6.1)$$

The mean of a binomially distributed variable is np and the variance is $np(1-p)$ (Hoel,1971). When n is a large number the binomial distribution approximates the Poisson distribution $P(k;\mu)$ where,

$$P(k;\mu) = e^{-\mu}\frac{\mu^k}{k!} \qquad (6.6.2)$$

and, $\mu = np =$ mean number of events. The Poisson distribution has the characteristic feature of having a variance which is equivalent to the mean. Thus with μ representing the mean number of events between R and $R + dR$ the probability of k events occurring is given by $P(k;\mu)$ when there are a large number of bins. The probability of no event ($k = 0$) is represented by an exponential,

$$P(0;\mu) = e^{-\mu}. \qquad (6.6.3)$$

The distribution of space or time between events $D(\eta,\mu)$ is then given by,

$$D(\eta,\mu) = e^{-\eta\mu} \qquad (6.6.4)$$

where η is the number of bins between events.

$$\begin{array}{ll}
1 & 010011010001001100 \\
2 & 101000010110001010 \\
\vdots & \vdots \qquad\qquad\qquad\qquad \vdots \\
l & \underline{100101100111000101} \\
 & S_1 \quad \cdots \quad S_j \quad \cdots \quad S_n
\end{array}$$

Figure 6.6 Scatterer positions simulated by a binary string and the cummulative addition of these strings.

The coherent processing scheme simulates higher scatterer densities because it incorporates the superposition of the scattered signal from each target. This can also be represented by the addition of binary strings. Figure 6.6 represents superposition as binary addition. Each row corresponds to the distribution of unit targets within a range gate. The sums $S_1, \ldots, S_n$ correspond to the number of successes in l trials for each column of digits. When each trial is independent of previous values (the adjacent digital strings are uncorrelated) all 3 neccessary conditions are satisfied to classify the columns in Figure 6.6.1 as Poisson processes. Thus the probability that S_j will have k events is given by $P(k;l,p)$ (see 6.6.1). As the number of coherently processed signals (l) increases the Poisson distribution becomes a good approximation with $\mu = lp$ and standard deviation $\sigma = \sqrt{\mu}$. When $\mu \geq 30$ the Poisson distribution approximates a Gaussian distribution (Barford,1967) with,

$$P(k,\mu) \simeq \frac{1}{\sqrt{2\pi\mu}} \exp\left[\frac{(k-\mu)^2}{2\mu}\right] \quad \text{for k} \geq 0. \tag{6.6.5}$$

This transition from a Poisson distribution to a Gaussian distribution has the same physical interpretation as the Ricean distribution in section 6.2. The mean corresponds to the specular component and the standard deviation corresponds to the incoherent component. Using the definitions of σ_T and γ developed in section 6.2 we can now relate the coherent processing statistics to these acoustic parameters. With $\hat{a}$ representing the echo amplitude of a signal backscattered by a unit target we obtain,

$$\sigma_T = \kappa^2 \hat{a}^2 (\mu^2 + 2\mu) \tag{6.6.6}$$

and,

$$\gamma = \frac{\mu}{2} = \frac{lp}{2}. \tag{6.6.7}$$

This analysis confirms that a discrete system of random events when superimposed will transform from a random sequence (Poisson distribution) to one which is Gaussian. As the number of superimposed systems increases the ratio between the mean and second moment increases. This corresponds to an increase in the coherent to incoherent ratio (γ increases).

7 COMMENTS ON THE SECOND MOMENT OF PHASE STATISTICS

The previous chapter developed the statistical properties of a 2 dimensional Gaussian. When this joint probability density function has a peak value which is offset from the zero location then both the amplitude and phase statistics of this distribution are no longer described by their respective Rayleigh and uniform distributions. The properties of the amplitude signal have been utilized in many applications. The phase statistics however have not been utilized to the same extent.

A practical example of this neglect of the phase statistics is found in measurements of currents in the ocean. Physical oceanographers measure oceanic currents with a variety of devices. The basic principle is that in moored recording current meters of traditional design, the amplitude (speed) and phase (direction) of the current are measured independently. Some of these devices average the amplitude before recording a value and only sample the phase at one specific time for each estimate of the current vector. During data analysis of the current field the accuracy of the amplitude can be estimated by measuring its second moment. The phase or direction accuracy is seldom addressed and is complicated by $\pm 2\pi$ ambiguities when attempts to find its accuracy are made. For a proper analysis of a 2 dimensional vector field the mean in-phase and quadrature components of the signal should be measured in the field. This corresponds to finding the mean x component and mean y component (for a 3D field the mean z component is needed). An analysis of the first and second moments of these two components completely describes the mean current vector and its error vector. The corresponding amplitude and phase accuracies are then found directly from the relationships developed in sections 6.3 and 6.5 respectively.

For the acoustic interferometric applications which are the basis of this thesis, the second moment of the phase is the indicator which determines both the accuracy and utility of the phase signal. For example, if the variance of the phase is $\approx \pi^2/3$ then the phase signal has a uniform distribution and has no useful information for an acoustic interferometer. When the phase accuracy falls within the bounds $\pm\pi/4$ then the phase signal can be utilized. For phase measurements with accuracies outside this bound, the path between consecutive realizations cannot be determined unambiguously. This corresponds to not being able to discriminate which direction of rotation a new vector takes relative to the previous vector (clockwise or anti-clockwise).

The establishment of a meaningful phase measurement for an acoustic interferometer is dependent upon the number or density of acoustic scatterers ρ_n, the carrier wavelength λ, the mean acoustic scattering cross-section of the individual scatterers $\bar{\sigma}_A$, and the number of independent echoes l which are available for coherent processing. The rate at which the superimposed echo field approximates to a scattering continuum is also dependent upon these parameters. Euphausiids, the primary scatterers, have been introduced in section 3.1. These crustaceous zooplankton can be modelled as a distribution of Huygenian sources to represent their complex acoustic topography. An optional model is a scatterer continuum of similar dimensions to the physical size, with an effective mean cylindrical size of 18mm length and 2mm radius. With a scatterer density of $\rho_n = 418\text{m}^{-3}$ the average center to center distance between scatterers is 15cm (assuming closest packing of spheres).

When independent echo fields from the same insonified region or range gate are superimposed much higher scatterer densities can be simulated. This process is called coherent processing in this thesis. The previous chapter showed how the phase signal from discrete scatterers converges towards a single value as the coherent scatterering field dominates the incoherent field. Section 6.5 establishes that the variance in the phase signal is dependent only on the γ value which is defined in equation 6.5.12. When the range separation between scatterers is greater than the carrier wavelength, the parameter γ is equal to zero. The received amplitude echo then has a Rayleigh distribution and the phase distribution is uniform. However as γ increases through coherent processing the phase signal becomes bounded. The relationship between the second moment of phase and γ is given in Figure 6.5. By finding the relationship between γ and the simulated scatterer number density $l\rho_n$ it becomes possible to estimate ρ_n from measurements of $\langle\phi^2\rangle$.

The received signal from a typical in situ scatterer distribution is the time convolution of the transmit pulse with a discrete distribution of scatterers. Coherent processing increases the effective scatterer density and in doing so the mean separation in range is reduced. Changes in the discrete impulse weighting function as the effective scatterer density is increased can be simulated numerically. The mean cylindrical shape of the euphausiid population can be used to estimate the mean cross-sectional area of the scatterers. For example, during the evening, the euphausiid population is feeding so their spacial orientation can be assumed to be random. If L denotes the mean length and D the mean diameter then the general expression for the cross-sectional area is given by,

$$\sigma_A = \frac{\pi}{4} D^2 \cos\phi + DL\sin\phi. \tag{7.1.1}$$

where ϕ is the angle from the axis of rotation of the cylinder. The mean area is then found by averaging over all possible solid angles. This gives,

$$\bar{\sigma}_A = \frac{\pi DL}{4}. \tag{7.1.2}$$

This expression can also be used to estimate the mean thichness $\bar{d}$ of this scattering mechanism by finding the diameter of a circle with an area equivalent to $\bar{\sigma}_A$. This gives,

$$\bar{d} = \sqrt{DL}. \qquad (7.1.3)$$

For example, a euphausiid with $L = 18\text{mm}$ and $D = 2\text{mm}$ will have a mean cross-sectional area ($\bar{\sigma}_A$) of 28mm^2 and a mean depth $\bar{d}$ of 6mm.

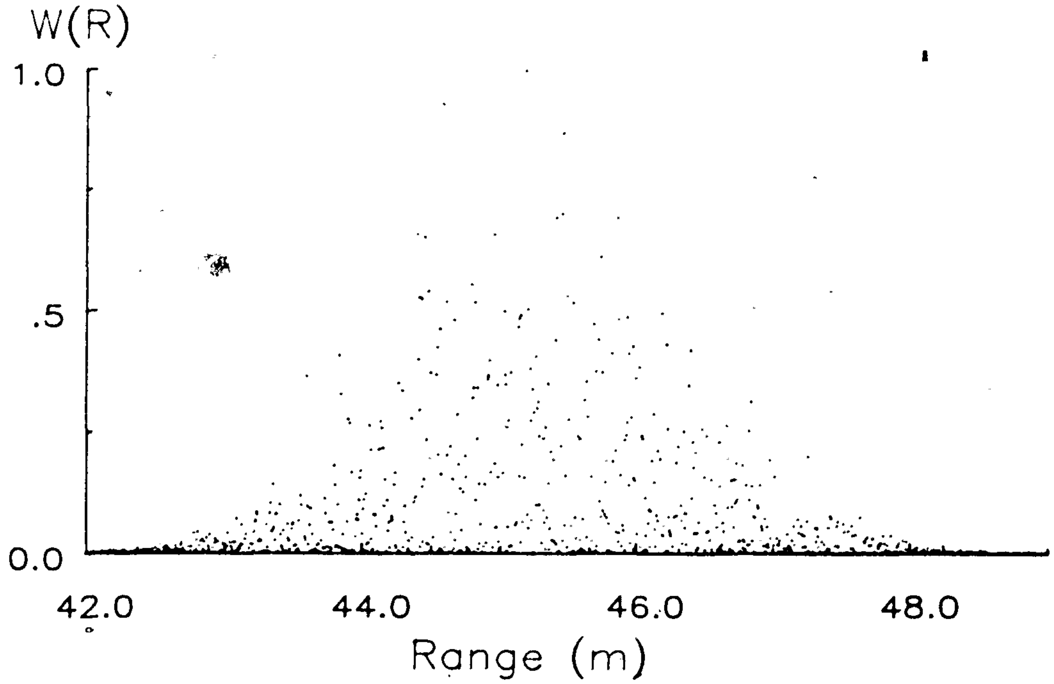

Figure 7.1 A scatter diagram of the scattering distribution for fringe 7 with $\rho_n = 500\text{m}^{-3}$. Each point represents the normalized scattering strength within a 6mm range window. The normalization factor of $1.77\bar{\sigma}_A$ represents the maximum scattering strength per unit volume.

Section 5.1 demonstrates how the received signal is range dependent. This reduces the 3 dimension spacial positions of the discrete scatterers into 1 dimension. The insonified volume is defined by the intersection of the two acoustic beams (see Figure 1.2). The number of discrete scatterers within any range R and $R + dR$ of the insonified volume determines the structure of the impulse weighting function. Chapter 5 dealt with the idealized case of a smooth continuous impulse weighting function ($W(R)$) to describe the scattering mechanism. A more realistic representation of $W(R)$ can be constructed from a high resolution histogram by using $\bar{d}$ (=6mm) to represent the bin width dR. The total scattering cross-section within each bin will then be the weighted sum of $\bar{\sigma}_A$ times the total gain weighting function H (see equation 4.1.3). The number of discrete scatterers within any unit volume dV will have a Poisson distribution. Using the number density of scatterers ρ_n the mean value for the Poisson distribution will then be $\rho_n dV$. For modelling purposes, the number of scatterers N within a range window can be found from these statistical properties by choosing a unit volume with a range depth dR which intersects the insonified volume. The spacial positions of N scatterers within any range window will be uniformly distributed. Once the positions are determined relative to the transducers then H can be evaluated. The scattering strength within the range window will then be proportional to the sum of H values. Figure 7.1 shows one realization of the impulse weighting function $W(R)$ for fringe 7 with $\rho_n = 500\text{m}^{-3}$. Each point represents the normalized scattering strength within a 6mm range window. The normalization factor was $1.77\bar{\sigma}_A$ in this case and represents the maximum scattering strength per unit volume. The variations between adjacent points range between 0 and 1 and indicate that a Rayleigh distribution is describing the volume target strength within a range window. This hypothesis was confirmed by repeating the model with independent distributions and measuring the ratio of the 1st and 2nd moment within a range gate.

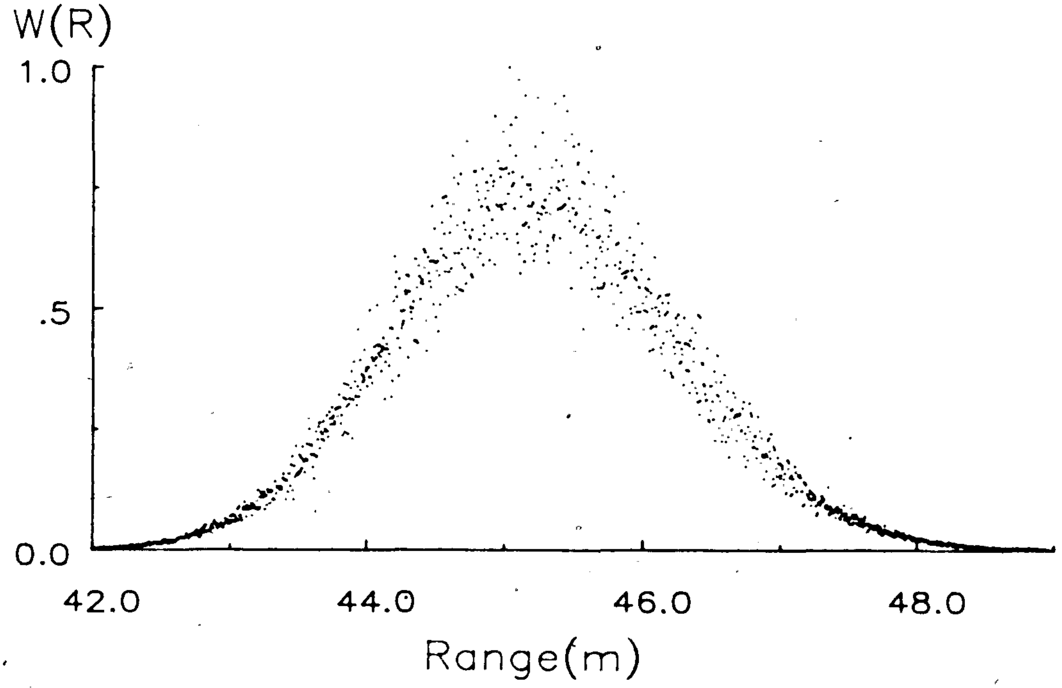

Figure 7.2 A scatter diagram of the scattering distribution for fringe 7 with $l = 100$ and $\rho_o = 500\text{m}^{-3}$ or $\rho_n = 50,000\text{m}^{-3}$. Each point represents the normalized scattering strength within a 6mm range window. The normalization factor of $37.4\bar{\sigma}_A$ represents the maximum scattering strength per unit volume.

The effects of coherent processing on the scatterer distribution are simulated with this model by adding the values within each range gate over a number of independent trials l. This is equivalent to using a higher scatterer number density which is a multiple of ρ_n. Figure 7.2 shows one possible realization of the impulse weighting function $W(R)$ when $l = 100$ and $\rho_n = 500\text{m}^{-3}$. Notice the dramatic change compared to the previous figure. The volume target strengths within the range windows are distributed about a Gaussian shape.

When l is further increased the scatter about the mean reduces and the result becomes a closer approximation to the ideal case in Figure 4.3.

This demonstration of the scattering mechanism with increasing l or ρ_n shows the transition between a random scatterer distribution to one which has a definite structure. The received echo is the time convolution of the transmit pulse and the impulse weighting function such as given in Figure 7.1. The superposition of the received waveforms produces a signal which is the convolution of the transmit pulse with distributions as shown in Figure 7.2. A convolution involves an integration which is a smoothing operation. The effects of bumps or spikes in the range dependent volume scattering strength are difficult to quantify. In addition, the distribution of euphausiid sizes is asymmetrical and these effects complicate rates of convergence towards a scatterer continuum.

Insight to the relationship between the second moment of phase (or γ) and ρ_N can be obtained through a numerical model by using the impulse weighting functions as shown in Figures 7.1 and 7.2 and point scatterers to represent the scattering mechanism. Point scatterers have the advantage of being the simplest scattering mechanism to simulate numerically. In Chapter 4 a numerical model of the acoustic phase as a function of mean target separation revealed that large computational times were required to compute stable phase values from a point scatterer model. This computation time can be reduced significantly by using larger carrier wavelengths in the numerical simulation of the received complex echo. In Chapter 5 the structure of the received echo from the time convolution of the transmit pulse and the impulse weighting function was shown to be independent of the transmit frequency (see Figure 5.10). This result proves that results from this point scatterer numerical model can be expressed in λ units.

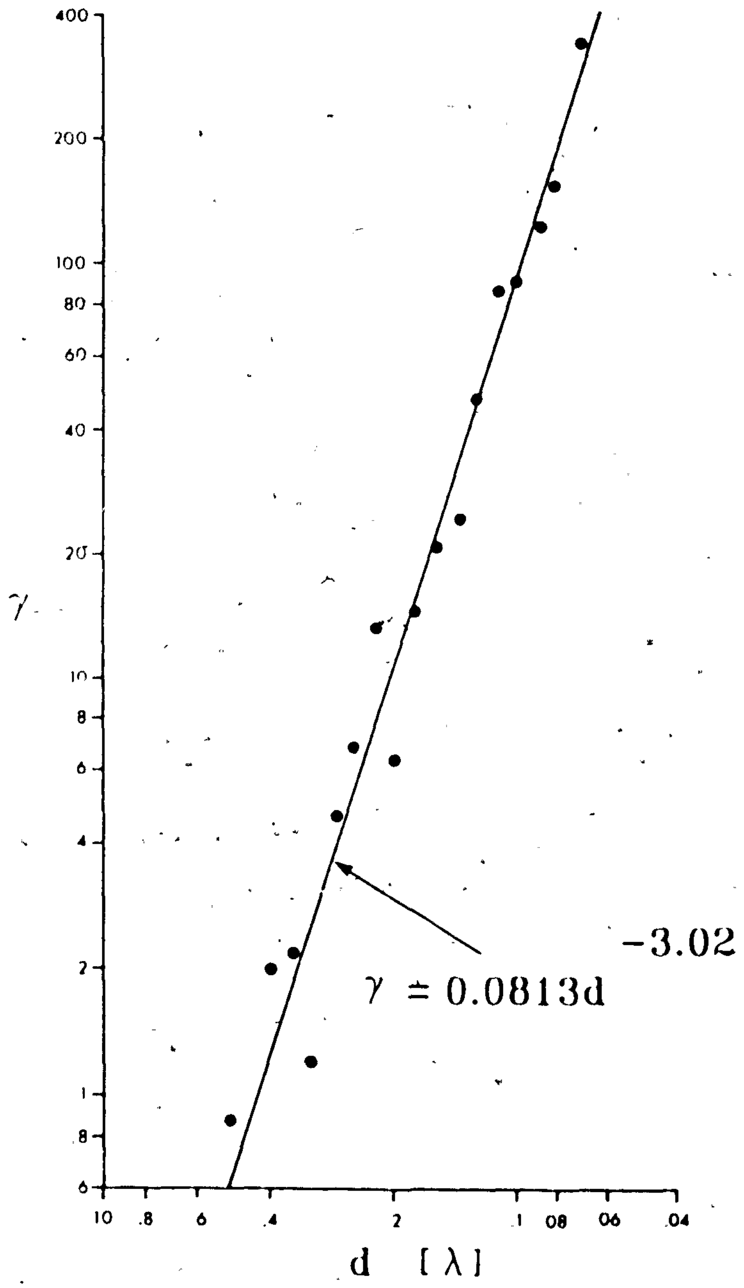

Figure 7.3 Results from a numerical simulation of the received phase signal from the impulse weighting functions shown in Figures 7.1 and 7.2. The parameter γ is the coherent to incoherent echo energy as defined in section 6.2 and d is the mean target separation in acoustic carrier wavelength units (λ).

As in the simulation presented in Figure 4.4, the properties of the received phase signal at a fixed arrival time can be simulated by assuming that each scatterer pulse in the impulse weighting function can be superimposed for this particular arrival time. Estimates of both γ and the phase variance were obtained by repeating 10 times the simulation at each density ρ_N. Figure 7.3 shows the resulting points on a log-log scale of γ versus d (mean target separation) in λ units. A straight line fit through these points has a correlation coefficient of -0.98 and gives,

$$\gamma = 0.0813 d^{-3.02}. \tag{7.1.4}$$

This expression can be rewritten in terms of ρ_N through equation 4.1.1 to give,

$$\gamma = 0.0575 \rho_N^{1.01} \tag{7.1.5}$$

with ρ_N in units of number of targets per cubic wavelength in this case.

These results provide further confirmation of the convergent properties of coherently processed complex echoes. For a carrier frequency of 215kHz ($\lambda =$ 7mm) and $\gamma = 1.28$ (a ±45° phase accuracy), the implied scatterer density ρ_N becomes very large ($\sim 6 \times 10^7/\mathrm{m}^3$). A more realistic numerical model can be generated by representing each scatterer by an array of closely spaced point scatterers. This added complexity to the model should increase the convergence rate. Experimental results (Chapter 11) gave phase accuracies of ±45° after coherently processing 600 independent complex echoes. This corresponds to a simulated scatterer density of $\sim 3 \times 10^5/\mathrm{m}^3$. In this case bounded phase signals from zooplankton scatterers required a much lower ρ_N than for point scatterers.

These results show that the rate of phase convergence is dependent upon ρ_N, λ and the mean effective size of the scattering mechanism. By transmitting at different frequencies and comparing the rates of phase convergence,additional information on the effective acoustic size of the mean scattering cross-section may also be inferred.

A sharp transition occurs in the second moment of the phase statistics when the discrete scattering mechanism begins to represent a coherent scattering field ($\gamma > 0$ in Figure 6.5). This corresponds to a mean range separation of less than the carrier wavelength λ. Most in situ scatterer densities have mean scatterer separations much greater than λ so that the received phase distribution is uniform. By coherently processing every l independent transmissions from the same range gate and computing $\langle \Phi^2 \rangle$ over a population of N (the parent population is lN) the transition from a uniform phase distribution can be monitored. The coherent processing is simply the addition of the in-phase and quadrature components of the received echo from the same range gate. As with other methods of estimating ρ_n, an initial calibration of the system with a ground truth reference is required.

Two other methods for estimating ρ_n from the statistical properties of the received echo are found in the literature. Spindel and McElroy (1973) describe a technique which uses the phase or zero crossing statistics from individual echoes. This method relies on establishing a near-Gaussian regime in the statistics of the received phase signal and is limited in its practical applications. A second approach which utilizes the amplitude statistics has been developed by Stanton and Clay (1986). Amplitude statistics lend themselves to applications with standard echo sounder systems and have found applications ranging from estimating fish and zooplankton populations to finding the correlation length of a rough ocean floor. Both of these methods limit themselves to utilizing only one component of a 2 dimensional signal. Since estimates of statistical moments are used in both of these methods their accuracy can be improved by first finding the moments of I and Q and then transforming to the amplitude or phase statistics by the transformations in chapter 6.

The motivation for investigating the relationship between $\langle \Phi^2 \rangle$ and $l\rho_n$ is that most methods for measuring ρ_n are contaminated by the acoustic beam properties and are directly dependent on the strength of the received signal. The beam properties in a monostatic system are stable (in the far field) and the ideal impulse function for a scatterer continuum is primarily a function of spherical spreading and absorption losses. The beam width properties only cause a change to a multiplying constant. For a sparse distribution of scatterers, increasing l compensates for the weak signals. Field measurements are complicated by both the natural diversity of biological species and the problems of correlating acoustic signatures with the products from towed sampling nets. In a controlled environment where the scatterer population and distribution of scatterer sizes are known, direct measurements of the relationship between the second moment of phase in the received echo and ρ_n can be made. A laboratory water tank using micro bubbles generated by hydrolysis can provide the required measurements. In addition the methods of Stanton and Clay (1986) and Spindel and McElroy(1973) can be tested and compared in a controlled environment. This is a subject for future research.

8 APPARATUS AND EXPERIMENTAL DEVELOPMENTS

Development of the experimental apparatus involved both electronic and mechanical challenges. The evolution of the design is briefly described here, although only data from the final configuration, which was used in the November, 1985 cruise, is used in the subsequent analysis.

The bistatic configuration used in this thesis requires a stable platform to separate the projector and hydrophone. For the first 3 experiments the IOS research vessel VECTOR allowed collection of data in a variety of locations and environments. A diagram of the basic components attached to the ship is given in Figure 8.1. This cross-section of the VECTOR, which is not to scale, shows the transducers suspended by steel struts. These struts were attached to the ship as indicated in the figure with 2 additional steel cables attached to the base of each strut and secured on the forward and aft decks respectively. By keeping tension on these cables, deflections of the struts while underway were minimized. Figure 8.1 also shows the conductivity temperature and depth (CTD) sensors which were used to establish the reference sound speed at the transducer depth and to collect regular profiles of the sound speed. An additional transducer used in the earlier experiments was the hull mounted 100kHz echosounder (not shown in the figure).

Both the echometer projector and hydrophone in the bistatic system were unique transducer designs. Figure 8.2 shows a photograph of the echometer projector. It is composed of 2 separate banks of linear arrays. Each array (A and B) contains 6 hexagonal elements which are 5cm wide and separated by 10cm. The 2 arrays were built for redundancy and to allow different fringe groups to receive more acoustic energy. Figure 8.3 shows a photograph of the narrow beam hydrophone when attached to its support mast. This transducer,

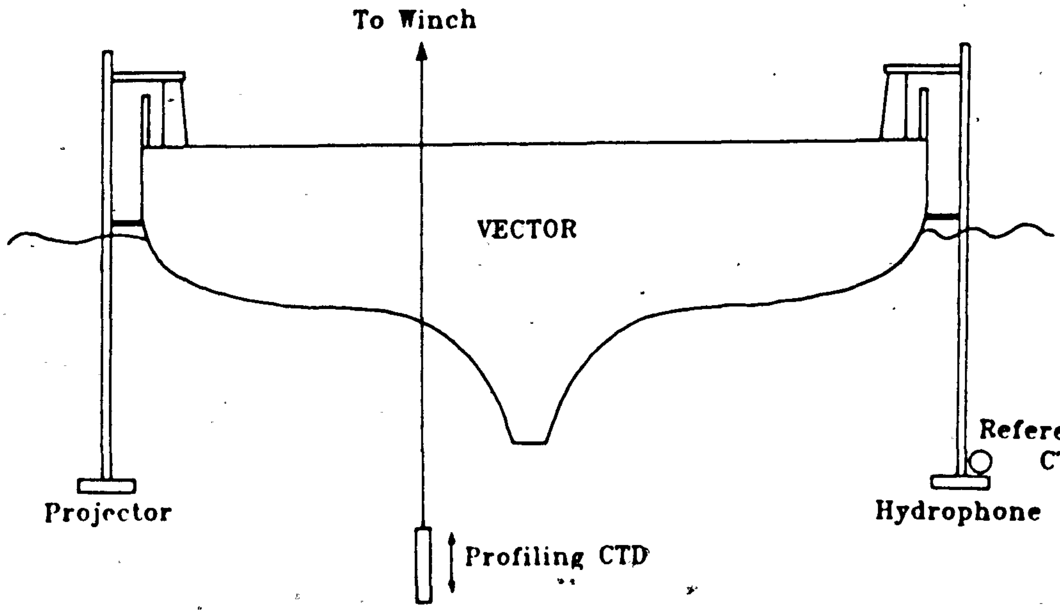

Figure 8.1 A diagram (not to scale) of the apparatus used on the IOS research vessel VECTOR to separate the echometer projector and hydrophone.

originally designed for Doppler profiling, is composed of 72 hexagonal elements and has a 75cm diameter.

Following the method of Brown et al. (1984) the electronic circuitry for transmitting 2 frequencies simultaneously through the echometer projector was initially utilized. Previous experiments were limited in the flexibility with which different frequency pairs could be used. Theory suggested that the $\pm 2\pi$ ambiguities in the received phase signal could be resolved by initially transmitting a frequency pair with a larger difference frequency. To meet this objective and to increase the number of experiments while onboard the ship, a micro computer controlled system was developed. With the bounds on variable parameters de-

Figure 8.2 Photograph of the echometer projector (June 1983) which is composed of 2 banks of six element arrays. Bank A has its individual elements tilted 25° off vertical while bank B elements have a 30° orientation.

fined and the modes of operations selected the following list of parameters were made accessable through a menu.

1. A range of frequency pairs with Δf between 500 Hz and 5kHz.
2. Transmission of up to 3 different frequency pairs sequentially.
3. A range of pulse lengths from 0.1ms to 10ms.
4. Programmed cut-off frequencies in the low pass filters.
5. A variable power level (0 to 100%).

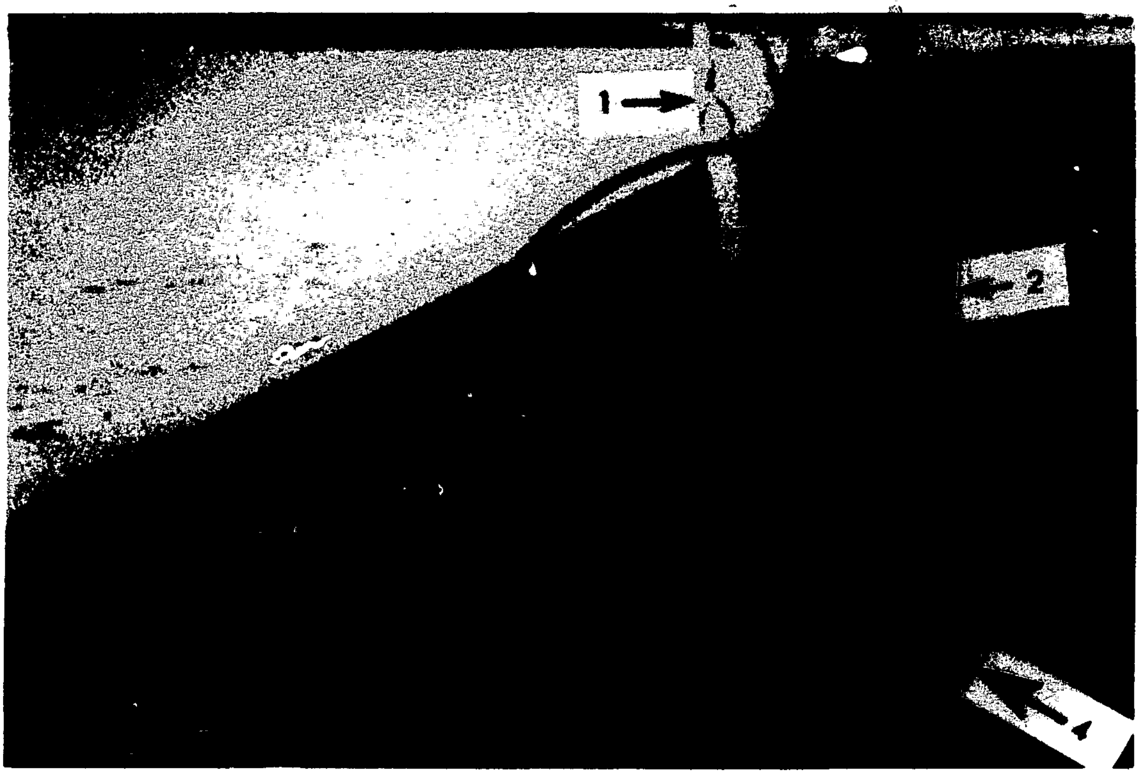

Figure 8.3 Photograph of the equipment at the base of the port side instrument mast(1) while onboard the VECTOR (June 1983). Showing (2) the digital CTD, (3) the transducer for a 200kHz echosounder, and (4) the large aperature narrow beam 215kHz hydrophone.

6. Transmission from projector bank A, B or alternately between A and B. This allows automatic control of the orientation of the projector, so as to insonify either the deeper or shallower fringes.
7. The ability to alternately shift the elements in one of the 2 projector banks by 180° in phase. This capability was incorporated to provide simple tests on the geometric properties of the projector fringes.
8. Variable repetition times between transmissions with a minimum time of

250ms.

The microcomputer was also programmed to record automatically the relevant parameters for each transmission including time, pulse length, frequency, operating mode, power level and the digital values from the reference CTD. The demodulation technique used in the initial version of the instrument provided a signal with the difference in phase between the two received echoes. This required digitization of 2 channels (in-phase and quadrature) for each echo time series. In addition the linear and logarithmic amplitude of the received echo was digitized. In the initial configuration, the 5kHz digitization rate was limited to 8 bit resolution and 4 channels of data were written onto 9 track tape (at 1600 bpi) under the control of a mini computer.

A schematic of the equipment and its interrelationships is given in Figure 8.4 for the November 1985 experiment. The individual components within this diagram were changed during the various experiments as new equipment became available but the basic flowchart remained the same.

The instrument was completed and thoroughly tested on the VECTOR cruise in June 1983. An extensive data set was obtained for a wide range of system parameters in both turbulent and quiescent coastal waters. A field test of projector and hydrophone beam patterns revealed that the projector fringes were displaced from their theoretical positions, which is of fundamental importance to the subsequent data analysis. Analysis of the received echometer phase information gave essentially random results under several oceanographic conditions and with two different phase detecting schemes (the analogue method proposed by E.Brown and another version using hard limiting).

On the basis of further numerical models and previous experimental results, a variety of modifications were made to the echometer instrument in

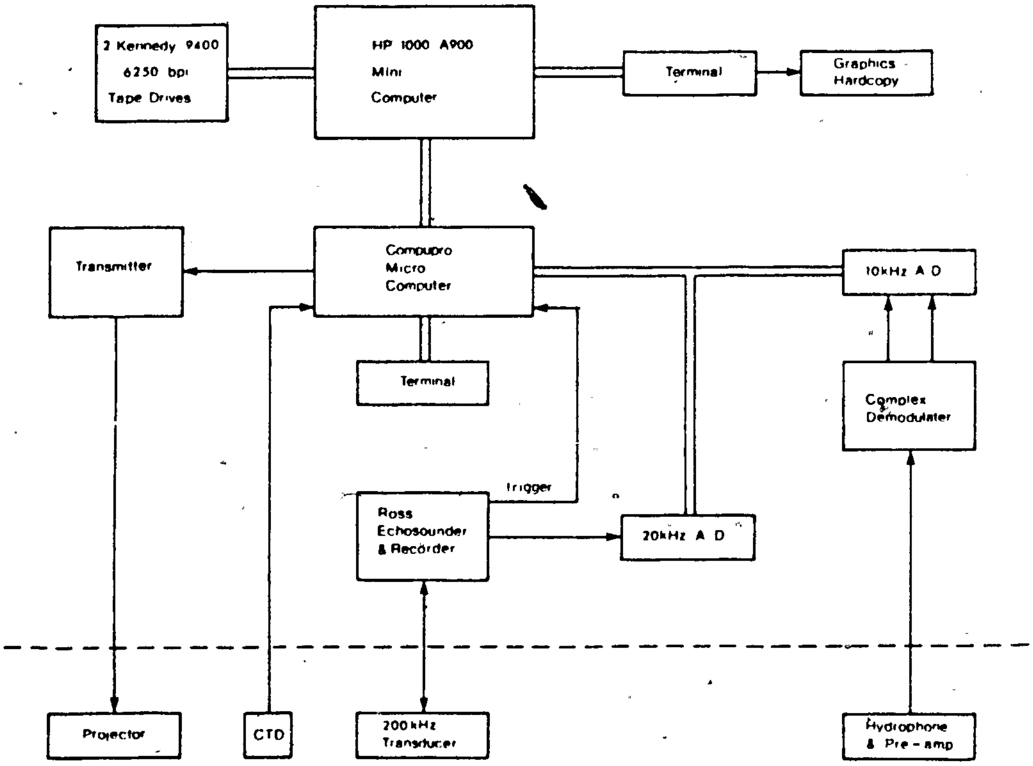

Figure 8.4 A schematic showing the components which were used to measure and record the complex echo signal from a bistatic configuration.

preparation for the June 1984 cruise on the VECTOR. In particular the objective was to sum in-phase and quadrature components of the echo over independent transmissions so that higher scatterer densities could be simulated which give stable phase measurements as implied by the model as described in chapter 4. Other modifications were also incorporated to improve instrument performance, on the basis of experience gained in the June 1983 experiment. For example, the option of using a hard limiter which had been incorporated in the earlier design was discarded and the A/D converters were upgraded to 16 bits. The large dynamic range in the received amplitude caused resolution problems at the lower end of the scale for the 8 bit A/D system used earlier. With the transmit circuit simplified to allow single frequency transmission, the complex signal processing circuitry of the original system was replaced by standard quadrature demodulation followed by the digitization of the resulting in-phase and quadrature components of the received signal (2 data channels). The system was set up to transmit either a single frequency repetitively, or to transmit first one frequency and then another.

Real time analysis during data logging was made possible by the generation of various plots of amplitude and phase. The software was developed to process single frequency transmissions by coherent processing between transmissions. This monitoring system gave valuable insight into the system's performance and provided feedback for system diagnostics and verification of data while logging.

In March 1984 the projector was calibrated at the International Transducer Corporation in Goleta, California (see chapter 9). One of the more significant results was the directivity of the beam pattern which revealed that only 4 of the possible 14 fringes could be observed above a -10dB reference.

Results of the June 1984 cruise revealed that coherent processing could indeed provide stable phase estimates. However, satisfactory results required higher repetition rates than were readily obtained with the existing system. Only a short section of data was acquired using a single frequency with transmission times of 125 ms. This data set however demonstrated the convergence of independent phase estimates with coherent processing of successive pulses.

Coherent processing places special demands on the stability of the baseline separating the projector and hydrophone, since a change in baseline produces a corresponding change in phase of the received signal. With an acoustic wavelength of only 0.7 cm it was obvious that vibrations on the masts supporting the hydrophone and projector would produce noise in the resulting phase observations. An acoustic interferometer, using the direct acoustic path between transmitter and receiver, was set up to detect baseline variations under normal operating conditions. The results showed that while substantial fluctuations occurred in the mast positions, the maximum change in separation was less than one wavelength. Thus, although subject to spurious noise from the mast vibrations, the results should not be subject to phase ambiguity from this source.

With the existing system it was not possible to record continuously the baseline fluctuations; however the phase angle of the direct path signal was measured to obtain an instantaneous baseline deviation for each transmission. This measurement allowed a first order correction of measured phase for individual transmissions, which was found to reduce the variance in the final phase estimates.

From the encouraging results obtained in this cruise a new experiment was proposed which would continuously monitor both masts independently by using two acoustic interferometers and obtain a minimal repetition time (i.e. 100

ms) in the bistatic system. The objective of the December, 1984 cruise was to obtain large data sets of phase measurements with low variances after coherent averaging by correcting for phase offsets caused by baseline fluctuations. The acoustic interferometer system was designed so that both transmitter and receiver motions along the baseline were independently measured relative to the ships keel (Figure 8.5). This was accomplished by mounting a 150 kHz projector on each side of the keel and a similar receiver at the base of each instrument mast. By applying a quadrature technique to the received signal, phase measurements of both instrument masts along the baseline were obtained simultaneously with the echometer phase measurements. A criterion for stable phase measurements is a large data base (i.e. 500 transmissions/measurement) so the timing was upgraded by reducing the sampling window to 50 ms, and not recording the 100kHz echosounder signal while data logging.

Before collecting data, an in situ calibration of the echometer projector was performed in Saanich Inlet. An omnidirectional hydrophone and pressure transducer were lowered directly below the narrow beam hydrophone while the echometer projector transmitted a continuous single frequency. A real time plot of received signal versus pressure was recorded on an X-Y plotter and 4 fringes were observed. This was the first successful measurement of the fringe locations during a cruise.

Data were once again collected in both quiescent and dynamic oceanographic regimes. High repetition rate data were obtained in the quiescent waters of Saanich Inlet at night, with high scatterer densities in the upper 50 m. For dynamic measurements the VECTOR was anchored in Sansum Narrows and time series were collected during tidal changes.

A preliminary analysis of the backscattered echo data confirmed the convergent nature of coherent processing on the received phase derived from biological scatterers. However, a number of unexplained phenomena were also

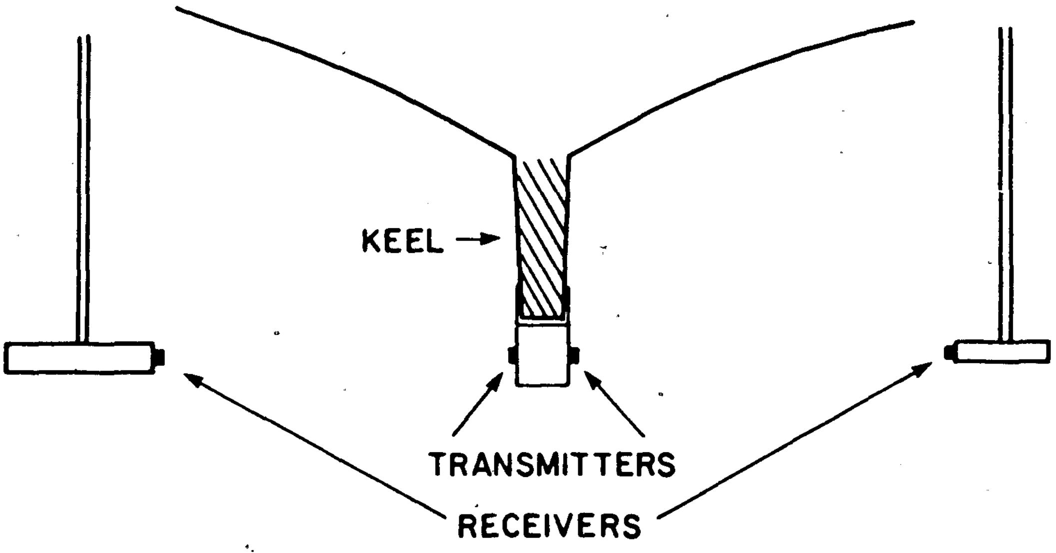

Figure 8.5 A diagram (not to scale) of the acoustic interferometer which was used to measure baseline fluctuations during the December, 1984 experiment on the VECTOR. Both transmitters and receivers were tuned to resonate at 150 kHz.

occurring. The variance in the phase after coherent processing increased when a phase correction based on system geometry and the baseline fluctuations was incorporated. Various explanations were investigated and an empirical approach was found which reduced the variance; however an analytic or optimal solution remained to be found. Another peculiarity in the results after processing the received signal every 500 transmissions for 26 independent groups, was that the mean phase value ϕ was bounded $(-90 < \phi < -15)$ for the results obtained at different ranges within the 4 fringes of interest. One would expect ϕ to be random between different fringe locations. In preparation of the final experiment in November, 1985 a software error controlling the triggering of the transmit pulse was found. This caused the transmit pulse to fluctuate between transmissions so that the phase signal in the received signal was contaminated. This error explained the inconsistent results in the December, 1984 data.

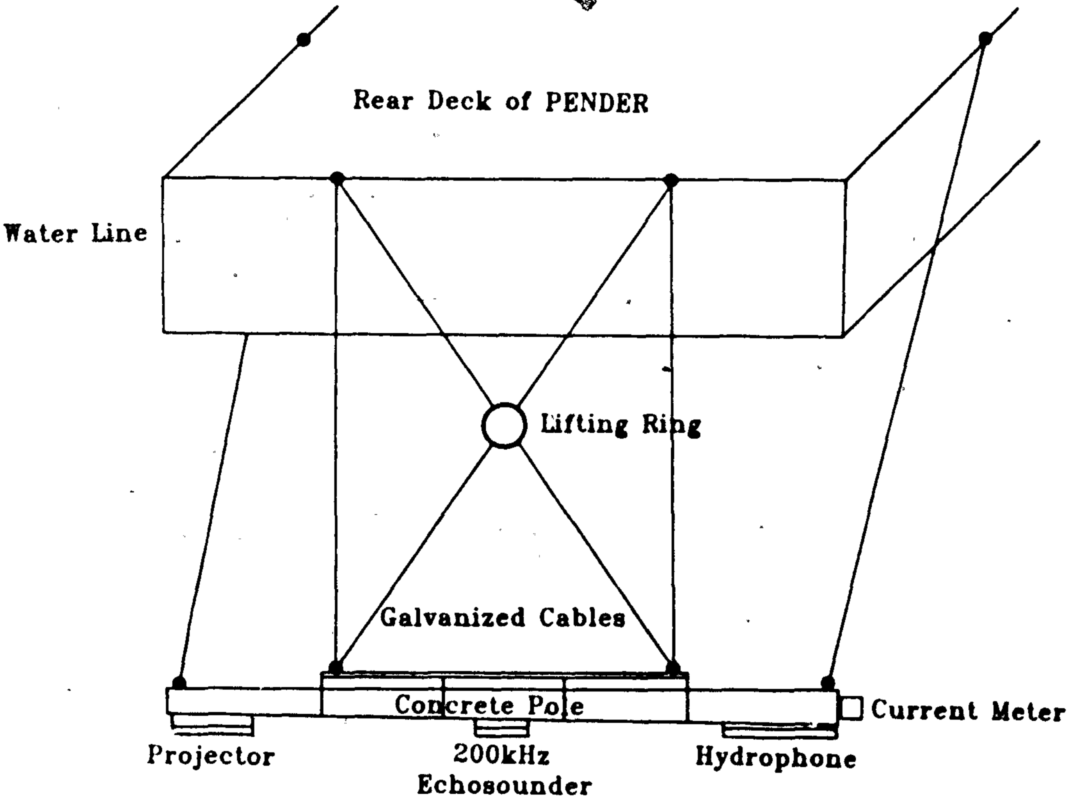

Figure 8.6 A diagram (not to scale) of the bistatic configuration which was used during the November, 1985 experiment from the IOS research barge PENDER.

The additional complications of correcting for mast motion were eliminated in the final experiment during November, 1985. This was accomplished by attaching the transducers to a concrete pole with prestressed steel reinforcement. The high moment of inertia and inelastic properties of this baseline ensured that deflections of the pole would be <<.7mm. The special contraints in securing this system to a vessel were overcome by working from the research barge PENDER. Figure 8.6 shows the configuration used off the rear deck of the PENDER. Galvanized steel cables secured the pole at a depth of 4.5 m and restricted pendulum motions when underway (by the navy tug GLENDALE). The lifting ring was kept under tension through an overhead rear winch (not shown in diagram) so as to minimize pole motion. The echometer projector and receiving hydrophone were secured to the pole as indicated in the figure with a separation of $B = 11.58$m (on the VECTOR it was 8.34m). A downward looking 200kHz echosounder was placed in the center of the pole and a current meter recorded the horizontal speed during the experiment. Additional instruments attached to the barge and not shown in Figure 8.6 included: a reference digital CTD at 4.5m depth, a thermistor chain with thermistors ranging from 10.5m to 35.0m in 1.5m increments, and an analogue profiling CTD. A summary of the system parameters used in the November, 1985 experiment is given in Table 8.1. Measurements obtained during this cruise form the basis for subsequent discussions and analysis.

Table 8.1 System characteristics of the November, 1985 experiment.

Transmit Frequency	215±n kHz ($n = 0, 1$, or 2)
Transmit Power	300 W (max)
Transmit Pulse Length	2 or 3 ms
Baseline (projector to hydrophone)	11.58m
Transmit Array	
Depth	4.5m
No. of elements	6
Element spacing	10cm
Tilt of individual elements	25° or 30°
Hydrophone Array	
Depth	4.5m
No. of elements	72
Diameter	75cm
Nominal beam width	0.7°
Transducer bandwidth	20kHz
Low Pass Filter Cuttoff	4kHz
Digitization Rate	10kHz at 16 bits

9 TRANSDUCER CALIBRATIONS

The acoustic transducers used in this research were all constructed of piezo-electric material. The design of a transducer can follow basic principles which assume ideal piston behaviour and simple equivalent circuit models. In practice non-linear and higher order effects cause the transducer to deviate from its designed properties. In many cases these deviations are minor but still must be measured. This requires a calibration of the transducer properties such as; transmit response, receive response, complex impedance and beam properties - which are all frequency dependent.

9.1 Echometer projector laboratory calibration

Figure 8.2 shows a photograph of the echometer projector. It is composed of 2 separate banks of linear arrays. Each array (A and B) contains 6 hexagonal elements which are 5cm wide and separated by 10cm. The 2 arrays were built for redundancy and to allow different fringe groups to receive more acoustic energy. A field calibration of the projector was performed on the VECTOR in June 1983 and gave a beam pattern inconsistent with the theoretical results. On this basis a detailed calibration was carried out at International Transducers Corp. in Goleta, California.

Initially the characteristics of a single element were investigated. Since the echometer projector is composed of these elements, their individual behaviour is fundamental to the composite transmit signal. Figure 9.1 shows the complex impedance of a single hexagonal element over a frequency range of 30kHz. The modulus of the complex impedance (solid line) has a minimum at 214.5kHz which corresponds to a resonance peak. The phase of the complex impedance (broken line) undergoes a sharp change near the resonance peak. The echometer projector was used within a 4kHz window about 215kHz during the field

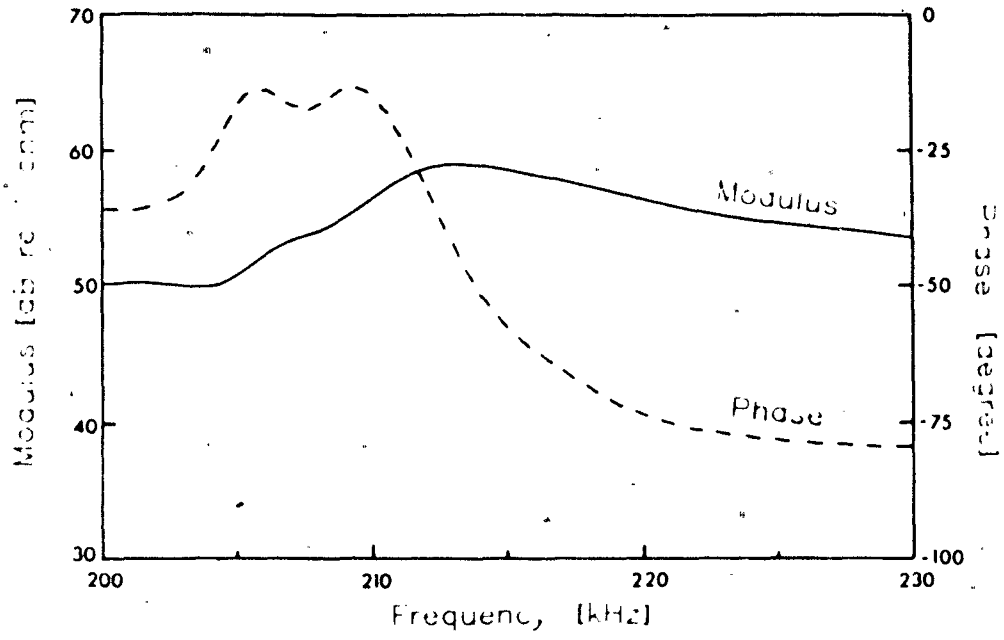

Figure 9.1 The complex impedance of a single hexagonal element used in the echometer projector.

work. At this frequency range the transducer becomes less efficient but the associated changes with frequency are more symmetric and less dynamic. For a 2 frequency bistatic device (such as used in the June, 1983 experiment) the associated phase shift from the transducer for each frequency must be corrected.

The beam patterns for single elements were determined at various cuts across the transducer face for comparison with the theoretical prediction. Figure 9.2a shows one quadrant of the intensity response (in dB) when a vertical arc is swept through opposite points on a single hexagon. The result here is a digitized version of the real data to allow comparisons with the theoretical pattern (Booth, 1983) on the same scale as shown in Figure 9.2b. Deviation from theory begins at the side lobes for angles greater than 10°, with the mainlobes being in excellent agreement. Clearly the element does not behave as a perfect

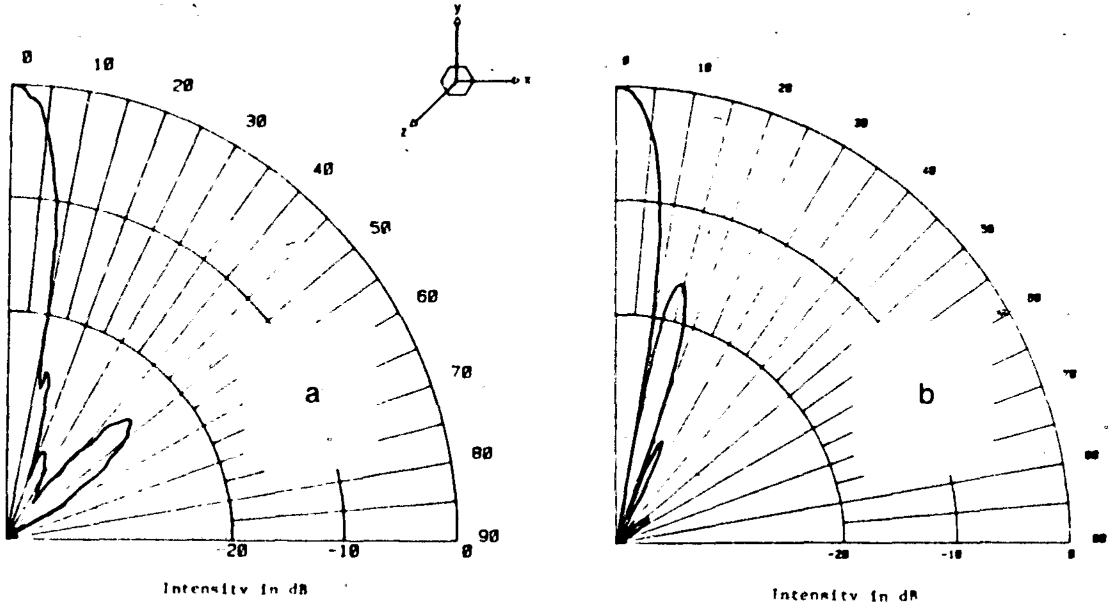

Figure 9.2 Radial plots of projector beam patterns for a single hexagonal element separated 2m from the calibration hydrophone. The plane of measurement was the xz plane as shown (zero degrees corresponds with the z axis). The calibrated and theoretical results are shown in (a) and (b) respectively.

piston. With a cut in the vertical plane from the middle of one side and across the face, a similar set of results can be observed in Figures 9.3a and b. A comparison between these last 2 figures shows that the side lobes are stronger in 9.3a than 9.2a. This suggests that a linear array of hexagons aligned point to point will have less side lobe interference than for a side to side alignment.

All calibrations were performed at a 2m separation between the projector and calibrated hydrophone. For single elements this distance corresponds with the far field; however for the 6 element array the hydrophone was in the nearfield. Figure 9.4 shows the amplitude response of the projector with individual elements tilted 30° off vertical and aligned point to point (as in Figure

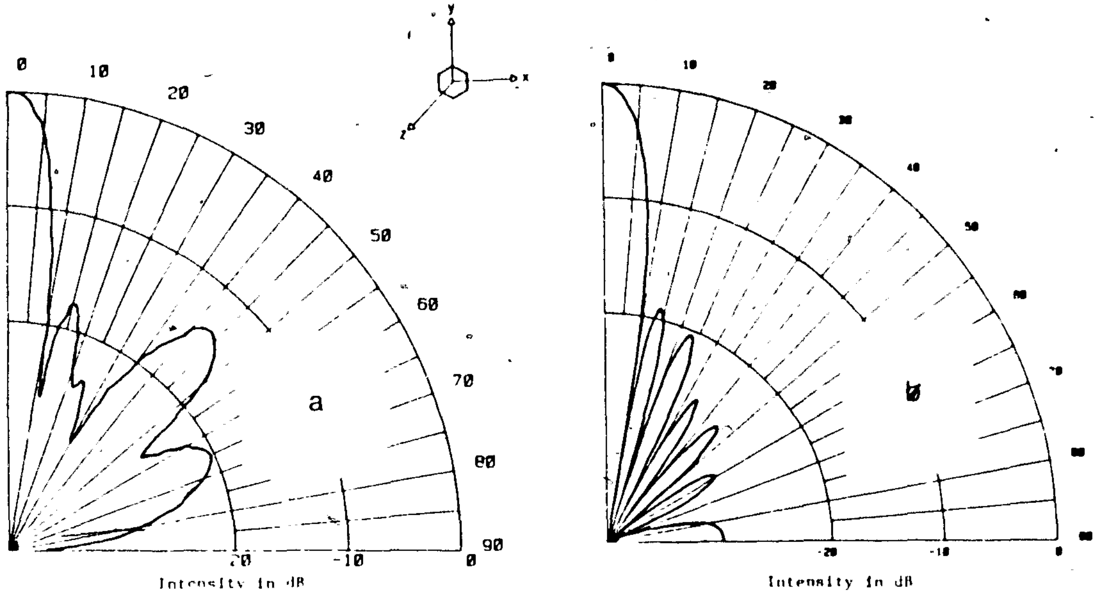

Figure 9.3 Similar to Figure 9.2 but with the orientation of the hexagon rotated 30° as shown.

9.2a). This result deviates from the expected return from an array of hexagons behaving like perfect pistons which would give 14 narrow beamed fringes. The calibrated fringes in Figure 9.4 are close together and bounded by ±20° about 30°. The high wave-number structure superimposed on the calibrated fringe pattern is an artifact of the calibration equipment and should be neglected. To extract further information from the calibration results, in particular to test the validity of extrapolation of the projector beam pattern into the far field, the digitized amplitude response for a single element (Figure 9.2a) was used to simulate numerically the six element array. The results from this computation, using a 2m range, are shown in Figure 9.5a. Comparison of this plot with the calibration result in Figure 9.4 provides excellent agreement in beam pattern which gives confidence in an extrapolation to the far field. Figure 9.5b dis-

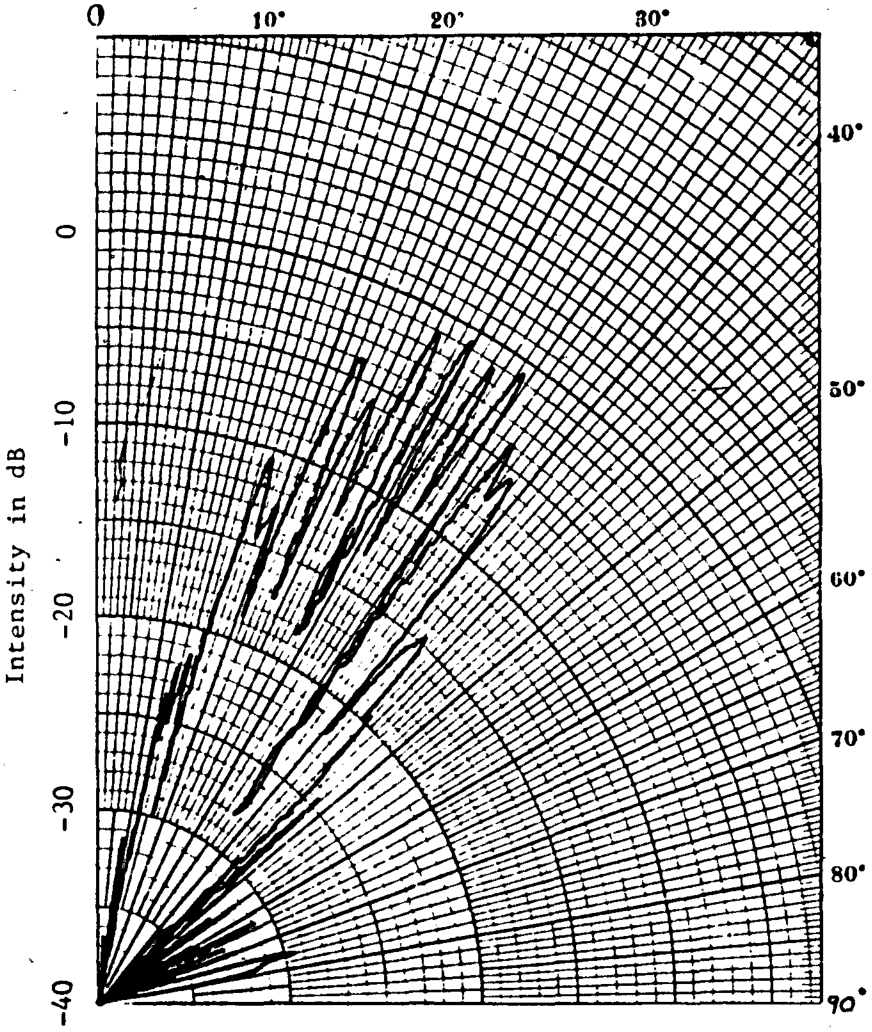

Figure 9.4 A radial plot of the beam pattern of the echometer projector at a range of 2m (near field). The projector was rotated through the plane defined by the acoustic axis and the line passing through the individual elements. This plot was produced at ITC.

plays the far field simulation of a beam pattern based on the calibrated beam pattern of single elements aligned point to point. This figure gave the best indication of the echometer projector directivity during the first 3 experiments.

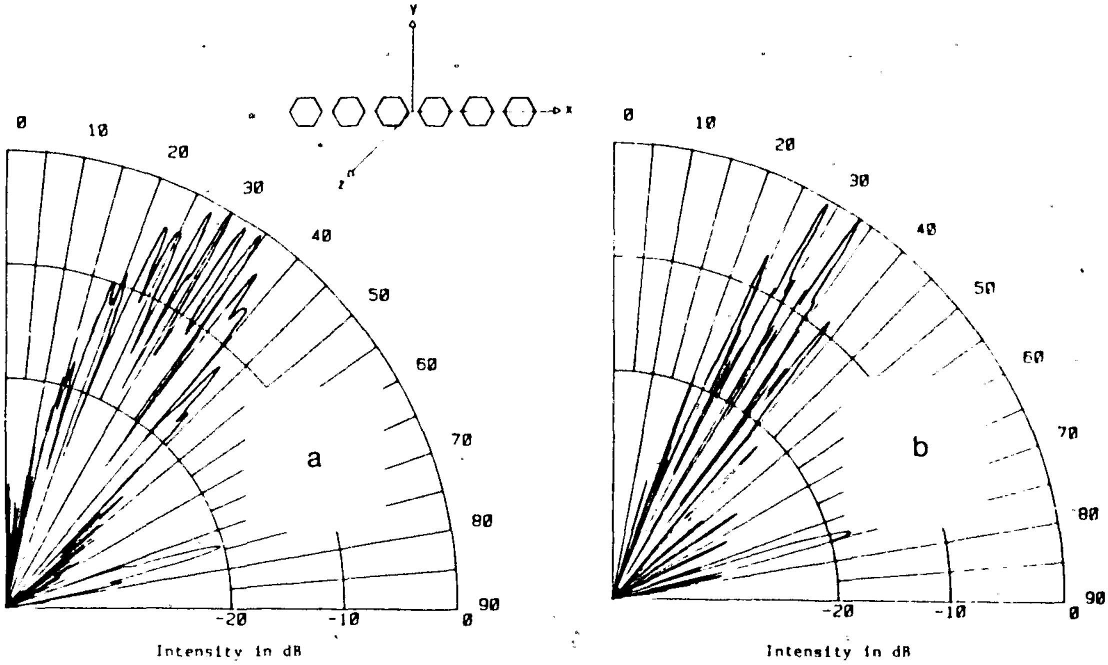

Figure 9.5 Theoretical plots of the echometer projector beam pattern for a 2m range (a) and a farfield range of 20m (b). The relative orientation and the plane of calibration are as shown.

Notice that only fringes close to the vertical tilt angle of 30° are above -10dB. This is caused by the prominent main lobe in Figure 9.2a. Thus only a select group of fringes had significant power.

Clearly it was desirable to spread the power so as to insonify more fringes than was possible using the orientation of the elements consistent with the beam patterns shown in Figure 9.5b. This could be achieved by rotating each element on its acoustic axis by 30° (as in Figure 9.3), so that individual elements were aligned edge to edge. The calculated beam pattern for this configuration, which was used in the June 1984 and subsequent experiments, is shown in Figure 9.6a. For assistance in estimating the nature of the received time series from a homogeneous scatterer distribution a plot of the beam pattern as

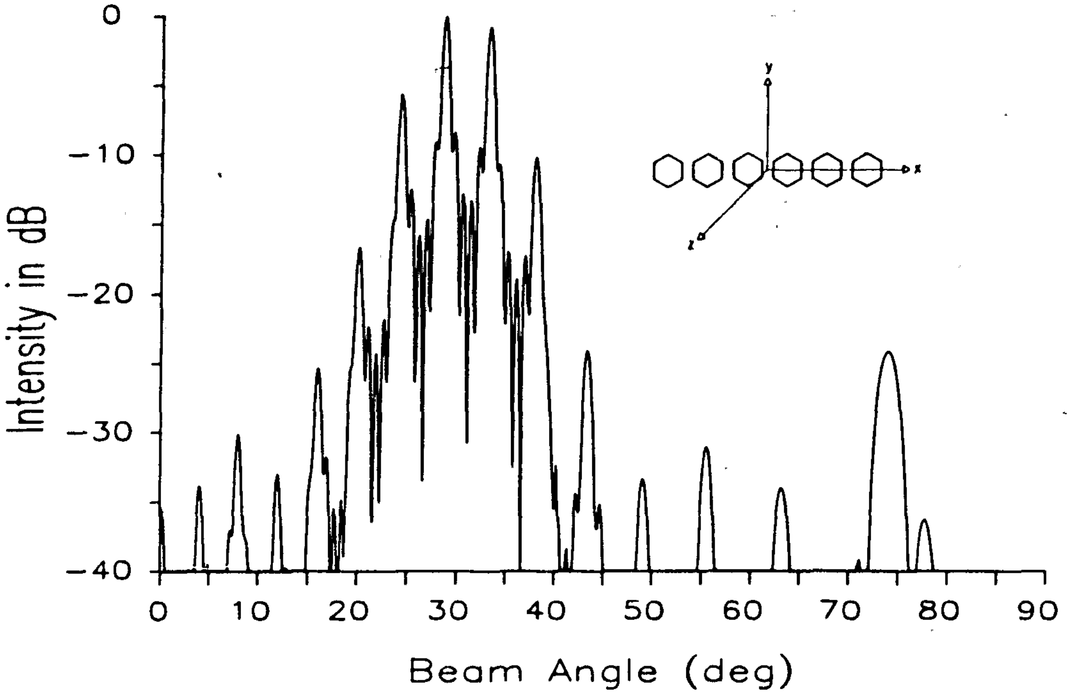

Figure 9.6a Theoretical beam pattern versus initial angle of the echometer projector based on the single element calibrated beam pattern in Figure 9.3. The element orientation is a shown.

a function of pulse arrival time is given in Figure 9.6b.

9.5 In situ calibration of the projector beam pattern

Experiments prior to 1985 with the bistatic system relied on indirect methods to infer the projector fringe locations and gave some ambiguous values. A direct measurement of the projector beam pattern was obtained in situ during the November,1985 experiment. This was accomplished by lowering an omnidirectional hydrophone directly below the large hydrophone while transmitting a continuous 215kHz signal from the projector. Figure 9.7 shows a diagram of the receiving apparatus. A sealed pressure case contained the electronic circuitry for the pressure transducer and provided a mechanical support

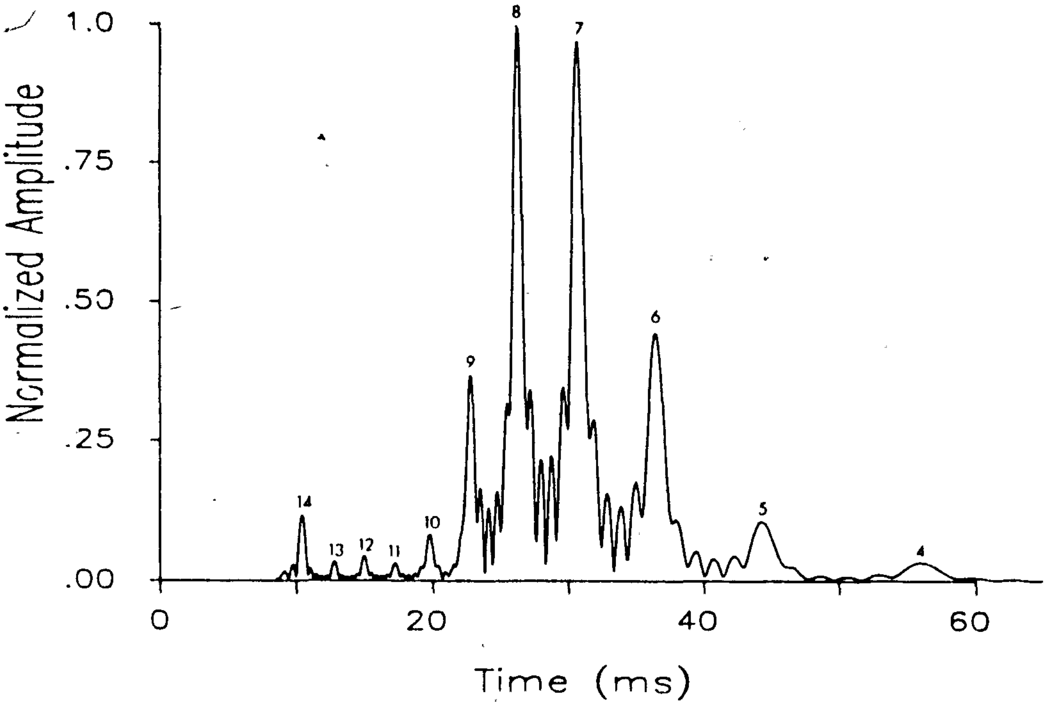

Figure 9.6b Theoretical beam pattern versus arrival time of the echometer projector based on the single element calibrated beam pattern in Figure 9.3.

structure for attaching the hydrophone. Scattering from the pressure casing was minimized by extending the hydrophone with a 1m plastic tube. This hydrophone was kept in a vertical orientation by a 25kg cast iron weight which was attached to the pressure casing by 30m of nylon fishing line. An EDO model 6660 hydrophone with an integrated circuit pre-amplifier was selected for these measurements because of its good receiving response (-174.2dB re 1V per 1μPa at 215kHz) and its symmetrical beam properties. The manufacturer calibrated the horizontal and vertical beam patterns at 200kHz. The horizontal beam pattern was omnidirectional to within ±1.2dB over 360°. Figure 9.8 shows the vertical beam pattern with arrows locating the relevant positions of the projector fringes. The 50m cable length on this hydrophone and other mechanical contraints bounded the received transmit signal between 20°

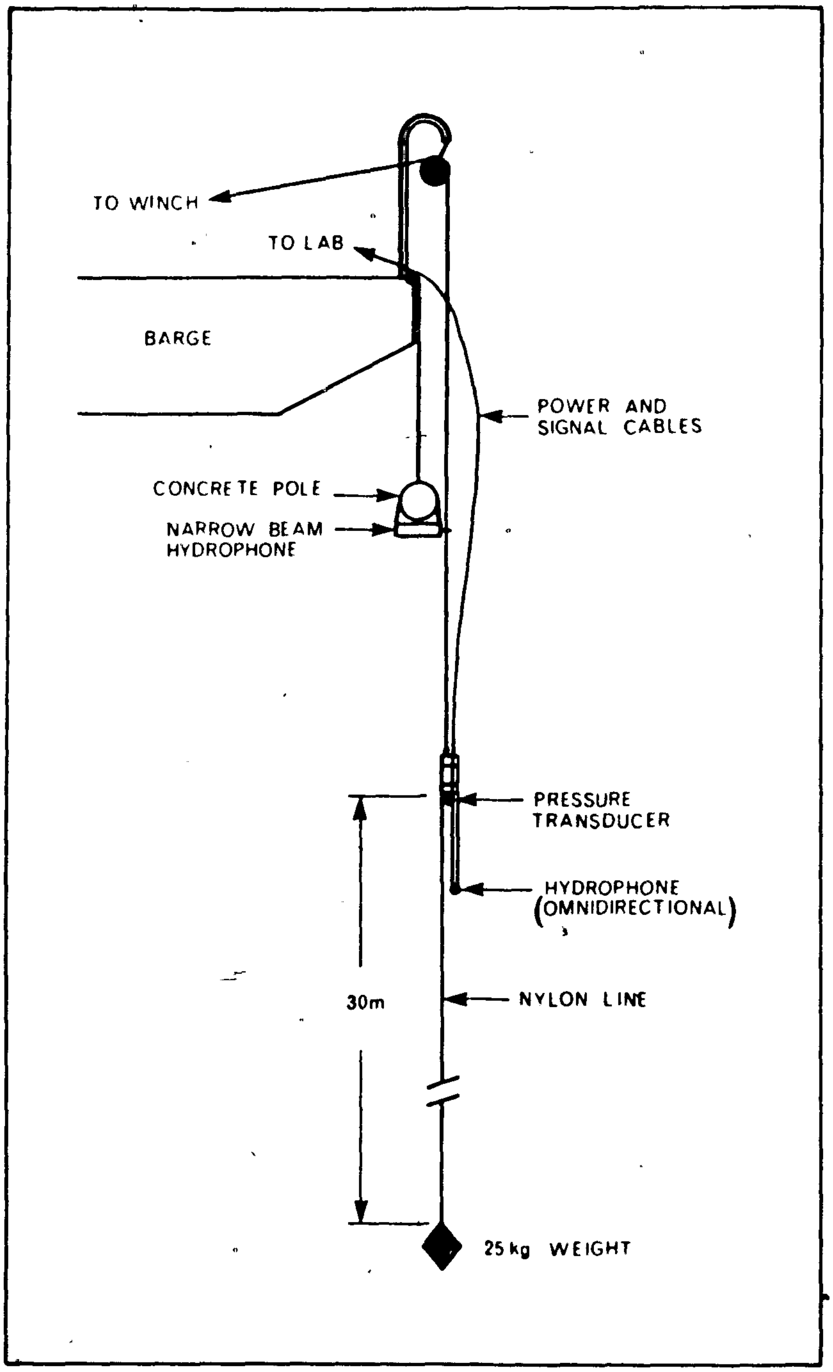

Figure 9.7 A diagram (not to scale) of receiving apparatus used to sample beam pattern of the echometer projector in situ.

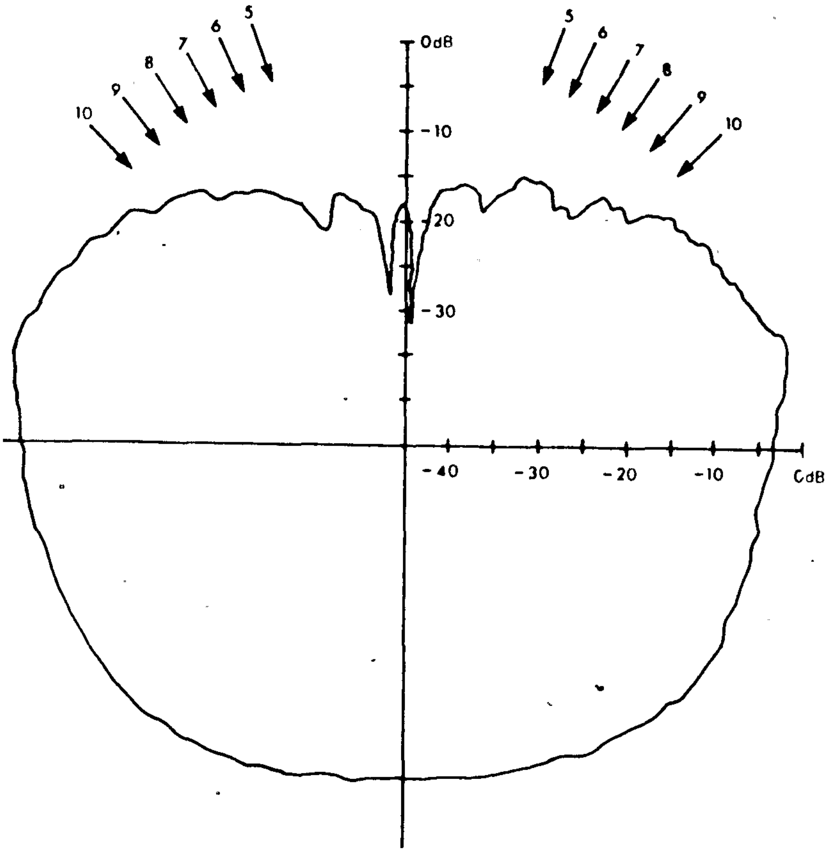

Figure 9.8 Beam pattern of the calibrated omnidirectional hydrophone used in Figure 9.7. The relative positions of the fringes generated by the projector are also represented here by arrows.

and 60° relative to the vertical axis. As the fringe number decreases from 10 to 5 the received signal is attenuated by approximately -0.2dB per degree. This attenuation becomes less symmetrical as the fringe number decreases contrary to the manufacturers initial specifications. These effects will cause the received projector beam pattern amplitude to be distorted from its initial values. By restricting the measuring hydrophone from horizontal rototions the non-symetrical effects were minimized.

The pressure transducer was calibrated by direct comparison with a Paroscientific Inc. standard (accurate to ±.015% below 50 psi) and gave a ±0.2m accuracy in its linear fit for increasing pressure (depth) profiles and a ±0.4m accuracy for decreasing pressure profiles. Strain gauge pressure transducers follow a hysterisis in their pressure load cycle so that separate calibrations are required for increasing or decreasing pressure profiles. The results of this calibration showed the offsets to change from 0.5m to 0.9m between pressure directions while the slopes remained identical to within the accuracy of the least squares fit. To correct for changes in the pressure offsets the winch cable was marked so that each data profile started and stopped at the same depth.

The procedure for obtaining the in situ measurements of the projected 215kHz acoustic signal required 3 people. One deckhand lowered or raised the system by a hand winch and a second deckhand controlled the signal and power cables in an attempt to minimize deflections and rotations of the measuring hydrophone. A third operator controlled the x-y plotter output and transmit signal. Typically a 100 mV continuous sinusoid was fed into the 55dB power amplifier to drive the projector.

Examples of these received signals are displayed in Figure 9.9. This data was collected in Saanich Inlet, British Columbia during calm weather and slack tide with the PENDER anchored to a navy buoy to minimize ship motion. Measurements at a fixed depth gave strong signal variability, particularily near a fringe location, due to small rotations and/or deflections of the probe assembly. Figure 9.9a and b show a down cast and up cast respectively for bank B of the projector (individual elements were tilted 30° relative to the vertical). The characteristic pattern of dominant fringes and subsiduary maxima are consistently observed in both plots. The shape and height of the fringes were distorted primarily by rotations of the measuring hydrophone which altered

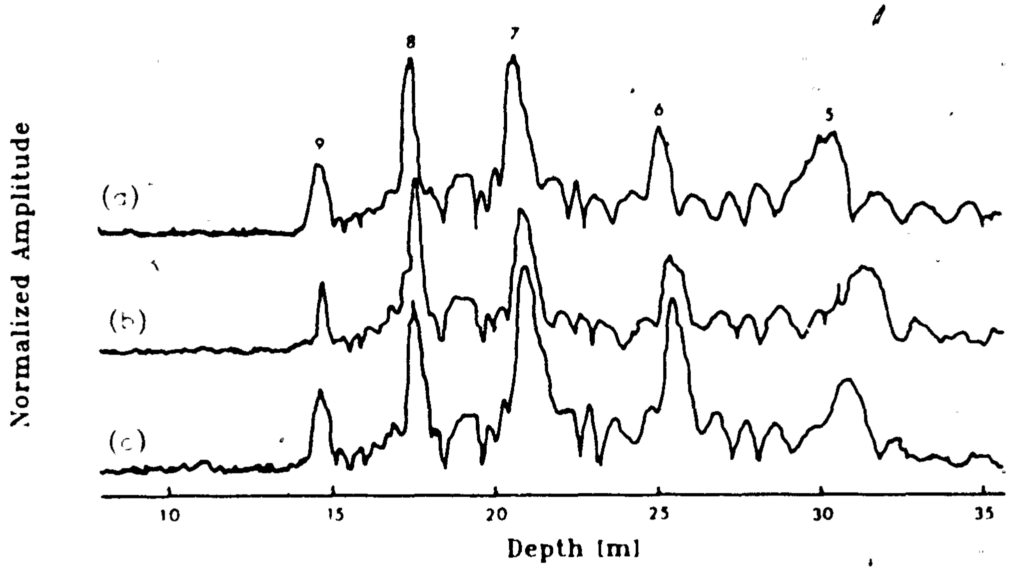

Figure 9.9 Received amplitude signals from the in situ calibration. Signals from bank B of the projector are given in (a) and (b) for down cast and up cast profiles respectively. An up cast profile with bank A transmitting is given in (c).

the effective receive response and non-linear changes in the hydrophone beam pattern as the probe was lowered in the water column. In comparing Figures 9.9a and b the signals with depths $>$ 20m have positions which become more uncorrelated with increasing depth. This effect is likely caused by currents shifting the hydrophone position since the distortions are more pronounced as the depth is increased. In practice the up casts gave more consistent results due to fewer problems with the signal cables rotating the hydrophone probe. Figure 9.9c shows an up cast profile for bank A (elements 25° from vertical). This profile is very similar to the previous examples and shows a stronger return for the deeper fringes as expected.

The effect of refraction on the measured fringe locations was determined by measuring the sound speed profile with a CTD and applying Snell's law to find the change in fringe depth. The sound speed profile approximated a linear increasing function with depth, which causes upwards refraction to acoustic ray paths. The maximum change in the depth of a fringe due to refraction was -10cm for fringe numbers 14 to 5. Since this change is less than the resolution of the pressure transducer used with the hydrophone probe, the effects of refraction were insignificant in the in situ beam pattern measurements.

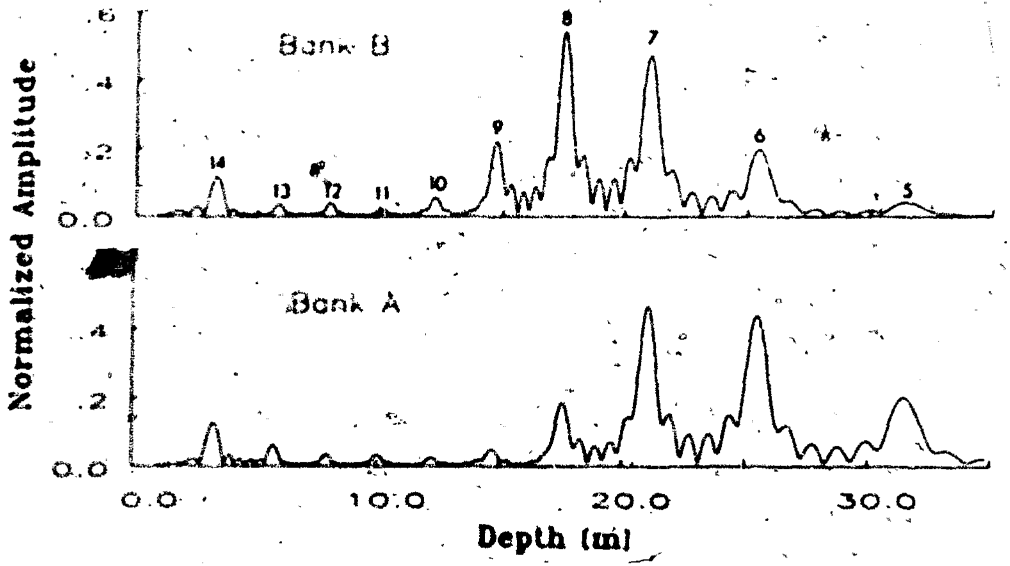

Figure 9.10 Theoretical beam patterns of the echometer projector as a function of linear normalized amplitude and depth for the two banks of arrays.

A comparison of the results in Figure 9.9 with the those in figures 9.5b and 9.6 requires incorporation of the beam pattern in Figure 9.7. For fringe numbers 5 to 10 the received signal will be attenuated by approximatly -0.2dB per degree. By including this factor when simulating the projector beam pattern from its laboratory calibrations and plotting the results as normalized amplitude versus depth, the in situ results can be better understood. Figure 9.10 provides this theoretical beam pattern for both bank A and bank B orientations. The distribution of the fringe height with depth peaks at 17.5m for bank B and 21m for bank A. In both cases the fringe height increases at a quick rate before the largest amplitude fringe location and then decreases at a slower rate as the depth increases. This pattern of the fringe amplitudes is also observed in Figure 9.9. The fringe at 31m ($m = 5$) lies within a region of strong variability in the hydrophone's vertical beam pattern (see Figure 9.8) this explains the larger amplitude values for bank B in Figure 9.9.

In summary, an in situ direct measurement of the projector beam pattern was obtained for the two element orientations (25° and 30°) during the November, 1985 experiment in Saanich Inlet, British Columbia. The resulting beam patterns with relative amplitude versus depth were consistent with their expected values to within the accuracy of the measurments.

9.3 Calibration of the large hydrophone

Calibration of the large aperature (75cm diameter) hydrophone (see Figure 8.3), used throughout this research, presented a challenging problem. With a mass of ≈ 100kg civilian calibration facilities were not capable of handling the transducer or providing measurements in its far field (20m or more). This led to the development of a large range calibration facility at IOS. By taking advantage of the 'U' shaped dock, support struts were designed to secure the transducer to the inside edge of the wharf. Ranges of 46m to ≈ 120m between transducers were then possible within a 10m water column. Direct measurement of the beam pattern of the 72 element hydrophone were obtained.

in August, 1985 at the IOS wharf facility. At this time only manual measurements of the beam pattern orientation(at 215kHz) were possible. Figure 9.11 shows the narrow beam characteristics on a decibel versus linear scale. This result confirmed the 0.7° beam width between -3dB points and the -17dB suppression of side lobes.

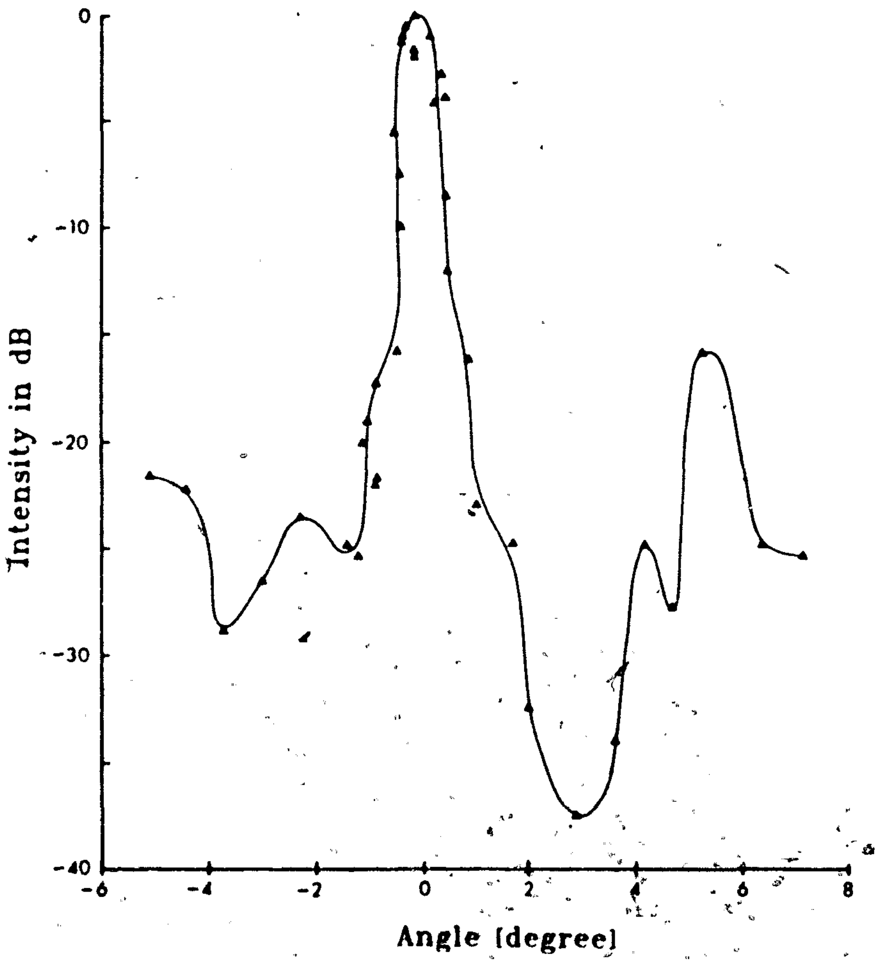

Figure 9.11 Beam pattern of the 72 element hydrophone at a frequency of 215kHz and a range of 45m.

10 CALIBRATION AND SINGLE TRANSMISSION RESULTS

This chapter presents a detailed analysis of bistatic echo data that were collected using the configuration in Figure 8.6. The first section describes the automatic calibration of the analogue components in the demodulation circuitry. The remaining 2 sections show a typical echogram for the bistatic configuration and present the statistical properties of these echoes.

10.1 Self Calibrations

The analogue circuitry which demodulates the received signal is subject to fluctuations in relative gains and offsets during the course of an experiment. Ten records at the beginning and end of each data run were dedicated to calibrations so as to monitor these variations. This method of self calibration relied on sending a pure sinusoid (216kHz) in place of the real received signal while keeping the reference frequency at 215kHz. The resulting in-phase and quadrature signals after demodulation were then pure 1kHz sinusoids. The A/D digitized at 10kHz and 600 samples of each channel (in-phase and quadrature or X and Y respectively) were recorded for each transmission.

Prior to processing the real data, the calibration runs were processed to determine the d.c. offsets (dc_X, dc_Y), and the amplitude (a_X, a_Y) and phase (ϕ_X, ϕ_Y) of the 1kHz calibration signal for each channel. This was accomplished by computing a 300 point (30 cycles) discrete Fourier transform for both channels in the calibration run. Each calibration run provided 10 estimates of the offsets and gains for each channel which were used to determine averages and accuracy of the measurements. The relative gain rg and relative phase $\Delta\phi$ between the two channels were computed to reconstruct the unbiased signals with,

$$rg = a_X / a_Y \tag{10.1.1}$$

and,

$$\Delta\phi = \phi_Y - \phi_X. \tag{10.1.2}$$

Then, by assuming any bias in the relative phase occurs in the Y channel, the true signals $(\hat{x}, \hat{y})$ will be given by,

$$\hat{x} = x - \mathrm{dc_X} \tag{10.1.3}$$

$$\hat{y} = ((y - \mathrm{dc_Y})/\mathrm{rg} - \hat{x}\sin(\Delta\phi))/\cos(\Delta\phi) \tag{10.1.4}$$

where x and y represent the measured in-phase and quadrature component of the received signal from a specific range gate.

During the course of the experiment only minor fluctuations in the calibration coefficients were observed. Table 10.1 shows the range and accuracy of the calibration values during the 15 day period of data collection for the November 1985 experiment.

Table 10.1 Range and accuracy of offsets and gains from the analogue circuitry.

Variable	Min	Max	Accuracy	Units
rg	0.992	0.995	±.001	—
$\Delta\phi$	-0.24	-0.11	±.01	degrees
$\mathrm{dc_X}$	-0.200	-0.230	±.002	normalized
$\mathrm{dc_Y}$	-0.230	-0.260	±.002	normalized

Once the offsets and gains in the quadrature components have been corrected the amplitude and phase profiles of the received signal can be computed with a greater confidence. The resulting accuracy of the amplitude and phase depends on the error vector $\vec{a_e}$ which is determined from the accuracy of $\hat{x}$ and $\hat{y}$. $\vec{a_e}$ has a length of $\sqrt{.002^2 + .002^2} = 0.0028$ in normalized units. This error vector has a uniform phase distribution so that the confidence interval of the final amplitude estimate a_s is ±0.0028. The phase accuracy is also dependent upon the error vector and can be approximated by $\arctan(\vec{a_e}/a_s)$ when $a_s > a_e$. For example, to achieve a 10 degree or better accuracy in phase then a_s must be greater than 0.016. In most cases the mean a_s value was ~ 0.2 which gives a phase accuracy of 0.8 degrees.

All further calculations have incorporated equations 10.1.3 and 10.1.4 to correct the measured in-phase and quadrature signals for the offsets and differential gains caused by the analogue circuitry.

10.2 Single transmissions

The received signal corresponds to the cumulative echoes of the transmit pulse scattered by biological targets. Although scattering can occur throughout all regions insonified by the echometer projector only the echoes which originate from the region directly below the narrow beam hydrophone will be received. Since the sidelobes of the hydrophone are below -17dB, sidelobe echoes will be assumed negligible. The relative strength of a single echo depends upon both its position within the projector and hydrophone acoustic beams and reflectivity of the target. In addition, the population distribution of targets will influence the strength of the received signal. Thus the received amplitude signal depends both upon the acoustic beam properties and the spacial distribution of acoustic targets.

On November 13, 1985 a data set with over 24000 independent transmissions (40 minutes) was obtained. These data were collected in the center of

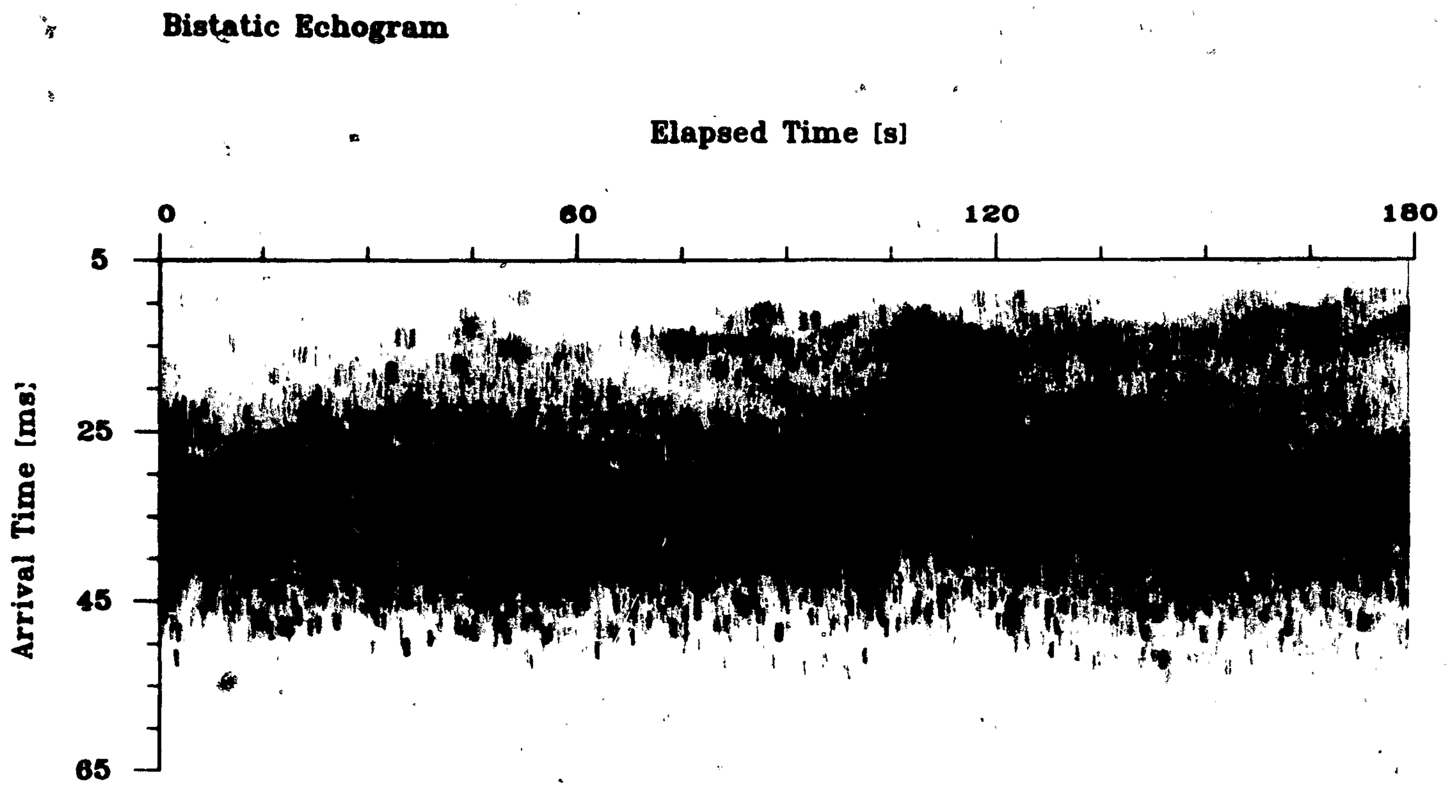

Bistatic Echogram

Figure 10.1 Received amplitude profiles with elapsed time(s) versus arrival time(ms). Relative amplitude is displayed by the grey scale with black representing the largest values. Collected on November 13,1985 starting at 20:28:47 hours in Saanich Inlet, British Columbia (data file E85-13:1).

Saanich Inlet, British Columbia. The ocean surface was calm and the barge drifted slowly with the wind and tide. The amplitude and phase returns from a single transmission have a stochastic nature. Figure 10.1 shows the first 1800 amplitude profiles by plotting elapsed time (s) verses arrival time (ms). Elapsed time represents the time of transmission while the arrival time corresponds to the time at which an echo arrives relative to the time of transmission. A grey scale with 9 levels represents the relative amplitude, with black corresponding to the strongest signals (0.8 - 1.0) and white the weaker signals (0. - 0.1). The intermediate grey levels are linearly scaled in 0.1 relative amplitude values. In this representation the amplitude is displayed in a finite number of discrete steps. The resolution of the display is such that the finite transmit pulse duration is clearly revealed in echoes from targets at different depths. Notice how consistently the 2ms pulse is represented in this ensemble of echoes. In an ideal system with negligible side-lobes and a uniform distribution of identical isotropic targets, the narrow beam fringe pattern in the projector would be clearly represented in the received amplitude profiles. This fine structure is obscured by variations in target strength in Figure 10.1 but these experimental results do represent the general features of the projector beam pattern and scatterer distribution.

10.3 Echo statistics

Figure 10.2 shows the mean and root-mean-square (rms) amplitude profile of the received signal from the first 1800 transmissions (3 minutes of data). The amplitude scale is normalized and any value greater than 1 was a clipped signal and hence rejected in the analysis. The profile has been presented in terms of arrival time in ms. However, with knowledge of the sound speed

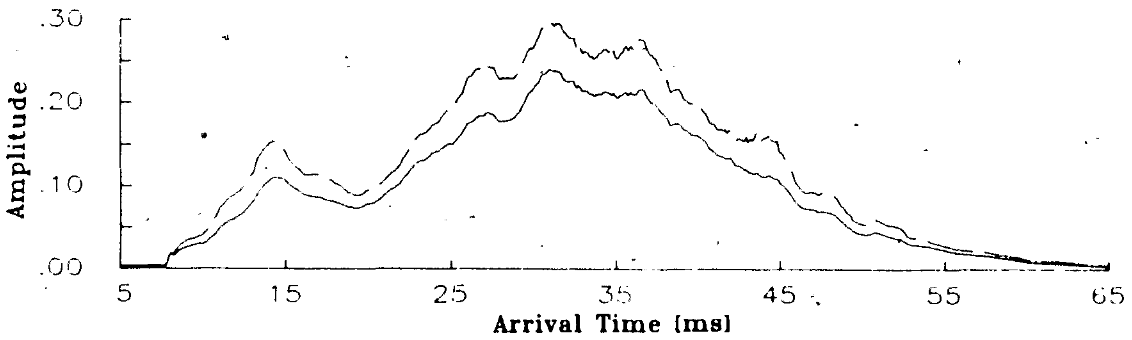

Figure 10.2 The mean(solid) and rms(broken) amplitude profile of the received signal using the first 1800 transmissions (3 minutes of E85-13:1 data). The amplitude has been normalized to its full scale value.

profile $c(z)$ the x-axis could also be represented as a depth profile. In comparing Figure 10.2 with the echometer projector beam pattern in Figure 9.6b the signals within 25 to 45ms correspond to fringe locations; the peak at 15ms, however is anomalous and was likely caused by a high density of euphausiids. As discussed in section 6.2 the amplitude signal from a fixed range cell should follow a Rayleigh distribution. The basic property,

$$\begin{aligned} \mathrm{R} &= \frac{\langle a \rangle}{\langle a^2 \rangle^{1/2}} \\ &= \frac{\int_0^\infty a^2/\sigma^2 \exp[-a^2/(2\sigma^2)]da}{\left[\int_0^\infty a^3/\sigma^2 \exp[-a^2/(2\sigma^2)]da\right]^{1/2}} \\ &= \frac{\sqrt{\pi}}{2} = 0.886 \end{aligned} \tag{10.3.1}$$

can be utilized to test this hypothesis. The value of the ratio R varies from 0.75 to 0.81 in the 25 to 45ms region; the rms amplitude is therefore greater than a Rayleigh pdf would imply. This result is not surprising however, since as Pieper(1983) has demonstrated, a zooplankton cloud often contains larger acoustic targets such as fish. The presence of fish will cause spikes in the tail of the amplitude pdf and bias the simple ratio test for Rayleigh statistics.

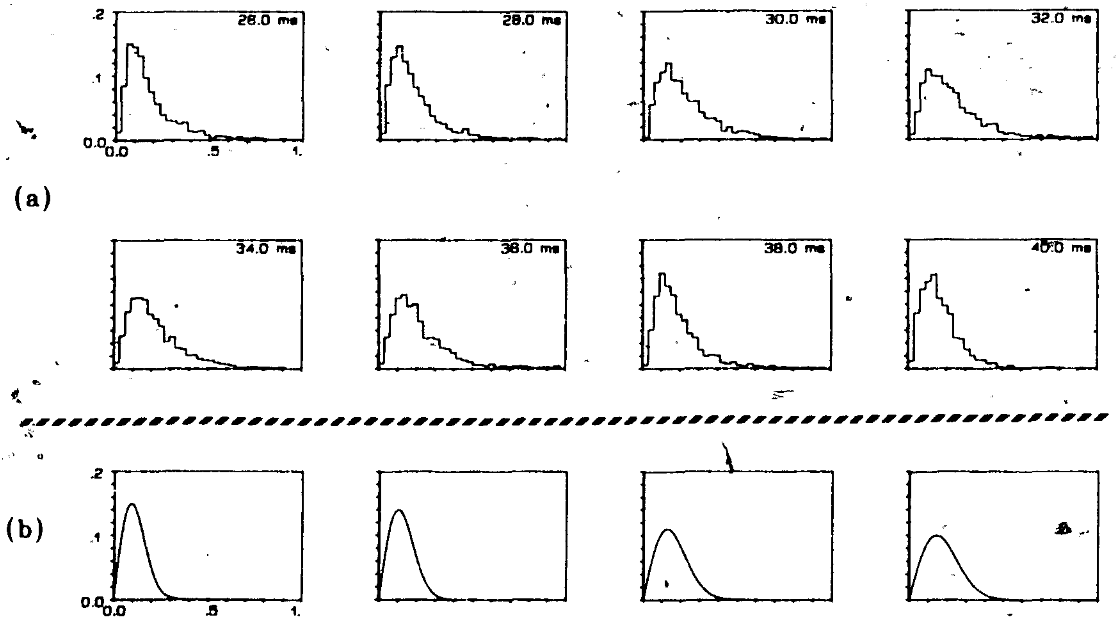

Figure 10.3 These plots show the frequency of occurrence per amplitude bin. They show amplitude histograms at fixed arrival times ranging from 26ms to 40ms in 2ms steps in (a) and in (b) fit Rayleigh ditstributions to the peaks in (a) for arrival times 26 to 32ms.

Alternatively, if the target strength distribution is Gaussian or even bimodal then the resulting amplitude pdf will be the sum of many Rayleigh pdf's.

Using the same data set amplitude histograms were computed with arrival times ranging from 26ms to 40ms in 2ms steps. These plots are shown in Figure 10.3a, with relative amplitude on the horizontal axis and frequency of occurrence on the vertical axis. Unique distributions occur at each of these locations. A noticeable shift in the peak location and broadening of the distribution occurs as the arrival time increment increases. A few large amplitude returns probably from fish, contribute to the high amplitude tail in the pdf. Their frequency of occurrence however is much less than the peak value. This confirms the assumption that the fish (or large acoustic target) population is much smaller than the euphausiid (or small acoustic target) population. Figure 10.3b fits the first four histograms in Figure 10.3a (26 to 32ms) to a Rayleigh distribution using the location of the peak. These examples demonstrate that the target strength distribution has a dominant peak, with other contributions from stronger acoustic targets which occur less frequently.

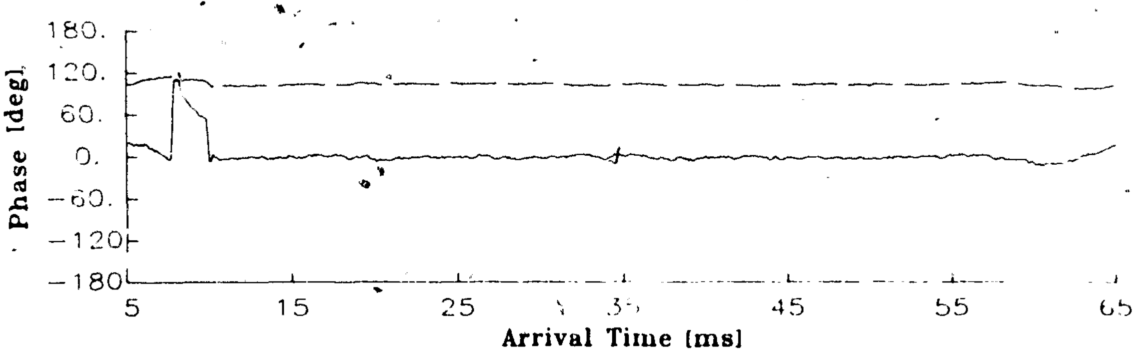

Figure 10.4 The mean (solid) and rms (broken) phase profile of the received signal using the first 1800 transmissions.

The phase statistics are well behaved. Figure 10.4 shows the mean and rms phase profile for the same data set as in Figure 10.2. The direct pulse which travels between projector and hydrophone causes a disturbance at the beginning of the profile, and after 55ms the large received signal becomes closer to the result for a monostatic echosounder which likely causes the slight bias in mean phase. The remainder of the profile has,

$$\langle \phi \rangle \simeq 0^{o}$$

and,

$$\begin{aligned} \langle \phi^2 \rangle^{1/2} &= \left[\int_{-\pi}^{\pi} \frac{\sigma^2}{2\pi} d\sigma \right]^{1/2} \\ &= \pi/\sqrt{3} = 103.9^{o} \end{aligned} \qquad (10.3.2)$$

which corresponds to a uniform phase distribution.

Before coherently processing the received echo data it was necessary to test for statistical independence of successive profiles. The maximum repetition rate between transmissions was 10Hz. By selecting a fringe location (26.8ms) and performing an autocorrelation of both the amplitude and phase time series the coherence of these signals can be determined. Figure 10.5 shows the resulting autocorrelations versus transmission number lag (there are 5000 transmissions in the 500s time series). The phase autocorrelation in Figure 10.5b falls into its noise level after one digital lag step which verifies that the system of scatterers have been sufficiently perturbed to provide a completely unique phase between adjacent transmissions.

Assuming that the scatterers swim in random directions a $\lambda/2$ displacement of the scatterer positions will cause the phase signal to be unique between adjacent transmissions from the same range gate. For the 10Hz repetition rate of the transmitted pulse a $\lambda/2$ (3.43mm) displacement corresponds to a minimal swim velocity of 0.35cm/s. When in an escape mode euphausiids attain speeds of 11 times their body length per second (11 to 22 cm/s) and during normal behaviour their mean speed stays close to 8 times their body length (8 to 16 cm/s) (Kils,1979). These results indicate that even with negligible ship motion the euphausiid spacial distribution relative to the acoustic beam will be perturbed significantly by their random swimming patterns to achieve unique phase signatures between pulse transmissions.

The amplitude autocorrelation in Figure 10.5a has a much broader peak about zero lag than that shown in Figure 10.5b and shows that ~2sec must evolve before a unique amplitude signature is obtained. The physical factors which influence the width of the amplitude autocorrelation are speckle and the

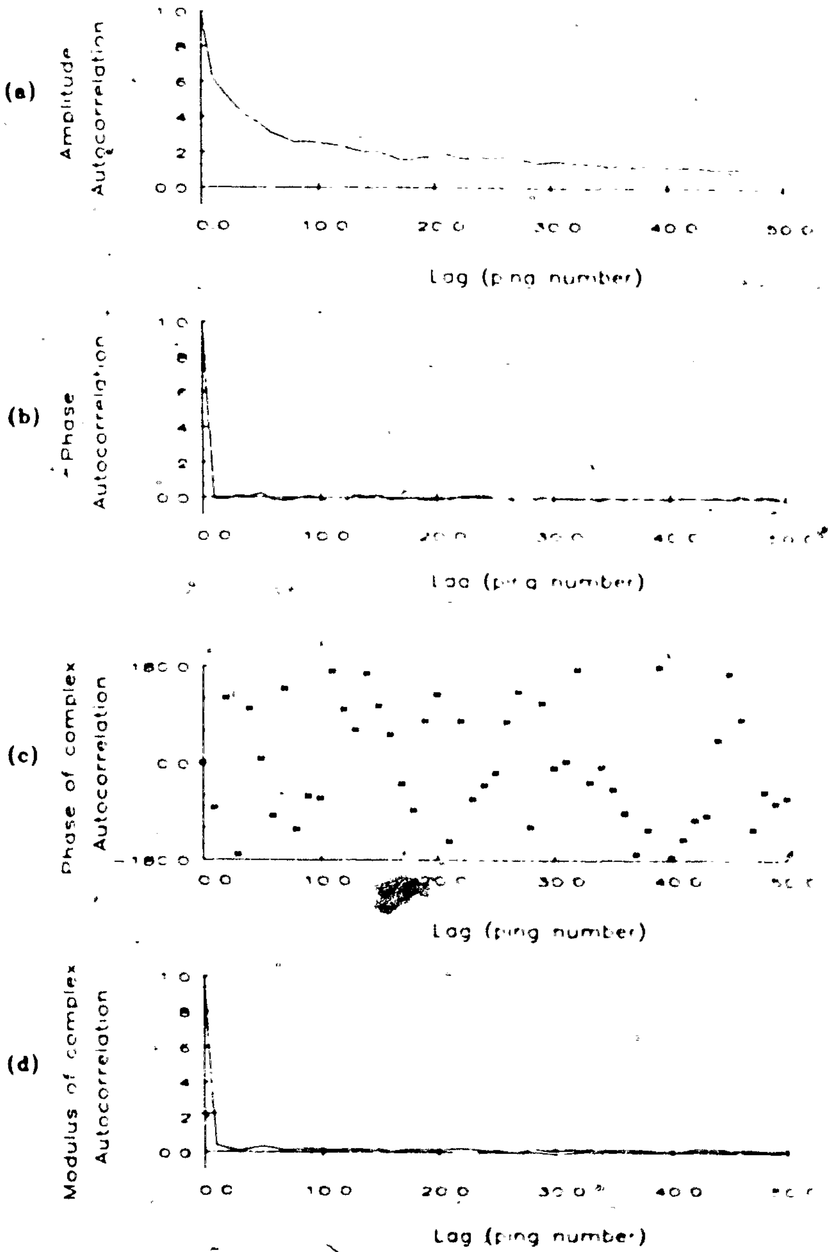

Figure 10.5 Autocorrelations versus lag time using the 5000 point complex time series of the data for the 26.0ms arrival time. The amplitude and phase time series are used in a) and b) respectively while the complex time series is used in computing c) and d).

rate at which the volume target strength fluctuates (i.e. the patchiness scale of the euphausiid distribution).

The effect of the scatterer motion and speckle are better represented by evaluating the complex autocorrelation function $R_\tau(t')$ at arrival time τ which is defined by,

$$R_\tau(t') = \langle S_\tau(t) S_\tau^*(t+t') \rangle \qquad (10.3.3)$$

where,

$S_\tau(t)$ = time series of the complex received echo with fixed arrival time τ.

t' = time lag.

The motions of the i^{th} scatterer within a range gate of the transmit pulse can be represented by a group velocity vector $\vec{v}$ which gives the mean advection of the scatterers through the range gate and an individual velocity vector $\vec{u_i}$ with random orientation. Only the velocity components which cause a change in phase to the echo from an individual scatterer after time lag t' will cause $S_\tau(t)$ to decorrelate. For a monostatic echosounder the direction of transception will determine the effective velocity components which can be represented by v_ζ and $u_{i\zeta}$. In the bistatic echosounder the effective velocity component will be dependent on the initial angle of the transmit pulse but for simplicity of notation this will also be referred to as the ζ direction.

An evaluation of $R_\tau(t')$ has been performed by Edwards(1978) and a more complete derivation is given in Appendix II of Farmer, B[illegible]th and Kamitakihara(1981). The normalized evaluation is,

$$\frac{R_\tau(t')}{R_\tau(0)} = \exp[-\imath 4\pi v_\zeta t'/\lambda] \exp[-8\pi^2 \langle u_\zeta^2 \rangle t'^2/\lambda^2]. \qquad (10.3.4)$$

This expression shows that the group velocity component and variance of the random scatterer motions in the ζ direction are separable quantities. By plotting the modulus of $R_\tau(t')/R_\tau(0)$ as derived from the data, estimates of v_ζ and $\langle u_\zeta^2 \rangle$ can be obtained.

In both of the above cited references the interpretation of $\langle u_\zeta^2 \rangle$ is idealized and confused by the notation. A full derivation of $\langle u_\zeta^2 \rangle$ for realistic scatterer speed distributions is presented in Appendix 6. The resulting expression is,

$$\langle u_\zeta^2 \rangle = \frac{1}{3}\left\{ \frac{3u_o\sigma_u}{\sqrt{2\pi}} \exp[-u_o^2/2\sigma_u^2] + \frac{u_o^2+\sigma_u^2}{2}\left(1+\mathrm{erf}\left(\frac{u_o}{\sqrt{2}\sigma_u}\right)\right)\right\} \tag{10.3.5}$$

when the speed of the randomly oriented scatterer velocities has a Gaussian distribution with standard deviation σ_u and a mean value of u_o. This is a reasonable representation for euphausiids since their length frequency histogram can be modelled by a Gaussian with an offset (Heath,1976 and Kristensen and Dalen,1986) and the length is proportional to the normal swimming speed (Kils,1979).

For a typical November euphausiid length distribution in Saanich Inlet, B.C. the corresponding speed distribution is approximately 12cm/s ± 4cm/s. Using this ratio of u_o/σ_u equation 10.3.5 simplifies to give,

$$\langle u_\zeta^2 \rangle = 1.11\frac{u_o^2}{3}. \tag{10.3.6}$$

This example shows that the inclusion of the σ_u term adds 11% to the influence of u_o on the variance term.

The phase and modulus of the normalized complex autocorrelation for the same 5000 point time series used in Figures 10.5a and b are displayed in Figures 10.5c and d respectively. An estimate of v_ζ (the group velocity component in the ζ direction) from Figure 10.5c would be possible if a linear slope developed for the initial non-zero lag values. In this case the linear signal is not observed because the sampling period is too long to catch the signal when it is still well correlated. The random nature of the phase versus lag plot is caused by the long pulse repetition period relative to the complex decorrelation time of the targets. The plot of $|R_{26.5}(t')/R_{26.5}(0)|$ in Figure 10.5d approximates a Dirac-delta function to within the resolution of the lag values. This plot demonstrates that the individual scatterers are being sufficiently perturbed to cause a unique echo between adjacent transmissions. It also provides an estimate of the scatterer speed u_o. Using equations 10.3.4 and 10.3.6 with $t' = .1$s, $\lambda = 6.86$mm and $|R_{26.5}(t')/R_{26.5}(0)| = 0.05$ the estimated mean scatterer speed is at least 2.2cm/s. This application demonstrates that either a much higher repetition rate and/or a smaller operating frequency are necessary for more accurate estimates of the scatterer velocities. In addition a cross correlation in arrival time (τ) between pairs of echo profiles separated by t' leads to better interpretation of the v_ζ component.

For the purpose of coherent processing the autocorrelations in Figures 10.5b and d demonstrates that each new transmission provides a statistically independent sample at the 10Hz repetition rate.

In chapter 6 the amplitude and phase pdf are derived from the statistics of the in-phase and quadrature components. These components were measured directly from the received signal during the November 1985 experiment and when normalized by the full scale value are bounded by ±1. Equation 6.2.4 shows how each measured value of X or Y can be represented by the summation of both coherent and incoherent echoes. As the number of echoes approaches infinity the law of large numbers asserts that these variables (X and Y) will have Gaussian statistics. The experimental data was subject to the local population densities so that the extent to which X and Y approximate Gaussian statistics will give an indication of the number of targets insonified within a range gate. Information about the target strength distribution will also be embedded in this representation of the data.

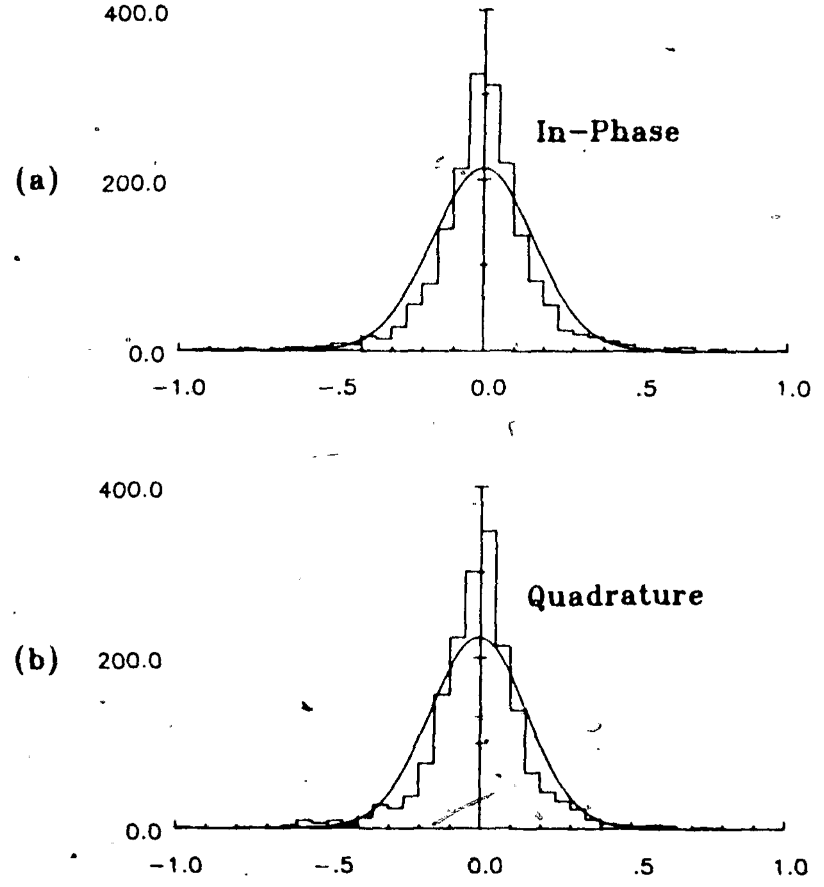

Figure 10.6 Histograms of the in-phase and quadrature signals based on the first 1800 transmissions from signals with a 26.0ms arrival time. These plots show the number of events per bin as a functions of the normalized signal strength.

Figure 10.6 shows a typical histogram of the in-phase and quadrature signals using 40 bins to represent the signal strength, and 1800 data points (3 minutes of data). The vertical scale gives the number of occurrences per bin. The mean and standard deviation were computed and used to plot the Gaussian distribution from these parameters. Both histograms have similar features, and deviate significantly from a Gaussian distribution. The bins with absolute values $> -.4$ occur less frequently but cause the standard deviation to be biased towards larger values. By eliminating these values in estimating the Gaussian parameters a closer match between the experimental data and a Gaussian pdf is obtained (see Figure 10.6). These distributions only approximate a Gaussian qualitatively. A chi square goodness of fit test was performed on this data set to quantify the confidence levels. Using all the range cells between 25ms and 45ms and the 1800 data points all the histograms were non-Gaussian to better than 99.5% confidence. However when all amplitude values $> -.4$ were rejected from the analysis all estimates of the chi squared summation terms were improved. This resulted in better than 50% confidence that the signal with arrival times between 30.5 ms and 37.5 ms was Gaussian. Confidence levels of 90% were also observed in this region. When compared to the profile of mean amplitude in Figure 10.2 the improved Gaussian statistics are correlated with the higher mean amplitude values. Signal degradation occurs when weak signals from a fringe location are contaminated by strong acoustic scatterers in the side lobe regions. This example demonstrated that estimates of the standard deviation are biased by the larger amplitude events and that distributions with larger mean amplitude signals have a higher probability of being Gaussian distributed.

The statistics of the amplitude and phase (a, ϕ) signals at a fixed arrival time are related to the in-phase and quadrature (x, y) representation by a geometric transformation. By computing the joint pdf of the x and y signals the statistics of the a and ϕ signals are also represented. A 3 dimensional histogram was computed to investigate the joint pdf behavior, using the same 1800 point data set. The xy plane was subdivided to contain 160 square bins with each bin area $=0.05^2$ (in units of relative amplitude squared) and used

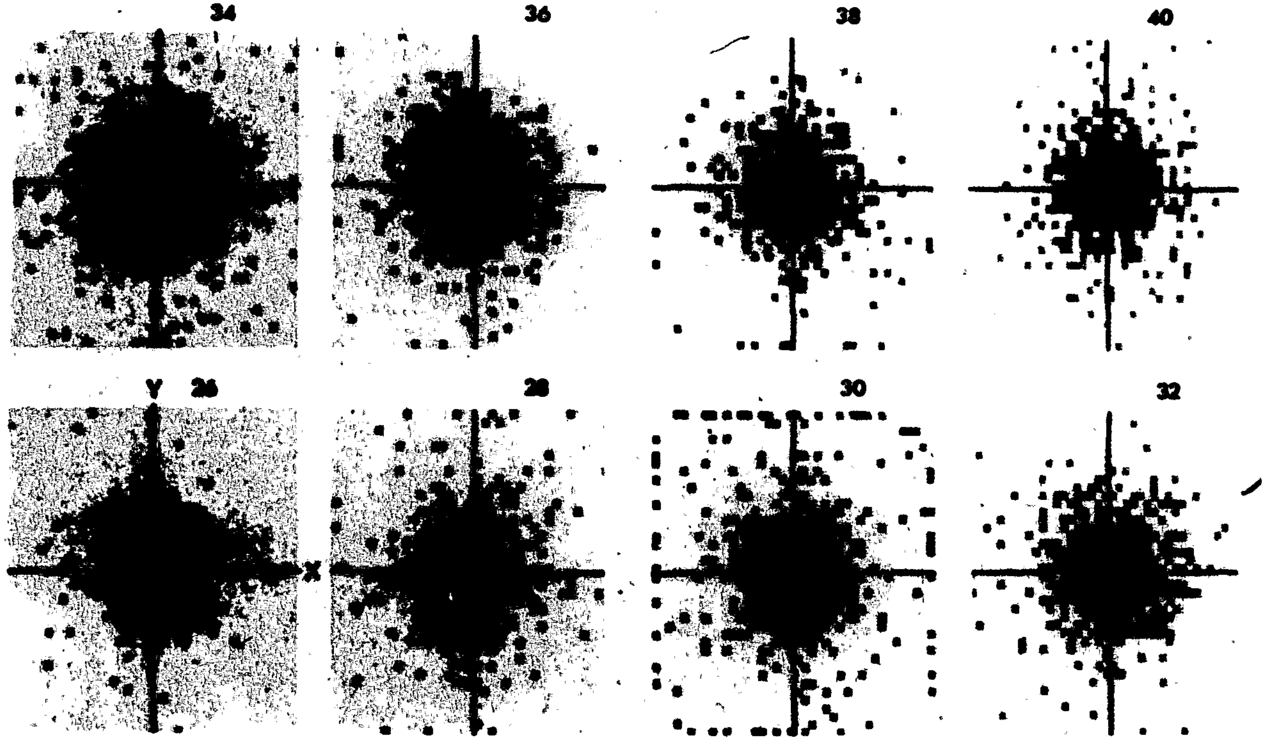

Figure 10.7 Two dimensional histograms of the relative (x, y) or (a, ϕ) signal regions for arrival times ranging from 26ms to 40ms in 2ms steps. The frequency of occurrence per bin area is displayed by a linear grey scale with black representing the largest values.

to count the number of events in each bin area. The resulting histogram was then plotted by using a grey scale to represent the number of events per bin area. Similar to the set of amplitude histograms in Figure 10.3 arrival times ranging from 26ms to 40ms in 2ms increments were selected as representative locations. Figure 10.7 displays this set of 3 dimensional histograms. Each level of grey corresponds to an increment of 5 events with white $=$ 0 events and black representing bin areas with more than 45 events. Notice the variability of the large amplitude events ($a > 0.5$) . They are limited to the lowest grey level and are scattered throughout the xy plane. In most cases they are uniformly distributed about the center, but if by chance they are dense in one quadrant then they will bias the phase estimates. Each histogram in Figure 10.7 is unique and demonstrates the variability of the received signal at various arrival time locations. In addition each histogram shows a peak value near the origin and a concentric bell shaped decay as the signal amplitude increases.

This configuration demonstrates the uniform phase distribution for single returns. If this histogram approximated a narrow bi-variant distribution with an off-axis center, then reliable phase estimates from the received signal are possible. This condition can occur if the scatterer populations are sufficiently dense and homogeneous to provide a coherent to incoherent signal ratio greater than 1. In this special case, the location of the joint pdf peak and its width can then be used to estimate the received phase value and its accuracy. However, such a bivariant distribution does not, and probably cannot occur for the scatterer densities encountered in the ocean, as shown with a numerical model in Chapter 4. These results confirm the necessity for the coherent processing concept introduced in Chapter 4, in which superposition of many independent data sets allows reconstruction of a quasi-continuous scattering field while yet retaining the validity of the single scattering approximation.

11 COHERENT PROCESSING OF BACKSCATTER DATA

The previous chapter demonstrated that independent transmissions have independent phase measurements and that these phase values are uniformly distributed between ±180°. These single phase measurements are of no direct value to an interferometric system. By using coherent processing (CP) much higher population densities can be simulated which can provide meaningful phase values. This chapter applies the coherent processing technique to the data set used in the previous chapter. The accuracy of the technique is discussed in the second section. An overview of other data sets and a comparison between monostatic and bistatic echoes from the same scatterer distribution are found in the third section. A final section removes the effects of refraction from the bistatic echoes and estimates the repeatability of coherently processed phase estimates.

11.1 Coherent Processing Technique

This section applies coherent processing (CP) to the same data used in Figure 10.1 and demonstrates the characteristics of the resulting signals. Two perspectives are taken to represent the data; 1) profiles of arrival time (τ) which present all the final values after CP and, 2) times series which show how CP evolves in time (t) at specific arrival times. The first case will be used to identify significant features and to select locations for displaying by the second method.

Arrival time profiles of amplitude and phase were initially computed by summing the in-phase and quadrature components at each of the 600 arrival times over a large number of consecutive data records. The final values of these sums were then converted into their corresponding amplitude and phase

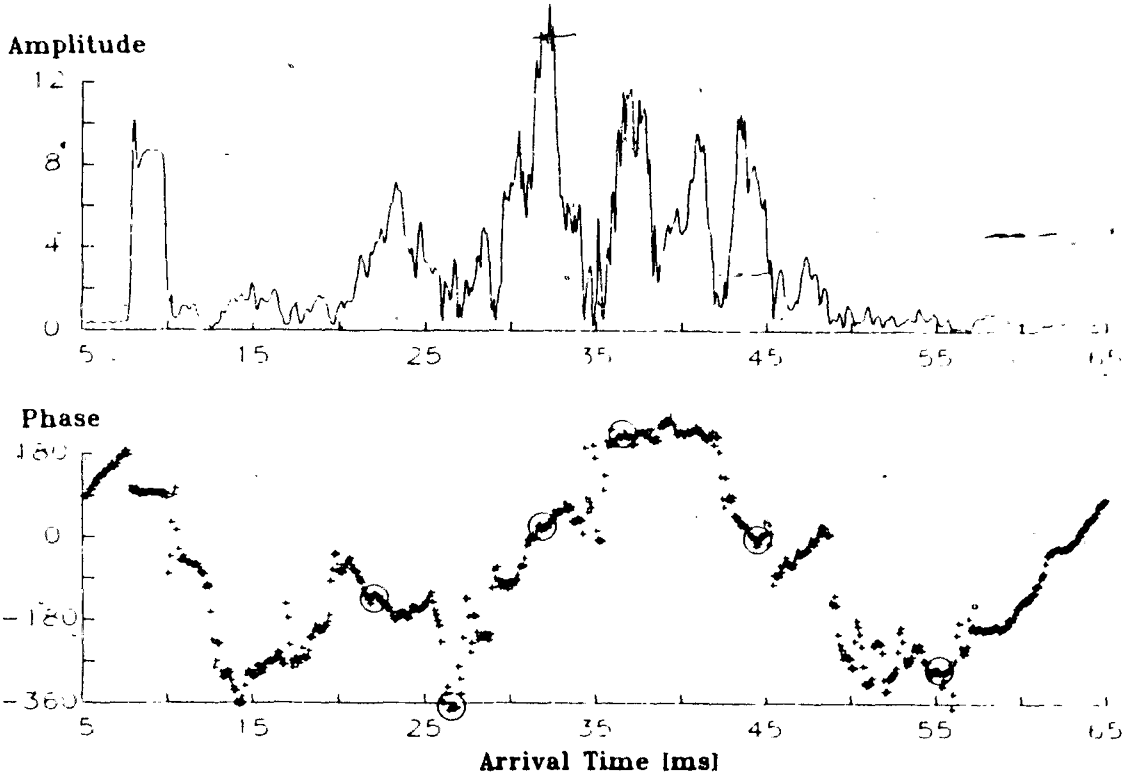

Figure 11.1 Amplitude and phase profiles of 600 coherently processed echoes using the first minute of data (600 transmissions). The circled phase values correspond to fringe locations.

values. Figure 11.1 demonstrates the resulting profiles after coherent processing of one minute of data (600 echoes). The amplitude profile has a number of characteristic features. A 2ms pulse corresponding to the unreflected direct path transmission between the projector and hydrophone is detected between 8 and 10ms. The ringing in this envelope is an artifact of the 4kHz Butterworth low pass filter used for complex demodulation. The other predominant features lie within the region of the dominant echometer projector lobes (20-45ms) and represent convolutions of the transmit pulse with the scatterer distribution. A fundamental objective in this analysis is to determine if a correlation exists between the peaks in amplitude (1-2ms wide) and the phase signal.

The phase profile in Figure 11.1 clearly demonstrates that CP provides a specific signature in arrival time. The direct pulse return provides an example of an ideal echo return. The phase signature between 8 and 10ms is a relatively constant value and as expected it differs from neighboring values. Notice that the effects of ringing are minimal. This result is expected since the Butterworth filters are applied only to the analogue in-phase and quadrature signals. The phase is computed from the ratio of these two signals so the artifacts of ringing cancel.

There are two general features in this phase profile. As shown in Figure 11.1 the fringe locations usually have peaks in amplitude and a phase signal with relatively constant values (±45°) in the region bounded by the amplitude peak (circled region in the phase plots). Outside of these regions however the phase values have a more complex representation. The most common of these is an increasing signature which is particularly noticeable in the echoes originating from the deeper locations, 60-65ms and 5-8ms (= 105-108ms). The 5-8ms echo return includes the signal from 105-108ms because the system was transmitting every 100ms during this data set. This monostonic increase in phase corresponds to the presence of a changing gradient in the impulse weighting function at these deeper locations. Arrival times $> 55ms$ approximate the properties of a conventional monotstatic echosounder with an impulse weighting function $W(R)$ proportional to $1/R^2$. Section 5.3 demonstrated how only small changes in phase are associated with changes in slope of $W(R)$ (see Figure 5.13(3)).

The profiles in Figure 11.1 represent one realization of a composite set of echoes derived from the superposition of echoes from individual returns. During a set of measurements, the population distribution of scatterers below the

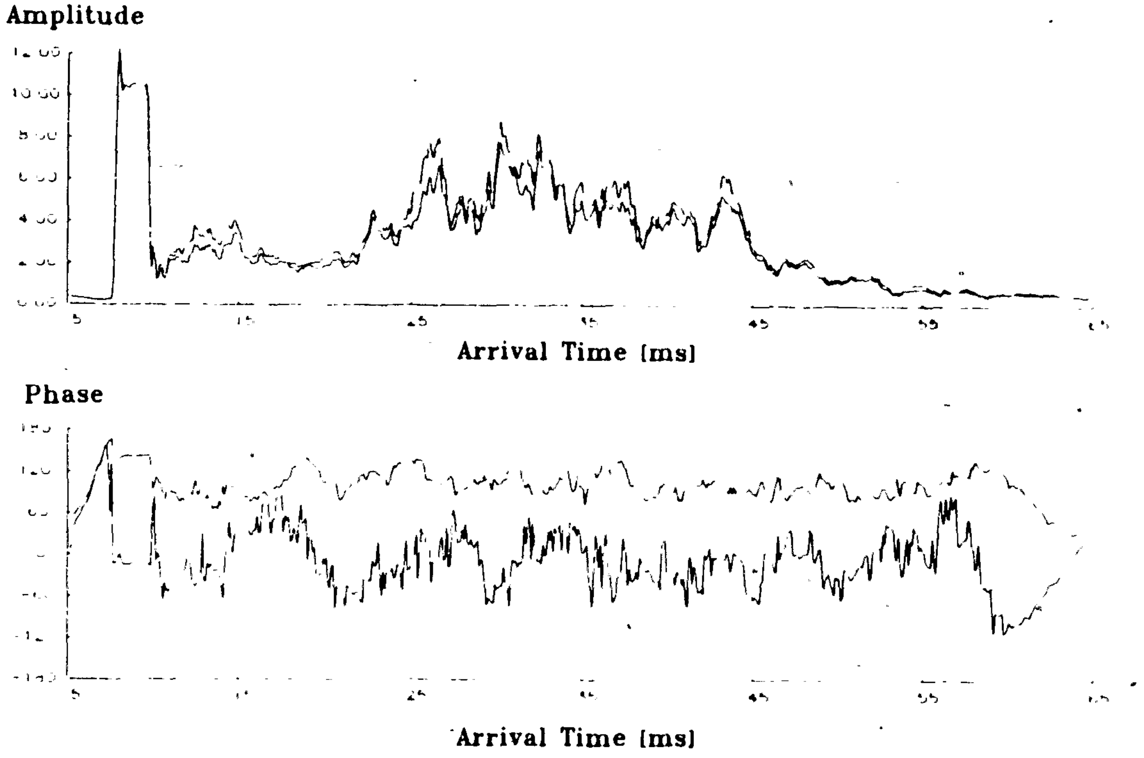

Figure 11.2 Mean amplitude and phase profile (solid line) after averaging 10 consecutive profiles each of which is created by coherently processing 600 echoes (1 minute). The broken line shows the variance profile.

hydrophone may change significantly. Zooplankton are often observed in clouds or patches. This temporal variability is directly observable in consecutive CP amplitude profiles. The height, width and even location of the amplitude peaks can vary significantly. Figure 11.2 shows the resulting mean amplitude profile after 10 realizations are averaged, where each realization represents one minute of CP. The solid line represents the mean amplitude $\langle a(\tau)\rangle$ and the broken line shows the standard deviation $\sigma_a(\tau)$.. Notice how $\sigma_a(\tau) \geq \langle a(\tau)\rangle$ is true throughout the profile. This result demonstrates the sensitivity of CP to the particular scatterer distribution since a new group of CP transmissions produces amplitude and phase profiles which often vary significantly from previous realizations.

The second perspective utilizes time series which show the convergent nature of CP on both the amplitude and phase at a fixed arrival time(τ). Since both Figure 11.1 and 11.2 show an amplitude peak about $\tau = 31$ms this arrival time was selected to investigate the time series behaviour. The following nomenclature will be used for a given τ,

$$\begin{aligned} a_o(t) &= \sqrt{x^2(t) + y^2(t)} \\ a_{\mathrm{CP}}(t) &= \sqrt{(\sum x)^2 + (\sum y)^2} \\ \phi_{\mathrm{CP}}(t) &= \tan^{-1}\left(\frac{\sum y}{\sum x}\right) \end{aligned} \tag{11.1.1}$$

where,

$$\begin{aligned} \sum x &= \sum_{j=1}^{i} x(j\Delta t) \\ \sum y &= \sum_{j=1}^{i} y(j\Delta t) \\ t &= i\Delta t \\ \Delta t &= \text{time between transmissions.} \end{aligned}$$

Figures 11.3a,b,c and d each show the time evolving signals of raw amplitude $a_o(t)$ (no CP), CP amplitude $a_{\mathrm{CP}}(t)$, and CP phase $\phi_{\mathrm{CP}}(t)$ over a 1 minute interval for the τ values 30, 31 and 32ms respectively. The raw amplitude time series demonstrate the stochastic nature of the received signal. It is plotted in relative units where 1.0 represents full scale deflection. Any raw amplitude values ≥ 1 (a clipped signal) were rejected. An example of this is observed in Figures 11.3b and c at t=28ms. Notice that no change occurs to the CP amplitude or CP phase when a signal is rejected. Referring to Figure 11.3a a number of features can be observed. 1) $a_o(t)$ is a noisy times series

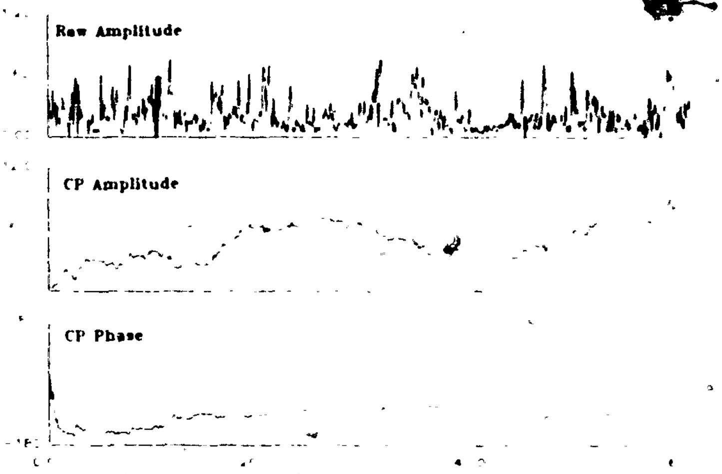

Figure 11.3a Time series of the raw amplitude echo $a(t)$, the coherently processed amplitude $a_{CP}(t)$, and the coherently processed phase $\phi_{CP}(t)$, for the 30.0ms arrival time.

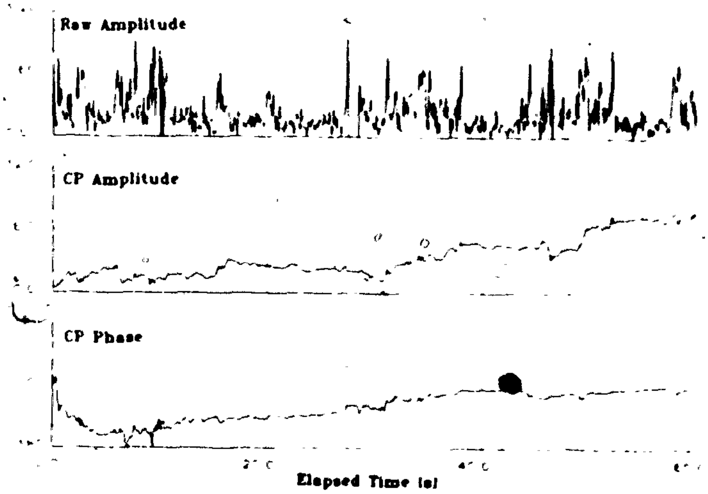

Figure 11.3b Same as Figure 11.3a for the 31.0ms arrival time.

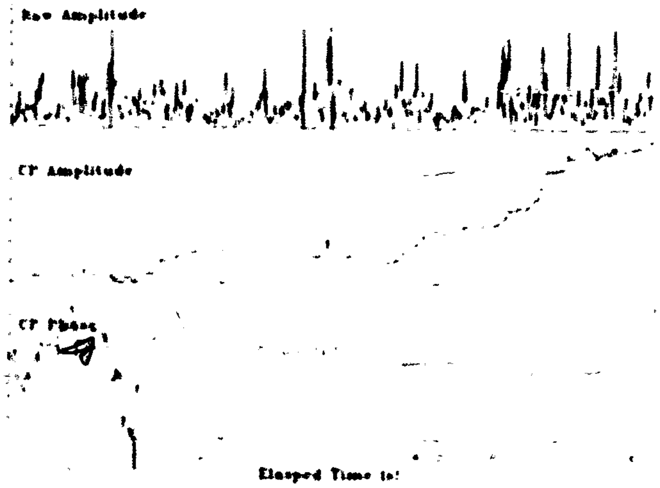

Figure 11.3c Same as Figure 11.3a for the 32.0ms arrival time.

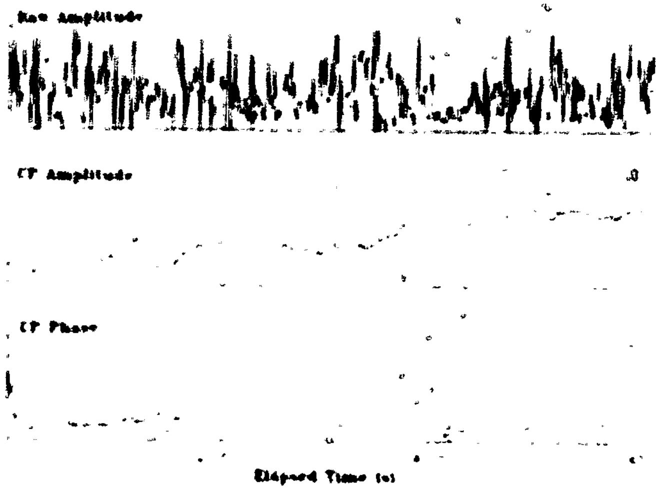

Figure 11.3d Same as Figure 11.3a but removing all echoes with $a(t) \geq 0.5$.

with spikes of various widths and heights. 2) $a_{CP}(t)$ coarsely approximates a linearly increasing signal. 3) $\phi_{CP}(t)$ initially changes significantly and then converges towards a stable value. 4) Large spikes in $a_o(t)$ can cause noticeable perturbations to both $a_{CP}(t)$ and $\phi_{CP}(t)$.

The time series in Figure 11.3b are derived from the $\tau = 31$ms arrival time and have similar characteristics to Figure 11.3a. The raw amplitude profile in Figure 11.3b although similar to Figure 11.3a has a unique high frequency signature. These time series also exibit characteristic features. In particular, the $a_{CP}(t)$ signals have a similar final value at $t \doteq 60$s but take a different path while the $\phi_{CP}(t)$ signals have a similar initial shape and different final value.

The CP time series with $\tau = 32$ms (Figure 11.3c) demonstrates a different result from the previous examples. $a_{CP}(t)$ has a negligible increase in the first 10 seconds and increases quickly in the last 20 seconds. Corresponding effects to the CP phase are also observed. When $a_{CP}(t) \leq 1$ then $\phi_{CP}(t)$ is unstable, but as $a_{CP}(t)$ gets increasingly larger the variance in $\phi_{CP}(t)$ decreases.

The effects of large amplitude spikes on these time series can be demonstrated by reprocessing the data and removing all echoes with $a(t) \geq 0.5$. Figure 11.3d shows the resulting time series with $\tau = 30$ms. In comparing with Figure 11.3a the variance in $a_{CP}(t)$ is greatly reduced and $\phi_{CP}(t)$ is similar in shape but converges to a different phase value.

11.2 Accuracy of coherent processing estimates

The last two figures have demonstrated that the final CP amplitude and phase are subject to fluctuations in their values and accuracy. Since both $a_{CP}(t)$ and $\phi_{CP}(t)$ approximate linear functions in the latter half of the time series (for a fixed arrival time), a linear regression analysis should provide a better estimate of the final values. By using the last 100 points in these time series a linear fit through the data and a measure of the standard error can be found. The in-phase $x(t)$ and quadrature $y(t)$ components of these time series can be fit to linear segments to avoid complications of 2π ambiguities in the phase signal. This leads to final estimates of $\dot{x} \pm \sigma_{\dot{x}}$ and $\dot{y} \pm \sigma_{\dot{y}}$ at t=final time. A simple algorithm can convert the standard errors $(\sigma_{\dot{x}}, \sigma_{\dot{y}})$ into amplitude and phase errors (σ_a, σ_ϕ) by computing the four angles and amplitudes from the error bounds on $\dot{x}$ and $\dot{y}$, and then using their extremal values to estimate σ_a and σ_ϕ.

Although this method is at first intuitively pleasing it does not necessarily provide the best estimate of the final value and its accuracy. CP involves computing cumulative sums. As the number of points in the summation increases the effect of a single term diminishes. The horizontal axis can be transformed into a logarithmic scale in base two to remove this effect. Then when a linear regression is applied it will not be biased to sampling the results of a slowly changing function.

A more precise method for determining CP accuracy is based on statistical principles. The cumulative sums of x and y are numerically equivalent to computing the un-normalized mean values of the x and y distributions, $\bar{x}$ and $\bar{y}$ respectively. When these distributions are Gaussian with standard deviations σ_x and σ_y then estimates of their mean values are also Gaussian distributed variables (Miller,1985) with standard deviations determined by,

$$\begin{aligned} \sigma_{\bar{x}} &= \sigma_x / \sqrt{n} \\ \sigma_{\bar{y}} &= \sigma_y / \sqrt{n} \end{aligned} \tag{11.2.1}$$

where, n=number of terms used to compute the mean. Section 10.3 showed that x and y can have non-Gaussian statistics when all the signals are utilized in computing their distributions. The central limit theorem also applies to non-Gaussian distributions. In practice, the normal distribution provides an excellent approximation to the sampling distribution of the mean for n as small as 25 regardless of the original pdf from which the samples are obtained (Miller,1985,p.175).

Chapter 6 derives the Rician pdf and its associated phase pdf from Gaussian distributed variables. Since $\bar{x}$ and $\bar{y}$ have normal distributions the results of chapter 6 can be applied to the estimation of accuracy of the corresponding amplitude and phase values. The amplitude accuracy is simply represented by,

$$\sigma_a = \sigma_{\bar{x}} + \sigma_{\bar{y}}. \qquad (11.2.2)$$

The phase accuracy requires calculation of the single parameter γ, where,

$$\gamma = \frac{\bar{x}^2 + y^2}{\sigma_{\bar{x}}^2 + \sigma_{\bar{y}}^2}. \qquad (11.2.3)$$

Then by using the empirical equation 6.5.6 the variance of the phase about its mean value can be found directly.

By using this statistical method to determine the accuracy of CP phase time series $\phi_{\mathrm{CP}}(t)$ a more accurate representation of the data is possible. Figure 11.4 shows $\phi_{\mathrm{CP}}(t)$ at $\tau = 26.5\mathrm{ms}$ with the upper and lower error bounds ($\phi + \sigma_\phi$ and $\phi - \sigma_\phi$). Notice that most of these phase estimates can fluctuate by more than 45^o within these error bars. This plot shows a low frequency signal by using a simple algorithm to remove 2π ambiguities. This was accomplished by comparing each new point with a moving average of the previous 3 values. If the difference was greater than $\pm\pi$ then the appropriate $\pm 2\pi$ value was added to the new phase value. The relatively large phase errors, provide a degree of freedom to this time series so that the representation in Figure 11.4

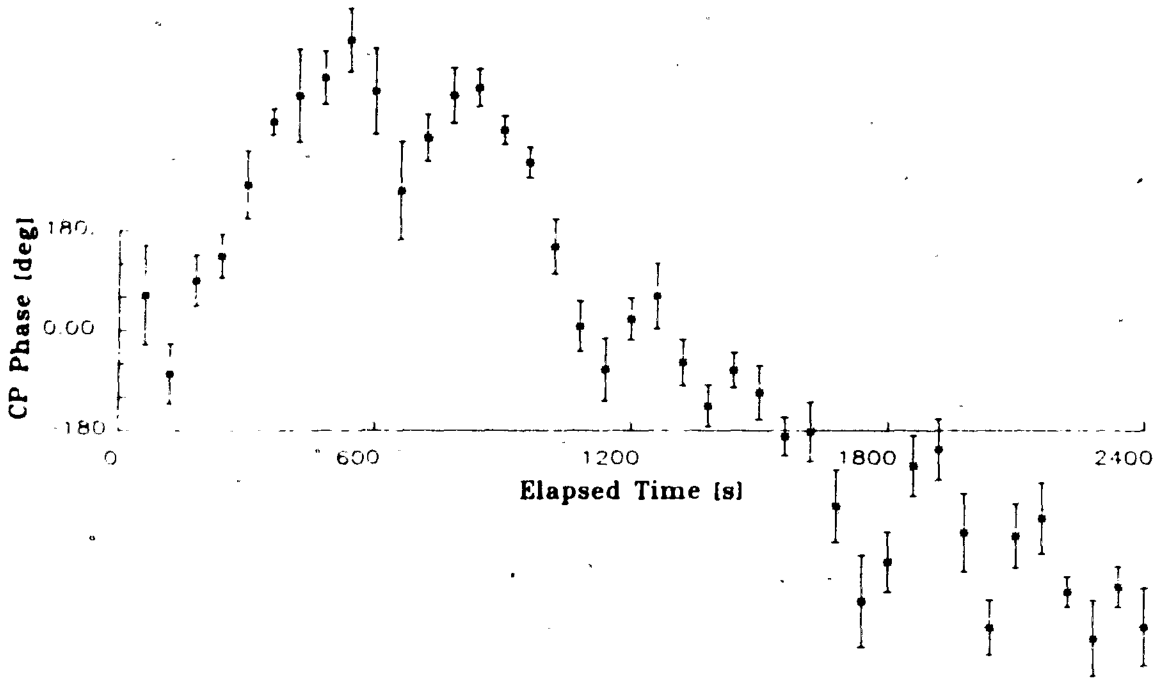

Figure 11.4 Coherently processed phase time series showing the resulting phase values and error bars after processing 600 transmissions with arrival time $\tau = 26.5$ms.

is not the only possible result. For example, if the data point at $\tau = 600$s is shifted to its upper error bound then the next phase value will be shifted up 360^o . This change results in the remaining points also being shifted by 360^o. This demonstrates that the resolution in time is not fine enough and/or the accuracy in phase small enough to provide an unambiguous $\phi_{CP}(t)$ profile.

Consecutive $\phi_{CP}(t)$ plots with 0.1ms increments in arrival time demonstrated a high correlation in their raw phase values. Since a 2ms transmit pulse was used in this data set the 10kHz sampling rate provided redundancy in the received signal. By averaging m adjacent τ values, the system noise can be minimized to provide a more accurate phase estimate. Once again the av-

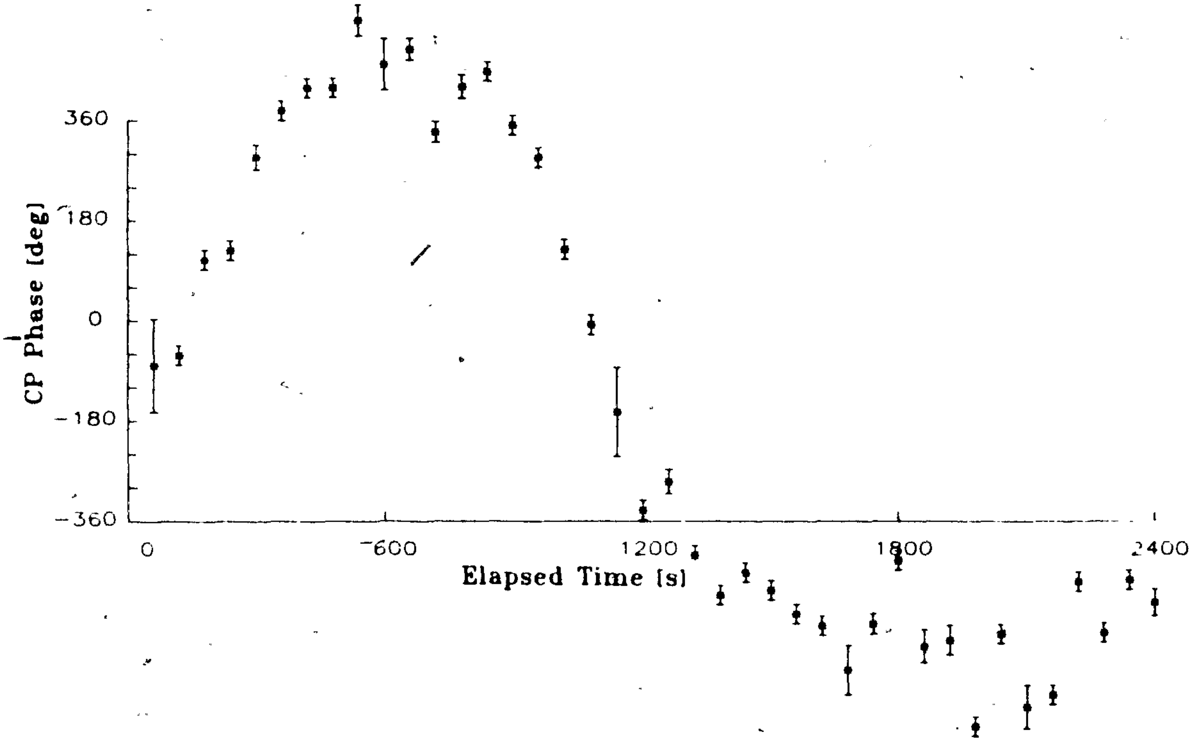

Figure 11.5 Averaging the results from Figure 11.4 over 10 arrival times bounded by $26.5 \leq \tau \leq 26.9$ms (fringe 8).

eraging of phase was accomplished indirectly. In this case however a simple vector averaging would be unpredictably biased by signals with large phase error bars. By including a weighting function proportional to the computed phase accuracy a more reliable estimate of the mean phase can be found. This was accomplished by forming $w(\sigma_\phi)$ where,

$$w(\sigma_\phi) = 1 - \frac{\sigma_\phi}{103.9^\circ}. \tag{11.2.4}$$

(see equation 10.3.2). This will remove the vector components which displayed random phase estimates. The first and second moments of the in-phase components were computed by,

$$\langle x \rangle = \frac{\sum_{i=1}^{m} w(\sigma_\phi) x_i}{\sum_{i=1}^{m} w(\sigma_\phi)} \tag{11.2.5}$$

and,

$$\langle x^2 \rangle = \frac{\sum_{i=1}^{m} w(\sigma_\phi) x_i^2}{\sum_{i=1}^{m} w(\sigma_\phi)}. \qquad (11.2.6)$$

Identical formulae were used for the quadrature components. These first moments were used to compute the mean phase and the accuracy was computed by equations 11.2.3 and 6.5.6. Figure 11.5 shows a $\phi_{\mathrm{CP}}(t)$ time series and its accuracy which results from averaging the processed signals for $26.5 \leq \tau \leq 26.9$ (ms). Notice how the phase error is significantly reduced from Figure 11.4. This average phase time series provides a smoother realization. However, differences in phase up to ±180° between adjacent times also occur which means the given times series representation has other equally probable displays. However, as will be shown subsequently, the phase ambiguity can be reduced significantly by separately smoothing the in-phase and quadrature components; this procedure confirms that Figure 11.5 is a correct representation.

Confirmation of the validity and usefulness of backscatter phase measurements gains support from the results discussed in this chapter, in particular the continuously evolving coherent pattern of phase change. A much sharper test, however can be based on the similarity of statistically independent data sets of backscatter from *identical environmental conditions*. This test is demonstrated in the final section of this chapter and shows that the concept of a volume mirror, capable of coherent reflection from a random and sparse set of acoustic targets, is indeed both valid and workable.

Before a meaningful interpretation of these phase time series can be made the environmental parameters which bias the phase in a single frequency system must be understood. The following sections will study the influence of the heterogeneous nature of the scatterer distribution and target strength distribution.

11.3 Sensitivity of bistatic echoes to the scatterer distribution

The amplitude of the received echo in the bistatic configuration is primarily dependent on the volume backscatter target strength and the transducer beam pattern for a given transmit pulse (i.e. 2ms at 215kHz). This amplitude signal will fluctuate stochastically due to; 1) the heterogeneous scatterer distribution, 2) the anisotropic nature of the reflectivity from individual targets and, 3) the constructive and destructive interference from adjacent scatterers which cause the amplitude statistics to approximate roughly a Rayleigh distribution. In order to better understand the received signal from the bistatic echosounder the echometer projector and hydrophone beam patterns can be used to simulate the ideal case.

The in situ calibration of the projector (section 9.2) verified that a beam pattern close to the theoretical case was being generated during the experiment. The received echoes at the hydrophone will spacially average this beam pattern even for an ideal distribution of isotropic and homogeneous scatterers. The echometer projector and hydrophone beam patterns were first combined by the following method to reconstruct an ideal received amplitude time series. Realizing that the narrow beam hydrophone acts as a spacial low pass filter to the projector beam, this filter can be numerically simulated by averaging adjacent spacial values. Referring to Figure 5.1 for a transmit pulse at initial angle θ from the projector the hydrophone will receive this pulse at $\beta = 0$. Since the hydrophone has a finite beam width other combinations of θ and β will result in a received pulse with the same arrival time. As discussed in chapter 5 these various reflection points define an ellipse. The narrow beam hydrophone ($-0.35^o \geq \beta \geq 0.35^o$) limits this to a small section of the ellipse which to a first order approximation is a straight line. The angle of inclination of this line will be $\theta_o/2$ from the horizontal. From the geometry of this problem the relationship between θ and $\beta \neq 0$ can be found by locating the (x, z) coordinates. The resulting equations are;

$$z = \frac{z_o/\tan(\theta_o/2) + b}{\tan\theta + 1/\tan(\theta_o/2)} \qquad (11.3.1)$$
$$x = z\tan\theta - b$$

where,

$\theta =$ initial projector angle which corresponds to $\beta = 0$.

$b =$ separation between transducers (11.58m in Nov. 85 experiment).

$z_o = b/\tan\theta_o$.

The corresponding β value is simply the arctangent of z/x. The hydrophone beam pattern, when converted from a dB scale is equivalent to an amplitude weighting function $w(\beta)$. The total beam weighting function $P'(\theta)$ of the system can be approximated by finding the weighted average of the projector $P(\theta)$ and hydrophone beams for each initial angle θ over the range of θ values which correspond to $-1^o \leq \beta \leq 1^o$. This was accomplished by computing,

$$P'(\theta) = \frac{\sum_{i=-n}^{n} w(\beta_i)P(\theta_o + i/10)}{\sum_{i=-n}^{n} w(\beta_i)} \qquad (11.3.2)$$

for each initial angle θ_o where n was selected so that the full range of β values were sampled to a 0.1^o resolution in θ_o. For a scaled comparison with actual received echo data the initial angle variable was transformed into arrival time in ms. The resulting profile with normalized amplitude versus arrival time, is shown in Figure 11.6. Notice how subsidiary minima and maxima are only observed in the near surface values (10ms-15ms). The other fringe patterns are increasingly broader and shorter with increasing arrival time than in the original projector pattern. This effect is due to the larger spacial area of the hydrophone beam with increasing depth which causes a larger angular slice of the projector beam to be spacially averaged. This profile also approximates the impulse weighting function of the system for an ideal scatterer continuum.

In Chapter 5 an ideal scatterering continuum was developed and found to produce a phase and amplitude signature which is dependent upon the ratio of the pulse length and width of the impulse weighting function (r_t). For a 3ms pulse length Figure 11.6 shows that all fringe values > 5 will have $r_t \geq 1$. Figure 5.11a shows the echo characteristics for these r_t ranges when the scattering mechanism approximates a continuum that is isotropic and homogeneous with the single scattering approximation also valid. Similarly, echoes from the other deeper fringe locations ($m \leq 5$) will have amplitude and phase profiles which correspond to Figure 5.11c.

The effect of a typical pulse length on the profile in Figure 11.6 can be found by applying a moving average to the profile where length is equal to the pulse length (i.e. 2ms). Interference occurs in volume scatter so it is more appropriate to spacially average the amplitude squared (proportional to energy) in the calculations and take the square root to transform the result back into an amplitude. Figure 11.7 shows the resulting profile for a 2ms pulse. The peaks are broadened and nulls are increased. The center fringes (5 to 8) and nulls (A,B,C) have been labelled (see Figure 11.9) and their amplitude ratios computed, to compare the strength of the fringe representation in these ideal profiles. Table 11.1 gives the resulting ratios for an impulse transmit, a 2ms pulse and a 3ms pulse. As expected the effects of increasing the pulse length on this ratio test becomes less pronounced as the fringe number decreases since the fringe separation increases with decreasing fringe number (increasing fringe depth).

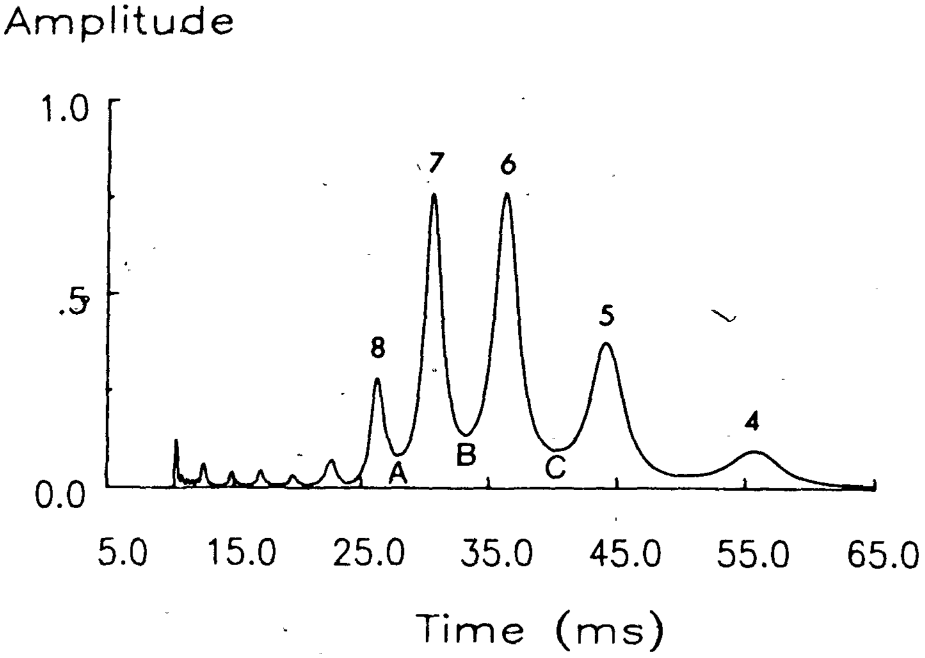

Figure 11.6 A simulation of the ideal received echo amplitude from the bistatic configuration using the calibrated beam patterns from chapter 9.

The mean amplitude profile in Figure 10.2 was collected from a 3ms transmit pulse and the fringe ratios 7/b, 6/b and 5/c for both the mean and rms amplitude were 1.3, 1.6 and 1.3 respectively. These measurements are all approximately 50% lower than their corresponding values in Table 11.1. This discrepancy gives some information about the target strength distribution. For example a cloud of euphausiids will typically have a population length distribution which ranges from 10 to 22 mm. Target strength measurements on individuals (Greenlaw,1977) show a linear relationship with length. Subgroups of the scatterer population with similar target strengths must be uniformly distributed to reconstruct the ideal profile in Figure 11.7. Therefore the amount

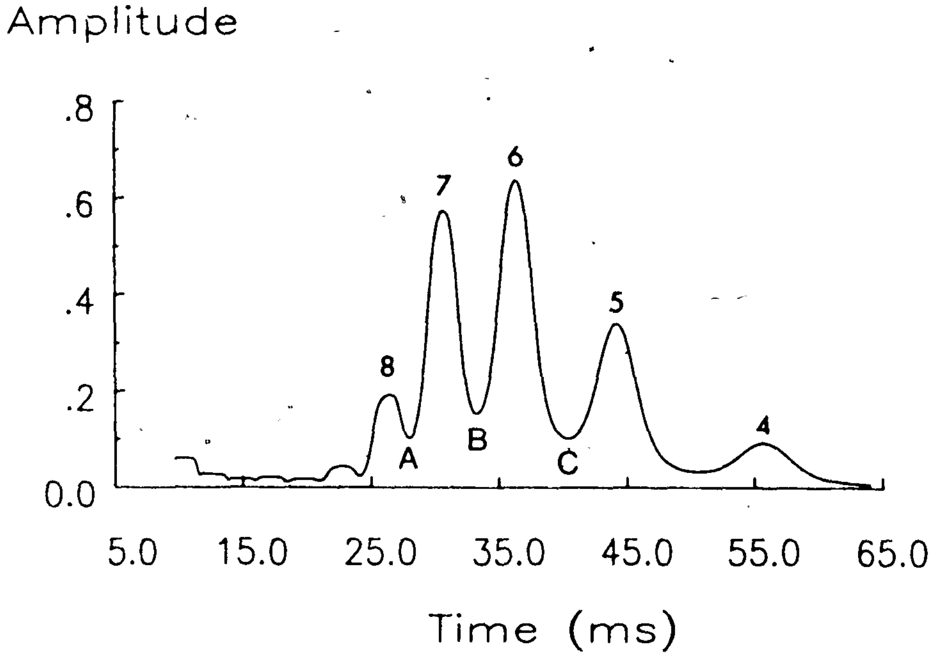

Figure 11.7 Applying a 2ms moving average to the ideal amplitude echo in Figure 11.6.

that the fringe ratios deviate from their theoretical values gives an indication of target strength distribution. In addition the deviations in the mean amplitude between fringe locations correlates with the variations in the volume backscatter at corresponding depth locations.

During the November 1985 experiment a variety of data sets were collected which alternately measured the echoes from the bistatic configuration and those from the 200kHz monostatic echosounder. When operating in this mode the echosounder provided the transmit trigger to keep both systems in synchronization. This constraint fixed the trigger repetition time at 274ms so the sampling rate for each profile was 1.82Hz. Snell's law was utilized in

Table 11.1 Ratios of fringe peak and nulls for an impulse signal, a 2ms pulse and a 3ms pulse.

Fringe /Null	Impulse	2ms	3ms
8/A	3.1	1.8	1.2
7/B	5.5	3.7	2.7
6/B	5.5	4.0	3.1
5/C	3.8	3.3	2.9

scaling the echosounder arrival time to fit the bistatic system. By using the method outlined in section 12.1 the bistatic and monostatic arrival times were computed for a set of initial fringe angles. A fourth order polynomial was fit to the data using the least squares method to provide the required scaling factor between the two systems. The resulting equation is,

$$\tau = 1.540 \times 10^{-6}\tau_m^4 - 2.458 \times 10^{-4}\tau_m^3 + 1.523 \times 10^{-2}\tau_m^2 + 0.529\tau_m + 7.73 \quad (11.3.3)$$

with τ_m representing the monostatic arrival time and τ accurate to ±0.01ms.

A survey of various scatterer distributions as represented by the monostatic echo and the bistatic echo in terms of mean and rms amplitude for the first 1000 transmissions is presented in Figure 11.8 to 11.11. These plots demonstrate the variable nature of the volume backscatter distribution and how it influences the amplitude returns in the bistatic system. All of these data sets were collected with the same transmit power and pulse lengths.

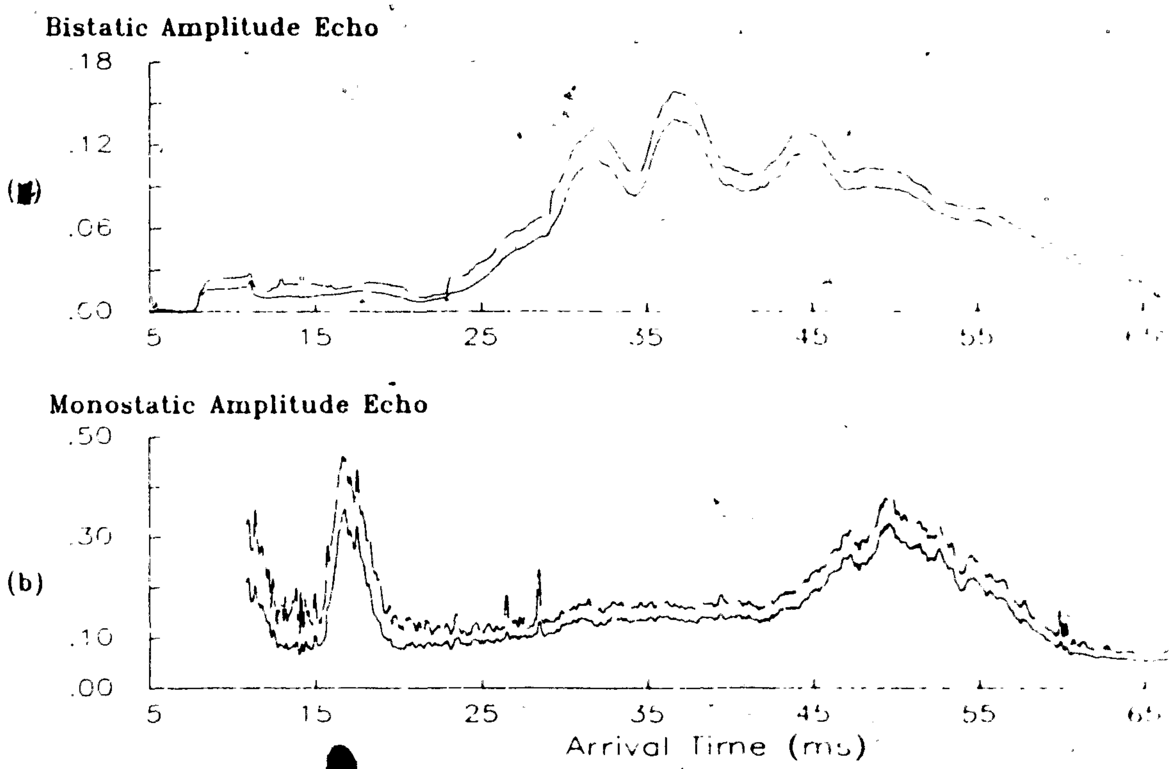

Figure 11.8 Mean and rms relative amplitude echoes for both the bistatic (a) and monostatic (b) configuration using the 1st 1000 received echoes. Data collected on November 21, 1985 at 21:27 hours (E85-37:1).

Figure 11.8 shows the mean and rms relative amplitude profiles for both echosounder systems based on their first 1000 transmissions. The three fringe locations in Figure 11.8a are well defined by both the mean and rms amplitude of the bistatic echo and are centered about 31.8ms, 37.3ms and 45.0ms, which correspond to fringe numbers 7,6 and 5 respectively. These data were collected on November 21.1985 at 21:27 hours. These fringe patterns are representative of the best peak definitions observed during the November 1985 cruise. The corresponding monostatic echosounding is displayed in Figure 11.8b. Notice that the mean and rms relative amplitude approximate constant values for $30 \leq \tau \leq 45$ which is the region with good fringe definition in Figure

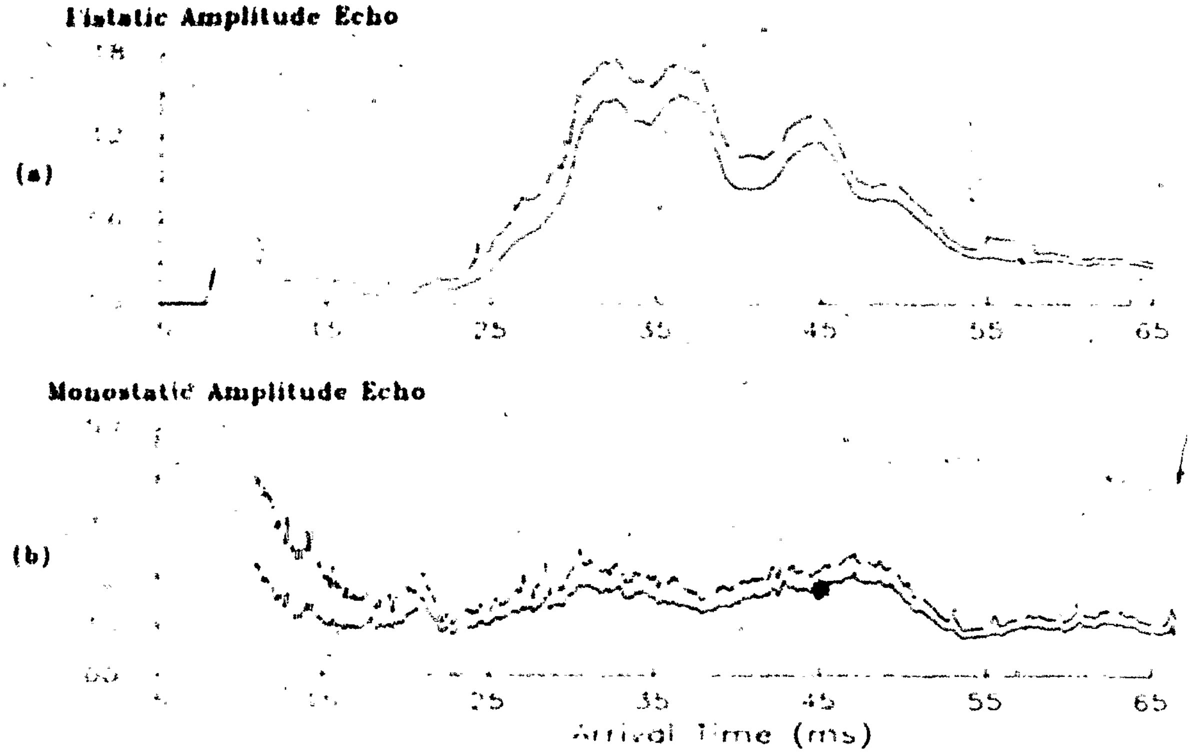

Figure 11.9 Mean and rms relative amplitude echoes for both the bistatic (a) and monostatic (b) configuration using the 1st 1000 received echoes. Data collected on November 21, 1985 at 18:41 hours (E85-36:1).

11.8a. Large scale features in Figure 11.8b, such as the peak between 45ms and 60ms, can also be seen in the bistatic echoes when they occur in locations with dominant insonification from the echometer projector. Comparing Figure 11.8a and 11.9a the fringes about 36ms and 45ms are essentially the same and the echosounder amplitudes have similar amplitude values at these locations. The fringe about 31.5ms undergoes a noticeable increase in the latter Figure which correlates with an increase in the echosounder amplitude. Figure 11.10a shows a much weaker echo profile relative to the previous two Figures with peak mean amplitudes reduced by approximately 1/3. Notice that the monostatic echoes between 30 and 43ms for Figures 11.8b, 11.9b and 11.10b are very

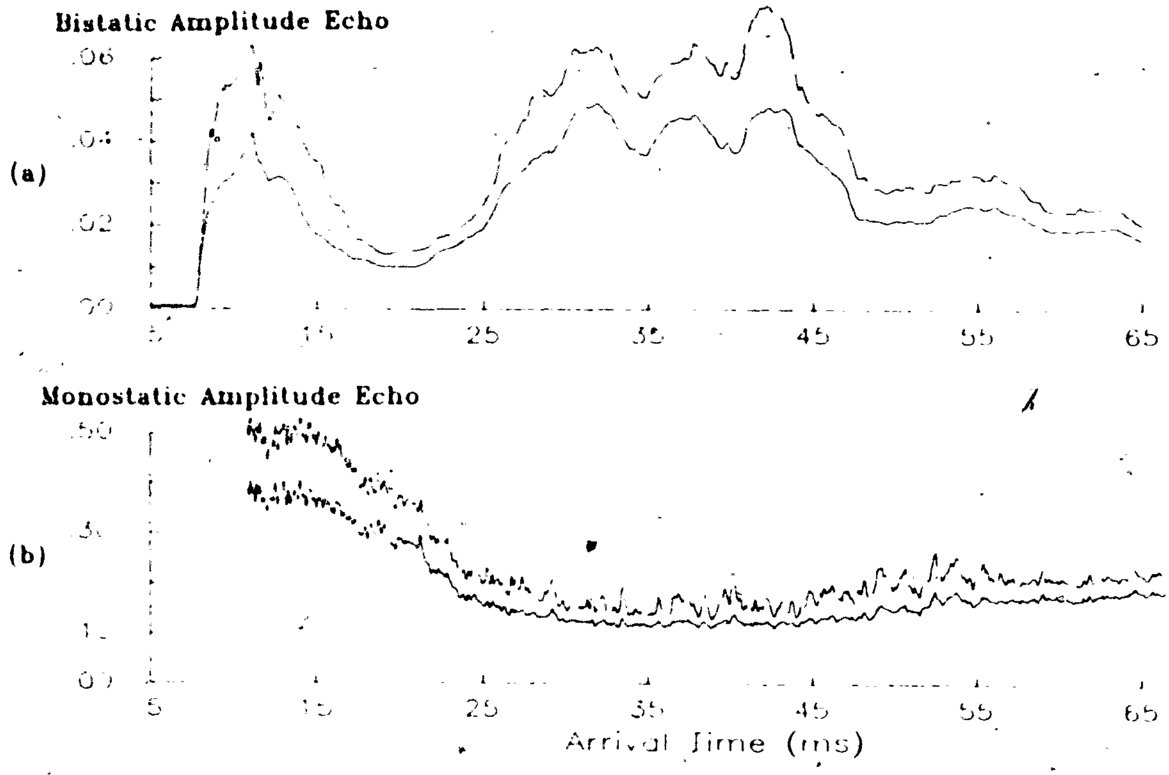

Figure 11.10 Mean and rms relative amplitude echoes for both the bistatic (a) and monostatic (b) configuration using the 1st 1000 received echoes. Data collected on November 20, 1985 at 18:19 hours (E85-22:1).

similar. A false fringe about 43ms is observed for no apparent reason in Figure 11.10a. The increased noise in the corresponding rms echosounder amplitude (Figure 11.10b) indicates that these discrepancies are caused by spatial variations in the scatterer distribution which may be caused by the presence of fish feeding on the zooplankton.

Another anomalous set of results are displayed in Figure 11.11. Comparing the signals between 30ms and 37ms, the echosounder mean amplitude has increased approximately 25% in Figure 11.10a from the previous examples (note the change in relative amplitude scale) while the corresponding echosounder rms amplitude is approximately 50% larger. In addition, both of these signals

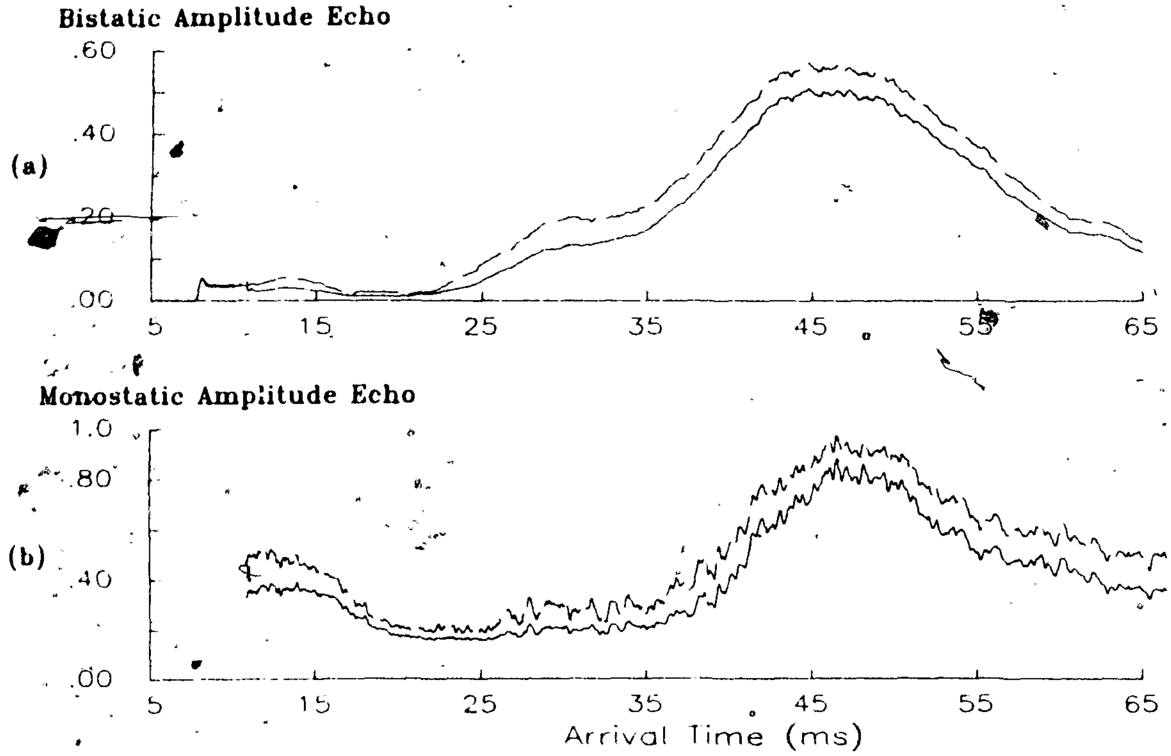

Figure 11.11 Mean and rms relative amplitude echoes for both the bistatic (a) and monostatic (b) configuration using the 1st 1000 received echoes. Data collected on November 21, 1985 at 03:21 hours (E85-35:1).

have a much larger spatial noise than the previous three Figures. The corresponding bistatic amplitude signals (notice the change in amplitude scale) in Figure 11.11a, have no distinct fringe resolutions. This indicates that on the average the stronger scatterers occurred in the side lobe region of the projector and hydrophone beam patterns (i.e. 35ms) rather than at the fringe peak. Notice the broad peak at 47ms in Figure 11.11a is strongly correlated with the echosounder mean amplitude signal in Figure 11.11b. These last two Figures have demonstrated some of the anomalous echoes observed in situ with the bistatic system. The short pulse length of the echosounder (0.3ms) shows the spatial variability of the scattering volume. These examples show qualitatively

Monostatic Echogram

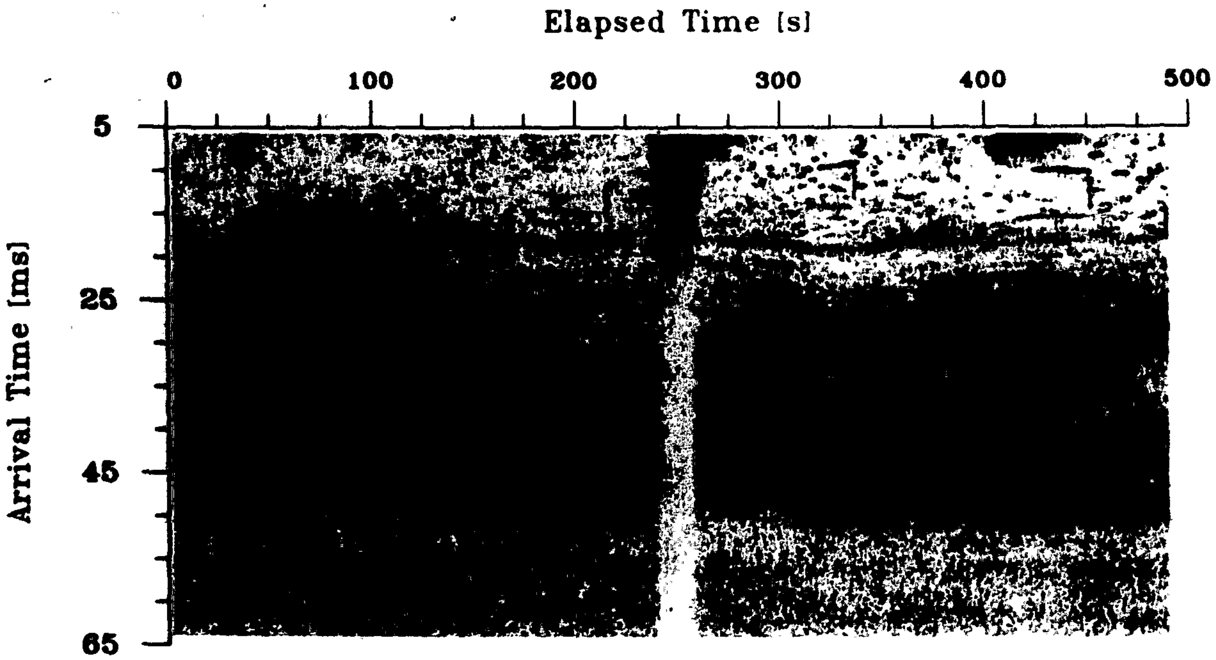

Bistatic Echogram

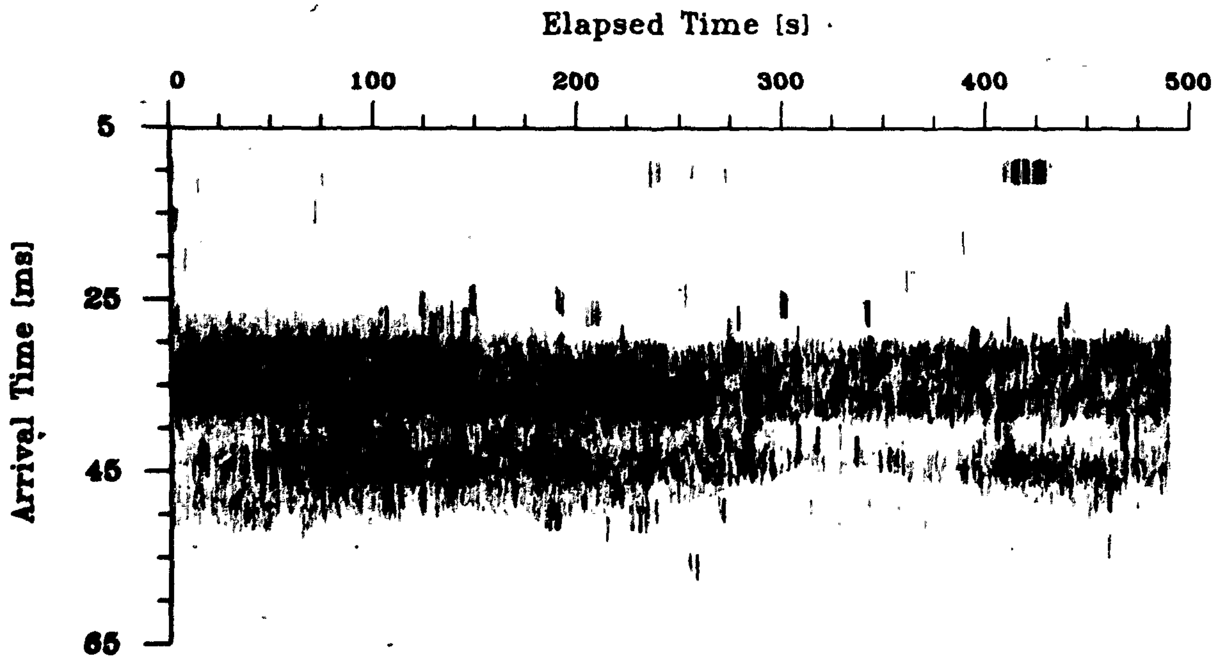

Figure 11.12a Echograms of the bistatic and monostatic amplitudes. Data collected on November 21, 1985 at 21:27 hours (E85-37:1). This data set was also used in Figure 11.8.

Monostatic Echogram

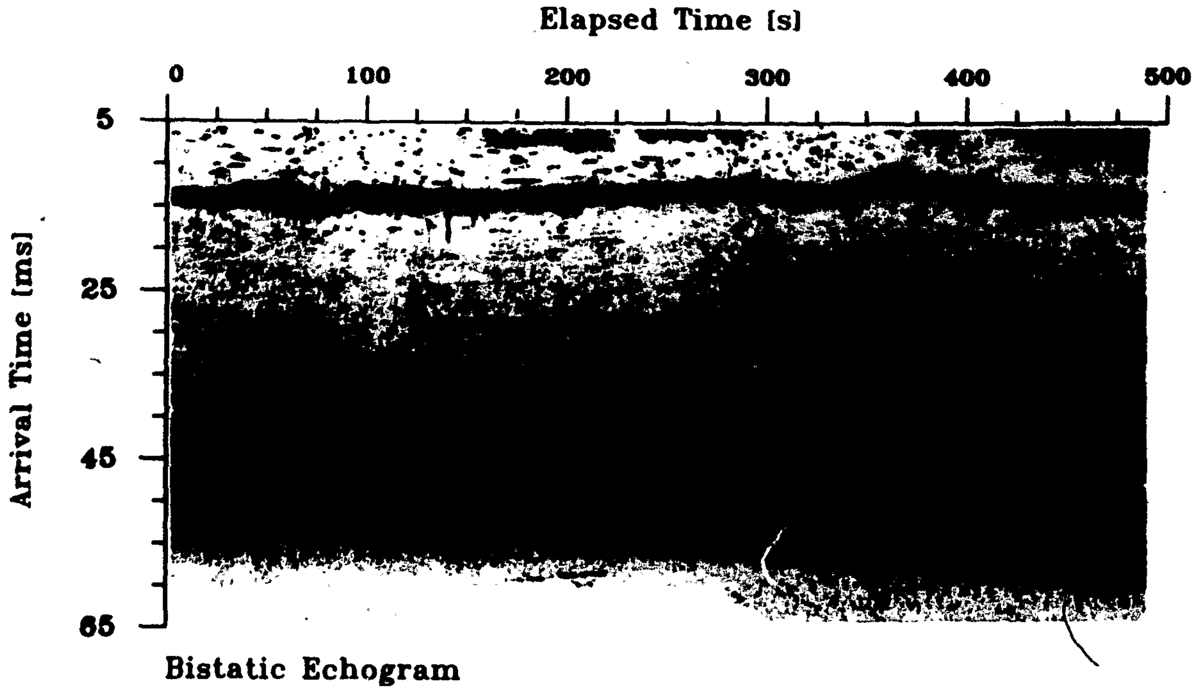

Bistatic Echogram

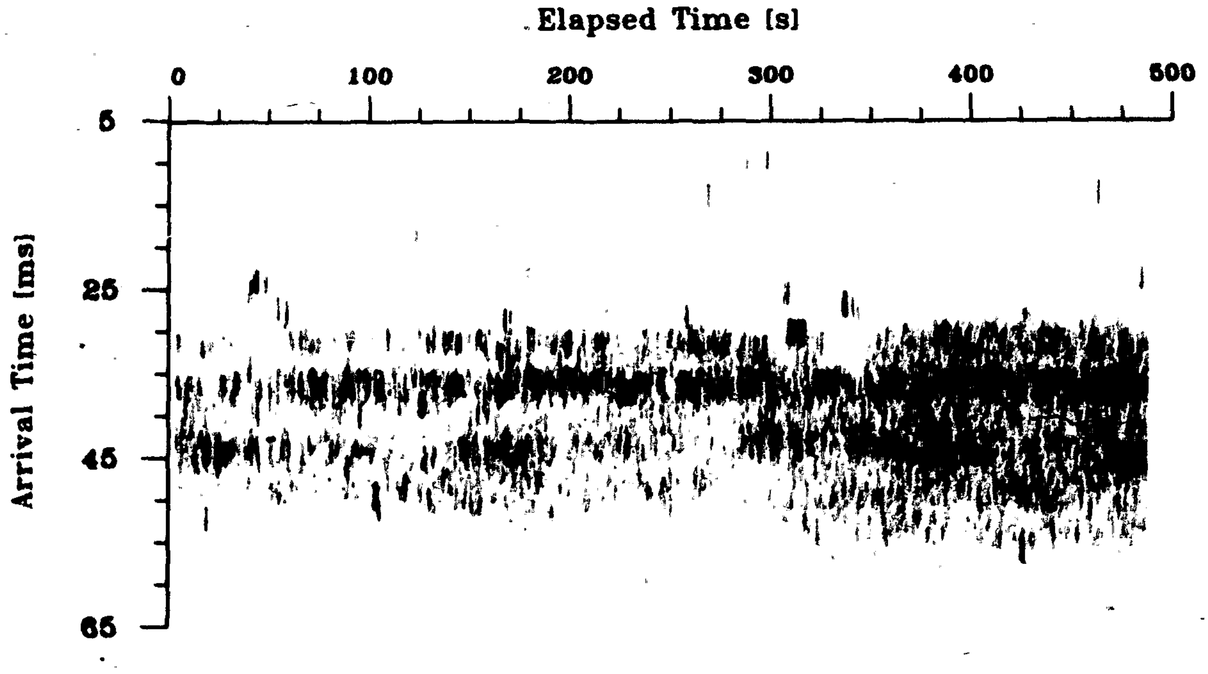

Figure 11.12b Echograms of the bistatic and monostatic amplitudes. Data collected on November 21, 1985 at 18:41 hours (E85-36:1). This data was also used in Figure 11.9.

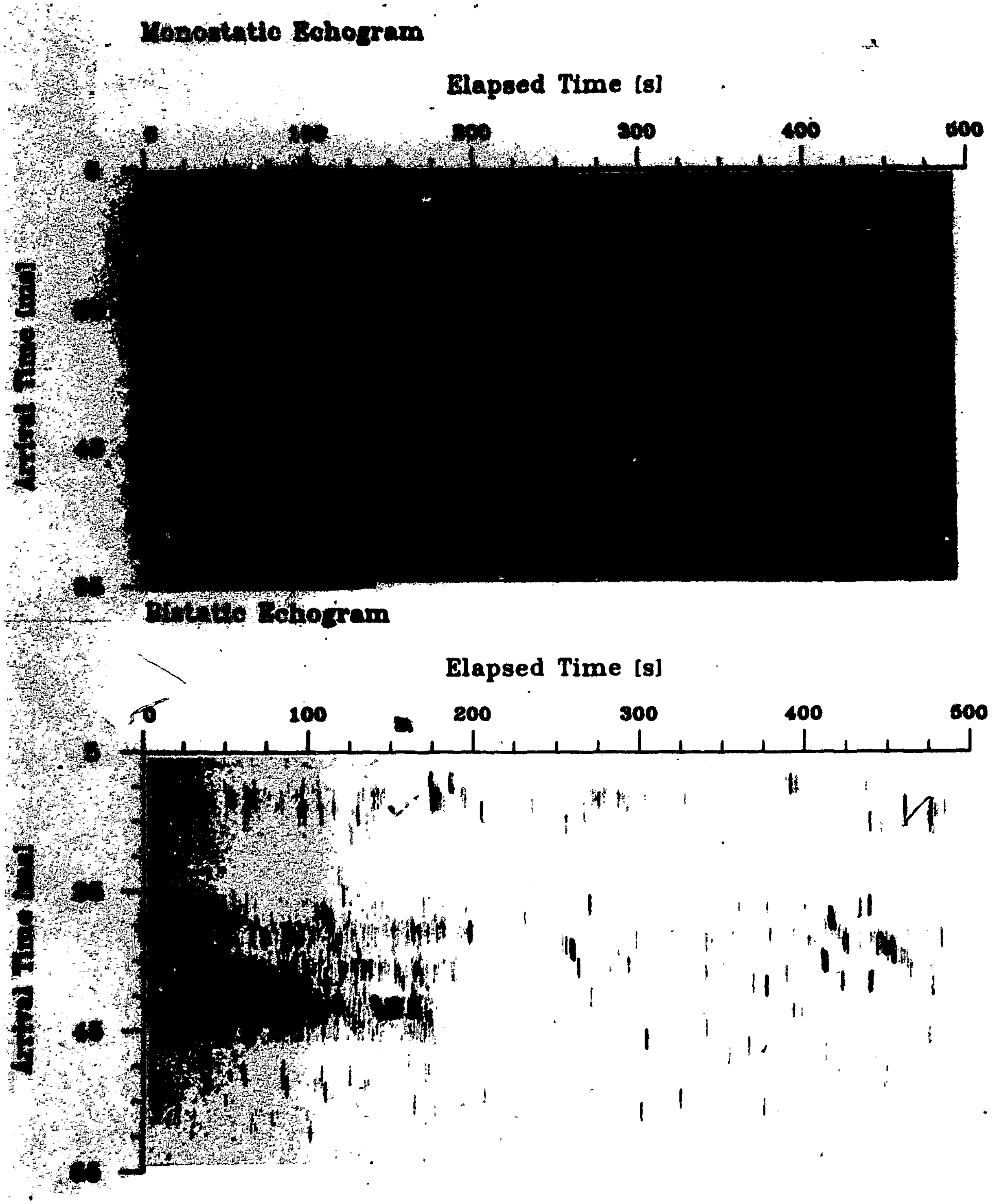

Figure 11.12c Echograms of the bistatic and monostatic amplitudes for Data collected on November 20, 1985 at 18:19 hours (E85-22:1). This data was also used in Figure 11.10. Floodlights turned on after an elasped time of 250s.

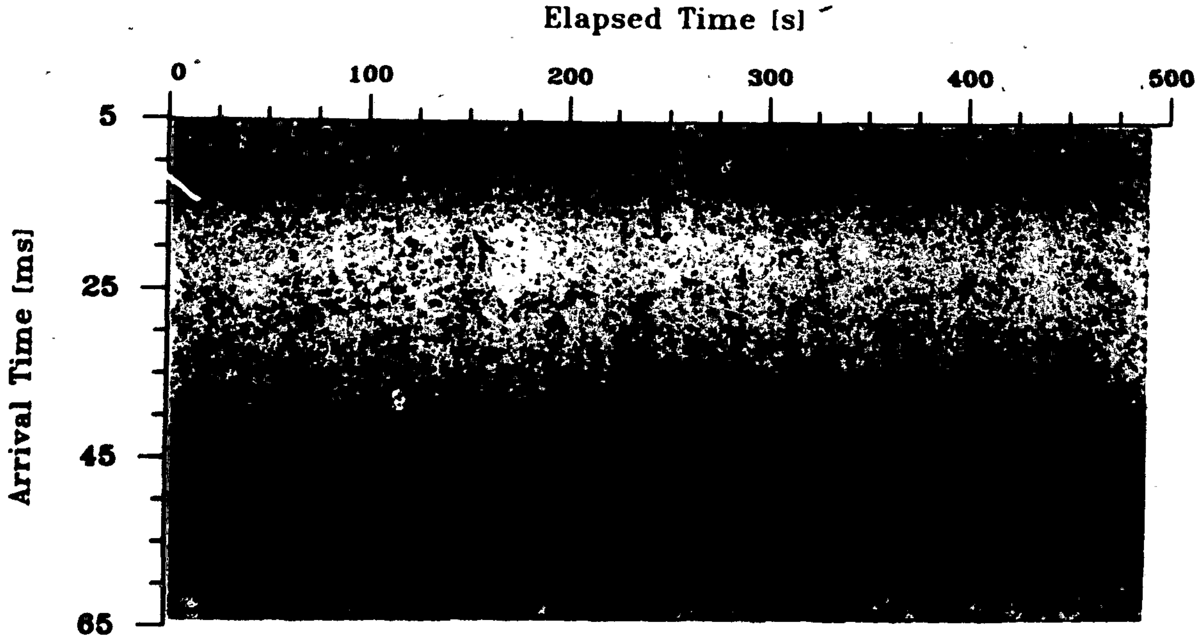

Monostatic Echogram

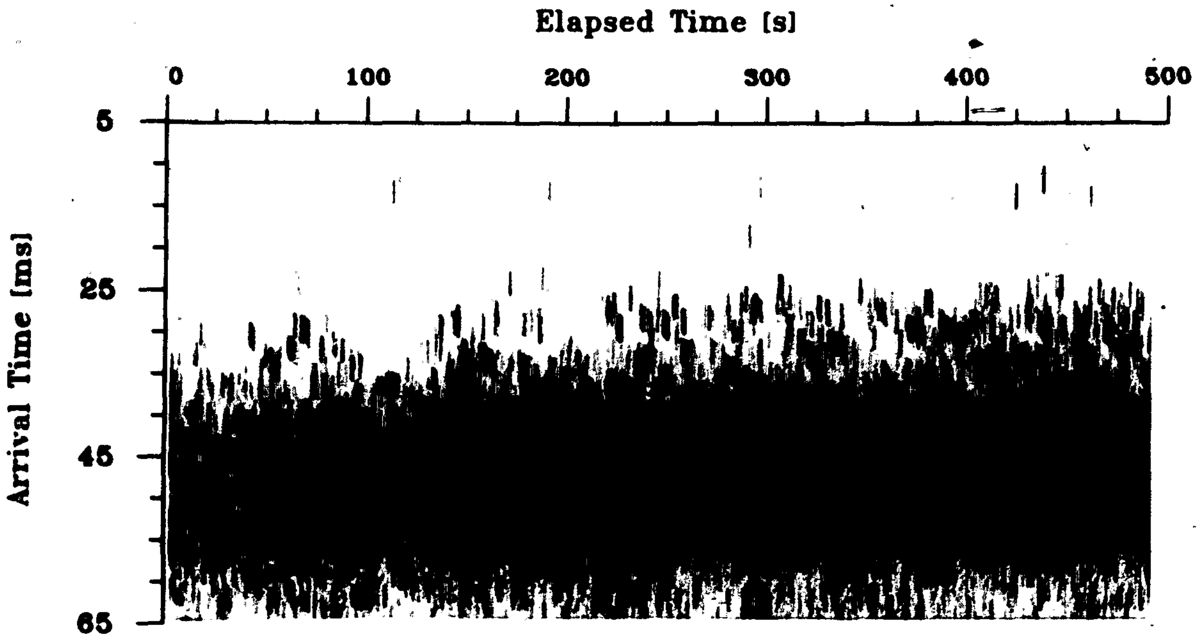

Bistatic Echogram

Figure 11.12d Echograms of the bistatic and monostatic amplitudes for Data collected on November 21, 1985 at 03:21 hours (E85-35:1). This data was also used in Figure 11.11.

that the bistatic fringe pattern has poorer resolution when the echosounder has a larger spacial noise component which is equivalent to saying the scatterer distribution is more heterogeneous.

Gradients have been observed in these monostatic mean amplitude echoes. In chapter 5 it was observed that vertical gradients in the scatterer distribution up to $500s^{-1}$ only have a negligible effect on most of the phase signature from a scattering continuum (see Figure 5.13(1) and 5.13(3)). The monostatic echoes in Figures 11.8 to 11.11 can be taken as a representation of the effective vertical gradients in the scatterer distribution. Figures 11.8b and 11.11b represent the largest gradients of approximately $100s^{-1}$ in the mid-fringe locations ($8 \leq m \leq 5$). Figure 5.13(2) shows that a maximum phase difference of only 10^o may occur in the middle region of the received fringe echo for these observed gradients. Thus, in situ gradients in the scatterer distribution will have a negligible affect on the coherently processed phase estimates.

A second perspective on the variability of the scatterer distribution is shown in Figures 11.12a,b,c and d. These plots display the echo amplitudes on a gray scale with arrival time versus elapsed time for both the monostatic and bistatic case and correspond to the data used to compute Figures 11.8 to 11.11 respectively. The presence of large single scatterers such as fish can be identified by solid dots or short line segments in the monostatic echogram. Notice the speckle pattern in the monostatic echoes. These correspond to regions of Rayleigh scattering statistics where the scatterer range separations are less than the transmit pulse length and greater than the acoustic wavelength. These regions have the zooplankton as the dominant scattering population.

The bistatic echogram in Figure 11.12a shows 3 parallel bands at fixed arrival time locations which correspond with the expected fringe locations. The echo contributions from larger scatterers such as salmon or hake cause a random arrangement of pulses throughout the echogram. Removal of these contaminating echoes is a first order correction. The bistatic echogram in Figure 11.12b presents a similar banded structure for a completely different scatterer distribution as seen in the associated monostatic echogram. The dark banding at 15ms (arrival time) in the monostatic echogram likely corresponds to the thermocline which also represents a sharp change in density. In Figure 11.12c a transition occurs after an elapse time of 250s. The band fringe structures become negligible and the relative monostatic amplitude is reduced appreciably. This event corresponds to a rear flood light being turned on and illuminating the surface of the water above the transducers. The photosensitive zooplankton respond by changing to a vertical orientation and the effective target strength is reduced. This phenomenon has been previously documented by Sameoto et.al.(1985) and confirms that the dense scattering clouds are primarily euphausiids. Notice that the fish become more active after this event (the dots become line segments).

Figure 11.12d represents echoes from a different scattering population. The monostatic echoes are representative of a school of fish – perhaps herring. The individual points are observed which are stronger than the zooplankton and initially devoid of speckle patterns. Line segments are also observed within the group of scatterers which corresponds with active directional swimming. The bistatic echogram for this scatterer distribution is contaminated by strong scatterers in the side lobe regions and has no resemblance to the fringe patterns observed previously.

This section has demonstrated some of the variations in echo structures which can occur in the ocean for both monostatic and bistatic echosounders.

A remote acoustic device which relies on the properties of specific biological scatterers must also be able to assess data quality and reject bad data.

11.4 Confirmation of the validity of the volume mirror concept

Previous estimates of the CP phase and its accuracy from a specific range gate have implicitly assumed stationarity of the sound speed profile over the length of the CP interval. However, a crucial test of meaningful phase measurements requires the comparison of independent data sets, subject to essentially identical refractive conditions. If it were possible to use two separate but adjacent instruments, probing the same sound speed structure and using similar but statistically independent scatterers, then convergence of the resulting phase estimates with successively greater periods of coherent summation would provide convincing evidence of the validity of the volume mirror concept. Such a test is possible through the use of interleaved data sets. The two data sets are derived by coherently processing the even and odd transmission numbers separately. The statistical independence of adjacent echo profiles has already been demonstrated (Chapter 10). Convergence of phase estimates, from the two independent and interleaved data sets, to a similar phase value provides the decisive test of validity that is needed.

This method provides two interleaved data sets which are subject to the same environmental conditions. For an ideal case (isotropic and homogeneous scatterer distribution) the resulting phase difference will be zero. In typical oceanographic situations fluctuations in the volume scattering distribution will cause the observed phase difference $\Delta\phi_{CP}$ to be distributed about zero. By using the rms value of $\Delta\phi_{CP}$ to verify the overall concept, it also provides a basis for determining the accuracy of phase measurement, the location within the fringe distribution of reliable phase data, and the optimum length of data to use in each coherent summation.

The computation of the rms phase difference (rms $\Delta\phi_{CP}$) from a specific arrival time or range gate can be expressed mathematically as,

$$\text{rms } \Delta\phi_{CP} = \sqrt{\frac{1}{M}\sum_{j=1}^{M}\left[\tan^{-1}\left(\frac{\sum_{i=k}^{2jN} Y_{2i-1}}{\sum_{i=k}^{2jN} X_{2i-1}}\right) - \tan^{-1}\left(\frac{\sum_{i=k}^{2jN} Y_{2i}}{\sum_{i=k}^{2jN} X_{2i}}\right)\right]^2} \qquad (11.4.1)$$

where,

N = number of coherently processed transmissions.

$k = 2N(j-1)+1$.

$2MN$ = total number of transmissions.

X_n = nth in-phase components at arrival time τ.

Y_n = nth quadrature components at arrival time τ.

The 24,000 transmissions in the November 13, 1985 data set provided a good basis for applying this method. By dividing the data into subsets where lengths are factors of 24,000 a variety of rms $\Delta\phi_{CP}$ computations were possible. Subsets with lengths of 300, 600, 1200, 2000, 2400, 3000 and 4800 were chosen which resulted in 80, 40, 20, 12, 10, 8, and 5 estimates for computing rms $\Delta\phi_{CP}$ respectively at each range gate. In this way comparisons between the effects of increasing the processing lengths within the same data set are possible.

Figure 11.13 displays the results of these computations for arrival times 26.3ms to 27.0ms. Notice the characteristic decrease in rms $\Delta\phi_{CP}$ with increasing processing length for arrival times 26.5ms to 26.8ms. Only the arrival times in close proximity to the fringe center give meaningful phase estimates. The other arrival time values outside the fringe center tend to be grouped above rms $\Delta\phi_{CP}$ = 100°. The rms $\Delta\phi_{CP}$ estimates at 2N=4800 have the largest

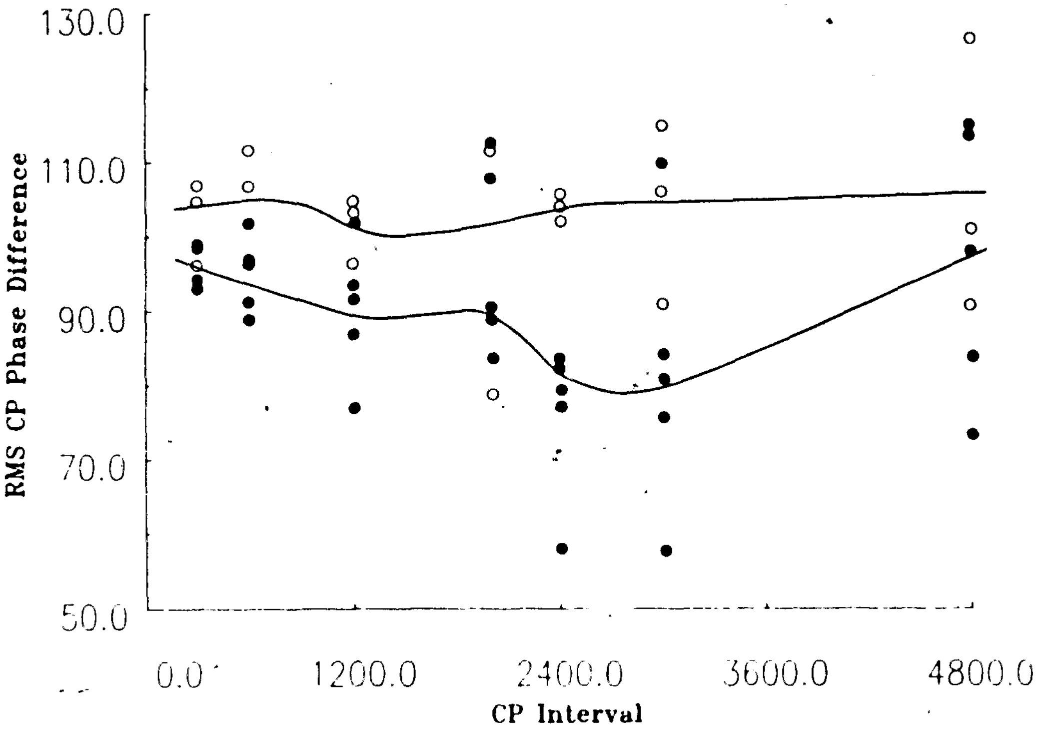

Figure 11.13 Root-mean-square CP phase difference (rms$\Delta\phi_{CP}$) versus number of terms in CP for $26.3 \leq \tau \leq 27.0$ms using the E85-13:1 data set. The solid dots correspond to $26.5 \leq \tau \leq 26.9$ms (fringe 8) and the solid line represents the mean value. Similarly the upper solid line represents the mean value through the outer fringe locations (26.3, 26.4 and 27.0ms) which are represented by circles.

mean phase error values and cover a larger dynamic range than the other 2N values. Since only 5 points were used in these calculations less confidence can be placed on their accuracy. The deviation of this group from a decreasing trend in rms $\Delta\phi_{CP}$ is likely caused by large scale fluctuations in the scatterer distributions. For example, if a group of fish or a school of small fish passes through the system every 3600 transmissions and has a time scale of 600 transmissions then the 2N=4800 processing interval will include an associated random-phase bias. Shorter 2N values will also be biased in their phase values but these effects will be averaged out by subsequent normal phase estimates. CP relies on increasing both the effective scatterer population density and its homogeneity. Both of these conditions are necessary for stable phase estimates. Therefore if the rms $\Delta\phi_{CP}$ value increases with increasing values of 2N then the simulated scatterer distribution is becoming more heterogeneous.

In addition to fringe 8, results for which are shown in Figure 11.13, a decreasing rms $\Delta\phi_{CP}$ with increasing sample number up to $2N = 1200$ was also found for fringe 5. On the other hand, fringes 6 and 7 showed no such decreases. Reasons for this include low scatterer densities and the presence of fish in the sidelobe regions of the acoustic beams.

These results show that calculation of rms $\Delta\phi_{CP}$ provides a simple test of data quality. Only data sets showing consistent convergence should be used for subsequent phase calculations. Moreover the convergence behaviour indicates the optimum number of samples over which to sum. In any practical measuring scheme these tests would be carried out automatically and used to screen the data and determine the length of the coherent summation.

Phase accuracy can also be derived from the rms $\Delta\phi_{CP}$ values. For example, from Figure 11.13 at 2N=1200 the rms $\Delta\phi_{CP} \sim 90^\circ$. Since this value is derived from 2 data sets, $\phi_{CP}(t)$ can be computed to an accuracy of $\pm 45^\circ$ over the interval $\tau = 26.5 - 26.9$ms. Thus for this data set the phase quadrant is bounded, and the phase estimate can be used for interferometric measurements.

A much clearer example was obtained on November 21, 1985 (data set E85-37:1). In this case the scatterer distribution was centered around three principle fringes (5,6,7) (see Figure 11.8) for which the projector array was optimally set. The scatterer distribution was relatively even during this data

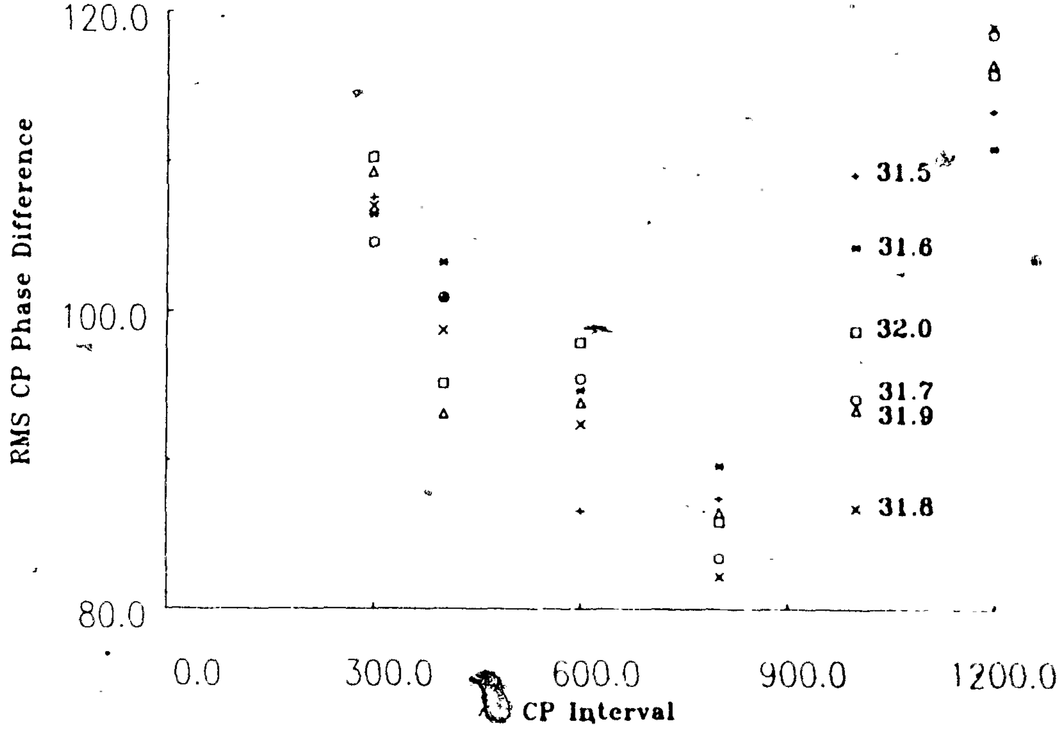

Figure 11.14a Same as Figure 11.13 but using data set E85-37:1 and looking at arrival times corresponding to fringe 7.

set and the fringes also showed up clearly in the corresponding facsimile image (Figure 11.12a).

The rms $\Delta\phi_{CP}$ versus CP interval for the E85-37:1 data set is given in Figures 11.14a, b, and c for arrival time ranges corresponding with fringes 7, 6 and 5 respectively. At fringe 7 (Figure 11.14a), for which the impulse weighting function has a large amplitude (Figure 11.7), the decline in rms $\Delta\phi_{CP}$ is especially clear and spread over a fringe width of $\tau = 31.5 - 32.0$ms. At an interval of 800 samples the coherently processed rms phase difference has dropped to 85°, yielding an accuracy bound for the $2N$ data set of ±42.5° which again allows unambiguous resolution to within a quadrant in practical

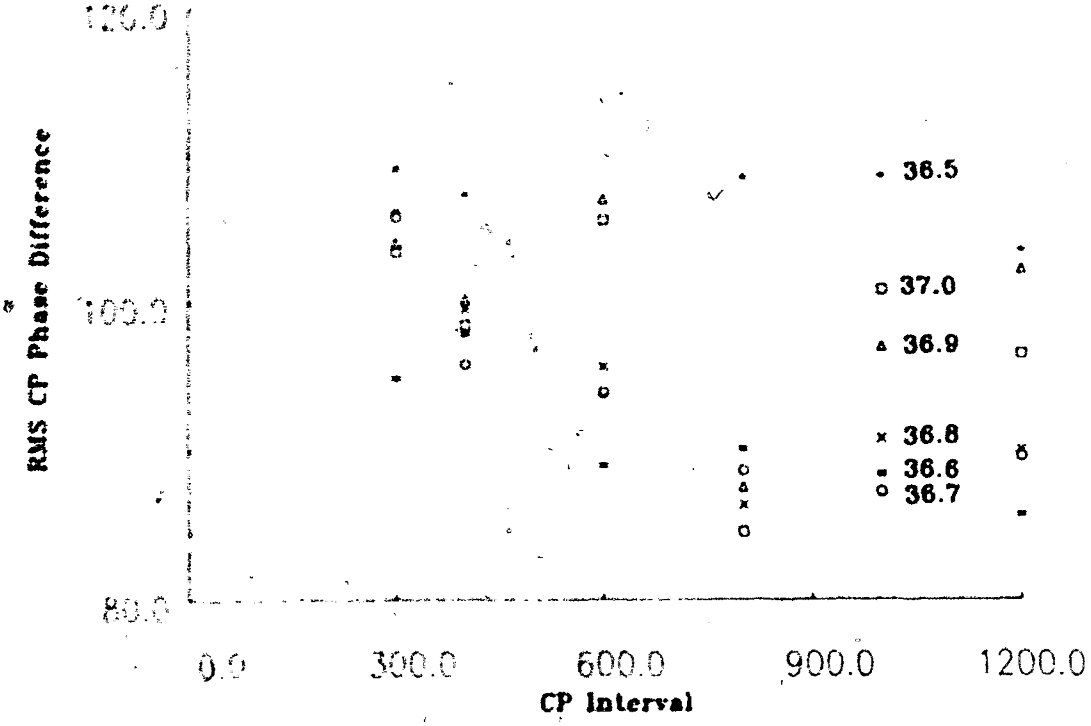

Figure 11.14b Same as Figure 11.14a using data set E85-37:1 and looking at arrival times corresponding to fringe 6. Only points lying close to the fringe center (i.e. $\tau = 36.6 - 37.0$ms) indicate a consistent decrease in rms$\Delta\phi_{CP}$.

interferometric measurements. Results of fringes 5 and 6 are similar, although the useful fringe width is slightly less and the minimum rms $\Delta\phi_{CP}$ occurs somewhat earlier ($\approx$ 600 for fringe 5). Note a phase accuracy of $\pm 42.5°$ has a corresponding coherent to incoherent ratio of $\gamma = 1.4$ which can be derived from Figure 6.5.

The significance of these results is that they provide decisive evidence that it is possible to acquire meaningful absolute phase measurements from volume backscatter in the ocean. Convergence of phase estimates from the interleaved (and independent) data sets is consistent with a progressive increase in the coherent portion of the scatterer distribution as discussed in the numerical

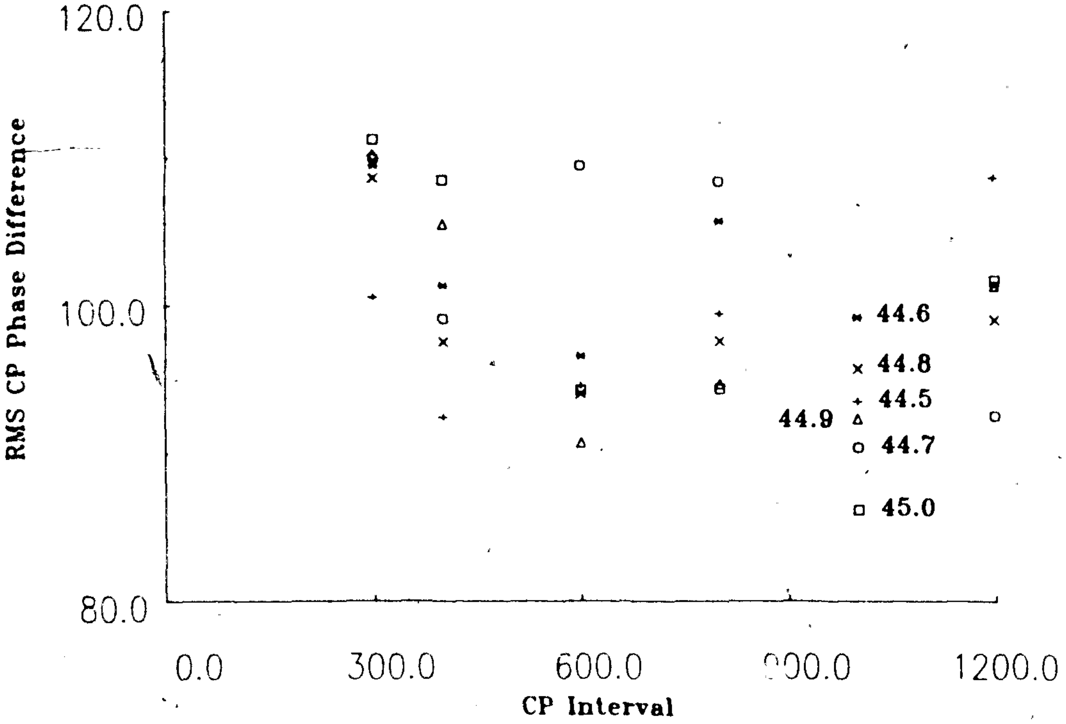

Figure 11.14c Same as Figure 11.14a using data set E85-37:1 and looking at arrival times corresponding to fringe 5. Points at τ = 44.5–44.9ms yield coherent returns.

and statistical developments of Chapters 4 and 6. Good target insonification is required (as observed by the lack of convergence outside the central fringe locations) and the distribution and nature of targets certainly governs the signal quality. These factors however lie, at least partially, within the control of good instrument design. The essential result acquired with this apparatus, is that the absolute orientation (phase) of the complex wave vector, can indeed be determined as predicted and thus provides a basis for interferometric measurements using volume backscatter.

12 COHERENTLY PROCESSED PHASE AND CTD PROFILES

A primary motivation for the foregoing study of absolute phase measurement in volume backscatter is the potential for relating observed phase information to actual temperature or sound speed distributions. In this chapter Snell's Law is applied to successive sound speed profiles derived from CTD data, and the resulting calculations of arrival time at fringe locations are compared with the corresponding acoustic phase measurement. While the successful results of this comparison do not constitute a test of the inverse problem, i.e. inferring the temperature distribution from the phase data, they do represent a necessary first step in validating the overall concept.

12.1 Sound speed profiles and coherently processed phase estimates

An analogue Guideline CTD collected the necessary conductivity, temperature, and depth information to compute the sound speed profile during the experiment. These sensors were calibrated in the laboratory prior to the cruise. In addition field measurements of salinity and temperature were obtained by collecting water samples and reversing thermometer data at a 30m depth. The pressure transducer was calibrated *in situ* by direct comparison between the receiving voltage and depth as read from measuring survey tape to a depth of 50m. The resulting accuracies in the temperature, salinity, and depth were then 0.01°C, 10ppm and 0.0125m respectively.

Three 50m c(z) profiles (T1,T2 and T3) were collected at 15 minute intervals during the 40 minute single frequency data set E85-13:1 and are displayed in Figure 12.1. Variations in the sound speed profile are greatest in the upper 10m. This region is subject to thermal heating and cooling by the atmosphere, and contains a characteristic large temperature gradient or thermocline. Temperature and sound speed are closely related so the thermocline corresponds to

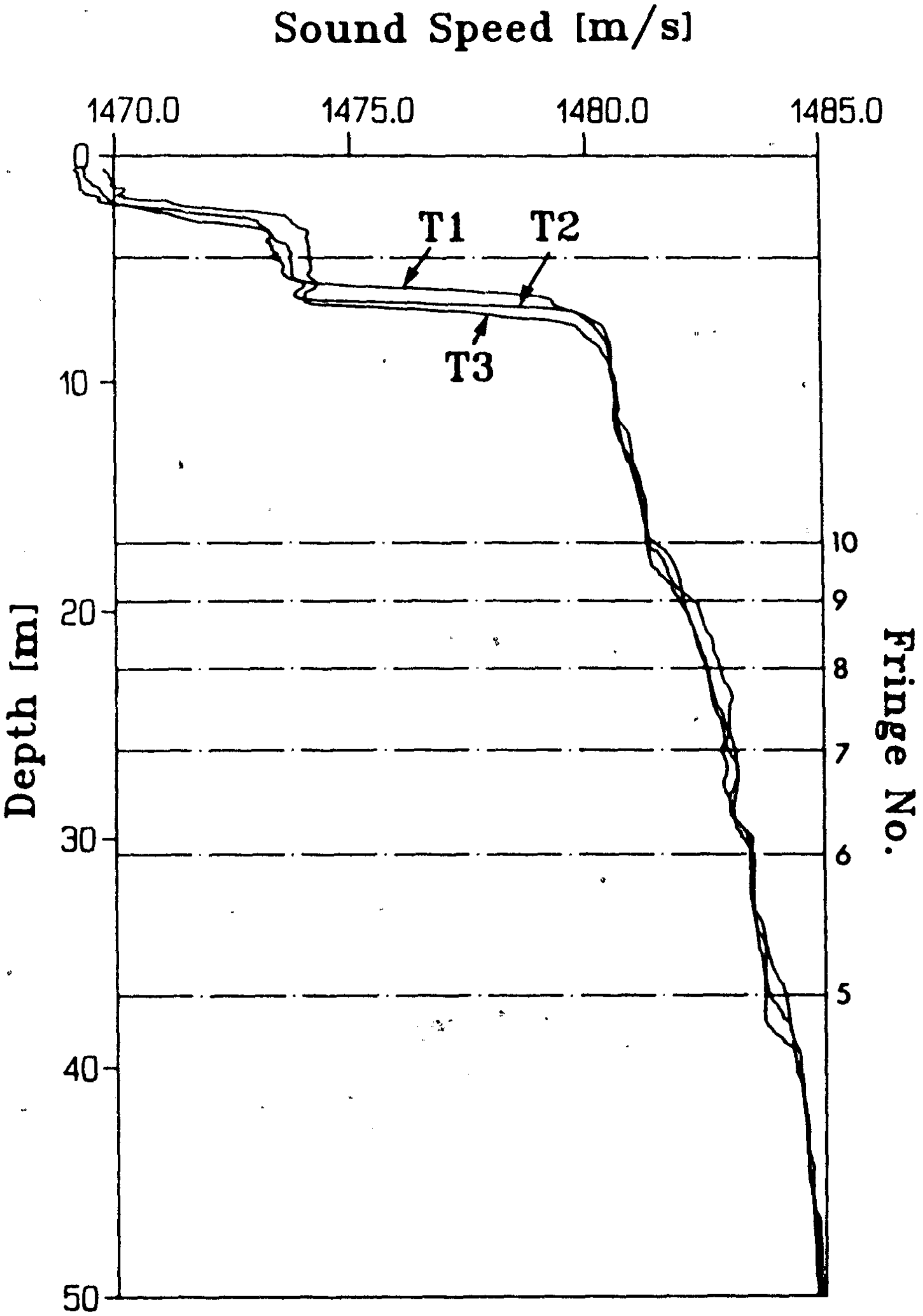

Figure 12.1 Sound speed depth profiles taken during data set 1 (E85-13:1) with 15 minute intervals designated as T1, T2 and T3 respectively. The broken line at 4.5m represents the depth of the acoustic transducers and the other broken lines correspond to the mean depth of fringes.

the large sound speed gradient at 7.5 m. The transducers were operated at a depth of 4.5 m to avoid complications from low salinity and large spacial temperature changes in the surface layer.

These c(z) profiles were measured at depth intervals of 10cm or better. With this high resolution of sampling Snell's law can easily be utilized to estimate the arrival time of a pulse for the experimental configuration. The distance between consecutive depth readings (z_{i-1} and z_i) defines the i^{th} layer with sound speed $c(z_i)$. The angle of incidence in the i^{th} layer (θ_i) is determined by,

$$p = \frac{\sin\theta_o}{c_o} = \frac{\sin\theta_i}{c(z_i)} \tag{12.1.1}$$

which is Snell's Law. The theoretical angle of a fringe provided the initial angle θ_o and the $c(z)$ value at $z = 4.5$m gave c_o. The travel time of the acoustic ray in both the diagonal and vertical directions were computed for each layer and summed to find the theoretical travel time. The depth of each ray trace can also be computed by this method.

Before estimates of the arrival time can be found the maximum depth of the ray must be found. This can be accomplished by evaluating equation 2.1.4 to find $\chi(z)$, the horizontal propagation length of the ray as a function of depth. The maximum depth (z_{max}) in the bistatic system can then be found by interpolation about $\chi(z) \equiv b = 11.580$m. Since c($z$) is measured at uneven intervals the trapezoidal rule for integration can be applied in evaluating $\chi(z)$. The discrete formula is then given by,

$$\begin{aligned} \chi(z) &= \sum_{i=1}^{n} \Delta z_i \tan(\theta_i) \\ &= \sum_{i=1}^{n} \frac{p\bar{c}_i \Delta z_i}{\sqrt{1 - p^2 \bar{c}_i^{\,2}}} \end{aligned} \tag{12.1.2}$$

where,

$$\bar{c}_i = \frac{1}{2}(c_{i-1} + c_i)$$

$$\Delta z_i = z_i - z_{i-1}.$$

Once z_{max} is known for a given ray then the arrival time T of the echoed pulse can also be found through numerical integration. The discrete representation is,

$$T = \sum_{i=1}^{n} \frac{\Delta z_i}{\bar{c}_i}\left[\frac{1}{\sqrt{1 - p^2\bar{c}_i^{\,2}}} + 1\right] \tag{12.1.3}$$

where the endpoints $c_1 = c(4.5)$ and $c_n = c(z_{max})$ are found by interpolation.

The trapezoidal rule is exact when evaluating linear functions and $\tan(\theta_i)$ in equation 12.1.2 is very close to linearity for typical $c(z)$ profiles. This is not true in general for the function being integrated in equation 12.1.3. The error term ϵ_i for the trapezoidal rule (Carnahan, et. al.,1969,p.72) is,

$$\epsilon_i \simeq \frac{\Delta z_i^3}{12} f''(\zeta)$$

where $f''(\zeta)$ is the second derivative of the function being integrated at some location ζ in Δz_i. For the 10cm spacing however, this error term becomes negligible.

A more significant source of error arises from uncertainty of the sound speed profile. Since the depth readings fluctuate (ϵ_z=0.0125m) and distort the $c(z)$ representation, the total error in $c(z)$ will be,

$$\begin{aligned} \epsilon &= \frac{\partial c}{\partial z}\epsilon_z + \epsilon_c \\ &\le 0.1\text{m/s} \end{aligned} \tag{12.1.4}$$

where $\partial c/\partial z \le 2\text{s}^{-1}$ and $\epsilon_c = 0.07$m/s (the accuracy of the sound speed as calculated by equation 1.1.4). Integration is a smoothing process since the perturbations of $c(z_i)$ about its true values will tend to cancel. The effect of

ϵ on equations 12.1.2 and 12.1.3 were estimated first assuming that ϵ is the standard deviation of a Gaussian distributed error function. The integrals were then evaluated 100 times using a pseudo random number generator (Gaussian distributed with standard deviation = 0.1m/s) to estimate the error ϵ for each $c(z_i)$ value. The accuracy of T and z_{max} were then found from the standard deviation of the resulting 100 trials. For fringe numbers 5 to 10 the resulting accuracies were ±0.3μs and ±0.1mm respectively.

Table 12.1 Ray tracing c(z) profiles T1,T2 and T3 in Figure 12.1, to compute the arrival time (ms) at fringe locations.

Fringe	Angle(deg)	T1(ms)	T2(ms)	T3(ms)
5	19.95	44.162	44.171	44.170
6	24.17	36.293	36.302	36.301
7	28.54	30.568	30.578	30.576
8	33.09	26.175	26.185	26.185
9	37.90	22.654	22.664	22.666
10	43.04	19.726	19.736	19.739

Ray traces of fringe locations with depths between 19m and 50m were computed for the three profiles in Figure 12.1. Table 12.1 lists the resulting computed arrival times for the three $c(z)$ profiles for fringe numbers 5 to 10. Notice that the largest arrival time difference at a fringe location is 0.010ms (10μs) over the 15 minute sampling interval. This corresponds to a maximum change in phase of 2.15 cycles because the 215kHz transmit frequency has a period of 4.65μs. The T3 profile shows that the maximum phase shift between T2 and T3 is less than 1 cycle (4.65μs) for fringes 5 to 10. These relatively small changes in arrival times between consecutive $c(z)$ profiles indicate that the direct phase measurements can be resolved without 2π ambiguities when the processing interval is less than 15 minutes.

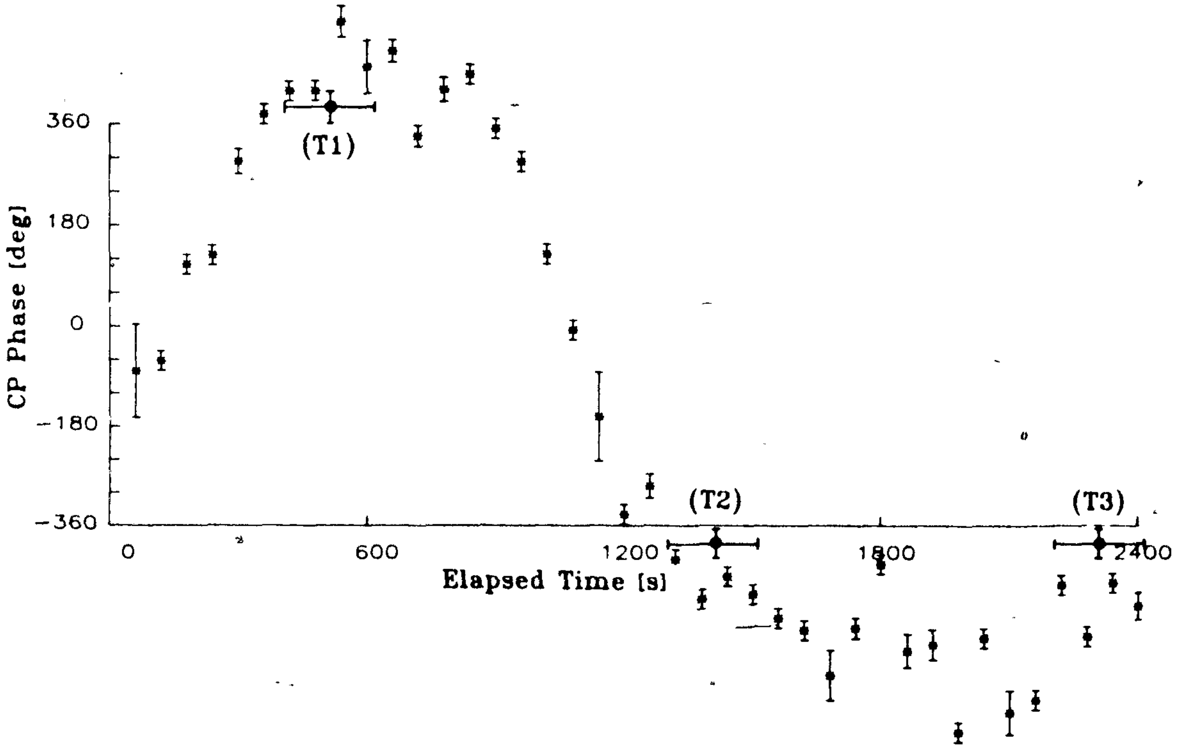

Figure 12.2 Same as Figure 11.5 which gives the CP phase estimates from fringe 8 for the E85-13:1 data set. The solid dots and associated error bars correspond to the theoretical phase estimates from the CTD profiles given in Table 12.1.

The CP phase time series in Figure 11.5 corresponds to fringe number 8. This figure has been replotted in Figure 12.2 with the corresponding theoretical phase values from Table 12.1 represented by solid dots and associated error bars. From Table 12.1 the expected change in phase between T1 and T2 is

774° ± 23° and between T2 and T3 is 0° ± 23°. Figure 12.2 shows the corresponding relative phase from the 3 $c(z)$ profiles (solid dots) to be consistent with the $\phi_{\mathrm{CP}}(t)$ values. In both cases the experimental phase differences are consistent with their theoretical values to within the accuracy of their measurement. These positive results give evidence that the direct $\phi_{\mathrm{CP}}(t)$ values can be correlated with temperature.

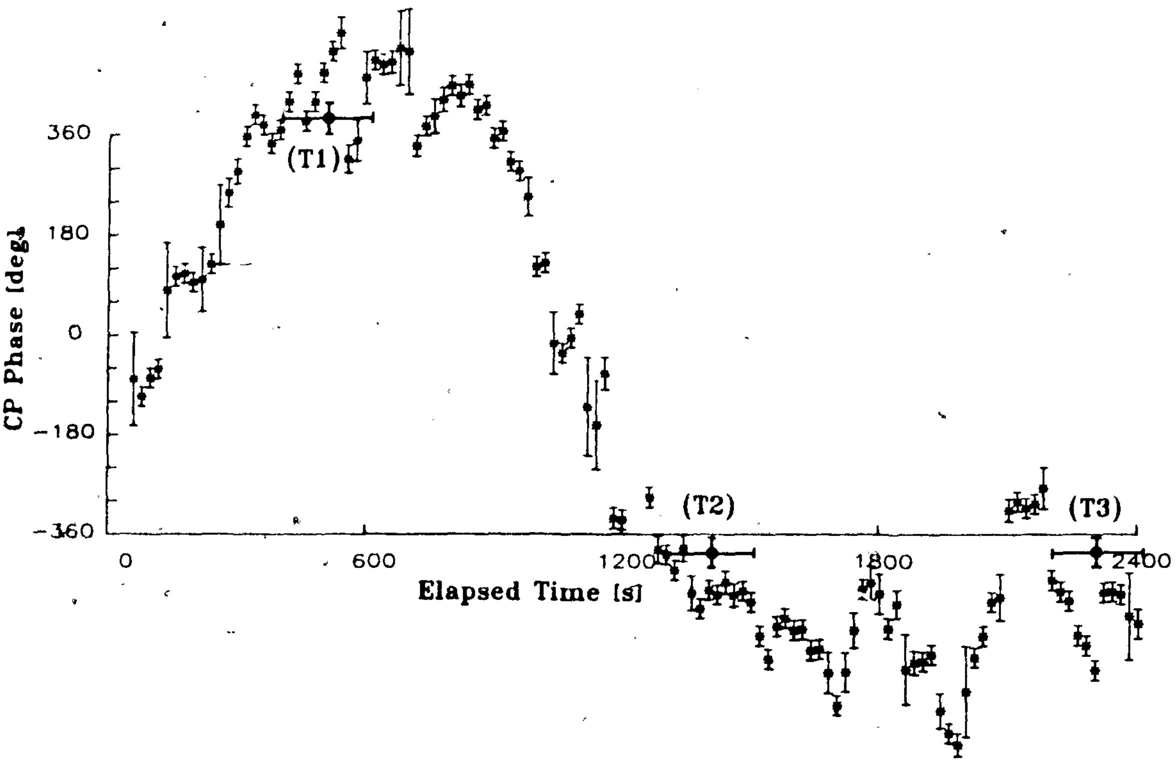

Figure 12.3 Same as Figure 12.2 (fringe 8 and data set E85-13:1) but with intermediate data points computed by applying a moving average to the CP scheme. The solid dots and associated error bars correspond to the theoretical phase estimates from the CTD profiles.

The computation of these results are still subject to phase ambiguities since the resolution and accuracy of the $\phi_{CP}(t)$ estimates are not sufficient to provide one unique time series. The spikes or irregular data points between 1800 and 2400s in Figure 12.2 are bothersome. Increasing the CP interval can provide phase estimates with smaller error bars at the cost of reducing the ability to measure gradients in the phase time series which are caused by refraction. In contrast a shorter CP interval will give a better time resolution with a less accurate phase estimate. By applying a moving average to the quadrature components a finer time step resolution is possible without changing the CP interval or phase accuracy. A test of this method was performed on the E85-13:1 data set by using a 600 point CP interval and 200 point data shift between moving averages. This is equivalent to applying a low pass filter to the resulting in-phase and quadrature sums and using the additional intermediate data points to reconstruct the associated phase time series. Figure 12.3 displays the resulting $\phi_{CP}(t)$ time series. Every fourth point in this plot is also displayed in Figure 12.2. The increased resolution in time in Figure 12.3 clarifies the sections of the phase time series which have smooth trends and those that are subject to abrupt changes and/or noise. A higher degree of confidence can be placed in the ability of this data set to remove any 2π phase shifts. It also confirms the representation of $\phi_{CP}(t)$ in Figure 12.2 (and Figure 11.5).

This concept of smoothing the in-phase and quadrature components can be used to reduce phase jumps between successive estimates to much smaller values and significantly reduce the probability of a $2\pi n$ ambiguity. Of course the resulting moving average phase time series has a time resolution that is limited by the length of the filter, but the resolution of the phase ambiguity in this way is an essential step in handling time series subject to rapid and unpredictable phase variability.

12.2 Relative phase estimates between fringes

The rms $\Delta\phi_{CP}$ plots for data set E85-37:1 in Figures 11.14a,b and c show that a phase signal is being consistently generated by coherent processing at three fringe locations (7,6,and 5). During this 2 hour data set a time varying $c(z)$ profile was observed. The 5 $c(z)$ profiles (C1 to C5) as computed from the CTD data are displayed in Figure 12.4. The changing sound speed structures between fringe locations 5,6 and 7 are of particular interest. These locations contain a time evolving change in sound speed ($\Delta c(t)$) between adjacent fringes. This signal provides an opportunity to test the ability to measure $\Delta c(t)$ from the phase difference between CP phase signals at the fringe locations. Before making these calculations the CP phase time series at the fringe locations will be discussed.

Table 12.2 Ray tracing c(z) profiles C1 to C5 in Figure 12.4.

Fringe	C1(ms)	C2(ms)	C3(ms)	C4(ms)	C5(ms)
5	44.027	44.023	44.042	44.035	44.030
6	36.201	36.196	36.215	36.207	36.200
7	30.507	30.500	30.519	30.510	30.501

As in section 12.1 the $c(z)$ profiles were used to estimate the transmit pulse arrival time by numerical integration. The resulting values are listed in Table 12.2 for the 3 fringe locations and 5 $c(z)$ profiles. By taking the difference between adjacent arrival times for any one fringe number in Table

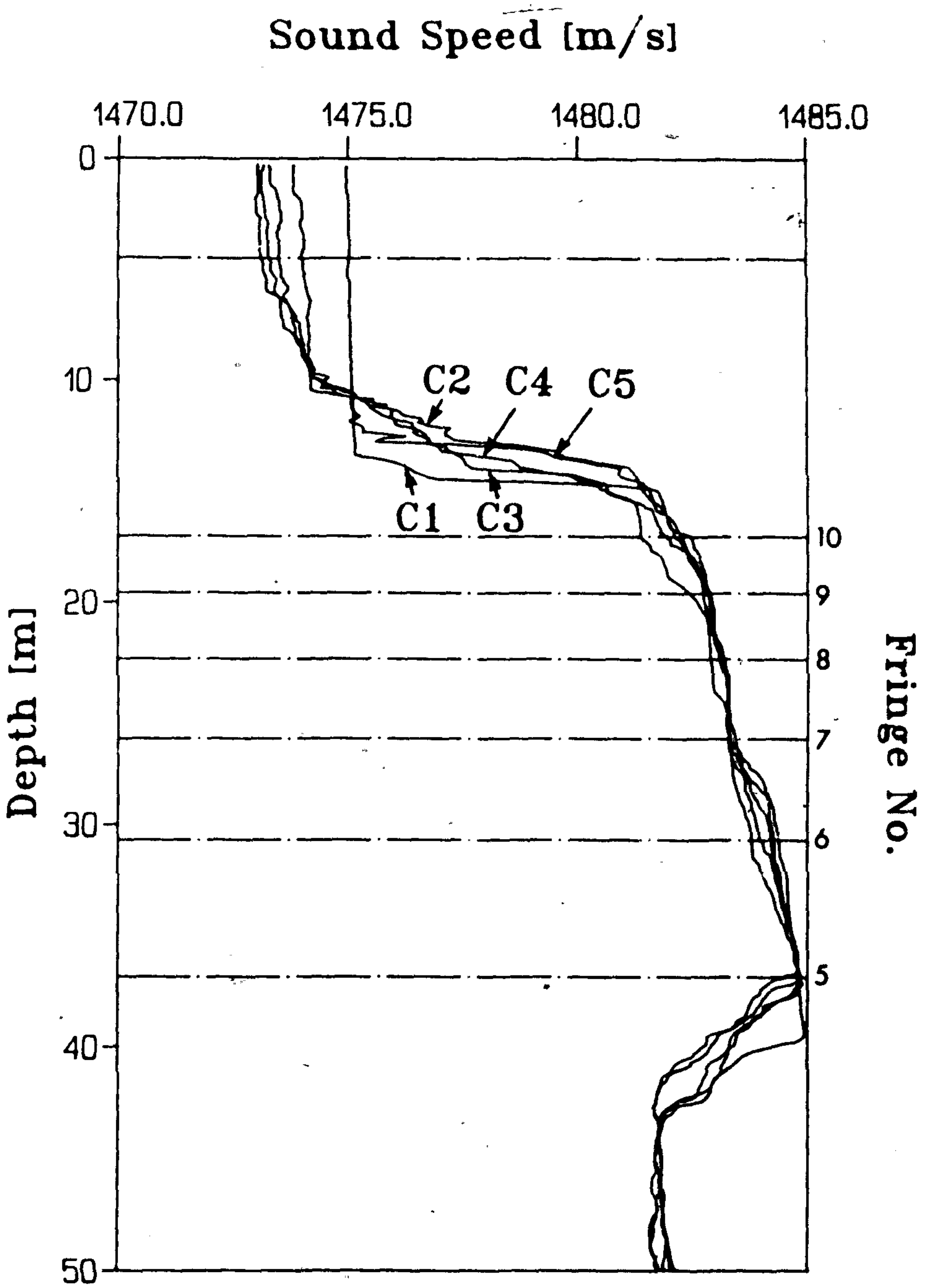

Figure 12.4 Sound speed depth profiles taken during data set (E85-37:1) with 30 minute intervals designated as C1 to C5 respectively. The broken line at 4.5m represents the depth of the acoustic transducers and the other broken lines correspond to the mean depth of fringes.

12.2 the changes are usually greater than 1 cycle (relative to a 215kHz carrier) where 1 cycle = 4.65 μs. While between C2 and C3 the change in arrival time corresponds to ~4 cycles at all of the fringe locations. These large fluctuations are primarily a consequence of the shifting thermocline in the top 20m of the water column. Resolving these multiple cyclic changes from the $\phi_{CP}(t)$ signal becomes a difficult problem. The E85-37:1 data were collected at a 1.82Hz repetition rate. For a 250 point CP interval this provides 13 phase samples between the $c(z)$ profiles which were collected at 30 minute intervals. By applying a moving average to the in-phase and quadrature sums (as discussed in section 12.1) the number of points between $c(z)$ profiles was increased by a factor of 5. The resulting plots showed time evolving structures in the phase signal but the time series was inconsistent with the expected changes from Table 12.2. Sharp discontinuities in the phase time series indicated that cyclic changes were occurring but the resolution of the phase time series was insufficient to provide an unambiguous representation.

With a higher sampling rate of the $c(z)$ profile these cyclic phase changes may be resolved by utilizing the additional information from the theoretical arrival time estimates. Thermistor data were collected every 10 minutes and were spaced at 2.5m intervals between 14.5m and 39.5m. Salinity values at the thermistor locations were interpolated from the 5 CTD profiles so that estimates of $c(z)$ at these discrete depths could be computed at the higher sampling rate. The subsurface locations at 4.5, 7.0, 9.5 and 12.0m were interpolated from the 5 $c(z)$ profiles so that discrete $c(z)$ profiles with 2.5m separation in depth and 10 minute time steps were reconstructed. These discrete profiles were then used to estimate the arrival time ~~from the~~ standard fringe angles. A cubic spline interpolation was applied to the discrete profiles so that a similar numerical integration could be used ~~to~~ estimate the arrival time. The resulting values from the thermistor chain data were consistent to first order with the results in Table 12.2. The differences between adjacent arrival time estimates however were inconsistent with the results obtained from the higher resolution CTD profiles which was sampled at ~0.10m intervals. This exercise showed that thermistor chain or $c(z)$ data at course intervals (2.5m) are unable to resolve the fine structure in arrival time necessary for detailed comparison with the acoustically derived phase changes.

Returning to phase measurements a basic test can still be made of the correlation between a time evolving phase difference and sound speed difference for two adjacent fringe locations. This test uses the difference in phase between CP phase signals at adjacent fringe locations $\Delta\phi$ and the difference in arrival times as computed from the CTD profiles. Table 12.3 gives the estimated differences in arrival time between 2 pairs of fringes (5-6 and 6-7) for each of the 5 CTD profiles. In both of these cases the maximum range in arrival time difference is bounded by 1 cycle of phase.

Table 12.3 Theoretically derived difference in arrival time between fringe locations.

Fringe Pair	c1(ms)	c2(ms)	c3(ms)	c4(ms)	c5(ms)
5-6	7.826	7.828	7.827	7.828	7.831
6-7	5.695	5.696	5.696	5.697	5.699

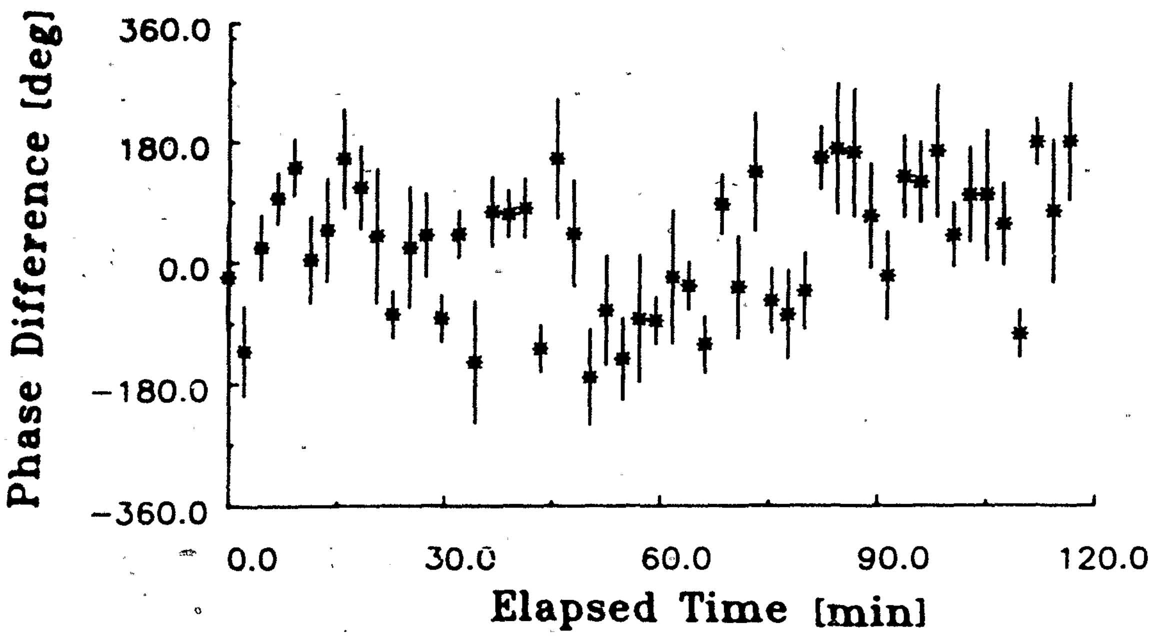

Figure 12.5a Phase difference between mean CP phase estimates at fringe locations 6 and 7 using the E85-37:1 data set.

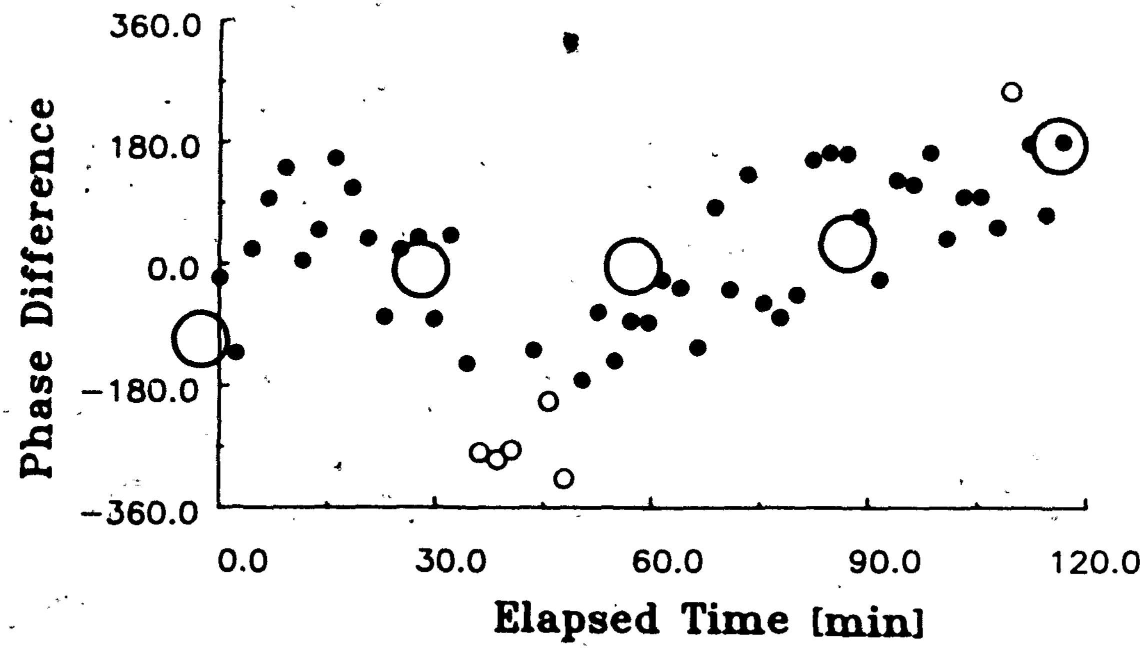

Figure 12.5b Reconstruction of Figure 12.5a showing estimated phase difference (solid dots) and theoretical phase difference (large circles). The small open circles correspond to data points shifted by ±360°.

The $\Delta\phi$ values were computed by first processing the $\phi_{\mathrm{CP}}(t)$ signals to determine the mean phase at each location to a better accuracy using the weighting method presented in section 11.2. The resulting difference in phase between fringes 6 and 7 is displayed in Figure 12.5a with its associated error bars. The large degree of scatter in these plots reflects the typical increase in error when differences are taken since the error terms add. As in other phase measurements individual data points can be shifted by ±360° to remove some of the spikes and discontinuities. In this case however the moving average algorithm for correcting phase ambiguities gives results which are inconsistent with the theoretical values from Table 12.3. This result is a consequence of the large noise component in the phase difference signal. For accurate resolution of any ambiguities in the phase signal the quadrant in which any small group of points lies must be known so that the path between quadrants can be traced out. However with *a priori* knowledge that the phase signal in Figure 12.5a is bounded by one cycle (i.e. a slow varying function over the 120 minute interval) the data points are found to be in good agreement with the theoretical positions as shown in Figure 12.5b. This figure uses the small open circles to indicate the data points which were shifted by ±360° relative to their positions in Figure 12.5a while the large circles represent the expected phase as computed from Table 12.3.

These reference phase values represent the dynamics of the true values and contain an undetermined offset. The initial angles used to compute the arrival times in Tables 12.2 and 12.3 were based on theoretical values since the *in situ* projector calibration (section 9.2) verified a first order agreement. Slight deviations in the true initial projector angle cause the estimates from Table 12.3 to be offset by a constant value from true phase difference. The correlation in the dynamics of the two signals in Figure 12.5b is the important is given in Figure 12.6. Once again the *a priori* information of a slow varying signal bounded by one cycle was utilized in the interpretation. Although the acoustically inferred points are scattered the trend towards positive phase is consistent with the CTD results. It should be noted that the rms $\Delta\phi_{CP}$ for fringe 5 (see Figure 11.14c) did not converge to such a low value as that for fringe 7. Thus the data quality is not as good in this example.

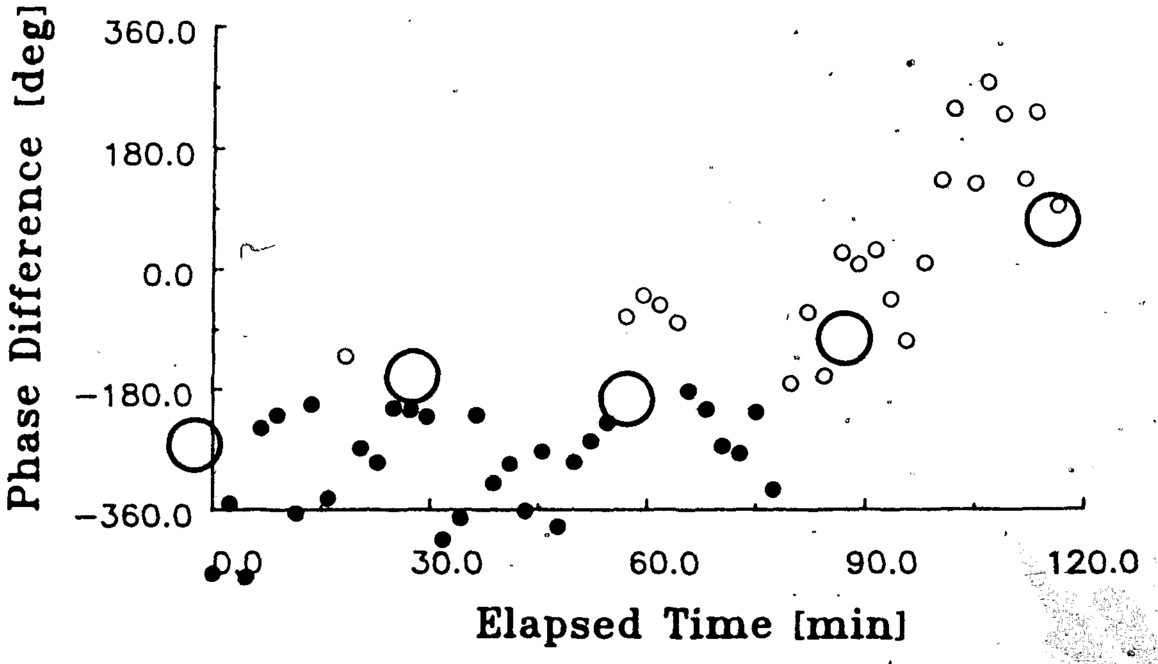

Figure 12.6 Scatter diagram of estimated phase difference (solid dots) and theoretical values (large circles) between fringe locations 5 and 6 for the E85-37:1 data set. The small open circles correspond to data points shifted by ±360°.

The previous 2 plots show that the phase difference between the CP phase signals at adjacent fringe locations (for E85-37:1 data) is too noisy to resolve the underlying $\Delta c(t)$ signal. However when the bounds on the difference in arrival time were utilized to interprete the phase difference signal then a consistent trend in the two time series was observed.

The original objective of this work was to obtain estimates of temperature or sound speed through measuring the difference in arrival time between fringe locations. The relationship between sound speed accuracy and arrival time accuracy was developed in section 2.5 and Figure 2.8 demonstrates the results for even fringe numbers. For the 215kHz carrier frequency used in the experimental work a $\pm 45^\circ$ phase difference accuracy has a corresponding arrival time accuracy of $\pm 0.6 \mu s$. This corresponds to an accuracy in $c(z)$ to at least ±.01m/s and a temperature accuracy of ±.002°C. Conventional CTD probes are capable of estimating sound speed to within ±.07m/s. These comparisons show that much lower operating frequencies can be used to obtain sound speed estimates from absolute acoustic phase measurements.

13 SUMMARY OF RESULTS AND RECOMMENDATIONS

A primary goal of this thesis has been to demonstrate that stable, useful measurements of the orientation of the acoustic signal vector as a function of range and time can be obtained from ocean backscatter, and that this orientation, or acoustic phase, can be related to the local sound speed distribution. Such a measurement is quite distinct from the related problem of detecting the rate of phase change, which forms the basis of Doppler technology. Doppler measurement can be made using echoes from a single point, or a sparsely distributed set of targets. Consistent and useful measurement of absolute phase is inherently more difficult, since it depends upon the positions of individual scatterers, which are normally random and sparse relative to the acoustic wavelength.

This difficulty has been overcome by coherent superposition of echoes from successive transmissions, such that the effective density of acoustic targets progressively increases as the summation proceeds. The theoretical basis of this type of coherent processing has been developed and examined in the limiting case, in which it approximates a scatterer continuum for which an analytic expression has been found. An important simplification in this development is the use of the single scatter approximation which remains valid, even in the limit, since individual transmissions result in echoes from a sparsely distributed set of scatterers. The theory provides fundamental insights to the behaviour of both the amplitude and phase of volume scatter including the effects of gradients in the scatterer distribution.

It has been shown that coherent superposition of echoes from successive transmissions may be represented by complex Ricean statistics. As the ratio of coherent to incoherent signal increases with successive superposition of the echoes, the phase statistics evolve from a uniform to a nearly Gaussian distribution. The rate at which the ratio of coherent to incoherent signal changes as a function of the number of superpositions, is related to the density of acoustic targets in the scattering volume. Once the phase signal is bounded to within ±45°, the basic requirement for a coherent 'volume mirror' has been met and reliable interferometric estimates are possible.

Implementation of this concept in a practical device for measuring sound speed (or temperature) structure, requires use of a bistatic echosounder whose separate transmitter and receiver transducers are secured to a rigid baseline. A detailed error analysis of both Brown et. al. (1984) and Ostashev's (1985) proposed schemes shows substantial difference in performance; a new approach for differential time (or phase) measurements is also introduced. Rigidity of the acoustic baseline was found to be an essential requirement for good measurements, although real time acoustic detection of vibrational motions and the application of corrections to the data offer a possible alternative in a more flexible deployment scheme.

Following a series of experiments in which both mechanical and signal processing difficulties were encountered and finally resolved, a good set of volume backscatter data were obtained in November 1985. Analysis of these results provided unequivocal evidence that stable and meaningful absolute phase measurements can be acheived using the new techniques developed in this thesis. Confirmation of this result was provided by a critical test in which the rms coherently processed phase difference between two interleaved, but statistically independent data sets, was shown to decrease with increasing sample number. In effect, two independent sets of measurements of backscatter from the same water column, steadily converge as the ratio of coherent to incoherent backscatter increases. This test yields a measurement of signal quality, which is a necessary component of the signal analysis, since the scatterer distribution is variable and can greatly influence the measurement. Convergence of independent time series to within ±45° was achieved and these data provided the basis for comparison with sound speed distributions derived from CTD (salinity and temperature) profiles.

Two types of comparison were made between acoustic phase and CTD profiles. The first of these involved integration of the observed sound speed profile, using Snell's Law, down to the depth of the fringe intersection selected for comparison ($\approx$ 21.5m). Slow changes in the sound speed profiles led to changes in the resulting calculated phase measurements, which were fully consistent with the acoustically derived result. An alternative approach, in which phase difference measurements were made between fringes was also carried out. The data analysis was complicated in this case by the extreme sensitivity of the interferometric measurement and the effects of a rapidly fluctuating, sharp thermocline just beneath the acoustic transducers which was poorly resolved by the relatively infrequent CTD profiles. However a differential comparison in these conditions was possible by bounding the phase ambiguity using the observed limits of sound speed variations between fringes. The results of the acoustic observations were again consistent with the CTD data, although more scattered, as would be expected for a differential measurement. The extreme sensitivity of the interferometric measurement places special demands on the independent profile measurement used for comparison; nevertheless these results do confirm that observed backscatter phase changes are consistent with changes in the sound speed profile.

These results do not constitute a test of the capability for inverting acoustic phase data so as to recover information about the sound speed profile, but they do constitute a necessary first step in demonstrating such a possibility.

Further experimental and theoretical work is required to determine the phase convergence behaviour under different backscatter conditions. Transducer design must be optimized for such measurements (our system was set to provide good backscatter from only three or four fringes). The acoustic frequency must be optimized (phase convergence will be more rapid and the baseline stability requirements will be reduced at lower frequencies). Rapid and accurate CTD data must be obtained over a long period so as to allow extended comparison with the acoustic measurement under a wide range of environmental conditions. The basic theoretical and experimental approaches for this technique have been laid down; future work must focus on refinement of the apparatus, improvement and streamlining of the signal analysis procedures and sufficiently extensive observations to test the capability for inversion of acoustic phase to sound speed profiles. Also, schemes for resolving the phase ambiguity must be developed using accurate pulse arrival time measurements from the amplitude signal.

Some form of differential measurement is required for recovery of the profile but an integral measurement of the sound speed properties, making use of volume scatter from a single range gate, could also prove useful. For example, the overall transit time for a single pulse in a bistatic system is related to the integral sound speed distribution, which in turn can be related to the integral heat content of the water above the scattering depth. Single valued time series of heat content could prove to be a useful measurement in climatic studies. The bistatic system could also be mounted on the sea-floor, or from sea-ice, allowing much longer baselines to be realised.

This work has utilised previous knowledge of oceanic scattering mechanisms. This is an active area of research and many basic issues remain unresolved. Biological acoustic targets present a difficult challenge with respect

L

to classification of their complicated frequency response. For example, separate investigators have found values of zooplankton target strengths as a function of frequency $\sigma(f)$ which differ by 20dB (Pieper, 1983). These laboratory and field measurements have relied exclusively on the amplitude of backscatter. A more accurate estimate of $\sigma(f)$ can be obtained through a deconvolution technique. The impulse weighting function or impulse response of the scatterering mechanism quantifies all the properties which alter the incident waveform in a linear system. By selecting transducers with narrow beams and large bandwidths, directional short pulses can be transmitted. A Fourier transform of the received complex echo and deconvolution with the transmit pulse will provide a real and imaginary representation of $\sigma(f)$. This differs from previous methods in two ways: (1) by measuring the target strength over a range of frequencies rather than one frequency for each transducer, and (2) by providing the complex representation of the target strength rather than just the intensity. Since zooplankton are not pressure release surfaces there will be a phase lag associated with the incident acoustic wave. This phase lag can also help quantify the scatterer characteristics by providing a second level of classification to the scattering properties. Apparatus, theory and signal processing approaches of the type developed in this thesis could be used to exploit this approach to zooplankton studies.

Additional information on the properties of the discrete scatterers can also be obtained from the complex autocorrelation of the time series from a fixed range gate. For a zooplankton population, the average swimming velocity is directly related to their physical length. The group velocity of the scatterers is contained within a Doppler signal and the variance of the random scatterer motions can be found from the complex autocorrelation. An inversion of equation 10.3.4 provides an estimate of the standard deviation of the scatterer velocities and hence the size distribution of the scatterers.

The analysis of phase convergence through coherent summation of individual echoes has shown that the ratio of coherent to incoherent signal energy γ is related to the scatterer density ρ_n (or alternately the mean target separation). This concept suggests a novel technique for measuring scatterer density; coherent processing of complex echoes from an echo-sounder can be used for calculation of γ (or the second moment of phase) and consequent inversion to recover mean target spacing as indicated in Chapter 7. This approach offers a substantial advantage over traditional techniques based on measurement of the amplitude signal alone.

These examples serve to illustrate the potential for volume backscatter measurement using the concepts developed in this thesis. The detection of absolute phase allows the principle of a volume backscatter mirror to be used in a sensitive interferometer measurement. The statistical properties of the signal can lead to a variety of insights and observational techniques for studying the acoustic scatterers. While the theoretical and experimental groundwork has been laid, further work is required before the full potential of this approach can be exploited. A program of additional work along these lines is now planned.

REFERENCES

Abramowitz, M. and Stegun, I.A. (editors), *Handbook of Mathematical Functions With Formulas, Graphs, and Mathematical Tables*, National Bureau of Standards Applied Math Series 55,1960.

Anderson, V.C., "Sound scattered from a fluid sphere," *J.Acous.Soc.Am.* **22**, 426-431 (1950).

Barford, N.C., *Experimental Measurements: Precision, Error, and Truth*, Addison-Wesley, London, 1967.

Beamish, P.C., *Quantitative Measurements of Marine Acoustic Scattering From Zooplanktonic Organisms*, Ph.D. Thesis, University of British Columbia, 1969.

Booth, A.D., "Modelling acoustic transducers", Unpublished manuscript, Institute of Ocean Sciences, Sidney, B.C., 1983.

Brown, E.H. and R.J.Keeler, "Acoustic Remote Sensing of Temperature", in *Proceedings of the International Symposium on Acoustic Remote Sensing of the Atmosphere and Oceans*, (1981).

Brown, E.H., C.G.Little, and W.M.Wright, "Echosonde Interferometer for Atmospheric Research", *J.Acous.Soc.Am.***63**, (1978).

Brown, E.H., D.Farmer, S.Gilheaney, and W.Woodward, "On the remote measurement of temperature profiles in the ocean", *Proc. IEEE*, No. 6, 641-647(1984).

Carnahan B., H.A.Luther and J.O.Wilkes, *Applied Numerical Methods*, John Wiley & Sons, Inc., Toronto, 1969.

Clay, C.S. and H.Medwin, *Acoustical Oceanography*. John Wiley and Sons, New York, 1977.

Clay, C.S. and B.G.Heist, "Acoustic scattering by fish–Acoustic models and a two-parameter fit". *J.Acous.Soc.Am.***75**, 1077-1083 (1984).

Crawford, G.B. and D.M. Farmer, "On the spatial distribution of ocean bubbles". To appear, *J.Geoph.Res., Oceans*, 1987.

Davenport W.B.(Jr.) and W.L. Root, *An Introduction to the Theory of Random Signals and Noise*. McGraw-Hill, New York, 1958.

Dickey, F.R., Jr., *Velocity measuring correlation sonar.* United States Patent, No. 4244026, 1981.

Edward, J. A. 1978. *Accuracy relationship in a Correlation Sonar System for the Remote Measurement of Water Currents.* Report by General Electric Company, Heavy Military Equipment Department, Syracuse, NY. Prepared for U.S. Department of Commerce/NOAA. (Private communication available through courtesy of the author).

Farmer, D. M. , Booth, A. D. and Kamitakahara, G., "Preliminary considerations in the design of a correlation sonar for remote velocity profile measurements in the ocean." *Proceedings of International Symposium on Acoustic Remote Sensing of the Atmosphere and Oceans.* (University of Calgary Printing Services, 1981).

Farmer, D.M. and S. Clifford, "Space-time acoustic scintillation analysis: A new technique for probing ocean flows". *IEEE Journal of Oceanic Engineering.* Vol. OE-11, No. 1, Jan. 1986.

Foote, K.G., "Rather-high-frequency sound scattering by swimmbladdered fish", *J.Acous.Soc.Am.***78**, 688-700(1985).

Fried, D.L., "Statistics of the laser radar cross section of a randomly rough target". *J.Opt.Soc.Am.***66**, 1150-1159(1976).

Goodman, J.W., "Some fundamental properties of speckle". *J.Opt.Soc.Am.* **66**, 1145-1150(1976).

Gradshteyn, I.S. and I.M.Ryzhik, *Table of Integra~~ls, Series~~, and Products*, Academic Press, New York, 1980.

Greenlaw, C.F., "Backscattering spectra of preserved zooplankton," *J. Acous. Soc. Am.***62**, 44-52(1977).

Heath, A.W., *The Ecology and Harvesting of Euphausiids in the Strait of Georgia*, Ph.D Thesis, University of British Columbia, 1976.

Hoel, G.H., S.C.Port, and C.J.Stone, *Introduction to Probability Theory*, Houghton Mifflin, New York, 1971.

Holliday, D.V. and R.E.Pieper, "Volume scattering strengths and zooplankton distributions at acoustic frequencies between 0.5 and 3MHz," *J.Acous.Soc.Am.***67**, 135-146 (1980).

Huber, T.B., *Investigation of the Two Pulse Correlation Sonar Technique for Water Current Measurement*, M.Sc. Thesis, University of Victoria, 1986.

Ishimaru, A., *Wave Propagation and Scattering in Random Media*, Vol.1, Academic Press, New York, 1978.

Jobst, W.J., *Acoustic Volume Reverberation in the Ocean: Theory, Experiment, and Simulation*, The Catholic University of America, Ph.D., 1972.

Johnson, R.K., "Sound scattering from a fluid spheres revisited". *J.Acous.Soc.Am.***61**, 375-377 (1977).

Kils, U. "Swimming speed and escape capacity of Antartic krill, Euphausia superba," *Meeresforch.***27**, 264-266(1979).

Kung, H., *Probability Density Function of Backscattered Sound From Live Fish*, M.Sc. thesis, University of Wisconsin, 1977.

Kinsler, L.E., et. al., *Fundamentals of Acoustics 3rd Edition*, John Wiley and Sons, Toronto, 1982.

Kristensen, A. and J.Dalen, "Acoustic estimation of size distribution and abundance of zooplankton," *J. Acous. Am.***80**, 601-611(1986).

Lathi, B.P., *Communication Systems*, John Wiley and Sons, New York, 1968.

Machlup, S., "A theoretical model for sound scattering by marine crustaceans". *J.Acous.Soc.Am.***24**, 290-293 (1952).

Mackenzie, K.V., "Formulas for the computation of sound speed in sea water," *J.Acous.Soc.Am.***32**, 1960.

Middleton, D., *An Introduction to Statistical Communication Theory*, McGraw-Hill, New York, 1960.

Miller, I. and J.E.Freund, *Probability and Statistics for Engineers*, Prentice-Hall, NJ, 1985.

Mills, M.H., *Patterns and Mechanisms of Vertical Distributions of Medusae and Ctenophores*, Ph.D Thesis, University of Victoria, (unpublished), 1982.

Orr, M.H., "Remote acoustic sensing of oceanic fluid and biological processes," *Woods Hole Oceanographic Institution Technical Report*, 1980.

Ostashev, V.E., "Possibility of reconstructing vertical profiles of the velocity of sound in a bistatic scheme of acoustic sounding of the atmosphere and the ocean," *Izvestiya, Atmospheric and Oceanic Physics*, Vol. 20, No. 2, 147-150 (1984).

Pieper, R.E., "Euphausiid distribution and biomass determined acoustically at 102 kHz". *Deep-Sea Research*, Vol.26/6A, 687-702 (1979).

Pieper, R.E., "Quantitative estimates of euphausiid biomass determined by high-frequency acoustics". *Biological Oceanography*, Vol. 2, No. 2-3-4, 133-149 (1983).

Pieper, R.E. and D.V. Holliday, "Acoustic measurements of zooplankton distributions in the sea," *J.Cons.int.Explor.Mer.* 41: 226-238 (1984).

Pinkel, R., "Acoustic Doppler Techniques." Reprinted from: *Air Sea Interactions*, Plenum Publishing Corp., New York, 1980.

Rayleigh, Lord [J.W.Strut], *The Theory of Sound Vol. 1* (2nd Eds., 1894 and 1896), Dover, New York, 1945.

Rice, S.O., "Mathematical analysis of random noise, II," *Bell System Tech. J.*, **24**: 46 (1945).

Sameoto, D., N.A. Cochrane, and A.W. Herman, "Response of biological acoutic backscattering to ship's lights". *Can.J.Fish.Aquat.Sci., Vol.*42, 1535-1541 (1985).

Sofoulis, N.G., *A Study of the Acoustic Strengths of Small Targets Relevant to the Prawning Industry*, M.App.Sc. Thesis, Western Australian Institute of Technology, 1978.

Spindel, R.C. and P.T. McElroy, "Level and zero crossings in volume reverberation signals." *J. Acous. Am.*53, 1417-1462(1973).

Stanton, T.K., "Sound scattering by fluid cylinders of finite length". Submitted to JASA Jan. 1986.

Stanton, T.K. and C.S. Clay, "Sonar echo statistics as a remote-sensing tool: volume and seafloor." *IEEE Journal of Oceanic Engineering*, Vol. OE-11, 79-96(1986).

Thorpe, S.A., "On the clouds of bubbles formed by breaking waves in deep water and their role in air-sea gas transfer." *Phil. Trans. Roy. Soc. London*, A304, 155-210(1982).

Urick, R.J., *Sound Propagation in the Sea*, Peninsula Publishing, Calif., 1982.

Van Vlack, L.H., *Material Science for Engineers*. Addison-Wesley, Ont., 1970.

Wood, A.B., *A Textbook of Sound*, Macmillan Co., New York, 1941 p.261.

Yeh, C., "Scattering of acoustic waves by a penetrable prolate spheroid. I. Liquid prolate spheroid," *J.Acous.Soc.Am.***42**, 518-521 (1967).

APPENDIX 1 THE EXACT FRINGE FORMULA

The angular dependence of fringe locations for a linear array of point sources will be derived from first principles. The system geometry in 3 dimensions is presented in Figure A1.1. A point in space can be represented by either the spherical coordinates (r, θ, ϕ) or the cartesian coordinates (x, y, z). In this system the main interest is in the $x - z$ plane which also contains the projector array so measurements will be related to the baseline distance b on the x axis. A position in space is defined by,

$$\begin{aligned} y &= b \sec \phi \\ z &= b \sec \phi \cot \theta. \end{aligned} \qquad (A1.1)$$

With point sources at $(-d/2, 0, 0)$ and $(d/2, 0, 0)$ the path lengths r_1 and r_2 to the point P are given by,

$$r_1^2 = s_1^2 + z^2 \qquad (A1.2)$$

$$r_2^2 = s_2^2 + z^2 \qquad (A1.3)$$

where the projection of r_1 and r_2 onto the x-y plane are given by,

$$s_1^2 = (b + d/2)^2 + (b \tan \phi)^2 \qquad (A1.4)$$

$$s_2^2 = (b - d/2)^2 + (b \tan \phi)^2. \qquad (A1.5)$$

A fringe is defined by,

$$r_1 - r_2 = m\lambda \qquad (A1.6)$$

where, $m = 0, 1, 2, \ldots$. By writing equation A1.6 in terms of r_1 and squaring we obtain,

$$r_1^2 = m^2\lambda^2 + 2m\lambda r_2 + r_2^2 \qquad (A1.7)$$

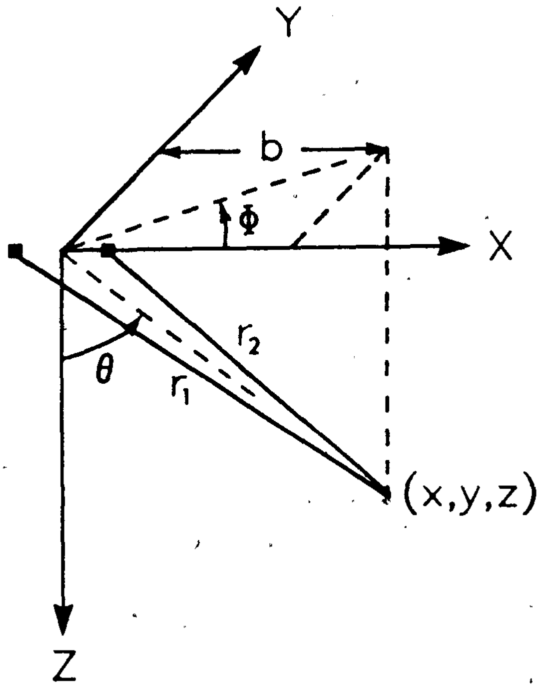

Figure A1.1 Geometry of an arbitrary field point (x, y, z) relative to an array with elements at $(-d/2, 0, 0)$ and $(d/2, 0, 0)$.

which rearranges to give,

$$r_1^2 - r_2^2 = m^2\lambda^2 + 2m\lambda r_2. \qquad (A1.8)$$

Subtracting equations A1.2 and A1.3 gives,

$$\begin{aligned} r_1^2 - r_2^2 &= s_1^2 - s_2^2 \\ &= (b + d/2)^2 - (b - d/2)^2 \qquad (A1.9) \\ &= 2bd \end{aligned}$$

which equates with equation A1.9 and provides the relationship,

$$2bd = m^2\lambda^2 + 2m\lambda r_2. \qquad (A1.10)$$

Expressing equation A1.10 in terms of r_2 and squaring both sides of the equation provides,

$$\begin{aligned} r_2^2 &= \frac{(2bd - m^2\lambda^2)^2}{4m^2\lambda^2} \\ &= \frac{1}{4m^2\lambda^2}(4b^2d^2 - 4m^2\lambda^2bd + m^4\lambda^4). \end{aligned} \tag{A1.11}$$

Expanding equation A1.3 gives,

$$\begin{aligned} r_2^2 &= b^2 - bd + d^2/4 + b^2\tan^2\phi + b^2\sec^2\phi\cot^2\theta \\ &= b^2\sec^2\phi(1 + \cot^2\theta) + d^2/4 - bd \end{aligned} \tag{A1.12}$$

Equating A1.11 with A1.12 results in,

$$4m^2\lambda^2b^2\sec^2\phi\csc^2\theta = 4b^2d^2 - m^2\lambda^2d^2 + m^4\lambda^4 \tag{A1.13}$$

A solution in terms of θ is wanted so equation A1.13 can be further manipulated to give,

$$\begin{aligned} \csc^2\theta &= \frac{d^2}{m^2\lambda^2\sec^2\phi}[1 - \frac{m^2\lambda^2}{4b^2} + \frac{m^4\lambda^4}{4b^2d^2}] \\ &= \frac{d^2}{m^2\lambda^2\sec^2\phi}[1 - (\frac{m\lambda}{2b})^2[1 - (\frac{m\lambda}{d})^2]] \end{aligned} \tag{A1.14}$$

and by both inverting and taking the square root,

$$\sin\theta = \frac{m\lambda}{d}\sec\phi\left[1 - (\frac{m\lambda}{2b})^2[1 - (\frac{m\lambda}{d})^2]\right]^{-\frac{1}{2}}. \tag{A1.15}$$

In the x-z plane which contains the projector, $\phi = 0$. By defining the far field case as $b >> d$, then equation A1.15 can be simplified. Since $m\lambda/d < 1$ it follows that $m\lambda/2b << 1$. The resulting farfield solution becomes,

$$\sin\theta = \frac{m\lambda}{d}. \tag{A1.16}$$

APPENDIX 2 BROWN'S METHOD OF MEASURING SOUND SPEED

The echometer system as proposed by Brown, et. al. (1976) utilized a linear array to create a projector with narrow beam fringes. These fringes have an angular dependence which is a function of the spacing d between elements, the sound speed at the projector c_o and the carrier frequency f. In the far field this relationship is given by,

$$\sin\theta = \frac{mc_o}{fd} \qquad (A2.1)$$

where m, the fringe number, is an integer. For two frequencies f_1 and f_2 it follows that if $f_1 > f_2$ then $\theta_2 > \theta_1$. Note, the subscipts 1 and 2 relate the variables to the corresponding frequency. This relationship and the system geometry is presented in Figure A2.1.

Denoting by $\bar{c}$ the mean sound speed in the first z meters, the arrival time at the receiver is given by,

$$\begin{aligned} t_1 &= \frac{1}{\bar{c}}(r_1 + z) \\ t_2 &= \frac{1}{\bar{c}}(r_2 + \Delta r + \Delta z + z), \end{aligned} \qquad (A2.2)$$

where the length dependent variables are defined in Figure A2.1. When the condition,

$$\frac{f_1 - f_2}{f_1} << 1$$

is true then the two rays will respond to the same environmental conditions in the first z meters. The echometer system relies on the detection of changes in the phase ϕ of the received signal. While propagating through the first z meters the relative phase shift introduced to paths 1 and 2 will be of the same order. The region of interest is then the small "V" at the bottom of path 2 as

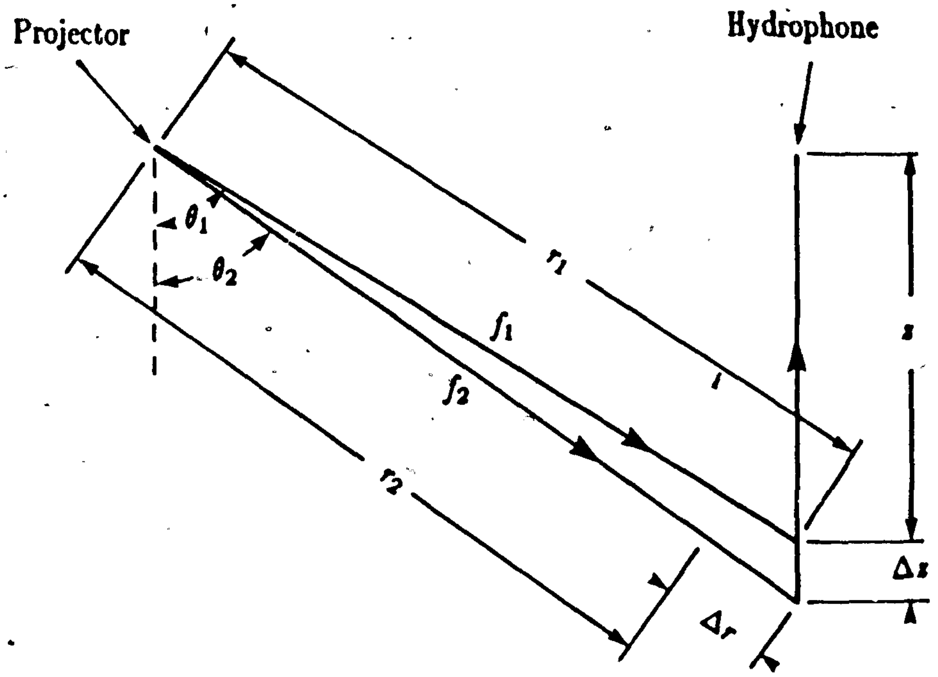

Figure A2.1 Geometry of the bistatic acoustic system with baseline b.

shown in Figure A2.1. The two phase signals in a constant sound speed profile ($\bar{c}$) are then,

$$\begin{aligned} \phi_1 &= \frac{f_1}{\bar{c}}(r_1 + z) \\ \phi_2 &= \frac{f_2}{\bar{c}}(r_2 + \Delta r + \Delta z + z) \end{aligned} \tag{A2.3}$$

A number of first order approximations can be made to the system geometry to express these equations in terms of measurable parameters. For typical sound speed profiles in the ocean the effects of refraction in the first 50m are small. This implies that the ray paths in Figure A2.1 approximate straight lines in a first order analysis. From the geometry of the system the variables in equation A2.2 and A2.3 can be expressed as,

$$\begin{aligned} r_1 &= \mathrm{b}/\sin\theta_1 \\ r_2 &= \mathrm{b}/\sin\theta_2 - \Delta \mathrm{r} \\ \mathrm{z} &= \mathrm{b}/\tan\theta_1 \end{aligned} \qquad (A2.4)$$

where b is the distance between the transmit and receive transducers. The two angles and frequencies can be related to themselves by,

$$\begin{aligned} \theta_1 &= \theta_2 + \Delta\theta \\ f_2 &= f_1(1+\epsilon) \end{aligned} \qquad (A2.5)$$

where both ϵ and $\Delta\theta$ are small numbers. The trigonometric terms in $\sin\theta_2$ can be expressed as,

$$\begin{aligned} \sin\theta_2 &\simeq \sin\theta_1 - \Delta\theta\cos\theta_1 \\ &= \frac{m\bar{c}}{f_1 d}(1-\epsilon) \end{aligned} \qquad (A2.6)$$

which equate to give,

$$\Delta\theta = \epsilon\tan\theta_1 . \qquad (A2.7)$$

By applying a trigonometric identity to $\cos\theta_2$ and then substituting in equation A2.7, the expression reduces to,

$$\begin{aligned} \cos\theta_2 &\simeq \cos\theta_1\cos\Delta\theta + \Delta\theta\sin\theta_1 \\ &= \cos\theta_1(1+\epsilon\tan^2\theta_1). \end{aligned} \qquad (A2.8)$$

The objective of all this algebra is to express ϕ_2 in terms of the variables used in ϕ_1 so that a relationship between these two phase measurements can be found. The first path dependent term r_2 in equation A2.3 simplifies to give,

$$\begin{aligned} r_2 &= \frac{\mathrm{z}}{\cos\theta_2} \\ &= \frac{\mathrm{b}}{\tan\theta_1}\frac{1}{\cos\theta_1(1+\epsilon\tan^2\theta_1)} \\ &= r_1(1-\epsilon\tan^2\theta_1). \end{aligned} \qquad (A2.9)$$

The expression for Δr utilizes this last equation and is given by,

$$\begin{aligned}\Delta r &= \frac{\mathrm{b}}{\sin\theta_2} - r_2 \\ &= \frac{\mathrm{b}}{\sin\theta_1(1-\epsilon)} - r_1(1-\epsilon\tan^2\theta_1) \\ &= r_1(1+\epsilon) - r_1(1+\epsilon-\epsilon\sec^2\theta_1) \\ &= \epsilon r_1\sec^2\theta_1\end{aligned} \qquad (A2.10)$$

The expression for $\Delta\mathrm{z}$ is found by the following expansion of the trigonometric relationships.

$$\begin{aligned}\Delta\mathrm{z} &= \frac{\mathrm{b}}{\tan\theta_2} - \mathrm{z} \\ &= \frac{\mathrm{z}\tan\theta_1}{\tan\theta_2} - \mathrm{z} \\ &= \mathrm{z}\frac{1+\epsilon\tan^2\theta_1}{1-\epsilon} - \mathrm{z} \\ &= \mathrm{z}(1+\epsilon\tan^2\theta_1+\epsilon) - \mathrm{z} \\ &= \mathrm{z}\epsilon\sec^2\theta_1 \\ &= r_1\epsilon\sec\theta_1\end{aligned} \qquad (A2.11)$$

When the sound speed in the "vee" is different from the mean sound speed by Δc the received phase from the second ray path becomes,

$$\phi_2 = \frac{f_2}{\bar{c}}\left[r_2 + \frac{\Delta r + d(\Delta r)}{1+\nu} + \frac{\Delta\mathrm{z} + \mathrm{d}(\Delta\mathrm{z})}{1+\nu} + \mathrm{z}\right] \qquad (A2.12)$$

where $\nu = \Delta c/\bar{c}$. The differential lengths in the "vee" are shown diagramatically in Figure A2.2. From the geometry,

$$\Delta r = \frac{\Delta x}{\sin\theta_2} \qquad (A2.13)$$

By differentiating this expression with respect to θ_2 we obtain,

$$\begin{aligned}\frac{d(\Delta r)}{d\theta_2} &= \frac{-\Delta x}{\sin^2\theta_2}\cos\theta_2 \\ &= \frac{-\Delta r}{\tan\theta_2}\end{aligned} \qquad (A2.14)$$

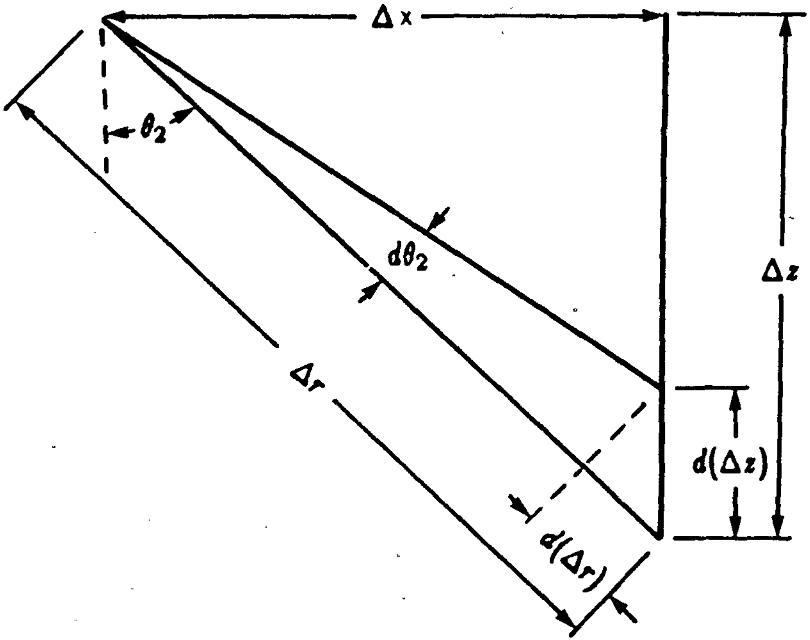

Figure A2.2 Differential lengths in the vee section of Figure A2.1.

The original fringe angle relationship (equation A2.1) can be expanded to determine an expression for $d\theta_2$. This gives,

$$\begin{aligned} \sin(\theta_2 + d\theta_2) &= \frac{m(\bar{c} + \Delta c)}{f_2 d} \\ \sin\theta_2 + d\theta_2\cos\theta_2 &= \frac{m\bar{c}}{f_2 d}(1+\nu) \\ &= \sin\theta_2 + \nu\sin\theta_2 \end{aligned} \qquad (A2.15)$$

from which it can be seen,

$$d\theta_2 = \nu\tan\theta_2. \qquad (A2.16)$$

Substituting this expression into equation A2.14 gives,

$$d(\Delta r) = -\nu\Delta r \qquad (A2.17)$$

The same method also applies to finding an expression for $d(\Delta z)$ in terms of the measurable quantities. From the geometry,

$$\Delta z = \frac{\Delta x}{\tan\theta_2} \tag{A2.18}$$

and differentiating gives,

$$\begin{aligned} \frac{d(\Delta z)}{d\theta_2} &= \frac{-\Delta x}{\sin^2\theta_2} \\ &= \frac{-\Delta z}{\tan\theta_2}\sec^2\theta_2 \end{aligned} \tag{A2.19}$$

Combining this expression with equation A2.16 and then A2.8 gives,

$$\begin{aligned} d(\Delta z) &= -\Delta z\nu\sec^2\theta_2 \\ &= -\Delta z\nu\sec^2\theta_1(1 - 2\epsilon\tan^2\theta_1). \end{aligned} \tag{A2.20}$$

The range dependent terms in equation A2.12 can now be expressed relative to r_1, θ_1, ϵ, and ν. The r_2 term as expressed in equation A2.9 becomes,

$$r_2 = r_1(1 + \epsilon - \epsilon\sec^2\theta_1). \tag{A2.21}$$

Combining equations A2.10 and A2.17 gives,

$$\begin{aligned} \frac{\Delta r + d(\Delta r)}{1+\nu} &= \frac{r_1}{1+\nu}\left(\frac{\Delta r}{r_1} + \frac{d(\Delta r)}{\Delta r_1}\right) \\ &= r_1(1-\nu)\frac{\Delta r}{r_1}\left(1 + \frac{d(\Delta r)}{\Delta r}\right) \\ &= r_1(1-\nu)\epsilon\sec^2\theta_1(1-\nu) \\ &= r_1(1-2\nu)\epsilon\sec^2\theta_1 \end{aligned} \tag{A2.22}$$

Combining equations A2.11 and A2.20 gives,

$$\begin{aligned} \frac{\Delta z + d(\Delta z)}{1+\nu} &= \frac{r_1}{1+\nu}\left(\frac{\Delta z}{r_1} + \frac{d(\Delta z)}{r_1}\right) \\ &= r_1(1-\nu)\frac{\Delta z}{r_1}\left(1 + \frac{d(\Delta z)}{\Delta z}\right) \\ &= r_1(1-\nu)\epsilon\sec\theta_1(1 - \nu\sec^2\theta_1(1 - 2\epsilon\tan^2\theta_1)). \\ &\simeq r_1\epsilon\sec\theta_1(1 - \nu(1 + \sec^2\theta_1)) \end{aligned} \tag{A2.23}$$

With $z = r_1 \cos\theta_1$ the substitution of equations A2.21, A2.22 and A2.23 into A2.12 gives,

$$\begin{aligned}\phi_2 &= f_1(1+\epsilon)\frac{r_1}{\bar{c}}\big[1+\epsilon-2\nu\epsilon\sec^2\theta_1 \\ &\quad +\epsilon\sec\theta_1(1-\nu(1+\sec^2\theta_1)+\cos\theta_1\big] \\ &= f_1(1+\epsilon)\frac{r_1}{\bar{c}}\big[1+\cos\theta_1+\epsilon(1+\sec\theta_1)-\nu\epsilon\sec\theta_1(1+2\sec\theta_1+\sec^2\theta_1)\big] \\ &= f_1(1+\epsilon)\frac{r_1}{\bar{c}}\big[1+\cos\theta_1+\epsilon(1+\sec\theta_1)-\nu\epsilon\sec\theta_1(1+\sec\theta_1)^2\big].\end{aligned} \tag{A2.24}$$

With the phase of path 1 expressed as,

$$\phi_1 = f_1\frac{r_1}{\bar{c}}(1+\cos\theta_1) \tag{A2.25}$$

the final form of equation A2.24 can be rewritten as,

$$\begin{aligned}\phi_2 &= \frac{\phi_1}{1+\cos\theta_1}(1+\epsilon)\big[1+\cos\theta_1+\epsilon(1+\sec\theta_1)-\nu\epsilon\sec\theta_1(1+\sec\theta_1)^2\big] \\ &= \phi_1(1+\epsilon)\big[1+\epsilon\sec\theta_1-\nu\epsilon\sec^2\theta_1(1+\sec\theta_1)\big] \\ &= \phi_1+\phi_1\epsilon(1+\sec\theta_1)(1-\nu\sec^2\theta_1).\end{aligned} \tag{A2.26}$$

By defining ,

$$\Delta\phi = \phi_2 - \phi_1 \tag{A2.27}$$

and,

$$\Delta\phi_o = \phi_1\epsilon(1+\sec\theta_1) \tag{A2.28}$$

the final expression in equation A2.26 can be rearranged to give,

$$\Delta\phi = \Delta\phi_o(1-\nu\sec^2\theta_1). \tag{A2.29}$$

By rewritting this equation in terms of ν we obtain,

$$\nu = \cos^2\theta_1(1-\frac{\Delta\phi}{\Delta\phi_o}). \tag{A2.30}$$

In summary this final expression relates the sound speed between z and $z+\Delta z$ to the mean sound speed from 0 to z ($\bar{c}$).

APPENDIX 3 THE EFFECT OF CURRENTS ON ARRIVAL TIME

This appendix derives the first order change in arrival time for a bistatic acoustic configuration when currents are present. A constant sound speed profile ($c(z) = c_o$) is assumed to keep the analysis simple; however the results will also apply in a refractive environment. This analysis is confined to the x-z plane where v represents currents in the x direction and w is the current speed in the z direction. Figure A3.1 demostrates schematically the effect of currents on a ray trace (solid line). The broken line shows the ray path in the absence of currents. By ~~representing~~ the time between transmission and reflection as t_1 and the time between reflection and reception as t_2 the horizontal distances $b + x$ and x are given by,

$$x + b = t_1(c_o \sin\theta + v) \qquad (A3.1)$$

and,

$$x = t_2 v. \qquad (A3.2)$$

While the depth of reflection z is given by both,

$$z = t_1(c_o \cos\theta + w) \qquad (A3.3)$$

and.

$$z = t_2(c_o - w). \qquad (A3.4)$$

In both the ocean and atmosphere v and w are always much smaller than their corresponding c_o value (1500m/s and 330m/s). Vertical fluid transport in the ocean is rare so w is negligible in the ocean but thermal plumes are common in the atmosphere.

Currents cause the transmit ray to rotate from its original orientation. For the echometer projector θ will also be perturbed by changes in wavelength. These two small rotations will be designated by $d\theta_{rot}$ and $d\theta_{\lambda}$ respectively.

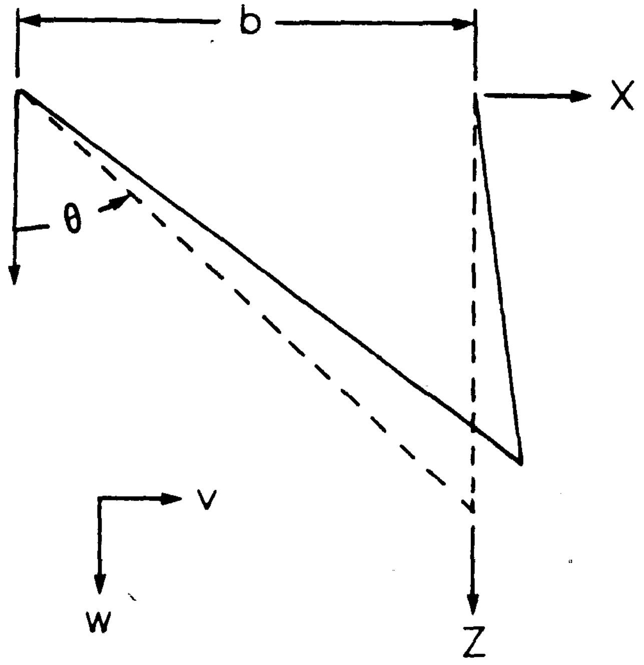

Figure A3.1 When no currents are present the ray trace (broken line) in a constant sound speed profile is defined by θ and b. For positive currents v and w the ray trace is rotated (solid line).

The derivation of $d\theta_{rot}$ requires an expression for the path length r_1 which is the distance from the transmitter to the point of reflection. From equations A3.1 and A3.3 the simple geometry gives.

$$\begin{aligned} r_1^2 &= c_o^2 t_1^2((\sin\theta + v/c_o)^2 + (\cos\theta + w/c_o)^2) \\ &\simeq c_o^2 t_1^2(1 + 2v/c_o \sin\theta + 2w/c_o \cos\theta) \end{aligned} \qquad (A3.5)$$

which further simplifies to,

$$r_1 \simeq c_o t_1(1 + v/c_o \sin\theta + w/c_o \cos\theta) \qquad (A3.6)$$

since $v/c_o << 1$ and $w/c_o << 1$ facilitate the first order analysis. The effective initial ray angle can be expressed by,

$$\begin{aligned}\sin(\theta + d\theta_{\mathrm{rot}}) &= (b + x)/r_1 \\ &= \frac{\sin\theta + v/c_o}{1 + v/c_o \sin\theta + w/c_o \cos\theta} \\ &\simeq \sin\theta + v/c_o \cos^2\theta - w/c_o \sin\theta\cos\theta.\end{aligned} \qquad (A3.7)$$

When combined with

$$\sin(\theta + d\theta_{\mathrm{rot}}) \simeq \sin\theta + d\theta_{\mathrm{rot}} \cos\theta \qquad (A3.8)$$

equation A3.7 produces a simplified expression for $d\theta_{\mathrm{rot}}$. This gives,

$$d\theta_{\mathrm{rot}} \simeq \frac{v}{c_o}\cos\theta - \frac{w}{c_o}\sin\theta. \qquad (A3.9)$$

Angular perturbation from changes in wavelength occurs when the projector is a linear array with spacing d between elements. For these conditions the initial angle is given by,

$$\sin\theta = \frac{mc_o}{fd} \qquad (A3.10)$$

where m is an integer constant and f is the carrier frequency. The effective sound speed along the diagonal ray path r_1 when currents are present becomes,

$$c_r = c_o + v\sin\theta + w\cos\theta. \qquad (A3.11)$$

Since the frequency remains constant the new initial angle will be given by,

$$\begin{aligned}\sin(\theta + d\theta_\lambda) &= \frac{mc_r}{fd} \\ &= \frac{mc_o}{fd}\left(1 + \frac{v}{c_o}\sin\theta + \frac{w}{c_o}\cos\theta\right).\end{aligned} \qquad (A3.12)$$

When combined with the trigonometric expansion (see equation A3.8) the first order estimate of $d\theta_\lambda$ becomes,

$$d\theta_\lambda \simeq \frac{v}{c_o}\sin\theta\tan\theta + \frac{w}{c_o}\sin\theta. \qquad (A3.13)$$

For the echometer system the total change in the initial angle ($d\theta$) is found by combining equations A3.9 and A3.13. This gives,

$$\begin{aligned} d\theta &\simeq d\theta_{rot} + d\theta_{\lambda} \\ &= \frac{v}{c_o}\sec\theta. \end{aligned} \tag{A3.14}$$

Notice that the effects of the vertical currents cancel so that the resulting angular perturbation is only affected by the horizontal current v.

In a current field the reflected ray path will be deflected from a vertical orientation. The amount of angular rotation is given by,

$$\begin{aligned} d\phi &= \tan^{-1}\left(\frac{vt_2}{(c_o - w)t_2}\right) \\ &\simeq \frac{v}{c_o}. \end{aligned} \tag{A3.15}$$

These small angular rotations can now be utilized to find both the diagonal and vertical ray path lengths. The ray paths define a triangle with the length of one side fixed (the baseline = b) and since the angles are known the law of sines can be applied to find the length of the two sides r' and z'. The resulting equations are,

$$\frac{r'}{\sin(\pi/2 + d\phi)} = \frac{b}{\sin(\theta + d\theta - d\phi)} = \frac{z'}{\sin(\pi/2 - \theta - d\theta)}. \tag{A3.16}$$

The sine terms in these equations can all be reduced to simpler forms by utilizing the previous analysis. From equation A3.15 we know that $d\phi$ is a small number so that,

$$\sin(\pi/2 + d\phi) \simeq 1. \tag{A3.17}$$

Substituting equations A3.14 and A3.15 into the second sine term in equation A3.16 and performing a first order analysis gives,

$$\begin{aligned} \sin(\theta + d\theta - d\phi) &= \sin\theta\cos\left(-\frac{v}{c_o} + \frac{v}{c_o}\sec\theta\right) + \cos\theta\sin\left(-\frac{v}{c_o} + \frac{v}{c_o}\sec\theta\right) \\ &\simeq \sin\theta + \cos\theta\left(-\frac{v}{c_o} + \frac{v}{c_o}\sec\theta\right) \\ &= \sin\theta + \frac{v}{c_o}(1 - \cos\theta) \end{aligned} \tag{A3.18}$$

when $\frac{v}{c_o}\sec\theta << 1$ is true. The third sine term in equation A3.16 can also be simplified when equation A3.14 is substituted into its argument. This gives,

$$\begin{aligned}\sin(\pi/2 - \theta - d\theta) &= \cos\theta\cos(\frac{v}{c_o}\sec\theta) - \sin\theta\sin(\frac{v}{c_o}\sec\theta)\\ &\simeq \cos\theta - \frac{v}{c_o}\tan\theta.\end{aligned} \tag{A3.19}$$

The diagonal path length in the presence of a current field can now be found. Combining equations A3.16, A3.17, and A3.18 gives,

$$\begin{aligned}r' &= \frac{b}{\sin\theta + \frac{v}{c_o}(1 - \cos\theta)}\\ &= \frac{b}{\sin\theta}\left[1 + \frac{v}{c_o}\frac{1 - \cos\theta}{\sin\theta}\right]^{-1}\\ &\simeq r(1 - \frac{v}{c_o}\frac{1 - \cos\theta}{\sin\theta})\end{aligned} \tag{A3.20}$$

where r is the path length when no currents are present.

The vertical path length in a current field is simplified by combining equations A3.16, A3.18, and A3.19. This gives,

$$\begin{aligned}z' &= \frac{b(\cos\theta - \frac{v}{c_o}\tan\theta)}{\sin\theta + \frac{v}{c_o}(1 - \cos\theta)}\\ &\simeq z(1 - \frac{v\sin\theta}{c_o\cos^2\theta})(1 - \frac{v}{c_o}\frac{1 - \cos\theta}{\sin\theta})\\ &\simeq z(1 - \frac{v}{c_o}\frac{1 - \cos^3\theta}{\sin\theta\cos^2\theta})\end{aligned} \tag{A3.21}$$

An estimate of the travel time in a current field can now be made by combining the last 2 equations with their effective sound speed. This gives,

$$\begin{aligned}t + dt &= \frac{r(1 - \frac{v}{c_o}\frac{1 - \cos\theta}{\sin\theta})}{c_o(1 + \frac{v}{c_o}\sin\theta + \frac{u}{c_o}\cos\theta)} + \frac{z}{c_o - u}(1 - \frac{v}{c_o}\frac{1 - \cos^3\theta}{\sin\theta\cos^2\theta})\\ &\simeq \frac{r}{c_o}(1 - \frac{v}{c_o}(\frac{1 - \cos\theta}{\sin\theta} + \sin\theta) - \frac{u}{c_o}\cos\theta) + \frac{z}{c_o}(1 - \frac{v}{c_o}\frac{1 - \cos^3\theta}{\sin\theta\cos^2\theta} + \frac{u}{c_o})\\ &\simeq \frac{r + z}{c_o} - \frac{v}{c_o}(\frac{r}{c_o})\sin\theta + \frac{1 - \cos\theta}{\sin\theta} + \frac{z}{c_o}(\frac{1 - \cos^3\theta}{\sin\theta\cos^2\theta}))\end{aligned} \tag{A3.22}$$

The first term in this last expression represents the arrival time when no currents are present. The difference in arrival time is then found directly from equation A3.22 which gives,

$$dt = -\frac{vb}{c_o^2}\left(\frac{2+\cos\theta}{1+\cos\theta} + \frac{1-\cos^3\theta}{\cos\theta - \cos^3\theta}\right) \qquad (A3.23)$$

since $r = b\csc\theta$ and $z = b\cot\theta$. Notice that vertical currents have a negligible effect on the change in arrival time. This result is valid for $\frac{v}{c_o}\sec\theta << 1$, $\frac{v}{c_o} << 1$, and $\frac{w}{c_o} << 1$.

For currents in the y direction (u) the transmitted pulse will also be deflected from its initial trajectory. Since u is orthogonal to the velocities in the xz plane there will be no change in the arrival time estimates.

APPENDIX 4 DOCUMENTATION OF THE NUMERICAL MODEL

In the ocean a bistatic acoustic device is parameterized by discrete scatterers, acoustic beam patterns, refraction, scatterer density, transmission losses, and target strength. These constraints have been modelled to provide a computer simulation of the instrument in a defined environment. A flowchart of the functional development within the model is given in Figure A4.1 to facilitate this description for a two-frequency scheme.

1. Initially the fundamental constants such as fringe number, frequency, reference sound speed, baseline, etc. are defined and the plotter is initiallized.

2. For quick access to the projector's beam pattern the theoretical pattern was stored on disk in a separate program. In this way the digital values, in 0.01° increments, are read in at the beginning of the program so that when the directivity at a specific angle is required its value can be extracted from its position within the array. An additional advantage of this method is that results from beam pattern calibrations could easily be incorporated. Recalling that the beam pattern is dependent on frequency and the reference sound speed, it must be recalculated each time these parameters are altered.

3. By using the mixed multiplication congruential method (a random reference number generator) repeatable random sequences are obtained for each unique numerical seed. Thus, each pseudo random number that is generated provides the basis for determining a new and unique scatterer location.

4. Before computing an ensemble of random scatterer positions within the insonified volume of the *m*th fringe, the bounds on the volume were obtained. Recalling the dependence of the *m*th fringe and θ on frequency f,

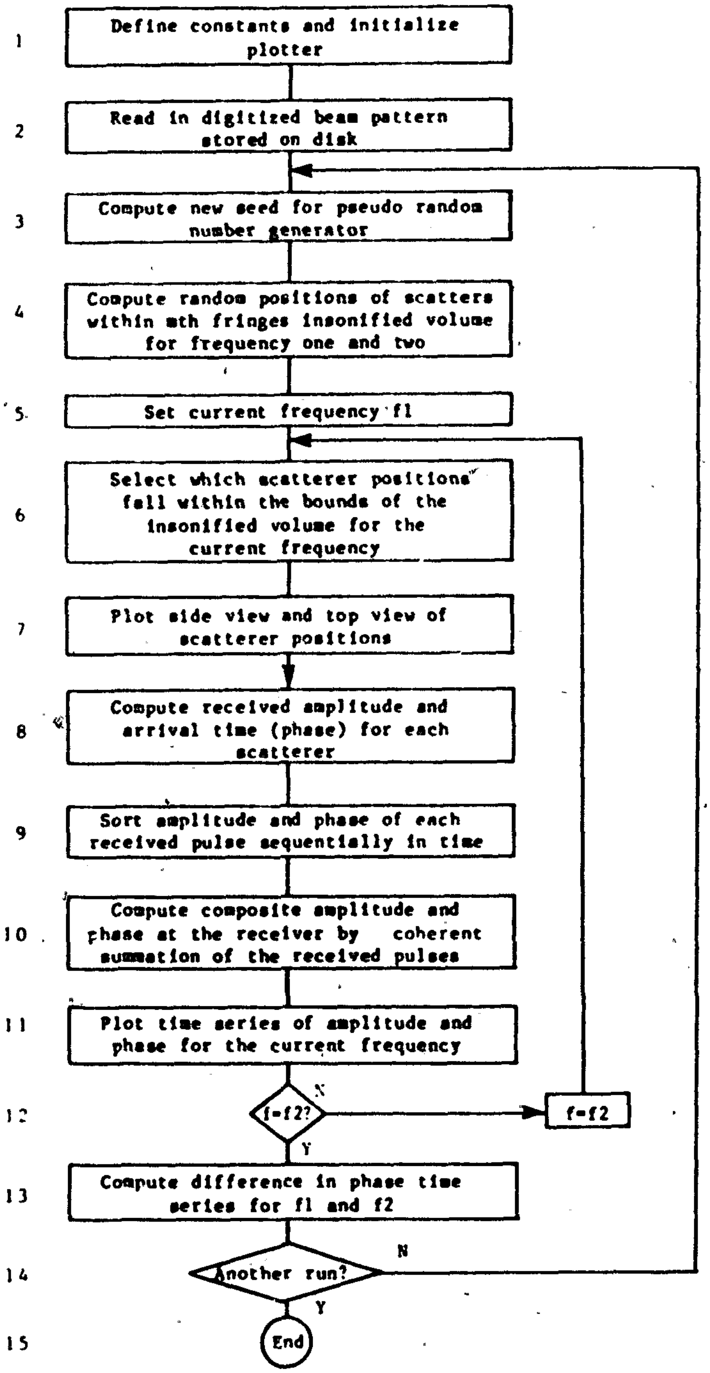

Figure A4.1 A functional flowchart of the numerical model which simulates the received echo from a set of discrete scatterers within an insonified volume.

reference sound speed c_o and element separation d,

$$\theta = \sin^{-1}(mc_o/df)$$

the volume of insonification is defined by the angles of destructive interference $\theta(m - 1/2)$ and $\theta(m + 1/2)$, by subtending these rays from the projector and slicing the cone of reception (defined by the -3dB points on the main lobe of the hydrophone). For details of this method refer to section A4.1. To facilitate a realistic comparison of the received signal for 2 closely separated frequencies, the upper bounding angle was computed for the lowest frequency and conversely for the lower bounding angle of the highest frequency. With these bounds determined, a minimal cylinder was computed which contained this general volume of insonification. After multiplying the volume of the cylinder by the scatterer density the resulting N scatterers were then assigned random positions within the cylinder.

5. On the first pass the acoustic frequency is set to the higher of the two values.

6. With the frequency now defined a set of conditions are applied to the general set of scatterer positions within the cylinder to select which points lie within the volume of insonification as defined by the current frequency. The details of these constraints are given in section A4.2.

7. Verify the scatterer positions and record the nature of the distribution by plots in the xy plane (side view) and yz plane (top view).

8. By applying formulae generated by Snell's law and integration for a linear sound speed profile, the intial angle γ_i from the projector was computed for each ith scatterer position (for details refer to section A4.3). For each

γ_i the corresponding directivity of the projector was retrieved from its position in the beam pattern array, so that accurate initial amplitudes could be simulated. Similarly the position of each target was also used to find its corresponding directivity relative to the hydrophone. The hydrophone directivity was modelled by a main lobe with parabolic shape and negligible side lobes. Using γ_i, scatterer position (x_i, y_i, z_i) and the relative hydrophone position the travel time t_i and range from projector to target and target to hydrophone were computed for all N targets. The values of range were then inserted in the sonar equation with their corresponding directivities and the amplitude of each ray a_i at the receiver was computed. For the ranges and frequencies used spherical spreading dominates over absorption for the transmission losses.

9. In order to facilitate interpretation of the composite amplitudes and phases, they were sorted in time from 1st to last.

10. The received signals are then summed to obtain the calculated sound pressure levels at the hydrophone as a function of time (or range).

$$\tilde{s}(t) = A\sin(\omega t + \Phi) = \sum_{i=1}^{N} a_i \sin(\omega t + \phi_i)$$

where the amplitude a_i and phase ϕ_i for each scatterer are a function of position and hence of time. Figure A4.2 gives simple examples of the summing process.

11. For practical reasons only the envelope of the received signal is plotted.

12. Steps 6-11 are repeated for the remaining frequencies to be simulated.

13. Using the phase time series for the 2 frequencies the phase difference as a function of time is computed by subtracting digital values at small increments in time.

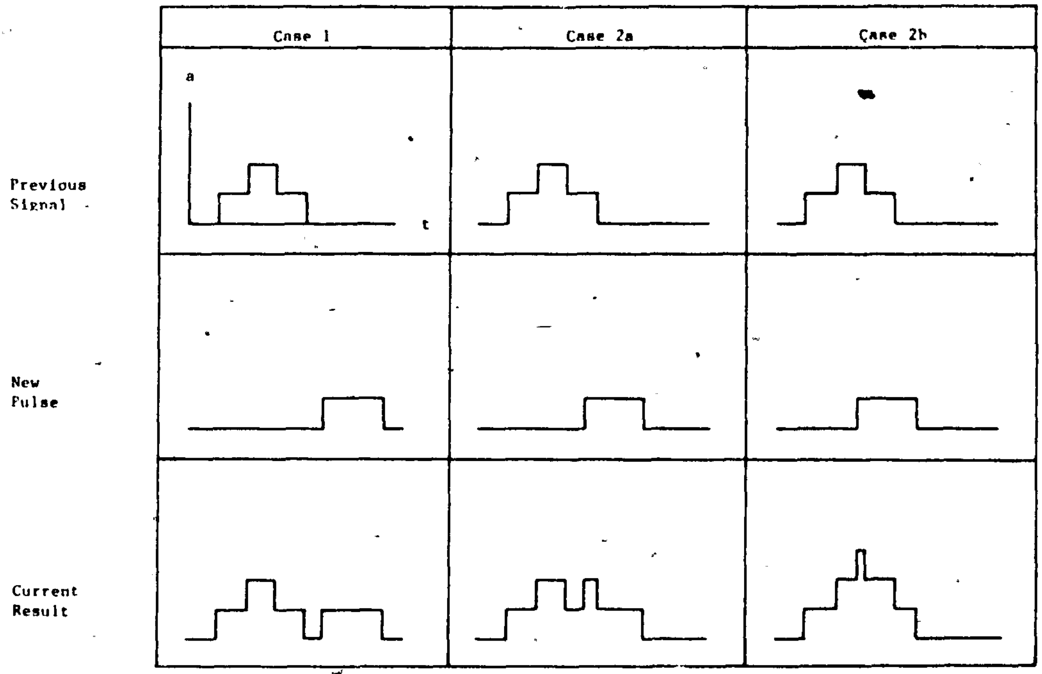

Figure A4.2 Possible combinations of a 3rd pulse with the previous signal when the pulses are added sequentially by arrival time.

14. If another run in requested, the program returns to step 3 to compute a new seed.

A4.1 Defining bounds on a cylinder

This section defines the bounds on the minimum cylinder which contains the insonified volume. The angles of destructive interference about the *m*th fringe are taken as the upper and lower bounds on the cylinder. Thus,

$$\alpha_1 = \sin^{-1}\left(\frac{(m+1/2)c_o}{df_1}\right) \qquad (A4.1.1)$$

and,

$$\alpha_2 = \sin^{-1}\left(\frac{(m-1/2)c_o}{df_1}\right) \qquad (A4.1.2)$$

where, $f_1 > f_2$, see Figure A4.3. The narrow beam hydrophone has a beam width 2β between the -3dB points, and is assumed to be symmetric. $Z1$ and $Z2$ are determined by assuming a linear sound speed profile $c(Z) = c_o + gZ$, where c_o is the surface sound speed and g is the slope. Applying Snell's Law and integrating gives,

$$Z = \frac{1}{g}\left(\sqrt{\frac{1 - (\eta - Bpg)^2}{p}} - c_o\right) \qquad (A4.1.3)$$

where,

$$\eta = \sqrt{1 - p^2 c_o^2}$$

and,

$$p = \frac{\sin\alpha}{c_o}.$$

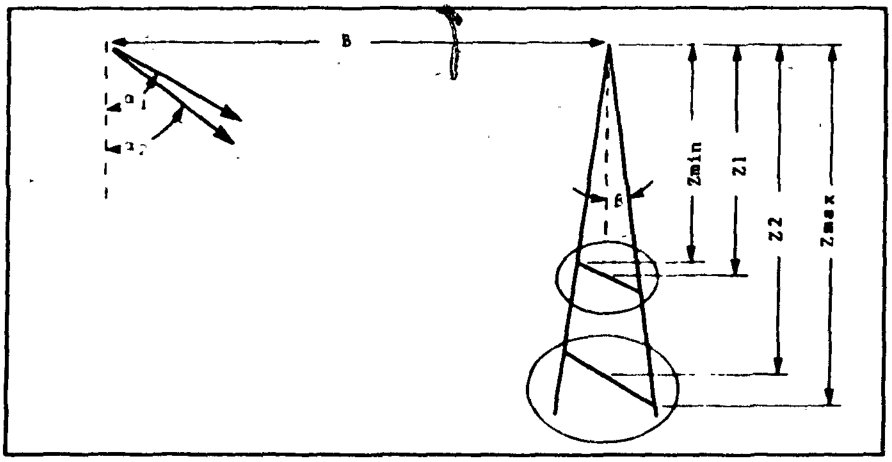

Figure A4.3 Geometry defining the insonified volume based on beam widths of the *m*th fringe and the hydrophone main lobe.

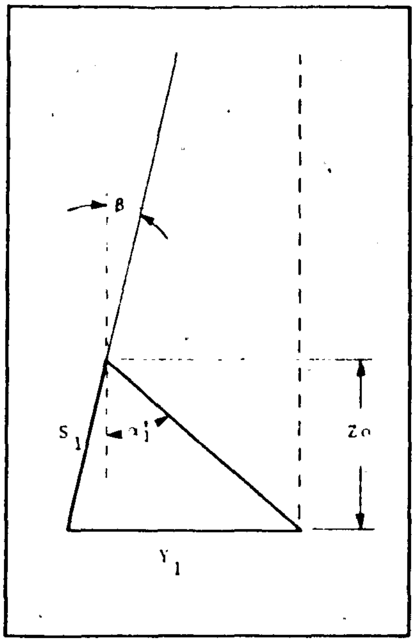

Figure A4.4 Geometry defining the minimum depth of the insonified volume.

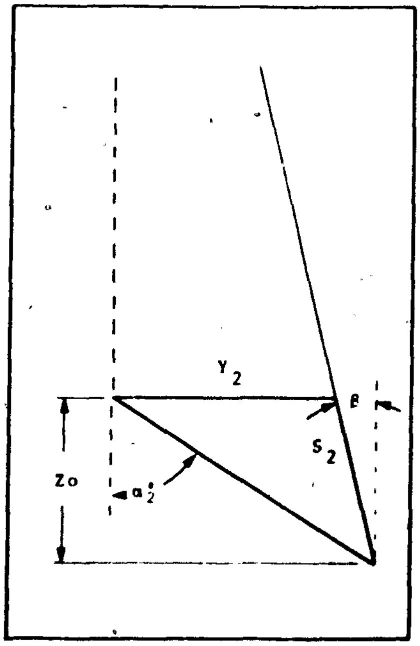

Figure A4.5 Geometry defining the maximum depth of the insonified volume.

The minimum depth of the volume is found from local geometry, Snell's Law, and the law of sines. Refering to Figure A4.4,

$$Y_1 = Z1 \tan\beta$$
$$\alpha_1' = \sin^{-1}(\frac{c_o + gZ1}{c_o} \sin\alpha_1)$$
$$S_1 = Y_1 \frac{\sin(\pi/2 - \alpha_1')}{\sin(\alpha_1' - \beta)}$$

then,

$$Z_{min} = Z1 - S_1 \cos\beta. \qquad (A4.1.4)$$

Similarly, to find the maximum depth of the volume as seen in Figure A4.5,

$$Y_2 = Z2 \tan\beta$$
$$\alpha_2' = \sin^{-1}(\frac{c_o + gZ2}{c_o} \sin\alpha_2)$$
$$S_2 = Y_2 \frac{\sin(\pi/2 - \alpha_2')}{\sin(\alpha_2' - \beta)}$$

then,

$$Z_{max} = Z2 + S_2 \cos\beta. \qquad (A4.1.5)$$

Using $Z - min$ and Z_{max} we can now compute the minimum volume of a cylinder V_c which contains the volume of interest.

$$V_c = \pi(Z_{max} - Z_{min})(Z_{max} \tan\beta)^2. \qquad (A4.1.6)$$

A4.2 Defining bounds on the insonified volume

With N scatterer positions randomly computed within a cylinder of minimal volume which contains the insonified volume for the mth fringe, it remains to define which positions are inside the insonified volume. Refering to Figure A4.6, the upper and lower corners in the XZ plane are defined by,

$$(X_1, Z_1) = (-Z_{min} \tan\beta, Z_{min})(X_3, Z_3) = (-Z_{max} \tan\beta, Z_{max})$$

The other two corners are found by the intersection of two linear equations. For $Z = m_2X + b_2$ and $Z = m_4X + b_4$,

$$X = (b_4 - b_2)/(m_2 - m_4)$$

To determine which positions (X, Y, Z) are within the bounds the following conditions must be satisfied:

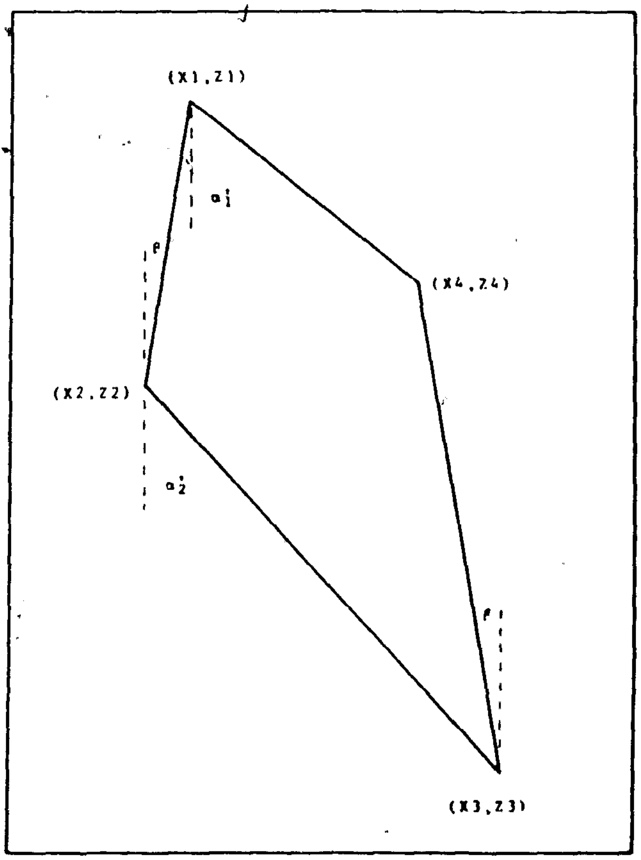

Figure A4.6 Positions of corners in the vertical plane of the insonified volume.

1/ The position must be within the cone subtended below the hydrophone,

$$\sqrt{X^2 + Y^2} < Z \tan\beta.$$

2/ The depth must be below the upper bounding ray from the projector,

$$Z > (X + Z_{min}\tan\beta)\cot\alpha_1' + Z_{min}.$$

3/ The depth must be above the lower bounding ray from the projector,

$$Z > Z_{max} - ((Z_{max}\tan\beta - X)\cot\alpha_2').$$

A4.3 Derivation of the initial angle

This section derives the initial projector angle in a linear sound speed profile when the end point of the ray is known.

For a linear sound speed profile $c(z) = c_o + gz$ ray theory can be applied to compute the horizontal range χ analytically.

$$\chi = \int_0^x dx = \int_0^z \tan\theta(z)dz \qquad (A4.3.1)$$

From Snell's Law,

$$\sin\theta(z) = pc(z)$$
$$\tan\theta(z) = \frac{\sin\theta}{\sqrt{1-\sin^2\theta}} = \frac{pc(z)}{\sqrt{1-p^2c^2(z)}}.$$

Substituting this expression into equation A4.3.1 and evaluating the integral gives,

$$\chi = \frac{1}{pg}\left(\sqrt{1-p^2c_o^2} - \sqrt{1-p^2(c_o+gz)^2}\right). \qquad (A4.3.2)$$

Expanding this equation and rewriting in terms of θ gives,

$$\theta = \tan^{-1}\left(\frac{2\chi g/c_o}{(\chi g/c_o)^2 + (1 + gz/c_o)^2 - 1}\right). \qquad (A4.3.3)$$

APPENDIX 5 EVALUATING $P(\Phi)$ FROM SECTION 6.4

An analytic expression for $P(\Phi)$ will be derived using the joint pdf $P(A,\Phi)$ in equation 6.2.7. This number of events per unit angle $d\Phi$ is given by.

$$P(\Phi)d\Phi = \int_0^\infty P(A,\Phi)\,dA\,d\Phi$$

$$= \frac{1}{2\pi\sigma^2}\int_0^\infty A\exp\left[-\frac{1}{2\sigma^2}(A^2 + a_o^2 - 2Aa_o\cos\Phi)\right]dA\,d\Phi$$

Let,

$$k = \frac{1}{2\pi\sigma^2}\exp\left[\frac{-a_o^2\sin^2\Phi}{2\sigma^2}\right],$$

$$u = \frac{A - a_o\cos\Phi}{\sigma\sqrt{2}},$$

$$U = \frac{a_o\cos\Phi}{\sigma\sqrt{2}},$$

$$du = \frac{dA}{\sigma\sqrt{2}}.$$

Then,

$$P(\Phi) = k\int_{-U}^\infty (\sqrt{\text{[illegible]}}u + a_o\cos\Phi)e^{-u^2}(\sqrt{2}\sigma)du$$

$$= -k\sigma^2 e^{-u^2}\Big|_{-U}^\infty + ka_o\cos\Phi\cdot\sqrt{2}\sigma\int_{-U}^\infty e^{-u^2}\,du.$$

Terms within this last expression can be simplified by the following definitions.

$$\operatorname{erf}(z) = \frac{2}{\sqrt{\pi}}\int_0^z e^{-t^2}\,dt$$

$$\gamma = \frac{a_o^2}{2\sigma^2}.$$

The final evaluation can now be expressed as,

$$P(\Phi) = \frac{1}{2\pi}e^{-\gamma} + \frac{\sqrt{\gamma}}{2\sqrt{\pi}}\cos\Phi e^{-\gamma\sin^2\Phi}\left(1 + \frac{\cos\Phi}{|\cos\Phi|}\operatorname{erf}(\sqrt{\gamma}\cos\Phi)\right).$$

APPENDIX 6 DERIVING EQUATION 10.3.5

Deriving the second moment of a velocity component in the ζ direction requires a knowledge of the three dimensional probability density function (pdf) of the velocity. Since the physical problem involves a uniform angular distribution in space the 3D pdf becomes,

$$P(u,\theta,\phi) = \frac{1}{k} p(u) u^2 du \sin\phi d\theta d\phi \tag{A6.1}$$

where p(u) is the speed pdf and k, the normalization factor, is determined by,

$$\begin{aligned} k &= \int_0^{\pi} \int_{-\pi}^{\pi} \int_0^{\infty} P(u,\theta,\phi) du d\theta d\phi \\ &= \frac{4}{3}\pi \int_0^{\infty} u^2 p(u) du \end{aligned} \tag{A6.2}$$

The speed pdf can often be represented by a Gaussian distribution with a speed offset u_o. The evaluation of the integral equations for the second moment cannot be solved explicitly for this case. A simplification to the speed pdf can be made by assuming a uniform distribution between $u_o - \delta$ and $u_o + \delta$. Then the normalization factor is,

$$\begin{aligned} k &= \frac{4}{3}\pi \int_{u_o-\delta}^{u_o+\delta} u^2 du \\ &= \frac{4}{3}\pi(6u_o^2\delta + 2\delta^3) \end{aligned} \tag{A6.3}$$

and the second moment of $u_\zeta = u\cos\phi$ is,

$$\begin{aligned} \langle u_\zeta^2 \rangle &= \frac{1}{k} \int_0^{\pi} \int_{-\pi}^{\pi} \int_{u_o-\delta}^{u_o+\delta} u^4 \cos^2\phi \sin\phi du d\theta d\phi \\ &= \frac{1}{k}\frac{4}{3}\pi\frac{1}{5}[(u_o+\delta)^5 - (u_o-\delta)^5] \\ &= \frac{u_o^4 + 2u_o^2\delta^2 + \delta^4/5}{3u_o^2 + \delta^2} \end{aligned} \tag{A6.4}$$

For $\delta << u_o$ the final equation in A6.4 simplifies to give,

$$\langle u_\zeta^2 \rangle \sim \frac{u_o^2}{3} \tag{A6.5}$$

Now if u has a Gaussian pdf with u_o representing the mean value and σ the standard deviation then the mean value of u^2 will be,

$$\langle u^2 \rangle = \frac{1}{\sqrt{2\pi}\sigma} \int_0^{\infty} u^2 \exp[-(u-u_o)^2/2\sigma^2] du. \qquad (A6.6)$$

By making the substitution $w = u - u_o$ and identifying the error function as,

$$\mathrm{erf}(z) = \frac{2}{\sqrt{\pi}} \int_0^{z} \mathrm{e}^{-t^2} \mathrm{d}t \qquad (A6.7)$$

then equation A6.6 becomes,

$$\langle u^2 \rangle = \frac{3}{\sqrt{2\pi}} u_o \sigma e^{-u_o^2/2\sigma^2} + (u_o^2 + \sigma^2) \left(\frac{1}{2} + \frac{1}{2} \mathrm{erf}\left(\frac{\mathrm{u_o}}{\sqrt{2}\sigma} \right) \right). \qquad (A6.8)$$

By combining equations A6.5 and A6.8 the second moment of the ζ component of a randomly oriented velocity vector with a Gaussian distributed speed is described by,

$$\langle u_\zeta^2 \rangle = \frac{1}{\sqrt{2\pi}} u_o \sigma e^{-u_o^2/2\sigma^2} + \frac{1}{3} (u_o^2 + \sigma^2) \left(\frac{1}{2} + \frac{1}{2} \mathrm{erf}\left(\frac{\mathrm{u_o}}{\sqrt{2}\sigma} \right) \right). \qquad (A6.9)$$